New frontiers of molecular beacons: signal amplification and nanomachines

Della Vedova, Paolo

Publication date:
2013

Document Version
Publisher's PDF, also known as Version of record

Ph.D. Thesis, *June 2013*

New frontiers of Molecular Beacons:

signal amplification and nanomachines.

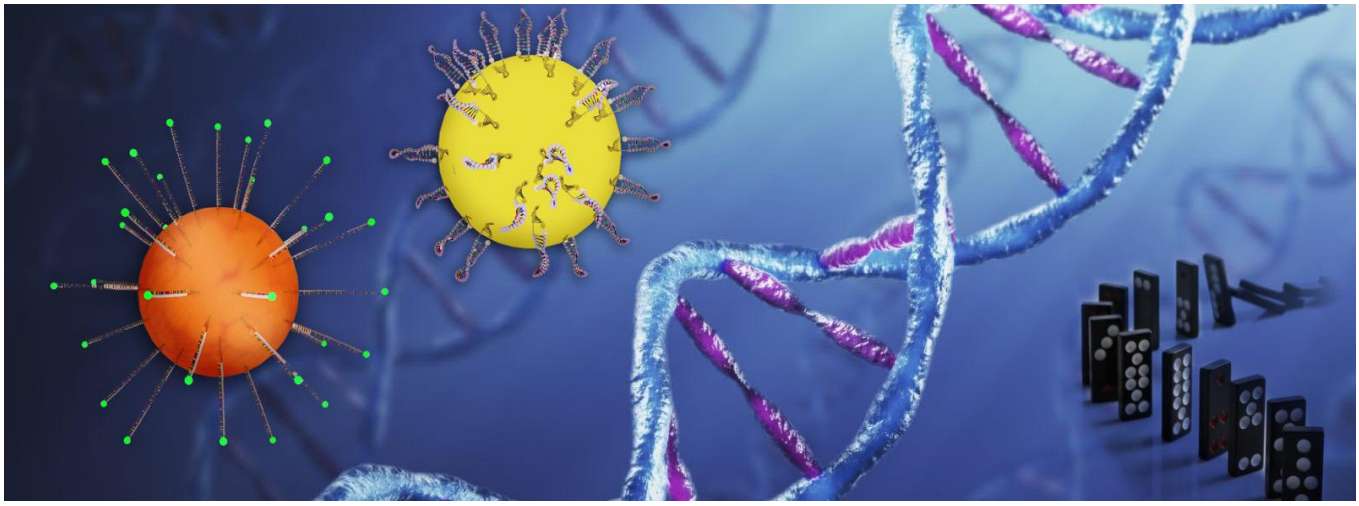

Ph.D Candidate:

Paolo Della Vedova

DTU Nanotech, Danmarks Tekniske Universitet

Supervisor:

Ole Hansen

Co-Supervisor:

Martin Dufva

DTU Nanotech

Department of Micro- and Nanotechnology

Qual è 'l geomètra che tutto s' affige
per misurar lo cerchio, e non ritrova,
pensando, quel principio ond' elli indige,

tal era io a quella vista nova;
veder volea come si convenne
l'imago al cerchio e come vi s' indova;

ma non eran da ció le proprie penne:
se non che la mia mente fu percossa
da un fulgore in che sua voglia venne.

Paradiso, Canto XXXIII.

Abstract

Gene expression is the process in which information stored into a gene is used to create a functional gene product, for example a protein or a functional RNA. Gene expression is used by all living organism to control cell life, differentiation, regeneration and cancer genesis. Molecular beacons provide a useful way to detect gene expression inside living cells without influencing the cell behavior. Molecular beacons are a particular kind of nucleic acid based probes composed by an oligonucleotide chain which assumes a hairpin configuration, encoding the target sequence of interest (loop) flanked by two complementary strands (stem), conjugated respectively with a fluorophore and a quencher. Upon hybridization with complementary target, the stem bonds break, parting the fluorophore from the quencher and resulting in a detectable signal.

This thesis is divided in two major sections.

The first section gives initially an overview of the molecular beacon technology usability and working principle. Later on the mechanism of molecular beacon's internalization by SLO treatment was theoretically and experimentally investigated to determine optimal transfection condition and actual cell loading. Finally the problem of signal generation by molecular beacons was tackled by developing two new methods. It was demonstrated that by carefully design of interacting beacons with a new geometrical configuration, it is possible to induce among them both a linear and an avalanche reaction which improve the signal emission greatly.

The second section of the thesis investigates the possibility to remotely activate gold nanoparticles conjugated to molecular beacons through an external radio frequency field. The gold nanoparticle will serve both as quencher for the fluorescence emission and as local point source of heat. The interaction between gold nanoparticles and a RF field will be investigated both theoretically and experimentally. The new gold-conjugated molecular beacon, called Nanomachine, could potentially be used in living cells to track e.g. down regulation of gene expression.

Resume

Genekspression er processen, hvor information, der er lagret i et gen, bruges til at skabe et funktionelt genprodukt, for eksempel et protein eller et funktionelt RNA. Genekspression benyttes af alle levende organismer til at regulere cellernes liv, deres differentiering, regenerering og desværre også til udviklingen af kræft. Molekylære beacons (MB'er) er et nyttigt værktøj til at detektere genekspression i levende celler uden at påvirke cellens opførsel. MB'er er særligt konstruerede nukleinsyre-baserede prober bestående af en oligonukleotidkæde i en hårnåls konfiguration, der består af nåleøjet, der koder for sekvensen, der skal detekteres, og er flankeret af to komplementære strenge (stammen), afsluttende med henholdsvis en fluorofor og en quencher, der kan slukke for fluoroforens fluorescens, når de er tæt på hinanden. Efter hybridisering med den komplementære sekvens, åbnes stammen og fluoroforen adskilles fra quencheren, så der kan måles et fluorescenssignal. Afhandlingen er opdelt i to hovedafsnit. Den første del giver først en introduktion til MB-teknologi, dens anvendelse og funktionsprincip. Derefter beskrives en metode til at internalisere MB'er i celler (transfektion) ved hjælp af SLO behandling. Dette undersøges både teoretisk og eksperimentelt for at bestemme optimale transfektions betingelser og den resulterende MB koncentration i cellerne. Endelig er problemet med lavt signalniveau fra MB'er blev løst ved udvikling af to nye metoder. Det bliver her vist, at ved omhyggeligt design af vekselvirkende MB'er i en ny geometrisk konfiguration, er det muligt at inducere både en lineær og en lavinereaktion, som forbedrer MB signalet meget. Anden del af afhandlingen undersøger muligheden for at aktivere guldnanopartikler bundet til molekylære beacons ved hjælp af et eksternt radiofrekvensfelt. Guldnanopartikelerne tjener både som quencher for fluorescensemissionen og som en lokal punktvarmekilde. Samspillet mellem guldnanopartikler og et radiofrekvensfelt er blevet undersøgt både teoretisk og eksperimentelt. Det nye MB med guldnanopartikler, en såkaldt nanomaskine, kan potentielt anvendes i levende celler til at følge f.eks nedregulering af genekspression.

Preface

The work described in this thesis has been carried out in the Silicon Microtechnology group and in Fluidic Array Systems and Technology (FAST) group at the Department of Micro- and Nanotechnology (DTU Nanotech), Technical University of Denmark (DTU) in the time period from April 2010 to June 2013. The work has been supervised by main supervisor prof. Ole Hansen and co-supervisor assoc. prof. Martin Dufva. The work was supported by FTP grant 09-070568.

Acknowledgements

As first I would like to thank all the people that made this project possible; my supervisor, Ole Hansen for his infinite knowledge about any topic and his incomparable ability and precision in reviewing each time my work. My co-supervisor Martin Dufva, which has been the irreplaceable column of this project, thanks for all the discussion we had and for always trying to be positive and give motivation even when the results seemed not to come along. Our brainstorming generates some good ideas but it was only thanks to his ability to endure that the results came. Thanks to Mira, my project mate, for having taken care of some of the biology related to the project. Thanks to Jens Hemmingsen for the help in the cleanroom and thanks to Vitaliy Zhurbenko for the antenna design and characterization. Thanks to Mette for the help with the cell experiments and Peder and David for the introduction to microfluidics. Grazie Claudia for the help with the thesis cover and graphic review. Finally thanks to all the people in both Silicon Microtechnology group and the FAST group.

I want to specially thank my family for the irreplaceable support that they provide me through the entire course of my life. I know that it has not been easy for you seeing me going far away for such long time, but, arrived at the very end of my education, I hope that you could always look back at all the sacrifices that you have done for me and be happy. I hope that I made you proud of me. Special thanks to my father, Giorgio, that is able every time to teach me something, even when the truth is difficult to accept.

A special thank goes to my best pal, Filippo. Since we meet, 8 years ago, our friendship has been simply invaluable. We have done, shared and experienced so many things together, and we taught each other every day, always keep pushing to get better. I would not be the person I am right now if it would not be for you and I know that you think the same. Thanks!

Grazie to all my friends back home, especially, Nicoló, Renato, Francesco and Filippo. I might be distant, but you guys are always a great reason to fly back home. Our path might diverge but we will never be far!

Finally thanks to all the awesome people I have met during this exciting

experience. It would be impossible to name you all but, whether or not you are reading these lines, I want to thank you for all the chat, drinks, parties, suggestions, sport, activities and whatever we have done together. You contribute significantly to make all this possible.

Contents

List of Figures

List of Tables

List of publications

Submitted Manuscripts

1. *Nanomachines - Gold Nanoparticle Based Sensors Activated by External Radio Frequency Fields.* **Paolo Della Vedova**, Mirolyuba Ilieva, Vitaliy Zhurbenko, Martin Dufva, Ole Hansen. Submitted to Small.

2. *Dynamic tracking of expression of neuronal markers in living human neurons detected using molecular beacons.* Ilieva M., **Della Vedova P.**, Hansen O., Dufva M. Submitted manuscript to Developmental Neurobiology.

Patents

1. *Enzyme free nucelic acid amplification of molecular beacon signal generation.* **Paolo Della Vedova**, Martin Dufva. Currently on novelty search.

Peer-reviewed conference proceedings

1. *Nanomachine Based Optical Sensors.* **Paolo Della Vedova**, Mirolyuba Ilieva, Ole Hansen, Martin Dufva 2012. IEEE-EMBS Micro and Nanotechnology in Medicine Conference, The Westin Maui Resort and Spa, Ka'anapali, Hawaii.

2. *Molecular Beacon Technology Based Sensor for Real-Time Detection and Tracking Neural Stem Cell Differentiation.* Mirolyuba Ilieva, **Paolo Della Vedova**, Martin Dufva. 2012 IEEE-EMBS Micro and Nanotechnology in Medicine Conference, The Westin Maui Resort and Spa, Ka'anapali, Hawaii.

Conference contribution

1. *Nanomachine for kinetic studies of gene activity in living cells***Paolo Della Vedova**, Mirolyuba Ilieva, Martin Dufva, Ole Hansen. NanoUpdate 2012, Helsingborg, 27-28 March 2012.

Manuscripts in preparation

1. *Biochemical characterization of RNA and DNA based molecular beacons.* **Paolo Della Vedova**, Mirolyuba Ilieva, Ole Hansen, Martin Dufva.

2. *Enzyme free nucelic acid signal amplification using nested molecular beacons.* **Paolo Della Vedova**, Martin Dufva.

Part I

Part 1 - Molecular Beacons and Signal Amplification

Chapter 1

Introduction

In this chapter I will give an introduction to the molecular beacon technology. The information provided here will constitute the basic knowledge package which the entire thesis is built upon. As a first step I will give an introduction regarding the structure and function of the molecular beacons, particularly focusing on the quenching phenomenon. Then I will present some application and advantages of molecular beacons over competing technologies.

1.1 Molecular beacons

The discovery of the double stranded structure of the DNA [1] unveiled the importance of nucleic acids in life processing. A wide range of cellular functions are related to expression of gene and transcription of it in functional ribonucleic acids (RNAs). To fully understand cellular processes it is necessary not only to be able to detect a particular RNA strand, but also to investigate its temporal evolution, its spatial distribution and transport. In the recent years the importance of localization of gene expression has been pointed out. Various studies have shown that abnormal expression and centering of mRNA can cause serious pathology, for example alteration of cell morphology [2]. The key role of inter cellular mRNA expression is also significant; cell-to-cell variation of gene expression in a small fraction of cancerogenic cells could lead to major effects, like drug resistance [3]. Many methods have been developed to investigate RNA expression between cellular population, such as polymerase chain reaction, [4] northern blot [5] or microarrays [6]. Although these techniques proves their usefulness in many assays, they all share some limitations. First of all they rely on fixed samples and most of the time dead cells, reducing the information about spatial and temporal dynamics. Furthermore they are quite laborious and time consum-

ing and the sample preparation can affect considerably the final result. The most adequate way to obtain information about dynamics of gene expression would therefore be to use living cells assays. In these condition there is the need for a new kind of probe, with high sensitivity, and specificity, good signal-to-noise ratio and suitable for low abundancy targets. Ideally this probe should be able to locate gradients of targets mRNAs inside cells, have a fast kinetic of hybridization at physiological temperature and support a delivery method that do not influence or produce damages to the cell.

The mechanism of base paring, which is one of the strongest and specific biomolecular interaction, opened the possibility for a new variety of oligonucleotides-based probes. At the present time, nucleic acid based probes are irreplaceable arrows in the quiver of any biologist. The Molecular Beacon (MB) [7] is an excellent example of nucleic acid probe. It is constituted by an oligonucleotide chain divided in two main sections, a loop sequence, usually 15-30 base pairs (bps) long which serve as recognition sequence, and a shorter sequence stem, 5-6 bps long, which flank the loop sequence on both sides and acts as a hinge, forcing the oligonucleotide in the hairpin configuration (Fig.1.1). The stem is, in the most common configuration, not related to the target sequence. A fluorophore is coupled covalently to one end of the stem sequence and a quenching moiety is linked to the other. When the beacon is in the hairpin configuration, fluorophore and quencher are forced together by the hybridization of the two stem region forming a double helix, therefore the fluorescence is quenched by proximity energy transfer and most of the light signal is transformed and dissipated as heat. If the beacon is in presence of the target DNA or RNA target, the hybridization among it and the loop sequence forms a long and stable double chain that causes the opening of the weaker stem double helix. The unfolding of the beacon causes the parting for the fluorescent dye from the quencher and therefore restoration of the emission.

Molecular beacons offer great advantages over conventional techniques for example high sensitivity and selectivity, possibility of multiplexing by preparing multiple beacons with different fluorophores and possibility of spatial and temporal localization of gene expression.

1.2 Fluorescence quenching

Molecular beacons and in general all the nucleic acid probes are based on fluorescence emission/quenching [8]. There are two main mechanisms that take part in the quenching process: static [9] and dynamic quenching [10] (Fig.1.2). The general difference is that while dynamic quenching occurs

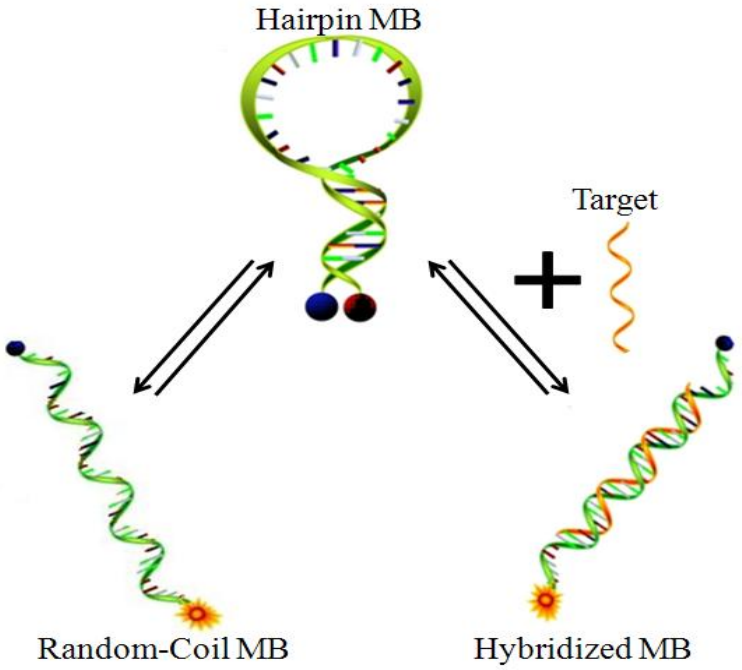

Figure 1.1: *Molecular beacons structure and working principle. At room temperature the MB assumes the hairpin configuration and the fluorescence is quenched. The increase of temperature causes the stem region to melt and MB assumes the random coil configuration. Hybridization to complementary sequence causes complete disruption of the hairpin structure and separation of the fluorophore quencher pair, restoring the fluorescence emission.*

during the excited state lifetime, static quenching occurs due to formation of complexes in the ground state.

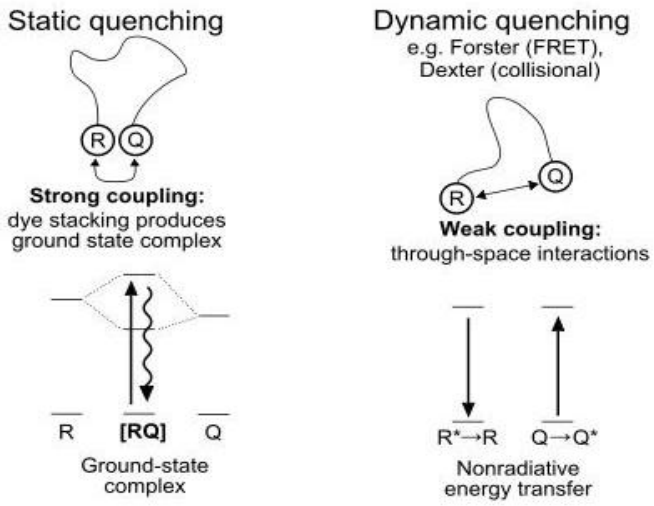

Figure 1.2: *Differences between static and dynamic quenching (Image reproduced from https://www.biosearchtech.com/).*

The static quenching involves the formation of a dimer between the fluorophore and the quencher, this dipole has an unique absorption spectrum that favors non radiative decay of excited electrons. The dependence of the fluorescence as function of the quencher concentration follows the relation:

$$\frac{F_0}{F} = 1 + K_a[Q] \tag{1.1}$$

where F_0 and F are the fluorescence intensity observed in the absence and presence, respectively, of the quencher, $[Q]$ is the quencher concentration and K_a is the association constant of the complex fluorophore-quencher. The plot of F_0/F versus $[Q]$ yield a straight line with the slope equal to K_a. The dimer resulting from the interaction of fluorophore and quencher is in itself non radiative, so the observed fluorescence comes from unconjugated fluorophore. This fluorescence entities are unperturbed hence their lifetime is unchanged.

In a similar way, the dynamic quenching, in its simplest case, follows the equation:

$$\frac{F_0}{F} = 1 + K_{SV}[Q] \tag{1.2}$$

where K_{SV} is Stern-Volmer quenching constant and $K_{SV} = k_q\tau_0$ with k_q is the biomolecular quenching rate constant and τ_0 is the excited state lifetime in the absence of quencher. The biomolecular quenching constant is a parameter that reflects the efficiency of the quenching and the accessibility of the fluorophore to the quencher. The so-called Stern-Volmer equation 1.2

can be derived from considerations about fluorescence emission intensity in absence and presence of the quencher, which are described by the following equations:

$$\frac{d[F^*]}{dt} = f(t) - \gamma|F^*|_0 = 0 \tag{1.3}$$

$$\frac{d[F^*]}{dt} = f(t) - (\gamma + k_q[Q])|F^*| = 0 \tag{1.4}$$

where $f(t)$ is the constant excitation function, $\gamma = \tau_o^{-1}$ is the decay rate of the fluorophore in absence of quencher and $[F^*]$ is the concentration of the fluorophore in the excited state. In absence of quencher, the excited-state population decays with a rate $\gamma = (\Gamma + k_{nr})$ where Γ is the radiative decay rate and k_{nr} is the non radiative decay rate. The presence of the quencher provides an additional decay pathway $k_q[Q]$. Division of eq.1.4 by eq. 1.3 yield to the Stern-Volmer equation:

$$\frac{F_0}{F} = \frac{\gamma + k_q[Q]}{\gamma} = 1 + k_q\tau_0[Q] \tag{1.5}$$

This consideration illustrates an important feature of the dynamic quenching, different from what derived for the static quenching: the fluorescence lifetime of the fluorophore decreases when in presence of the quencher.

In a mixed situation in which both static and dynamic quenching are present, the relationship changes as follow:

$$\frac{F_0}{F} = (1 + K_{SV}[Q])(1 + K_a[Q]) \tag{1.6}$$

And in this case, the plot of F_0/F versus $[Q]$ yield an upward curve due to the $[Q]^2$ term in the equation.

Förster's (or Fluorescence) Resonance Energy Transfer (FRET) is a mechanism of dynamic quenching which occurs without the release of a photon and it is the result of a long range dipole-dipole interaction between the donor and the acceptor. If the energy difference between two levels in the donor molecule matches that for a possible absorption transition in the acceptor molecule, with a sufficient energy coupling between these molecules (overlap of the emission spectrum of the donor with the absorption spectrum of the acceptor), both processes may occur simultaneously, resulting in a transfer of energy from the donor to the acceptor molecule. (Fig.1.3) The efficiency of the FRET depends upon many parameters: the emission spectrum of the donor, the absorption spectrum of the acceptor, the quantum yield of the donor, the relative orientation of the pair and, most importantly, the

distance between fluorophore and quencher. It is possible to define a particular distance at which the quenching efficiency drops to about 50%, i.e. the Förster distance, which typically ranges between 20 and 70 Å. Nearly all the quenching efficiency is lost at a distance of about 100 Å. (Fig.1.4)

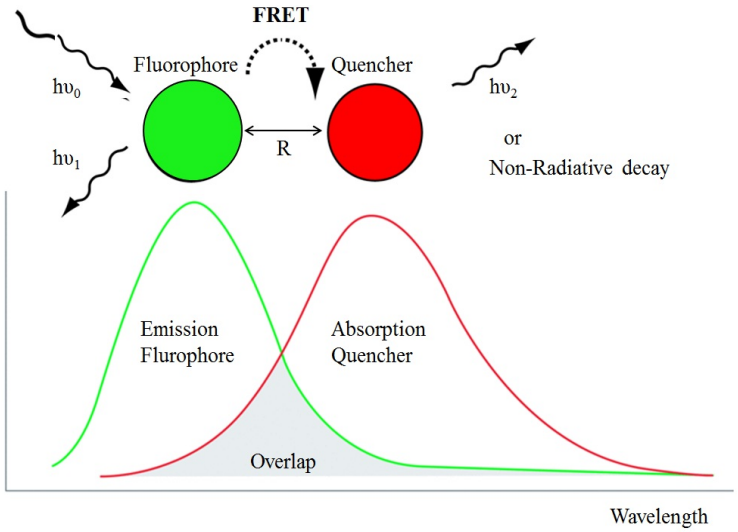

Figure 1.3: *FRET mechanism. The energy transfer depends strongly, among other parameters, on donor acceptor-distance and spectral overlap.*

In order to calculate the FRET efficiency, first the rate of energy transfer k_T must be derived. This requires a lengthy derivation, but it can be summarize as:

$$k_T = \frac{1}{\tau_d}(\frac{R_0}{R})^6 \tag{1.7}$$

where τ_d is the fluorescence lifetime of the donor without FRET, R is the distance between donor and acceptor and R_0 is the Förster's distance, introduced before, defined as:

$$R_0^6 = \frac{9000(ln10)}{128\pi^5 N_A}(n^{-4}\Phi_d k^2 J)[nm] \tag{1.8}$$

where n is the refractive index of the medium, N_A is the Avogadro's number, Φ_d is the fluorescence quantum yield of the donor in absence of FRET, k^2 is the orientation factor for the dipole-dipole interaction (usually assumed to be equal to 2/3) and J is the normalized spectral overlap integral. The FRET efficiency is therefore defined as:

$$E = \frac{k_T}{k_T + k_{nr} + k_r} = \frac{1}{1 + (R/R_o)^6} \tag{1.9}$$

The strong dependance of FRET on the distance of the fluorophore-quencher pair (R^{-6}), allows for applications of FRET probes such as molecular rulers [12, 13].

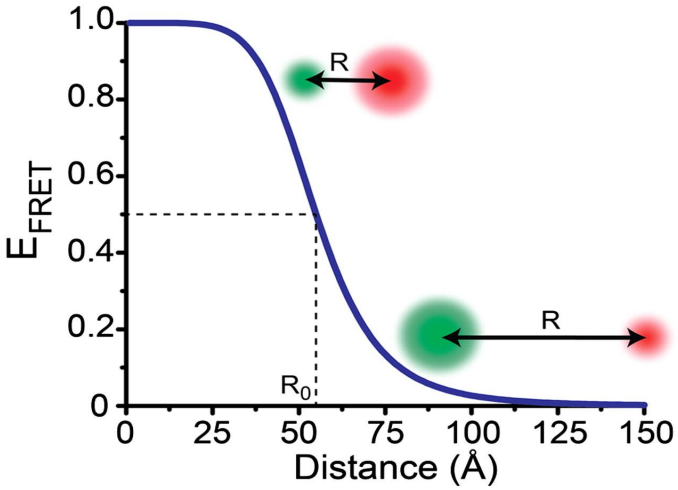

Figure 1.4: *FRET efficiency diagram: increasing the donor-acceptor distance greatly reduce the quenching efficiency. [11]*

The quenching efficiency in molecular beacons usually lies in between 85-97% even though recent development have increased this limit, Yang et al. [14] using multiple quenchers, could reach a quenching efficiency of 99.7 %. In [15] it was reported than a single 1.4 nm gold nanoparticle is able to quench the fluorescence emission of a given fluorophore as much as 100 times better than ordinary organic quencher DABCYL, resulting in a quenching efficiency of $99.966 \pm 0.026\%$.

1.3 Thermodynamic Aspect - Selectivity vs Kinetics

The behavior of a molecular beacons when hybridized to a complementary target could be explained to a large extent by the thermodynamic of the system. It has been shown that the melting temperature difference of a complementary target, compared to a single mismatched sequence could be as high as 10 °C [16]. Also that the selectivity towards mutation is dependent on the position of the mutation itself along the loop sequence, being the highest when placed in its center [17].

The high selectivity of molecular beacons its due to its peculiar hairpin configuration [18,19]. Linear probes for example have only **two** phases, either free or bound to the complementary target; conversely, molecular beacons have **three** possible phases: hairpin, hybridized to complementary target and free in a random coil. The stem-loop conformation has a lower free energy than the random coil state and its presence act in competition with the target hybridization. Hence, as in opposition to a linear probe, the presence of the hairpin configuration allows for a better discrimination of mismatched sequences increasing its melting temperature difference compared to the wild type target. (Fig.1.5).

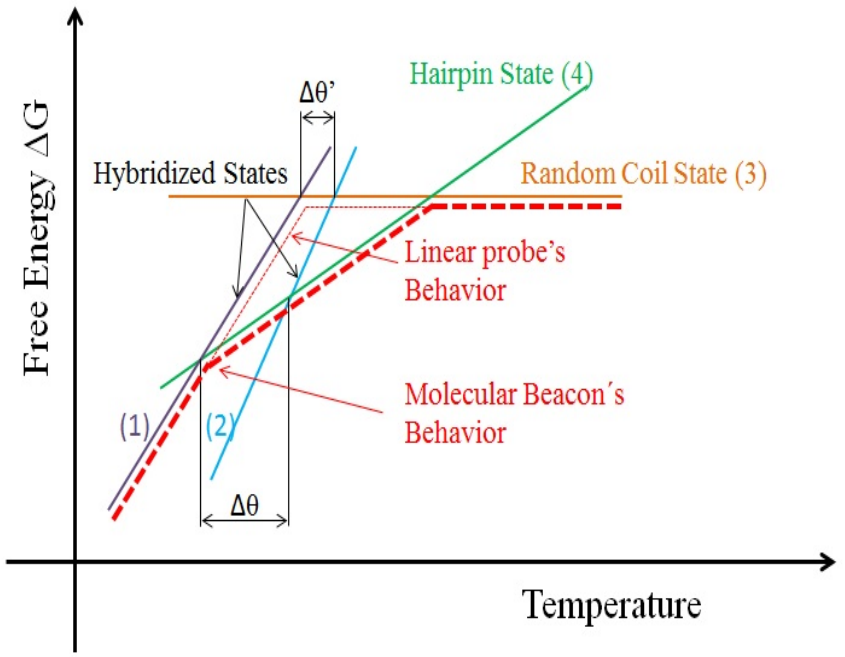

Figure 1.5: *Free energy versus temperature plot for a general MB (big-dashed red curve) and linear probe (small-dashed red curve). The violet and light blue lines represent the energy associated with the hybridized state of the beacon to a perfect complementary target (2) and single mismatched target (1). The orange curve (3) represent the random coil configuration while the green curve (4) represent the hairpin configuration assumed by the molecular beacon. It is possible to see that the presence of this third configurational state in the MB, causes a higher discrimination of single nucleotide polymorphism, lowering its melting point significantly compared to the linear probe case.*

It seems straightforward that, in order to increase the probe sensitivity, it would be enough to have a stronger stem, which could be simply longer or with an higher GC content. Unfortunately a more stable stem would cause a significant decrease in the rate of probe hybridization, for example it has

been shown that for a given MB the rate of hybridization decreases between one and two orders of magnitude when the length of the stem is increased from 2 to 4 nucleotides [20]. Additionally, a short stem causes an increase in background fluorescence. Therefore, a compromise between stem length and loop length has to be found in order to ensure low background, high selectivity and fast kinetics. One interesting strategy is the so called shared stem configuration [16, 20] in which one side of the stem region takes part also in the hybridization process, and may be considered also part of the loop section. In this way, the stem could be lengthen ensuring at the same time a strong hybridization of the loop region to its complementary target.

It is necessary to point out that each molecular beacon should be designed taking into account the specific temperature of operation. For some special applications that require high temperature, a conventional molecular beacon could be unstable and appear mostly in a random coil configuration, causing a high background level of fluorescence.

1.4 Application of molecular beacons

Some of the key applications of the molecular beacons are reported here. The first two are extra-cellular applications, while the second two applications are intra-cellular; here the key feature of MB is clearly evident: the possibility of working in living cells, maintaining high spatial and temporal sensitivity.

1.4.1 Real time PCR and Biosensors

Molecular beacons are commonly used in real time PCR in order to detect the DNA amplification of a target sequence [21]. After every PCR cycle, more DNA targets will be available for hybridization and their hybridization with the MBs will generate an increasing signal that will be proportional to the amount of amplified species after each cycle. Molecular beacons allows multiple detection of different products by changing the labelling moiety, which improves the throughput of the assay.

Molecular beacons can be immobilised on a solid surface and acquire the configuration of point marker biosensors [22]. There are two major aspects regarding this technology: first of all the different way in which the molecular beacons are effectively conjugated on the solid support and secondly the optimization of them for use in a liquid-solid environment.

1.4.2 mRNA detection in living cells and gene expression studies

MBs are ideal for studying mRNA in living cells [23] because of the following reasons: 1) The target is detected in real time and without the need of separating the bound from the unbound probes, the MBs which are not reacting will maintain their closed configuration and will not increase the fluorescence background. 2)The high sensitivity allows the tracking of targets with a low copy number.3)MBs have, as reported previously, high selectivity and can differentiate between sequences with a single-base mismatch.

Compared to the extra cellular applications initially reported, the use of molecular beacons inside living cells is more complicated. First of all the design of the loop sequence has to be carefully chosen in order to ensure that the exact part of the gene that is intended to be detected have high probability of being accessible and single stranded [24].(Fig.1.6)

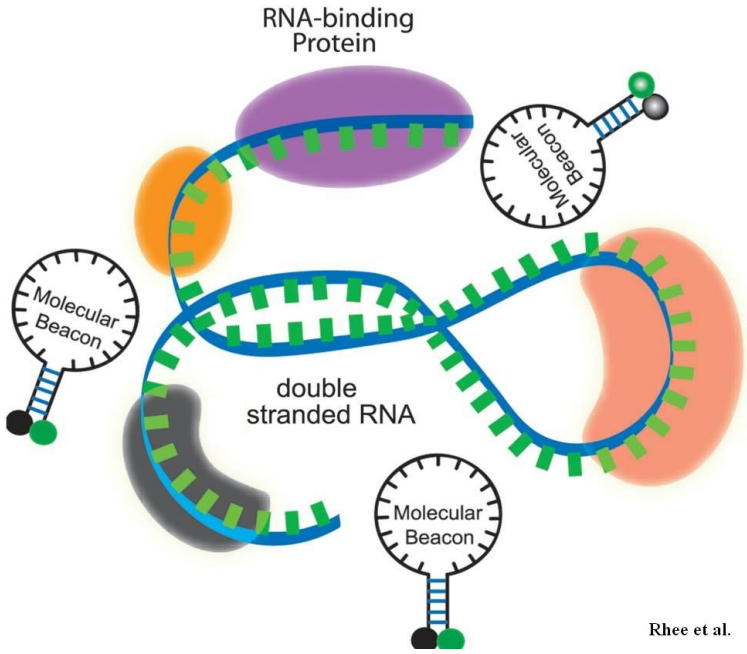

Figure 1.6: *Schematic representation of the accessibility problem for molecular beacons when targeting a specific mRNA sequence. The beacon has to anneal with a sequence which is free from binding proteins and in a single strand.*

Secondly to ensure that the selected region is not present in other nucleic acid inside the cell. There are many software tools available that are able to identify unique sequences [25, 26]. Another strategy consists in using two molecular beacons that act as FRET pair (Fig.1.7), which hybridize to adja-

cent sequences of interest. The generation of signal requires both the probes to be hybridized at the same time and this fact removes the possibility of false positive [27].

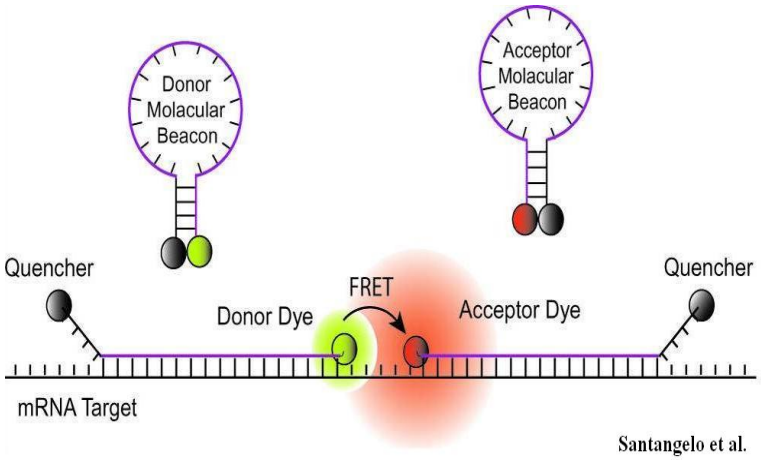

Figure 1.7: *Schematic representation of a FRET probe. Only the concurrent hybridization of the two beacons causes the emission of the detectable signal (Image from [27]).*

Another limitation in the use of MBs inside living cells is the requirement for efficient delivery inside the cell while, at the same time, leaving the cell undamaged (this particular issue will be discussed in a detailed fashion in chapter 3). Last but not least, the cellular environment is particularly harsh for unmodified oligonucleotides probes and show a lifetime that is not sufficient for real applications [17, 28]. Luckily, by modifying the backbone of the oligonucleotide chain, for example with a 2´ O-methyl RNA, the lifetime of the beacons is greatly improved (as discussed in details in chapter 2).

Bibliography

[1] J. D. Watson e F. H. C. Crick, *Molecular Structure of Nucleic Acids: A Structure for Deoxyribose Nucleic Acid*, Nature, **1953**, vol. 171, n. 4356, 737-738.

[2] Hughes, J. R., Bullock, S. L. Ish-Horowicz, D. Curr. Biol. **2004**, 14, 1950-1956.

[3] Visvader, J. E., Nature. **2011**, 469, 314-322.

[4] Saiki, R. K. et al. *Enzymatic amplification of beta-globin genomic sequences and restriction site analysis for diagnosis of sickle cell anemia.* Science 230, **1985**, 1350-1354

[5] Alwine, J. C. et al. *Detection of specific RNAs or specific fragments of DNA by fractionation in gels and transfer to diazobenzyloxymethyl paper.* Meth. Enzymol. **1979**, 68, 220-242.

[6] Schena, M., Shalon, D., Davis, R. W. Brown, P. O. *Quantitative monitoring of gene expression patterns with a complementary DNA microarray.* Science 270, **1995**, 467-470.

[7] S. Tyagi e F. R. Kramer, *Molecular beacons: Probes that fluoresce upon hybridization*, Nat. Biotechnol., **1996**, vol. 14, n. 3, 303-308.

[8] Lakowicz, JR. *Principles of Fluorescence Spectroscopy.*Springer,3rd. Edition, 2006.

[9] Weber, G. *The quenching of fluorescence in liquids by complex formation. Determination of the mean life of the complex.* Trans. Faraday Soc. 44, **1948**, 185-189.

[10] O. Stern and M. Volmer *Über die Abklingzeit der Fluoreszenz*, Physik. Zeitschr. **1919**, 20 183-188.

[11] Tinoco, I. Gonzalez, R. L. *Biological mechanisms, one molecule at a time.* Genes Dev. 25, **2011**, 1205-1231.

[12] Sönnichsen, C., Reinhard, B. M., Liphardt, J. Alivisatos, A. P. *A molecular ruler based on plasmon coupling of single gold and silver nanoparticles.* Nat Biotech 23, **2005**, 741-745.

[13] Ha, T., Enderle, T., Chemla, D. S. Weiss, S. *Dual-molecule spectroscopy: molecular rulers for the study of biological macromolecules*. IEEE Journal of Selected Topics in Quantum Electronics 2, **1996**, 1115-1128.

[14] C. J. Yang, H. Lin, e W. Tan, *Molecular Assembly of Superquenchers in Signaling Molecular Interactions*, **2005**, J. Am. Chem. Soc., vol. 127, n. 37, 12772-12773.

[15] B. Dubertret, M. Calame, e A. J. Libchaber, *Single-mismatch detection using gold-quenched fluorescent oligonucleotides*, Nat. Biotechnol.,

[16] Bonnet, G., Tyagi, S., Libchaber, A. Kramer, F. R. *Thermodynamic basis of the enhanced specificity of structured DNA probes*. Proceedings of the National Academy of Sciences 96, **1999**, 6171-6176.

[17] Tsourkas, A., Behlke, M. A., Rose, S. D. Bao, G. *Hybridization kinetics and thermodynamics of molecular beacons*. Nucleic Acids Res. 31, **2003**, 1319-1330.

[18] Liming Ying, M. I. W. *Two-state model of conformational fluctuation in a DNA hairpin-loop*. Chemical Physics Letters 145-150.

[19] Bonnet, G., Krichevsky, O. Libchaber, A. *Kinetics of conformational fluctuations in DNA hairpin-loops*. PNAS 95, **1998**, 8602-8606.

[20] Tsourkas, A., Behlke, M. A. Bao, G. *Structure-function relationships of shared-stem and conventional molecular beacons*. Nucleic Acids Res 30, **2002**, 4208-4215.

[21] Goel, G., Kumar, A., Puniya, A. k., Chen, W. Singh, K. *Molecular beacon: a multitask probe*. Journal of Applied Microbiology 99, **2005**, 435-442.

[22] Jin, R., Wu, G., Li, Z., Mirkin, C. A. Schatz, G. C. *What Controls the Melting Properties of DNA-Linked Gold Nanoparticle Assemblies?* J. Am. Chem. Soc., **2003**, 125, 1643-1654.

[23] Bratu, D. P., Cha, B.-J., Mhlanga, M. M., Kramer, F. R. Tyagi, S. *Visualizing the distribution and transport of mRNAs in living cells*. PNAS 100, **2003**, 13308-13313.

[24] Rhee, W. J., Santangelo, P. J., Jo, H. Bao, G. *Target accessibility and signal specificity in live-cell detection of BMP-4 mRNA using molecular beacons*. Nucleic Acids Res 36, **2008**.

[25] http://blast.ncbi.nlm.nih.gov/

[26] http : //www.premierbiosoft.com/molecular$_{\text{b}}$eacons/

[27] Santangelo, P. J., Nix, B., Tsourkas, A. Bao, G. *Dual FRET molecular beacons for mRNA detection in living cells*. Nucleic Acids Res. **2004**, 32.

[28] Majlessi, M., Nelson, N. C. Becker, M. M. *Advantages of 2'-O-methyl oligoribonucleotide probes for detecting RNA targets*. Nucleic Acids Res. 26, **1998**, 2224-2229.

Chapter 2

Characterization of molecular beacons with different backbones.

2.1 Introduction

The wide use of molecular beacon in living assays is threatened by numerous aspects, namely their toxicity and their functional stability over a long period. When tracking gene expression in living cells for example, one has to make sure that the beacons are not degraded during the detection. Molecular beacons comprising an oligonucleotide chain with unmodified backbone are very sensitive to nuclease [1]. The degradation of the nucleotide chain by nuclease attack causes total disruption of the beacon structure and separation between fluorophore-quencher pair, resulting in false positive. It was reported that the half-life time of unmodified oligonucleotide chains under the influence of nuclease could be as short as 10-20 minutes [2]. One way to prevent this problem and improve the kinetics of hybridization is to modify the backbone of the oligonucleotide [3]. These molecules carry a methyl group at the 2´OH residue of the ribose molecule [Fig.2.1]. 2´O-Methyl-RNA shows the same behavior as DNA, but is protected against nuclease degradation [4].

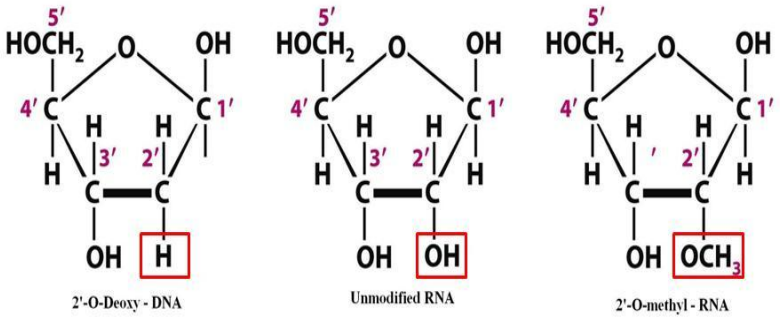

Figure 2.1: *Backbone modifications of different nucleic acids.*

In the following chapter two kind of backbone will be analysed, a 2´deoxy DNA strand and a 2´O-methyl RNA strand. Some groups reports that 2´-O-methyl RNA beacons have faster hybridization kinetics, increased T_m and increased specificity towards RNA targets [5, 6].

2.2 Target's sequences and beacon's design

The target sequences for molecular the molecular beacons were divided into mainly three groups: the first group contains the marker for pluripotency of stem cells, such as Oct4 and Sox2. The second group included markers for cells differentiated in neuronal linage, like NeuN, Map2, and Nestin. The last group contains a housekeeping gene that serve as negative control in cell experiments, such as GAPDH. A detailed discussion about the function of each of these markers is beyond the scope of this investigation and will therefore be omitted. The exact sequences for these targets are presented in the following chart:

Table 2.1: Sequences of the molecular beacons under investigation.

Name	Sequence
Oct4	CATGTTCTTGAAGCTAAGCTGCA
Sox2	CGCCGCCGATGATTGTTATTAT
NeuN	TCCCATTCAGCTTCTCCCG
Map2	GTTGTCTCTGGCTGAGAAACTAA
Nestin	TCTCACTACCTCCACATCCT
GAPDH	AGTTGGTGGTGCAGGAGG

The stem of the beacons consist of only 5 oligonucleotide pairs and was the same for all of beacons (example of beacon's structure in fig.2.2). Its

sequence, from 5´ end to 3´ end is: CGCUC (in the DNA probe uracil is replaced by thymine so the sequence from 5´ end to 3´ end is CGCTC). All the sequences were purchased from Invitrogen both with 2´deoxy and 2´O-methyl backbone. The DNA probes were labeled at the 5´ end with TexasRed while the 2´O-Methyl-RNA beacons have Cy3 as labeling agent on the 5´ end. The beacon structure was analyzed and predicted with available software such as mFOLD [7] and OligoAnalyzer [8].

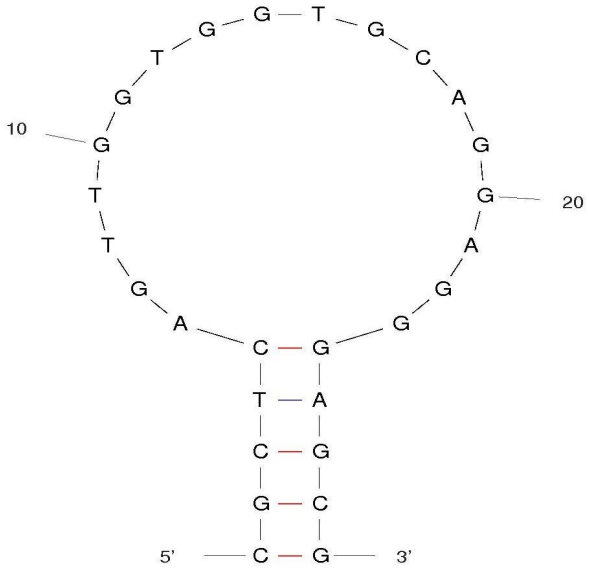

Figure 2.2: *Typical hairpin configuration of a MB, here encoded with GAPDH.*

2.3 Beacon Characterization

2.3.1 Melting curves

The first analysis consists in characterization of the fluorescence emission profile over a broad range of temperatures, the so-called melting curve. The temperature was ramped from 20 °C to 90 °C with steps of 0.3 °C and the fluorescence was measured at every step after 5minutes. 1 μl at 10 μM of each sample was incubated with 19 μl of 1xPBS buffer. The same beacon concentration was also incubated with the complementary DNA sequence in ratio 1:1 and subjected to the same gradient of temperature. Although each beacon show a different melting temperature, the general behavior of the beacons is similar and therefore only one curve will be shown as representative for all the probes [Fig.2.3].

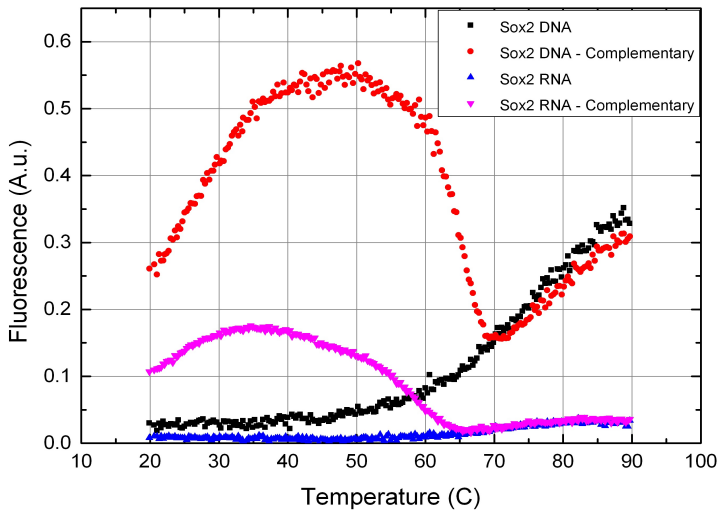

Figure 2.3: *Melting curves for molecular beacons for Sox2.*

The melting temperature for each beacon was estimated using the software [7, 8] and experimentally calculated from the melting curve [Fig.2.4]. The melting temperature is the value at which hybridized and unhybridized beacons are in a 50%/50% ratio in the solution. It appears that the calculated temperature is over estimated for both DNA and RNA probes, probably the effect is due to difference in the salt concentration of the solution that could alter significantly the value of T_m. The T_m values of the DNA probes generally have a higher value compared to the RNA probes. The value of the T_m was compared to the value of Gibbs free energy $\triangle G$ (see chapter 4 part I for a more detailed analysis) but it was impossible to find a clear correlation between the two parameters (data not shown)

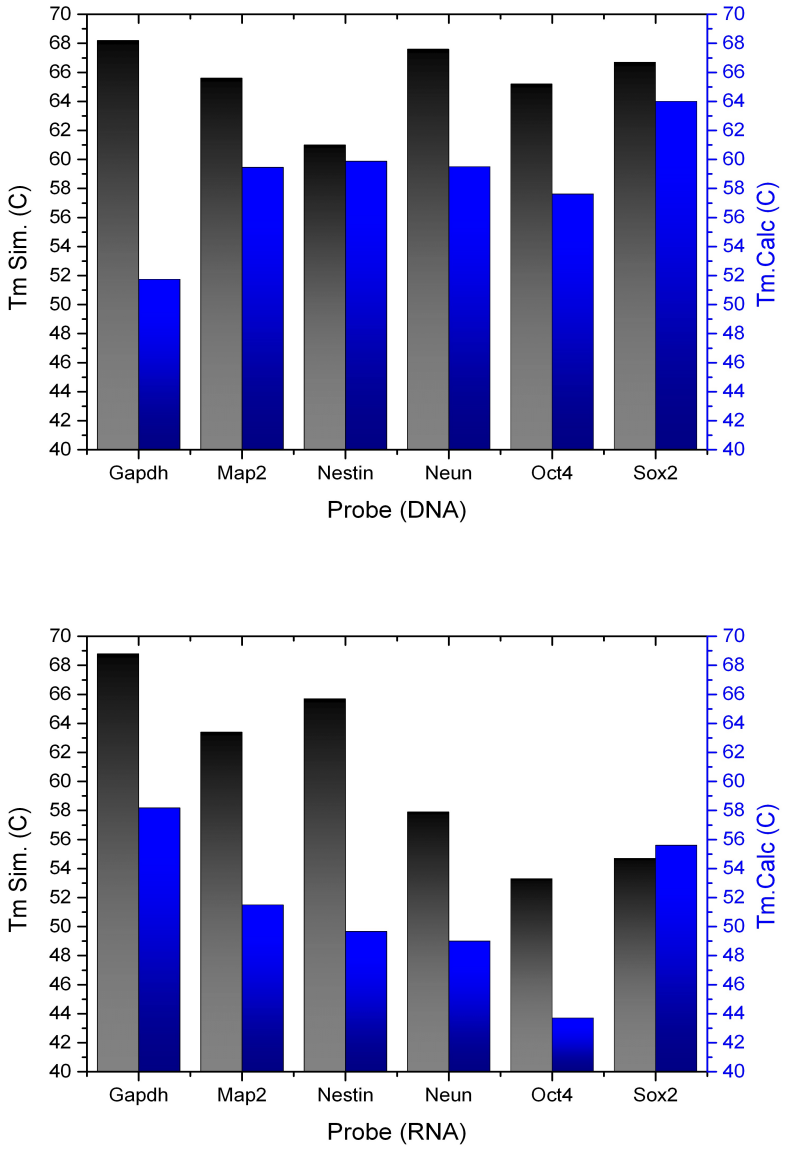

Figure 2.4: *Melting temperatures for the beacons hybridized to complementary target, theoretical and experimental, for DNA probes (upper graph) and RNA probes (lower graph).*

The S/N ratio is estimated for both the group of probes separately and plotted together with the maximum signal intensity in fig.2.5. The value of S/N ratio has been plotted against various parameters, such as experimental T_m, theoretical T_m, $\triangle G$ and maximum signal emission, but it was impossible to establish a clear trend (data not shown). The lower value of the maximum

signal emission for the RNA compared to the DNA ones is mostly likely due to the different labeling agent used for the two different groups and not a distinctive feature of the backbone modification.

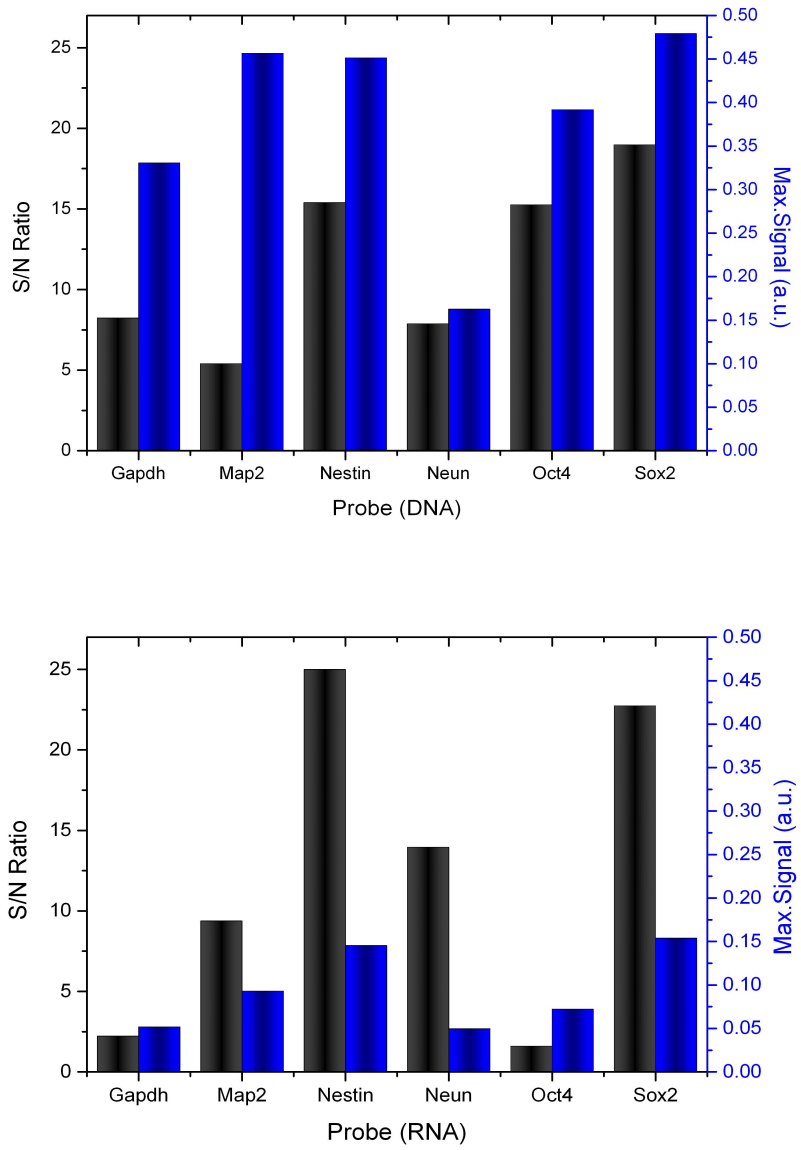

Figure 2.5: *S/N and maximum signal emission for the molecular beacons.*

2.3.2 Kinetic Analysis

The kinetic response of 2´deoxy and 2´O-methyl molecular beacons was tested against complementary DNA targets. A solution of 1 μl at 10 μM of MBs and 1 μl at 10 μM of complementary target diluted in 18 μl of PBS was incubated at 37 °C and the fluorescence emission was measured at different time-points. The fluorescence emission was inspected every 5 seconds for the first two minutes, then every 2 minutes for 10 minutes and finally every 15 minutes for 3 hours. The pipetting of the different samples inside the test tubes was performed inside an ice bath in order to increase the stringency of the MBs, therefore keeping them in hairpin configuration. This fact would slow down the hybridization reaction before the actual monitoring of emission can take place. It was possible to notice that all the probes show that hybridization of 2´O-methyl probes is faster compared to 2´deoxy beacons, even with DNA target. This is in contrast with some of the literature found previously, in which 2´deoxy probes had higher kinetics towards DNA target [5, 6]. Once again only one graph is reported as representative of the behavior of the all beacons [Fig.2.6]. The emission signal of the different probes was normalized on their maximum value to account for the different fluorophore labeling. Another experiment in which the beacons with the same concentration were tested for 48 hours was performed. The result shows that the emission intensity was constant for the entire period, therefore there is no degradation of the probe at in vitro conditions (data not shown).

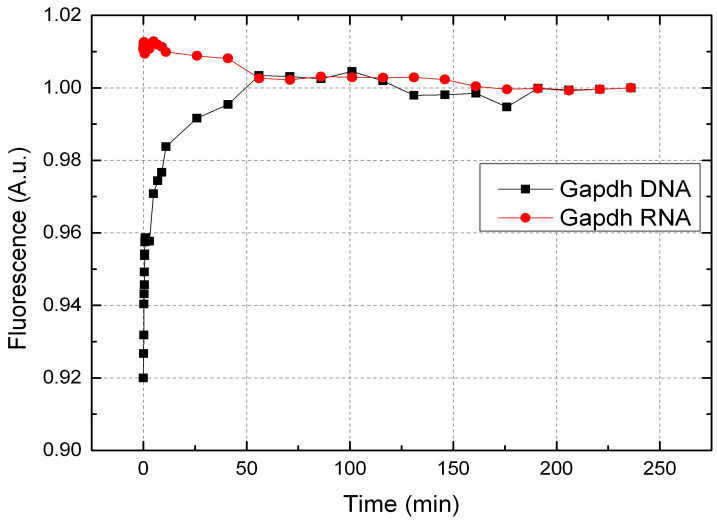

Figure 2.6: *Kinetics curve GAPDH*

It is interesting to see that Map2 shows for both the 2´deoxy and 2´O-methyl backbone a large signal increase over time [Fig.2.7], as sign of slow reaction kinetics. The analysis of the geometrical structure of the molecular beacons pointed out that Map2 exhibit an inner loop feature with 4 complementary bases (AGAG) [Fig.2.8]. In comparison, the other beacons under investigation show the simple hairpin configuration of fig2.2.

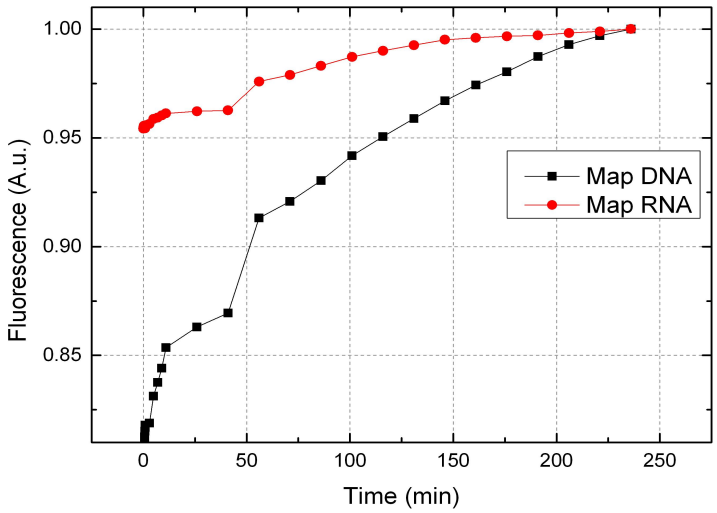

Figure 2.7: *Kinetics curve MAP2*

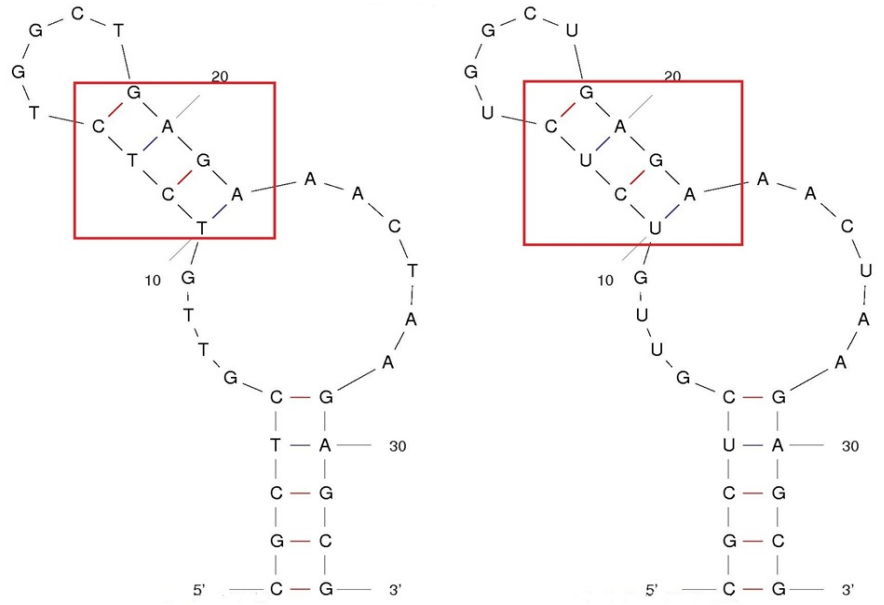

Figure 2.8: *Map2 conformational structure for both DNA (right) and RNA (left) probes.*

2.3.3 Maximum Signal Emission

The melting curves differences point out a characteristic feature regarding the maximum signal emitted by the probes. For this analysis the probe for Oct4 was chosen because it was labeled with the same fluorophore for both 2´deoxy and 2´O-methyl beacons, this allows direct comparison. In the chapter 1 part I, the conformational configuration of a molecular beacon was highlighted. A molecular beacon can assume three geometries, 1)hairpin, 2) hybridized to target and 3) random coil at high temperature. It is logical to assume that the maximum displacement distance between the fluorochrome and the quencher is achieved when the complementary target is annealed to the loop structure, so when the beacon is hybridized. Although at high temperature the stem of the beacon is melted and the beacon assumes a random coil configuration, the oligo strand will be constantly subjected to thermally vibration that could result in bending of the oligonucleotide chain. Consequently the fluorophore might approach in vicinity of the quencher and the fluorescence and emission will decrease.

When a 2´deoxy beacon hybridizes with its complementary target, the signal increases considerably and reaches its maximum value, higher than the emission of the beacon at high temperature. On the contrary, when a 2´O-methyl beacon is hybridized to a DNA target, the fluorescence signal that arises from the formation of the duplex is not the maximum along the

melting curve. Indeed, at 90 °C, the fluorescence emission from the molecular beacon alone is higher than the emission from the hybridized beacon [Fig. 2.9].

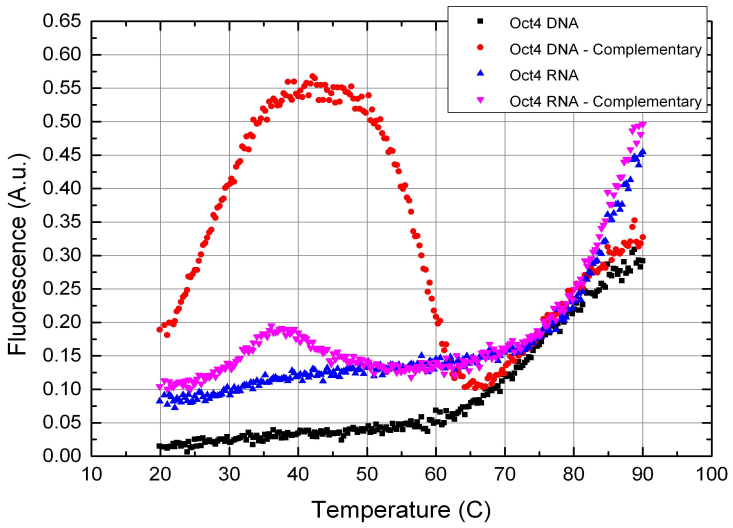

Figure 2.9: *Melting Curve of Oct4 probe*

This effect could be explained with the hypothesis that the DNA-DNA duplex is more rigid than the RNA-DNA duplex. Therefore, the 2´deoxy beacon maintains its maximum stretched configuration while the 2´O-methyl beacon has higher flexibility. The effect cannot be due to slower kinetics or less affinity; as we have shown previously, the hybridization can be considered complete after few minutes for the 2´O-methyl beacons and incubation for 72 hours is not changing the maximum emission signal.

2.4 Conclusion

The emission property of various beacons with 2´deoxy and 2´O-methyl backbones were analyzed. The S/N ratio seems not to be affected by the backbone modification. The kinetics of hybridization towards DNA complementary target is faster for 2´O-methyl RNA beacons. The conformational geometry plays an important role in the hybridization kinetics. The presence of a 4bps inner loop structure significantly reduced the kinetics of hybridization of the Map2 beacon, both RNA and DNA. The Oct4 probe, which was

equally labelled for both RNA and DNA backbone, showed that DNA probes generates high maximum signal emission upon hybridization.

Bibliography

[1] Li, J. J., Geyer, R. Tan, W. *Using molecular beacons as a sensitive fluorescence assay for enzymatic cleavage of single-stranded DNA.* Nucleic Acids Res 28, **2000**, 52.

[2] Uchiyama, H., Hirano, K., Kashiwasake-Jibu, M. Taira, K. *Detection of undegraded oligonucleotides in vivo by fluorescence resonance energy transfer. Nuclease activities in living sea urchin eggs.* J. Biol. Chem. 271, **1996**, 380-384.

[3] Cummins, L. L. et al. *Characterization of fully 2´modified oligoribonucleotide hetero- and homoduplex hybridization and nuclease sensitivity.* Nucleic Acids Res 23, **1995**, 2019-2024.

[4] Molenaar, C. et al. *Linear 2´O-Methyl RNA probes for the visualization of RNA in living cells.* Nucleic Acids Res. 29, **2001**.

[5] Majlessi, M., Nelson, N. C. Becker, M. M. *Advantages of 2´O-methyl oligoribonucleotide probes for detecting RNA targets.* Nucleic Acids Res. 26, **1998**, 2224-2229.

[6] Tsourkas, A., Behlke, M. A. Bao, G. *Hybridization of 2´O-methyl and 2´deoxy molecular beacons to RNA and DNA targets.* Nucl. Acids Res. 30, **2002**, 5168-5174.

[7] M. Zuker, *Mfold web server for nucleic acid folding and hybridization prediction*, **2003**, Nucl. Acids Res., vol. 31, n. 13, 3406-3415.

[8] http://eu.idtdna.com/analyzer/Applications/OligoAnalyzer/

Chapter 3

Diffusion model for molecular beacon uptake by cells

3.1 Introduction and literature

Molecular beacons [1]have proven to be an extremely valuable assets in cellular biology because of their capability of spatial and temporal profiling of RNA synthesis, processing and transport, which is impossible to obtain with conventional PCR or in-situ hybridization. This ability enables real time studies of gene expression and cellular response to external stimuli. One of the major challenges regarding MBs is to find an efficient way to deliver functional probes inside the cytoplasm while, at the same time, not risk cell viability or alter cell behavior. It is known that, when unassisted, oligonucleotide probes are not able to cross the plasma membrane. Also, common liposome or dendrimers driven delivery methods, commonly used to internalize DNA, are not efficient for molecular beacons and could cause entrapment of the probe and further degradation of the probe leading to high background. Experimental evidence shows that linear fluorescently labeled probes enter in the endosomal/lysosomal pathway with concomitant nuclease-mediated degradation [2]. In this chapter I will give a brief overview of some of the existing techniques for effective beacons internalization, with more emphasis on Streptolysin O (SLO) assisted transfection. This section will be followed by a theoretical model describing the diffusion of molecular beacons through pores in cellular membrane caused by SLO treatment, later I will show the results of a FEM model in COMSOL that simulate the diffusion process and in the end the results of the experiment the we carried out to verify the prediction of our models will be presented.

3.2 Transfection techniques

3.2.1 Microinjection

Microinjection is a direct method to deliver oligonucleotide probes into the cytoplasm of a living cell [3]. The DNA sample is loaded in a $0.5-5\mu$m needle that puncture the membrane and directly delivers the content inside [Fig.3.1] The advantage is that it is applicable to most of the cells, but it is rather time consuming and only relevant when few cells needs to be analyzed. Moreover, microinjection is a quite invasive methodology and could interruption normal cell functioning and results in cell death.

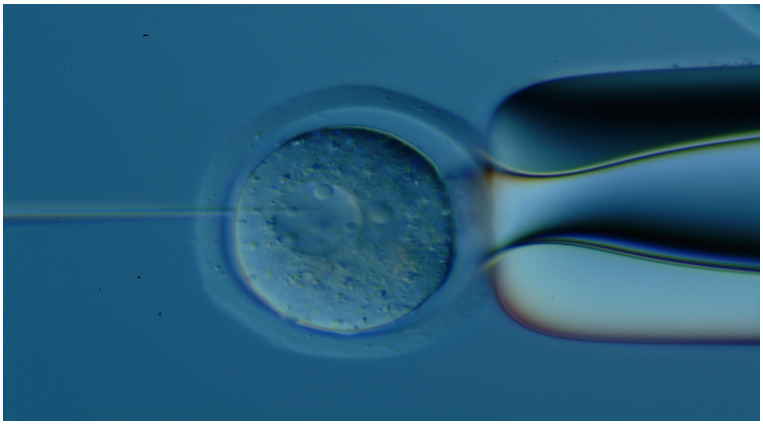

Figure 3.1: *Microinjection on a cell; the cell is fixed by suction from the right and the needle puncture the membrane from the left and inoculate the sample. [4]*

3.2.2 Microporation

Microporation is also another valuable direct technique of internalization; like electroporation, it is a technique based on the application of an electric field across two plates between which the cells are placed; when the local transmembrane voltage threshold is exceed, nm-scale water-filled holes in the membrane are created and allows the molecular beacons to diffuse inside the cells uniformly [5]. The scaling of the system to micrometer length allows to get rid of unwanted effect such as heat generation and pH variation, leading to an enhancement of cell viability compared to normal "bulk" electroporation [6]. Probe delivery takes only few seconds and the possibility of an integrated microfluidic system to handle cells results in high throughput transfection (see example device in Fig.3.2) [7–13].

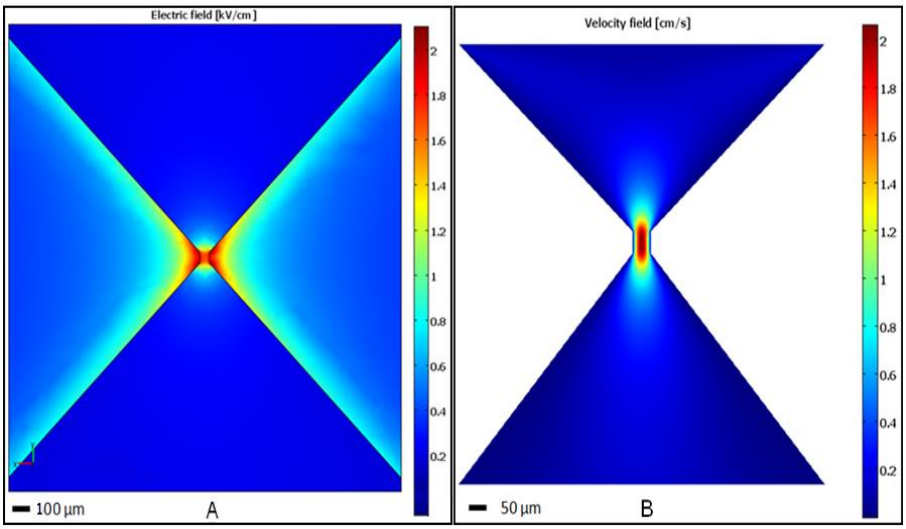

Figure 3.2: *Comsol simulation of the microelectroporation device of Andresen et al. [14]; (A)Electric field distribution at in the microchannel, (B)Fluid speed distribution inside the microchannel.*

3.2.3 Gene gun - Bio-ballistic

Bio-Ballistic or Biolistic technique was first reported in 1987 [15]and is based on heavy metal particles (made out of biocompatible metals, for example, gold, having diameters from 1 to 5 μm) coated with the desired DNA. These bio-bullets are later shoot inside the cell using a gas gun (usually helium or water vapor) [Fig.3.3] kept at very high pressure. The blast opens small pores independent from the endosomal pathways, avoiding previously stated degradation. A few disadvantages of this technique is the poor control over the amount of delivered beacons and the rather invasive mechanism of internalization that could result in reduced cell viability and function alteration, even thought it is considered less invasive than microinjection.

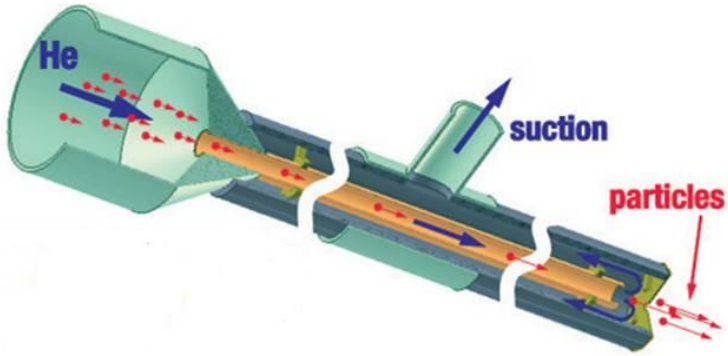

Figure 3.3: *Schematic view of the gas gun used in Bio-ballistic transfection. [16]*

3.2.4 Cell membrane permeabilization

Another possible technique involves the use of a bacterial exotoxin called Streptolysin O (SLO) that reversibly causes the formation of pores on the cell membrane [17]. The toxin molecules bind as a monomer to the exposed cholesterol of the membrane bilayer, and after binding of a single molecule, more toxins polymerize to form an arc- or ring- shape structure comprising 50-80 subunits. These ring shaped formations surround an area up to 30 nm radius depleted of cholesterol; this depletion causes lysis in the cell membrane and allows the small molecules to pass through it by diffusion. An essential feature of this technique is that the toxin-based permeabilization is reversible. This can be achieved by introducing oligonucleotides with SLO under serum-free conditions and then removing the mixture and adding normal media with serum [18]. Since the cholesterol composition varies with cell types, the permeabilization protocol needs to be optimized for each cell type by varying temperature, incubation time, cell number, and SLO concentration [19].

For our purposes, cell viability and transfection efficiency was investigated as a function of SLO concentration ranging from 1 ng/ml (corresponding to 0.07 U/ml) to 800 ng/ml (corresponding to 59.7 U/ml). Transfection efficiency was evaluated using a molecular beacon towards GAPDH mRNA (see chapter 2 for clarification on GAPDH). Cell viability was evaluated using calcein/propidium iodide staining. An SLO concentration of 17 U/ml (230 ng/ml) was determined to be the optimal concentration with 75% of the cells showing signal from MB-GAPDH 24 h post-transfection and with >95 cell showing viability[Fig.3.4 A]. Moreover, cells showed no growth or differentiation defects and they exhibited the same morphology in non-transfected cells [Fig.3.4 B] and transfected cells [Fig.3.4 C]. A SLO concentration of 17 U/ml (230 ng/ml) was used in further experiments.

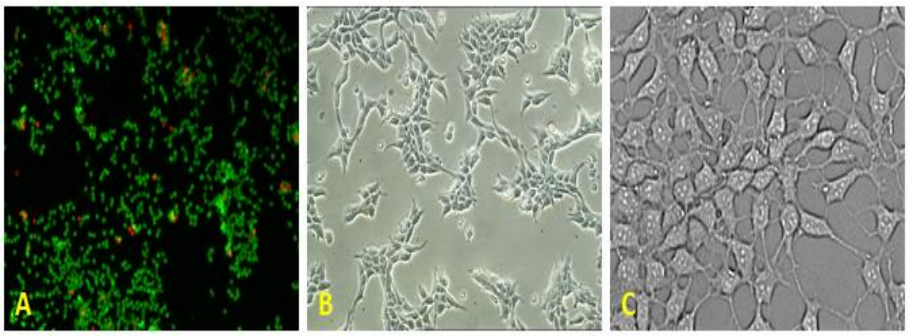

Figure 3.4: *(A) Cells treated with 17 U/ml SLO and stained with calcein/PI for detection of cell viability after toxin-based membrane permeabilization. Live cells are stained in green, dead cells are stained in red. (B) Morphology of non-transfected LUHMES in growth medium (GM) (C) and transfected cells after 24 hours incubation in GM.*

3.3 Theoretical model of Molecular beacons uptake

The transport of molecular beacons into the cells during transfection is a diffusion process, where the molecular beacons diffuse through open pores in the cell membrane. In order to estimate the number of beacons that are effectively transfected into the cells, one simplified diffusion model was developed. The cells are assumed to be spherical with the radius $a = 5\,\mu$m and have a cell membrane that is $x_{\mathrm{m}} = 10\,$nm thick, and in the membrane $N_{\mathrm{p}} \simeq 600$ pores (2 pores per $\mu\mathrm{m}^2$) with a pore radius of $a_{\mathrm{p}} = 15\,$nm are opened during transfection [20]. The molecular beacons are modeled as solid spheres with a radius of $a_{\mathrm{b}} = 2.5\,$nm, and a $C_0 = 2\mu$M concentration is used in a medium with the viscosity $\eta = 0.85 \times 10^{-3}\,$Pa s at 300 K; the viscosity of the cell interior is assumed to be identical.

Diffusion problems in dilute systems are governed by Fick's first and second Laws, Eqs. (3.1) and (3.2), respectively

$$\mathbf{J} = -D\nabla C, \tag{3.1}$$

where C is the concentration, $\mathbf{J}$ is the diffusion flux density, and D the diffusivity. Fick's second Law is a conservation law

$$\frac{\partial C}{\partial t} = -\nabla \cdot \mathbf{J} \simeq D\nabla^2 C, \tag{3.2}$$

where t is time. The approximation is valid if the diffusivity is constant. The diffusivity of the molecular beacons may be estimated using the Stokes-

Einstein equation

$$D = \frac{k_{\mathrm{B}} T}{6\pi\eta a_{\mathrm{b}}}, \tag{3.3}$$

where η is the viscosity of the medium, k_{B} is Boltzmann's constant and T the absolute temperature. A direct evaluation at 300 K yields a diffusivity of $D \simeq 100\,\mu\mathrm{m}^2\,\mathrm{s}^{-1}$ that agrees well with values from literature [21].

The real diffusion problem is a rather complicated 3D problem, however, the different length scales involved in the problem suggest that approximations may be made. Recognizing, that typical diffusion times are $t_{\mathrm{d}} = \lambda^2/(2D)$, where λ is the characteristic length scale, results in diffusion times for the pore regions that are five orders of magnitude lower than diffusion times relevant on the cell scale, and thus a quasi steady-state approximation may be applied to the pore regions. Furthermore, the pores are so far apart that they hardly interact in the diffusion process. As a result, we may estimate the diffusion flux through a single pore by the net flux I that results from 1) quasi steady-state diffusion to a disc of radius $a_{\mathrm{p}} - a_{\mathrm{b}}$ (to compensate for the finite size of the MBs), 2) steady state diffusion through a tube of radius $a_{\mathrm{p}} - a_{\mathrm{b}}$ and length x_{m}, and 3) quasi steady-state diffusion from a disc of radius $a_{\mathrm{p}} - a_{\mathrm{b}}$ to the cell interior. The fluxes 1) and 3) are given by $I_{1,3} = 4\,(a_{\mathrm{p}} - a_{\mathrm{b}})\,D\Delta C_{1,3}$ where $\Delta C_{1,3}$ is the concentration difference that drives the flux [22]. The flux 2) is $I_2 = \left(\pi\,(a_{\mathrm{p}} - a_{\mathrm{b}})^2 / x_m\right) D\Delta C_2$, where the symbols have the same significance as above. The three fluxes are identical while the sum of concentration differences $\Delta C_1 + \Delta C_2 + \Delta C_3 = C_0 - C_{\mathrm{c}}$ where C_{c} is the concentration inside the cell, which is considered approximately uniform. As a result the flux through a single pore is

$$I_{\mathrm{p}} = \left(\frac{2}{4\,(a_{\mathrm{p}} - a_{\mathrm{b}})\,D} + \frac{x_m}{\pi\,(a_{\mathrm{p}} - a_{\mathrm{b}})^2\,D} \right)^{-1} (C_0 - C_{\mathrm{c}})\,, \tag{3.4}$$

and the total flux through all pores is of course N_{p} times larger. Integrating Fick's second Law, (Eq.3.2), over the volume $V = \frac{4}{3}\pi a^3$ of the cell yields

$$\frac{\partial C_{\mathrm{c}}}{\partial t} = \frac{N_{\mathrm{p}} I_{\mathrm{p}}}{V} = \frac{3DN_{\mathrm{p}}\,(a_{\mathrm{p}} - a_{\mathrm{b}})^2}{2a^3\,[\pi\,(a_{\mathrm{p}} - a_{\mathrm{b}}) + 2x_m]}\,(C_0 - C_{\mathrm{c}}) \equiv \frac{C_0 - C_{\mathrm{c}}}{\tau_c}, \tag{3.5}$$

where τ_c is the time constant relevant for the transfection

$$\tau_c = \frac{2a^3\,[\pi\,(a_{\mathrm{p}} - a_{\mathrm{b}}) + 2x_m]}{3DN_{\mathrm{p}}\,(a_{\mathrm{p}} - a_{\mathrm{b}})^2}. \tag{3.6}$$

With the parameters given, the time constant $\tau_c \simeq 0.53$ s results. The solution to equation 3.4 is easily obtained

$$C_{\mathrm{c}} = C_0 \left(1 - \exp\frac{-t}{\tau_c}\right), \tag{3.7}$$

and within a few time constants (a few seconds) the concentration of molecular beacons saturates at C_0.

3.4 FEM Comsol simulation

Two different Comsol models were developed in order to simulate our system. In the first approach, a mean field approximation was used; the membrane structure was simplified to a uniform layer with an effective diffusivity D_e (3.8)that accounts for the presence of the pores [23]. In this way it was possible to reduce the complex 3D problem to a 1D diffusion problem, see insert in fig. 3.5. Effective diffusivity D_e is expressed as:

$$D_e = D\frac{\varepsilon\,(1-\delta)}{\tau}, \tag{3.8}$$

where ε is the porosity, i.e. the ratio of total pore volume to total membrane volume, δ is the constrictivity, i.e. the ratio of the radius of the diffusing particle to the pore radius, and τ is the tortuosity, which corrects for the curvature of the pores. Since the pores are short and straight we take $\tau = 1$, and then the effective diffusivity is estimated to $D_e \simeq 0.12\,\mu\mathrm{m}^2\,\mathrm{s}^{-1}$ approximately three orders of magnitude smaller than the diffusivity in the free fluid. Fig.3.5 shows the result of the diffusion simulation calculated for the first 1.5 sec of diffusion. It is possible to notice that the concentration drops significantly at the membrane but reaches a steady state already at the end of this small interval of time.

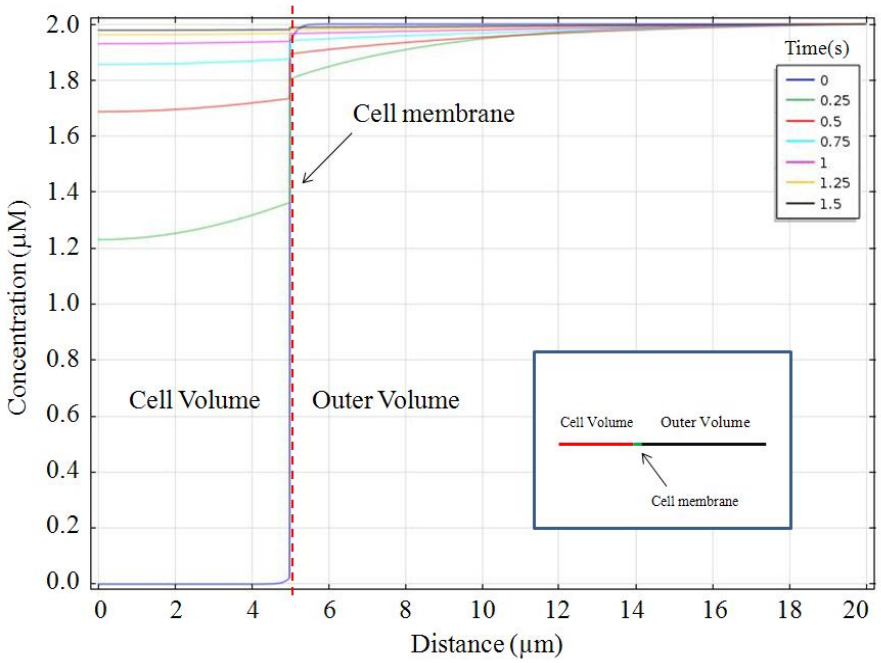

Figure 3.5: *Concentration profile for the 1D mean field approximation model over time.Insert, geometrical representation of the implemented model.*

With this model, the time constant may be estimated from

$$\tau_{c2} = \frac{V}{4\pi a^2}\frac{x_m}{D_e} = \frac{a x_m}{3 D_e},$$

and a numerical value of $\tau_{c2} \simeq 0.14\,\mathrm{s}$ is estimated, which is lower than the value calculated from the theoretical model, which we regard as more reliable. At such low porosity, the mean field approximation may not be sufficiently accurate since the effects of diffusion to and from the pores are excluded from the model, and in the first model these effects are seen to be dominant; this is the cause for the factor of 4 difference in magnitude of the two time constants. In order to overcome the limitation of the simple 1D model, we developed a more refined 3D Comsol model of the system. In this FEM model, a cone segment of the spherical cell with exactly one pore was used to represent a $1/N_p$ fraction of the cell volume. The cone region was extended far into the free fluid volume in order to also represent a $1/N_p$ fraction of that, see fig. 3.6 for geometrical model and concentration profile in the initial state.

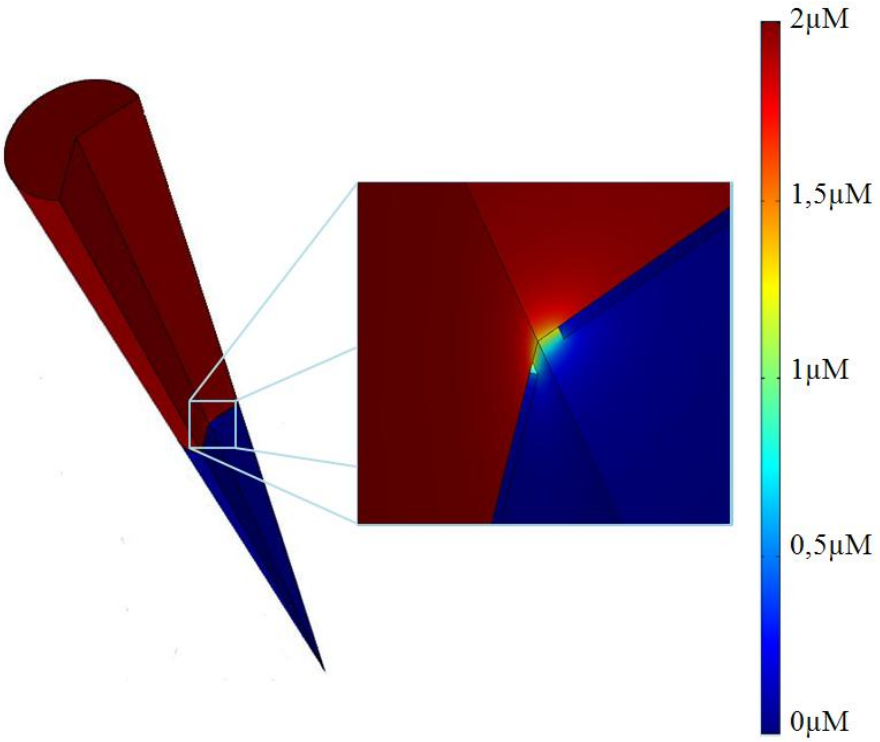

Figure 3.6: *Geometrical representation of the 3D model used, the concentration values represent its initial value.*

Figure 3.7 also illustrates the results of the analytical model using the calculated time constant of $\tau_{c2} = 0.53$ s as the solid line; the agreement between the FEM simulation and the analytic model is almost perfect.

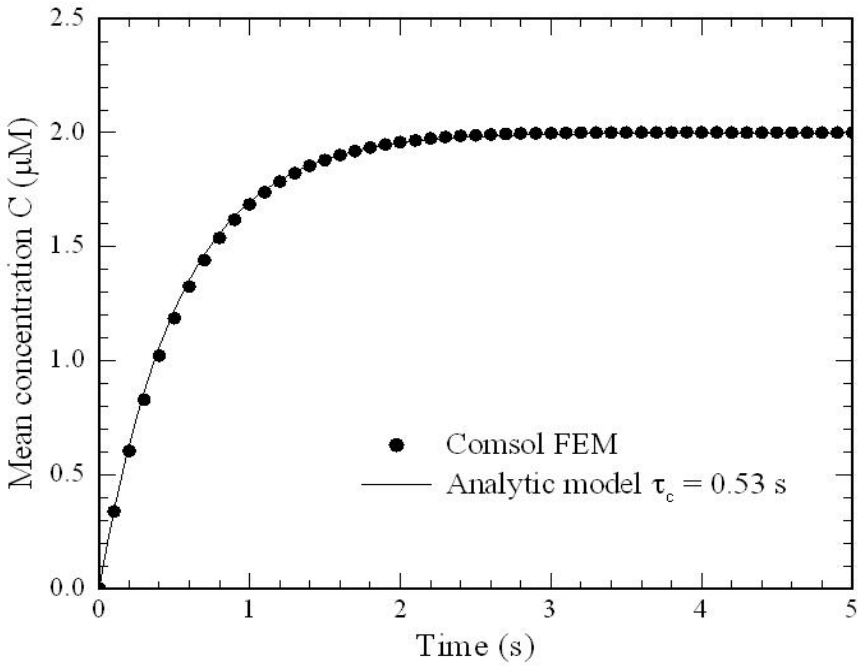

Figure 3.7: *The average concentration of MBs in the cell as a function of transfection time. Results from a COMSOL FEM model (dots) are compared to the analytical model (black line) with the time constant* $\tau_c = 0.53s$.

3.5 Experiment and results

Direct experimental verification of the diffusion model by tracking the fluorescence during transfection is difficult due to the high background from MBs in the medium. Therefore we instead tracked the decay of fluorescence from cells loaded with MBs after a second treatment with SLO to re-open pores and thus allow out-diffusion of MBs from the loaded cells to an initially MB free medium. The adherent cell line HeLa was transfected using the SLO protocol with MB towards TH (see chapter 2 for clarification on TH), but without a quencher attached. The pores were closed and cells were washed three times and incubated for 1 h to let cells recover while hybridization was not expected since TH was not expressed at that point in time. The cells were fluorescent as expected and had their normal morphology (data not shown) after transfection. At this point the cells were again treated with SLO reagent to re-open the pores and the fluorescent decay from the cells was monitored by time laps microscopy for 20 minutes. Figure 3.8 shows the fluorescence emission from a representative cell. After about 10 minutes, the fluorescence reached the base line level suggesting that all the transfected

fluorescent MBs had diffused out of the cells. The resulting time constant (200 s) however was much longer than that expected from the theoretical model. This suggests that other factors may dominate the transfection kinetics than diffusion of MBs over the membrane or that the parameters (number of pores and pore size) used in the diffusion model are incorrect. However, the results indicate that the 15 minute transfection period employed in this study is sufficient to obtain maximum load of MBs in the cells.

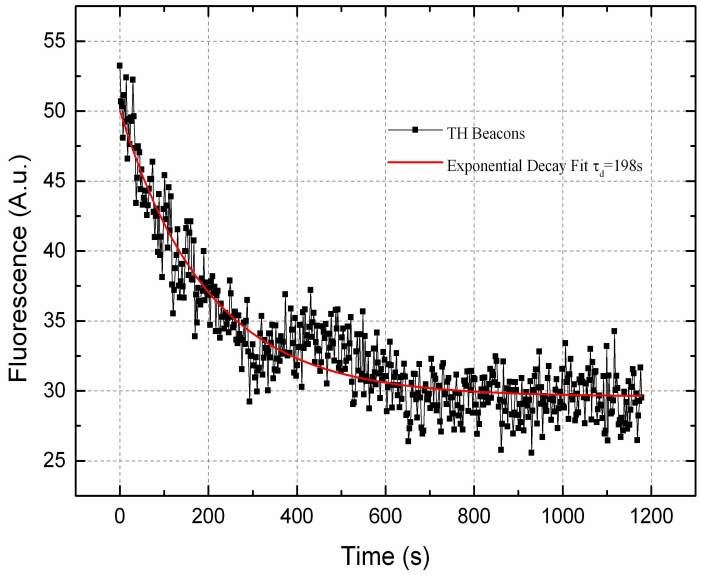

Figure 3.8: *Fluorescence emission decay as a function of time for a representative HeLa cell after the second treatment with SLO. The resulting time constant is* $\tau_{exp} = 198$ *s.*

The diffusion model suggests that within seconds MBs are moving into opened cells while the measured data suggest that steady state levels is reached after 10 minutes. While the discrepancy does not have any practical impact on a 15 minute transfection procedure, it points to other factors than diffusion of MBs affecting the speed of transfection. Firstly, the model takes into account only the diffusion process, assuming that all the pores are already open from the start. It is known from literature [19,24] that the pore formation involves the binding of streptolysin O molecules in arc- or ring-shaped structures comprising about 50-80 subunits that progressively form on the cellular membrane and cause lysis. This process depends on the SLO to cell concentration ratio. Furthermore, pore forming times between 10 s and 300 s have been recorded. Secondly, the pores exhibit a size distribution

and 30 nm is considered an upper limit for the diameter. Hence, an overall smaller pore size could be used in the model resulting in a lower permeability. Third, in the model the entire surface of the cells contains pores, while the adherent HeLa cells likely only had pores on cell surfaces facing the medium since it is likely that surfaces facing the bottom is inaccessible by SLO reagent and by MBs. Finally, the number of fully developed pores may be lower than assumed in the model. By contrast, the LUHMES cells are transfected in solution phase which of natural reasons provides pore formation all around the cells but also shorter diffusion distances of SLO reagents to the cells suggesting that LUHMES cells are more rapidly transfected than HeLa cells. In conclusion, the theoretical model shows that diffusion process alone is not a limiting factor and other time constants may play an important role in the transfection procedure. Despite that, since the standard transfection procedure was 15 minutes and all the MBs diffuse out of a HeLa cell in 10 minutes [Fig3.8], it is likely that LUHMES cells have the same concentration of MB inside as the concentration added to the medium. Given the cell size and the MB concentration, the number of MBs in the cell becomes approximately 56000 if the cell volume is corrected for the volume of the nucleus (approximately 10%), where MBs do not penetrate. Bustin [20.] found that there are about 108 mRNA copies of GAPDH per microgram of total RNA. Assuming that there is about 4 pg total RNA per cell, there would be about 400 GAPDH mRNA copies per cell, indicating that there is about 100-fold more MB than possible target.

Bibliography

[1] Tyagi S, Kramer FR.*Molecular beacons: probes that fluoresce upon hybridization.*Nat Biotechnol. **1996** Mar;14(3):303-8.

[2] Nitin N, Santangelo PJ, Kim G, Nie S, Bao G. *Peptide-linked molecular beacons for efficient delivery and rapid mRNA detection in living cells*. Nucleic Acids Res. **2004**; 32-58.

[3] Medley CD, Drake TJ, Tomasini JM, Rogers RJ, Tan W. *Simultaneous monitoring of the expression of multiple genes inside of single breast carcinoma cells*. Anal. Chem. **2005**, 77, 4713-4718.

[4] http://www.cdb.riken.jp/fsc2009/index.en.html

[5] Lundqvist, J.A. et al. *Altering the biochemical state of individual cultured cells and organelles with ultramicroelectrodes*. Proceedings of the National Academy of Sciences of the United States of America 95, 10356 -10360 (**1998**).

[6] Chen AK, Behlke MA, Tsourkas A. *Efficient cytosolic delivery of molecular beacon conjugates and flow cytometric analysis of target RNA*. Nucleic Acids Res. **2008**; 36.

[7] Gao J., *Integration of single cell injection, cell lysis, separation and detection of intracellular constituents on a microfluidic chip*, Lab On A Chip 4, **2004**.

[8] Huang Y., *Microfabricated electroporation chip for single cell membrane permeabilization*, Sensors And Actuators A-Physical 89 : 242 **2001**.

[9] Valero A., *Apoptotic cell death dynamics of HL60 cells studied using a microfluidic cell trap device*,Lab On A Chip 5, **2005**.

[10] Lee Sw.,*A micro cell lysis device*, Sensors And Actuators A-Physical 73-74 **1999**.

[11] Lu H, *A microfluidic electroporation device for cell lysis*, Lab On A Chip 5, **2005**.

[12] Lin Yc, *A microchip for electroporation of primary endothelial cells*, Sensors And Actuators A-Physical 108, **2003**.

[13] Hsiang-Yu Wang and Chang Lu,Anal. Chem., 2006.

[14] Andresen K. et al.*Injection molded chips with integrated conducting polymer electrodes for electroporation of cells*, J. Micromech. Microeng, vol.20, n.5, pag. 055010.

[15] Klein TM, Wolf ED, Wu R, Sanford J. C. *High-velocity microprojectiles for delivering nucleic acids into living cells.* Nature **1987**; 327(6117): 70-73.

[16] http://physics.ucsd.edu/ groisman/Gene%20guns.html

[17] Giles RV, Spiller DG, Grzybowski J, Clark RE, Nicklin P, Tidd DM. *Selecting optimal oligonucleotide composition for maximal antisense effect following Streptolysin Omediated delivery into human leukemia cells.* Nucleic Acids Res. **1998**; 26(7): 1567-1575

[18] Walev I, Bhakdi SC, Hofmann F, et al. *Delivery of proteins into living cells by reversible membrane permeabilization with Streptolysin-O.* Proc. Natl. Acad. Sci. USA **2001**; 98(6),3185-3190

[19] W. Niedermeyer, *Interaction of streptolysin-O with biomembranes: kinetic and morphological studies on erythrocyte membranes*, Toxicon, vol. 23, pagg.425-439, **1985**.

[20] Keyel P. A., Loultheva L., Roth R., Salter R. D., Watkins S. C., Yokoyama W. M., Heuser J. *Streptolysin O clearance through sequestration into blebs that bud passively from the plasma membrane.* Journal of Cell Science. **2011**, 124, 2414-2423.

[21] Lukacs GL, et al. *Size-dependent DNA mobility in cytoplasm and nucleus.* J Biol Chem. **2000** Jan 21 275(3):1625-9.

[22] H. S. Carslaw and J. C. Jaeger *"Conduction of heat in solids" 2 Ed.* (Oxford University Press, London, **1959**, p 215.

[23] Grathwohl, P. *Diffusion in natural porous media: Contaminant transport, sorption/desorption and dissolution kinetics.* **1998** Kluwer Academic.

[24] Palmer, M. et al. *Streptolysin O: A Proposed Model of Allosteric Interaction between a Pore-Forming Protein and Its Target Lipid Bilayer.* Biochemistry 37, 2378-2383, **1998**.

Chapter 4

Signal amplification with molecular beacons

4.1 Introduction

Realization of molecular beacons with high sensitivity has been always an issue. The selectivity of molecular beacons and the capacity to discriminate single nucleotide polymorphism have to pair with the ability to transduce a target recognition event into a measurable signal in the most efficient way. For target sequences that are low abundant in cells, the conventional molecular beacon is insufficient [1]. Therefore, most of the current applications of molecular beacons are limited to situation in which mRNA is present in high copy number. In order to improve the sensitivity of the probe, the signal-to-noise ratio (S/N) must be improved. The S/N ratio can be defined as:

$$\frac{F\text{unquenched} - F\text{quenched}}{F\text{quenched} - F\text{buffer}} \tag{4.1}$$

where FFunquenched is the fluorescence of the molecular beacon in the open state, i.e. bound to complementary target or otherwise linearized, Fquenched is the fluorescence emission of the MB in the close state, i.e. the background fluorescence due to incomplete quenching and Fbuffer is the background fluorescence of the buffer alone in the absence of MBs. In order to acquire higher S/N the strategy is dual; it is possible to improve Funquenched by perfecting the fluorochrome structure and obtain high signal emission, or it is possible to lower Fquenched by engineering a high efficiency quencher and suppress the background fluorescence of the unquenched probe. The latter strategy alone might not be sufficient. In some cases, a certain background fluorescence coming from the cellular environment (auto fluorescence) is always present, regardless how much the fluorescence from the donor is quenched.

4.1.1 Enhancement of $F_{\text{unquenched}}$

One strategy to improve the fluorescence emission is to employ Poly (phenylene ethynylene) (PPE) [2] as fluorophore [Fig.4.1]; it is a water soluble polyelectrolyte with high quantum yield. The use of PPE on the other hand is not straightforward and numerous problems arise: the conjugation of PPE to an oligonucleotide strand requires modification of PPE with a reactive group such as a carboxylic acid or an amine. The addition of this reactive pendant groups could change the properties of the polymer. Also, the electrostatic interaction between the PPE and the target molecule could inhibit the coupling reaction leading to a low efficiency of the conjugation process. Finally, the conjugated product has similar chemical and physical properties as the unconjugated one and could lead to difficulties in separation of the two. In [3] the issue regarding conjugation and purification of the final probe were solved. The fluorescence data for molecular beacon conjugated with various organic fluorophore (Cy3, FAM, Alexa Fluor 488) shows that PPE is much brighter and its emission is nearly 20 times higher than Cy3 and 6 times higher than Alexa Fluor 488.

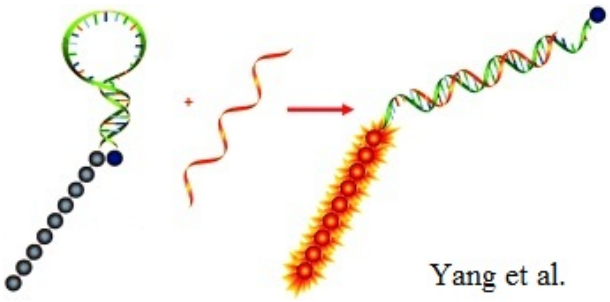

Figure 4.1: *The complementary target displace the PPE chain from the quencher releasing the fluorescence signal*

Another strategy consists in the use of quantum dots instead of organic fluorophore [4]. This substitution greatly increases the brightness of the beacons and allows simultaneous multiple tracking of different target. Different quantum dots can be excited with the same wavelength but, varying the core-shell composition, it is possible to obtain well-spaced different spectral emission and allow separation of each contribution on different channels. This would allow for multiplexing. Furthermore quantum dots have high stability against photobleaching, enabling longer imaging both for in vivo and in vitro application. Disadvantages in the use of QDs consist in issues regarding biocompatibility and limited transfection efficiency due to their size. As it was shown in the previous chapter, internalization of beacons is ultimately

a diffusion process of a "rigid" object through a porous membrane. If the size of these objects approach the size of the pores, the diffusion, and so the beacons internalization, is greatly reduced.

In another approach, the donor-acceptor pair was slightly changed; instead of an organic quencher to quench the fluorescence emission, the beacon has been synthesized with a fluorophore-fluorophore couple with absorption spectra from the "acceptor-F2" matching the emission spectra of the "donor-F1" [5]. In this way, when the beacon is in the closed state, fluorescence from F1 is absorbed by F2 causing it to shine. When complementary target hybridize to the loop, 1 and 2 are displaced from each other, FRET is disabled and F1 starts to emit while the emission of F2 drops significantly[Fig.4.2]. The advantage of having two fluorophores is that the S/N ratio is not anymore dependent on Funquenched coming from a single dye, rather it is dependent on $F1$ounquenched/$F2$unquenched, the ratio between emission from F1 and F2.

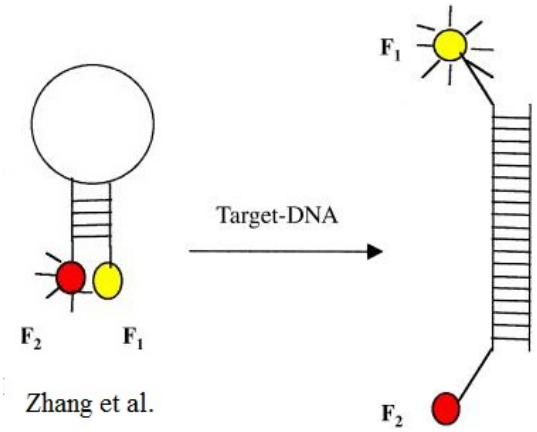

Figure 4.2: *Structure of the double labeled MB; the working principle is based on FRET between F1-F2 which is cancelled after hybridization.*

4.1.2 Enhancement of F_{quenched}

The problem of signal coming from unquenched probe, causing high background has been tackled in many ways. Yang et al. [6] had the idea to conjugate the DNA strands with multiple quenchers (Super Quenching, SQ) instead of having only one [Fig.4.3 left]. This approach resulted in considerable increase in the quenching efficiency, going from 92.9% for a single quencher, to 98.75% for double quencher and finally 99.7% for a series of three quenchers. The quenching improvement resulted also to an s/n of 320

fold for the three quencher configuration, opposed to 14 fold for the conventional beacon [Fig.4.3 right]. The multiple quencher configuration brings also advantages in purification of the probes; the hydrophobicity of the multiple quenchers improves separation time during high performance liquid chromatography, improving separation of labeled probes from unlabeled ones. SQ also causes stabilization of the hairpin structure, increasing the melting temperature significantly and therefore improving the ability of beacons to distinguish single base mismatches target DNA.

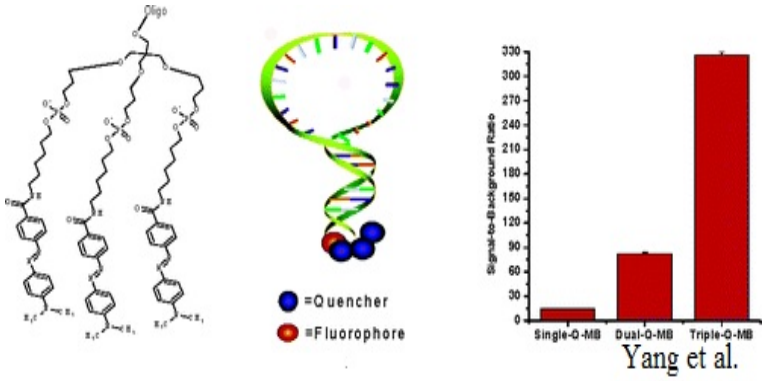

Figure 4.3: *Structure of multiple quenchers MB (left) and s/n performances of single, double and triple configuration (right).*

Gold nanoparticles also offer a valid alternative to increase the performances of MBs. In [7] it was reported than a single 1.4 nm gold nanoparticle was able to quench the fluorescence emission of a given fluorophore as much as 100 times better than ordinary organic quencher DABCYL, arriving to a quenching efficiency of $99.966 \pm 0.026\%$ [Fig.4.4]. The advantage in using GNPs as quencher lies also in the fact that their quenching performances are independent on the salt concentration of the solution and on the emission spectrum of the conjugated fluorophore.

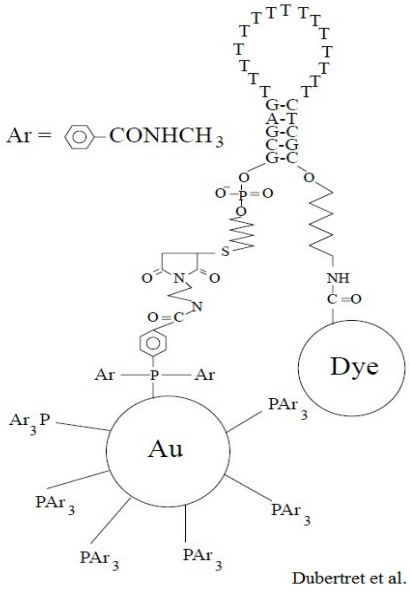

Figure 4.4: *Gold quenched MB*

4.1.3 Amplification techniques for signal enhancement

The techniques describes previously are able to increase the s/n generated by the opening of a single molecular beacon for each complementary target. A different approach would be to create a system that causes the opening of multiple beacons triggered by a single complementary target. One way to obtain this result is presented by Jacroux et al. [8]; here a special molecular beacon composed of a DNA-stem and an RNA-loop is combined with RNase H. When the beacon hybridized to its complementary DNA target, the RNase H interacts with the RNA-DNA double strand and digests the RNA part. In this way, the fluorophore-quencher pair, previously connected through the RNA filament, is not anymore held together and the quenching is completely suppressed. Also, the target DNA is now free from the beacon and could take part in another hybridization event together with a new beacon [Fig.4.5]. This method allows generation of a high signal even in presence of few complementary targets. The results show an improvement of the S/N compared to the conventional beacon configuration of about 2.8 times, leading to an S/N ratio for the RNase amplification system of about 30.

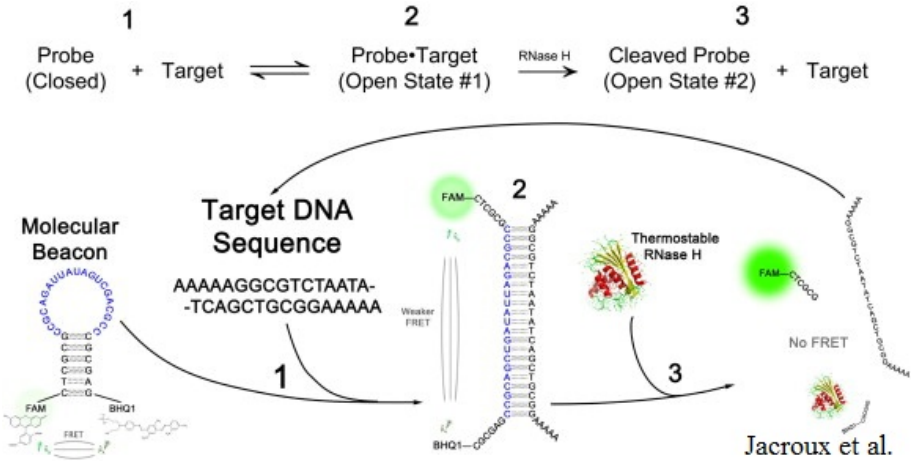

Figure 4.5: *Signal amplification using RNase*

4.2 Signal Amplification - Concept and working principle

We present here two strategies to improve the sensitivity of the molecular beacons by enhancing Funquenched. The concept is based on the idea of using a series of molecular beacons as "building blocks" that will hybridize to one and another in a chain reaction once the first one is triggered. The idea of using DNA strands as tiles to build complex shapes has been previously reported by many groups [9]. The clear advantage of our approach is that it does not require the addition of a cleaving agent, such as in [8, 10] and also the system can, in principle, be reversible. The methodologies reported previously involve the digestion of the molecular beacons involved in hybridization, leaving the fluorophore-quencher pair, now uncoupled, free in the solution. The solution presented here does not involve the destruction of the MBs structure and therefore could be reset to initial state, ready for another sensing. It should be pointed out that all the previously reported ways to improve both Funquenched and Fquenched can be successfully integrated with this system, leading to even better performances. Two approaches will be described in details: linear and avalanche signal amplification.

4.2.1 Linear signal amplification using molecular beacons

Working Principle

This rather simple approach consists in using a cascade of molecular beacons, each interacting with the next one. The idea is to design beacons based on the shared stem configuration [11] (i.e. when part of the stem is also part of the hybridization loop), but to extend the length of the stem in order to trigger the opening of another beacon. One example of the typical beacon used in these amplifications can be seen in figure 4.6; it is possible to recognize three main sections: 1) the loop section (corresponding to the grey are in figure 4.6) which, upon hybridization with its own complementary target, causes the opening of the beacon. 2) The t-spacer section (the pink area in figure 4.6) that corresponds to a short sequence of t bases that are not involved in any hybridization process but provide a bendable joint that increase the flexibility of the beacon. 3) Last, and most important, is the stem/loop section (red part of figure 4.6) which act at the same time as stem of its own beacon structure and hybridization sequence for the loop of the next beacon along the amplification chain. The black branch is the complementary stem segment; it does not take part in any further reaction and will remain single stranded after hybridization.

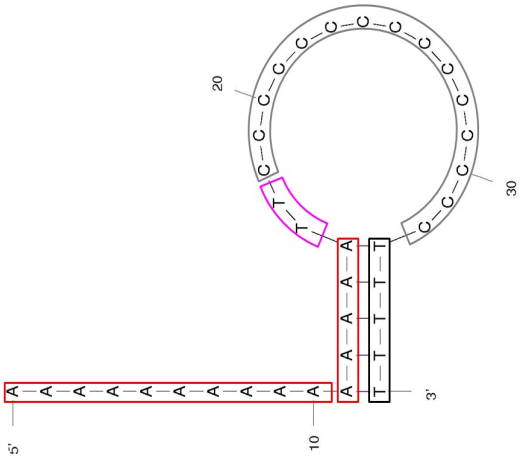

Figure 4.6: *: Schematic representation of a beacon used in the amplification system. Three different sections are highlighted, loop section in grey, t-spacer in pink and stem/loop region in red.*

The working principle of the linear amplification system is pictured in figure 4.7. The reaction starts with the opening of the first beacon, MB1,

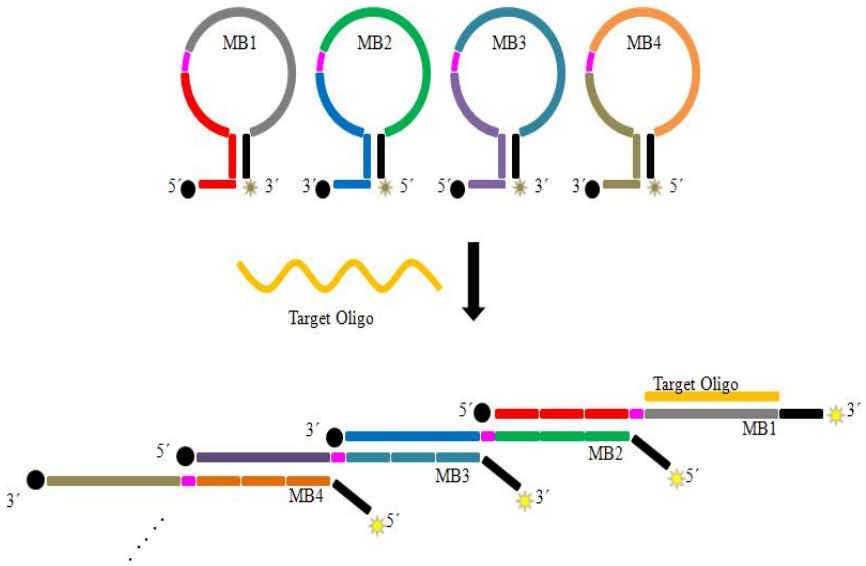

Figure 4.7: *Schematic process of the linear probe amplification*

which is the one encoded with the specific target sequence of interest. As described previously in the beacon structure, the stem and the protrusion of MB1 is complementary to the loop region of MB2. When MB1 hybridizes to its complementary target, the hairpin opens and fluorescence emission is restored. Furthermore, at this time, the free arm of MB1 hybridizes with the loop of MB2 that opens as well, freeing its own stem-arm that will interact in the same way with MB3 and so on [see Fig.4.7]. In this way, by wisely labeling and designing the cascade beacons, it is possible to obtain a signal amplification proportional to the number of beacons forming the cascade.

4.2.2 Signalling Avalanched Molecular Beacons Amplification - SAMBA

Working Principle

This system share the same beacon structures as described for the linear system and a similar working principle, but it has one major difference: instead of consequently adding new and different beacons,each responding only to the previous one, a self-amplified chain reaction of hybridization among a fixed amount of beacons is introduced. The operational principle is outlined in figure 4.8. Compared to the linear system, beacon nr.3 is designed so that its protruding arm will hybridize to the loop of MB2 and

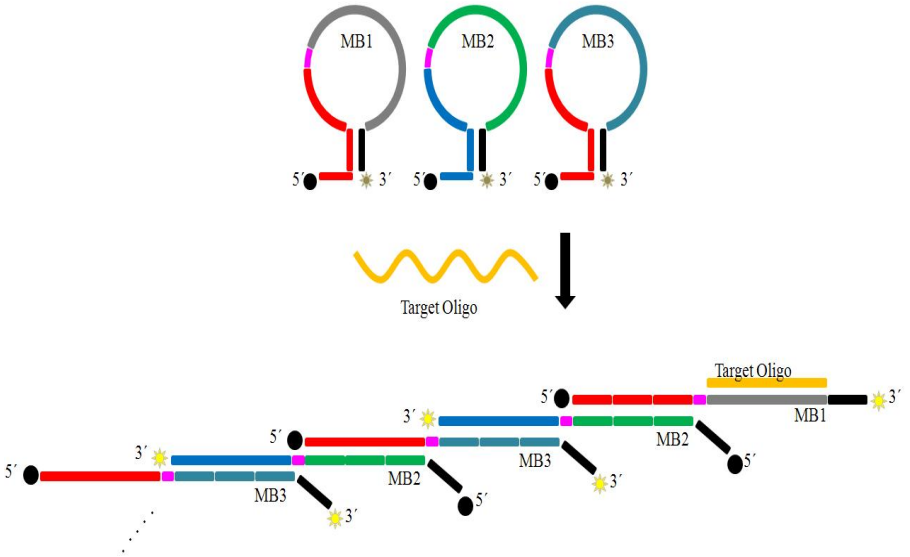

Figure 4.8: *Schematic process of the avalanche probe amplification*

trigger a chain reaction involving 2-3-2 .In more details the reaction takes place following the next steps:

1. MB1 hybridizes to its complementary target;
2. the free stem-arm protruding from MB1 hybridizes with the loop of MB2;
3. the free stem-arm protruding from MB2 hybridizes with the loop of MB3;
4. the stem-arm of MB3 hybridizes now with the loop of MB2 and the reaction continues following the pattern 2-3-2-3-;

The major limitation of molecular beacon technology, as pointed out before, lies in their intrinsic working principle. Each complementary target causes the opening of one and only one MB, so this method is mostly suitable for applications in which the target sequence is present in high copy number. In the SAMBA system the hybridization of MB1 towards one single complementary sequence triggers the opening of a cascade of labeled beacons, generating an explosive signal. The previously reported limitation of complementary target strands and beacons being in stoichiometric ratio of 1:1 is therefore removed.Also, another major advantage of this technique is that one need only to change the recognition sequence of MB1 in order to

have a functional detection setup for the target of interest, while MB2 and MB3 will be maintained with the same sequence, being them independent from the particular target.

The linear amplification is a fundamental step in order to obtain functional avalanche amplification. Therefore, there will not be a separation among the two methods along the description of the experiments. Each time the performance of one or the other system will become relevant, a clear distinction will be made.

4.3 Materials and Methods

4.3.1 Fluorescence Measurements

The fluorescence measurements were performed using the PCR machine Chromo4 real time detector from Bio-Rad Laboratories. This instrument allows the handling of 96 different samples at the same time, carefully controlling the incubation temperature (from 0 °C to 105 °C with 0.3 °C of accuracy). The fluorescence detection is calibrated to discriminate signal coming from different labeling agent, for example Cy3, Cy5, TAMRA, FAM, ROX, TET, JOE, Sybr Green I, TexasRed and VIC.

4.3.2 Gel Electrophoresis

Gel electrophoresis is a method used to achieve separation among macro molecules based on their size and charge. DNA fragments, which are negatively charged, are separated by the application of a voltage difference which pulls the filaments along the gel towards the positive end. The oligos are dragged onward the gel length by electrophoresis and along the path, they separate in distinct bands according to the length of the filaments. The DNA strands will have to diffuse along the gel porous medium and smaller strands will diffuse and travel faster, separating from the longer and heavier ones. The gel material can be stained using for example ethidium bromide which, when intercalated into DNA, fluoresce under ultraviolet light and allows the detection of the fragments. In the experimental setup used in the following sections, the DNA mixtures were injected inside wells of a 4% agarose gel in TAE buffer and a voltage difference of 100 V was applied across the gel slab for about 30 min. The particular filter set present in the fluorescence detection apparatus allows the detection of ethidium bromide which has is peak of emission around 605 nm. As previously pointed out, this particular dye is an intercalating agent that locates only in between a double stranded

chain. Being the DNA fragments under investigation rather short (15 bps) the detection could be difficult. Fortunately one of the labeling dye covalently linked to the beacons, TexasRed, has its maximum emission around 615 nm, close to the one of ethidium bromide. Therefore it will be possible to detect a high fluorescence signal when TexasRed is employed in the beacon design.

4.3.3 Beacons design

The molecular beacons for both the linear and the avalanche signal amplification were designed using beacons design software, such as mFOLD. [12] This software is able to calculate all the possible geometrical folding conformation of a given oligonucleotide strand listing them in order of their change in Gibbs free energy value ($\triangle G$). $\triangle G$ is a way to represent how thermodynamically stable a structure may be. When two single stranded oligos come together to form a duplex, there is a change in the energy of the system and $\triangle G$ represents the net exchange of energy between the system and its environment and can be described as the thermodynamic relation:

$$\triangle G = \triangle H - T \cdot \triangle S \tag{4.2}$$

where $\triangle H$ (Enthalpy) represent the total energy exchange between the system and the environment, while $T \triangle S$ (Entropy) stands for the total energy exchange spent by the system to reorganize itself. It is possible to distinguish three behaviors: if $\triangle G > 0$ the system is most likely to arrange in single strands, if $\triangle G < 0$ the system will tend to produce products of reaction, in this case a double stranded oligo. The special case in which $\triangle G = 0$ indicates that the system is at the equilibrium and the reversible reaction of product formation and reagent re-aggregation is balanced. For this reason it is possible to define the melting temperature T_m as the temperature at which $\triangle G = 0$ and single stranded and double stranded oligos are in ratio 1:1. The software allows the calculation of $\triangle G$ for different oligo's backbone chemistry and for different buffer conditions, such as salt concentration and temperature. These predictions were double checked using OligoAnalyzer 3.1 [13] and the melting temperature of each section of the beacons, which provides an indication of the hybridization strength of each segment, was studied in particular. For clarity see figure 4.9, the loop section (grey), the stem/loop section (red) and the proper stem section (black) were analyzed in order to find a compromise between the strength of the stem, which ensure that the beacon is closed, and the strength of the loop/stem region, which ensures that the next beacon would be opened after the hybridization of the

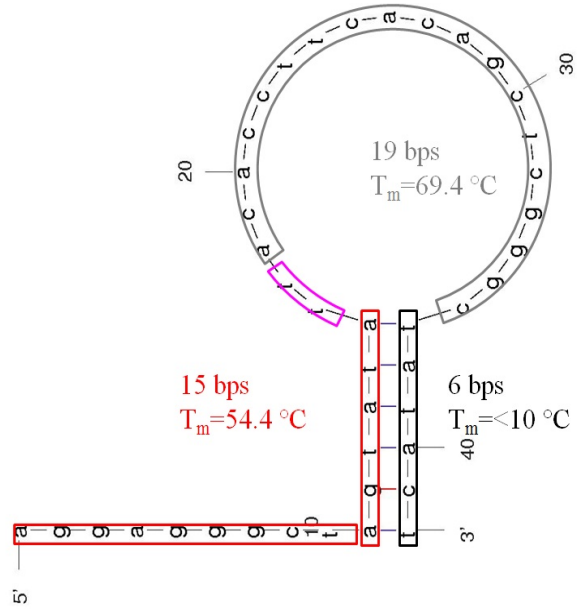

Figure 4.9: *Schematic representation of the analysis made on the beacons for the amplification system. Each section of the beacon has been studied independently in order to find a compromise between stem strength and hybridization capability.*

previous one. Another main characteristic of the designed beacons was to ensure that the hairpin structure was the first (if not only one) configuration possible at a rather high value of $\triangle G$. The final design of the beacons is the outcome of several design iteration.

4.4 Amplification First Version

4.4.1 Design of the system

The initial attempt to produce an amplification system was based on a three beacons system (figure 4.8). The first step in the design of the system was to determine the length of the beacons that offered a tradeoff between hybridization capability and stem strength, as pointed out above. The hybridization strength translates in the length of the loop region, where the longer the loop, the stronger the hybridization towards complementary target is, while the strength of the stem is also determined by its own length. Parallel to this aspect, the complexity of final conformational configuration of the beacon must be taken into account. As opposed to the previous issues, here, the shorter the total beacon length, the less the complexity will be, resulting in an easier task to ensure that the hairpin configuration is the only one

allowed. It is known from literature [14] that the balance between selectivity and hybridization rate is achieved with a stem of 5-7 nucleotides and a loop region of 15-25 nucleotides. We chose a strong stem, 5-6 bps long, and a relatively weaker loop of 15 bases to minimize complexity and reduce as much as possible background fluorescence (see an example beacon in figure 4.9) Each of the three beacons was labeled with a different fluorophore in order to follow the process dynamics in detail; MB1 was labeled in TexasRed, MB2 with FAM and MB3 with Cy3.

4.4.2 Results

In the first experiment 4.10 the mutual reaction between beacons was tested. Each couple of subsequent beacons, MB1+MB2 and MB2+MB3, was tested to study the cross hybridization even in absence of complementary target. In particular MB1 was incubated with MB2 at ambient temperature for 5 minutes and later, the complementary target for MB1 was added to the mix and the fluorescence was measured. In the same conditions, MB1 was incubated with its own complementary target for 5 minutes and later MB2 was added to the mix. In this way, the same samples were present at the end inside each test tube, but the pipetting order of insertion was different. The same experiment was repeated in the same fashion with MB2 and MB3. The signal MB2-MB3 in the presence of T2 is taken as example (the other cases show similar behavior). MB2+T2 were incubated first and the fluorescence was 1.16 a.u. MB3 was subsequently added and its resulting fluorescence emission was 0.011 a.u. from MB3[Fig.4.10]. When MB2 was first incubated with MB3 and later with T2, the signal intensity from MB2 reaches 0.56 a.u. while the level of MB3 was 0.018 a.u[Fig.4.10]. It is possible to notice how the different insertion order of the sample causes MB2 to half its signal and MB3 to nearly double it. Therefore the pipetting order influences the resulting emission. The experiment, repeated at 37 °C, showed a similar behavior.

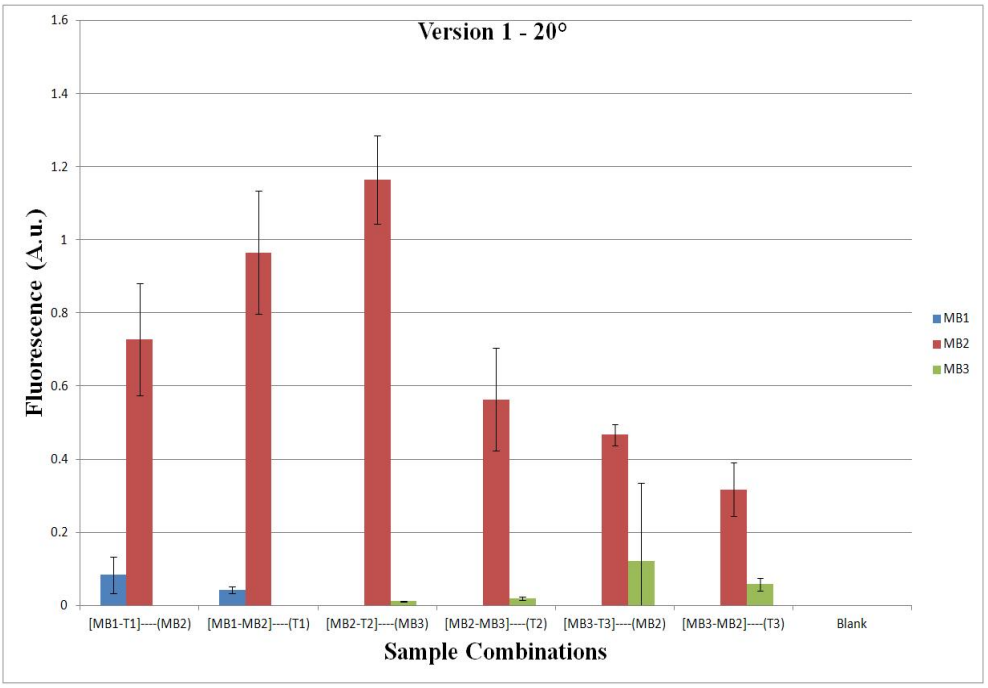

Figure 4.10: *Fluorescence emission of solution containing combination of beacons, pipetted with a different temporal order in the test tube. The first two samples incubated together are enclosed in the squared brackets in the x-axis, while the sample indicated in the round brackets was added after 5 minutes of incubation. The experiment was repeated 4 times and the value averaged among the experiments.*

4.4.3 Discussion

The beacons used in this first version had the stem region directly adjacent to the beginning of the loop part, leaving a rather large single stranded overhang protruding from the conventional hairpin structure (4.9). As previously described, this overhang (plus one side of the stem) will be responsible for the cascade amplification, serving as complementary sequence in charge of the hybridization of the "next" beacon along the cascade. The fluorescent emission experiment of figure 4.10 shows an unequal response for the two different orders of pipetting of the same samples. The system could be simplified as "on"-"off", meaning that only the triggering of the reaction by the complementary target should cause the avalanche response and that hybridization to complementary strand will cause complete linearization of the beacon. In this case then, the two combinations should display the same level of fluorescence emission, regardless the order of insertion in the test tube. The dissimilar intensities of emission indicate that cross hybridization between beacons is present. We speculate that the protruding section of the hybridization arm

was hybridizing to the loop region of the following beacon without causing its complete opening [Fig.]. This will prohibit the complementary target to take part in the hybridization reaction and to completely open the beacon, properly displacing fluorophore from the quencher and restoring the total signal intensity.

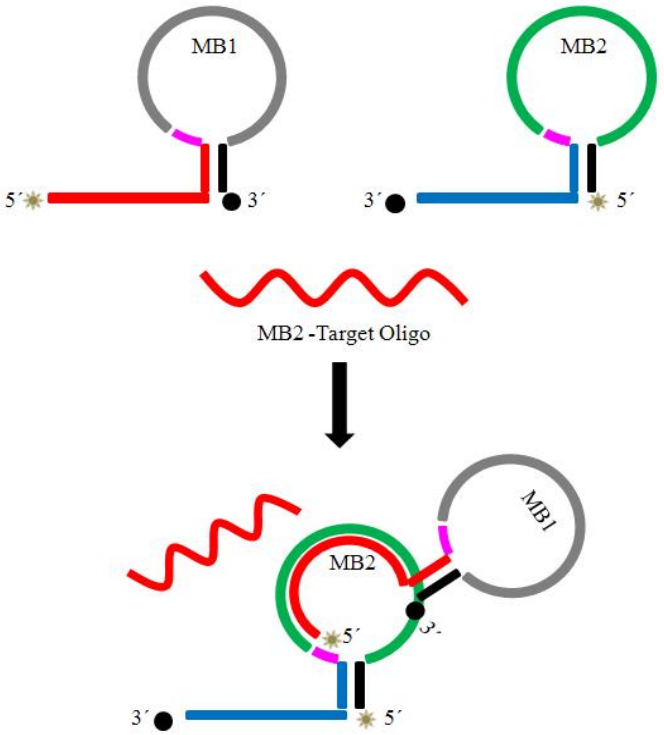

Figure 4.11: *Model of inhibition of probe hybridization caused by cross talking beacons.*

Therefore the following version of beacons was designed in order to place the stem more or less in the middle of the hybridization arm, as shown in fig. 4.12, avoiding a long segment of the hybridization of to be free and single stranded.

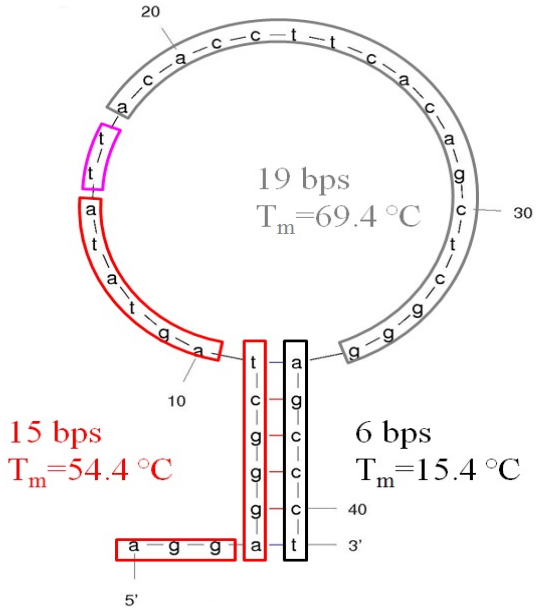

Figure 4.12: *Schematic representation of a beacon used in the amplification system, second version. The stem now lies in the center of the protruding arm, leaving only few bps sticking out.*

4.5 Amplification Second Version

4.5.1 Design of the system

In order to avoid unwanted cross hybridization among beacons, the position of the stem was changed in order to lay more or less in the center of the protruding arm responsible for the hybridization of the next beacon [Fig.4.12]. The beacon specifics are summed in the following tables:

Table 4.1: Properties of version 2 beacons

	MB1	MB2	MB3
Beacon length	41	38	35
Stem Length	6	6	6
Arm length	15	15	15
GC content stem	66%	66%	66%
GC content arm	46%	53%	46%
$\triangle G$	-3,75	-3,44	-3,76
N. of protruding bases	3	4	4

The three beacons have the following sequences and labels:

Table 4.2: Sequences of version 2 beacons

Beacon Name	Sequence	Label
MB1	aggagggctagtatattacaccttcacagctcgggagccct	TexasRed
MB2	gacgcttatactagccctcctttactgtagcgtcgatg	FAM
MB3	aggagggctagtatacatcgacgctacagtagccc	Cy3
T1	tcccgagctgtgaaggtgt	
T2	aggagggctagtata	
T3	actgtagcgtcgatg	

4.5.2 Results

The fluorescence emission of each molecular beacon and combinations of them was measured at different temperatures, here are reported the results obtained at 20 °C and 37 °C. Figures 4.13 shows the fluorescence emission for the individual beacon (background level) and each beacon incubated with its complementary target.

The following values of S/N (FFhybridized/FFunhybridized) were calculated:

- at 20 °C, MB1= 6.03, MB2= 6.67 ,MB3=26.32;
- at 37 °C, MB1= 13.15, MB2= 3.47, MB3= 17.49.

The autofluorescence of unhybridized beacons increases with temperature (Fig 4.13). MB2 has 2-3 fold higher autofluorescence as compared with MB1 and MB3 respectively. All beacons opened upon addition of the respective target with essentially no cross hybridization (data not shown). The s/n ratio of MB1 increased with temperature while both MB2 and MB3 displayed a decrease in s/n ratio with temperature. MB1 and MB3 have low background signal at both 20 °C and 37 °C. Specific hybridization to MB1 was more than doubled at 37 °C as compared to 20 °C. The specificMB2 has a high level of background emission compared to the other probes. MB2 autofluorescence increased with temperature.

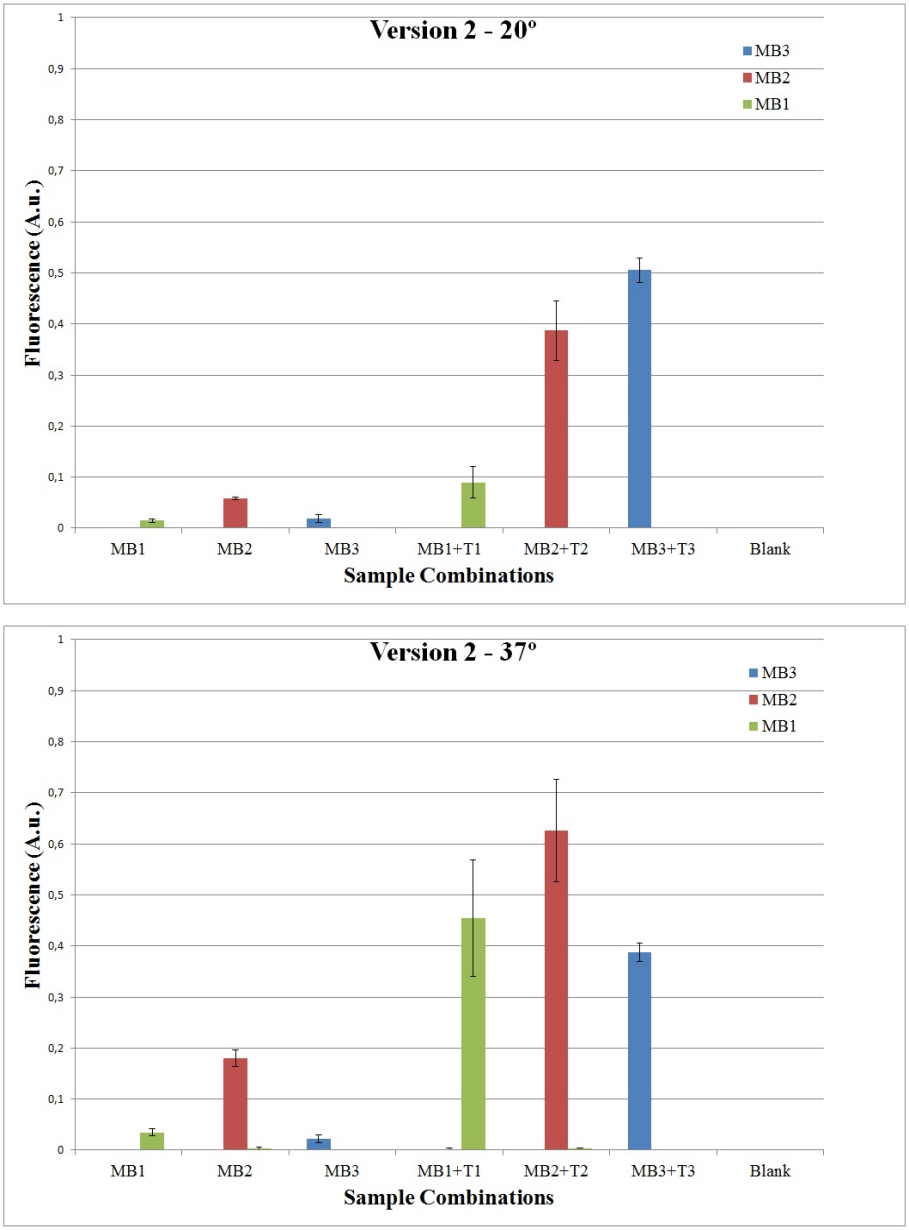

Figure 4.13: *Fluorescence results from avalanche system version 2; the graph shows the fluorescence emission from the singular MB1, MB2 and MB3 alone (background) and incubated with complementary target (maximum signal). Each experiment was repeated 4 times.*

In figure 4.14 the interaction between MB1 and the other probes singularly was investigated. MB1+MB2 interact with each other even in absence of target; their fluorescence level increases, especially the level of MB2. The fluorescence intensity of MB2 at 20 °C increases from 0.05 for the single probe

to 0.14 when incubated with MB1 and at 37 °C from 0.180 to 0.355. On the contrary, the fluorescence emission of MB1 is nearly unaffected. When complementary target T1 is added to the mix, the level of fluorescence of MB1 raises significantly as well the fluorescence from MB2. This indicates that the opening of MB1 causes its free stem/arm to hybridize to MB2. As control, the complementary target for MB2 was added and, in this case, a signal from MB2 but not MB1 was observed (Figure 4.14). Adding MB1 targets T1 to a mixture of MB1 and MB3 did not result in any signal from MB3 indicating no cross activity between MB1 and MB3. The same situation happens when T3 is added to the mixture of MB1 and MB3: MB3 hybridizes and increase its emission while MB1 remains silent. When the temperature was increased from 20 °C to 37 °C, the background coming from the combination of MB1+MB2 without the target increased considerably. The fluorescence increase from MB1 when hybridized to T1 and incubated together with MB2 did not produce the same value of fluorescence as the hybridized beacon alone does. If we consider only the signal coming from MB1, MB1+T1 signal is at 20 °C 0.089 and 0.455 at 37 °C. Instead, MB1+MB2+T intensity is 0.041 at 20 °C and 0.125 at 37 °C .Furthermore, because the background from unspecific hybridization increases, the S/N of MB1 drops to only 4.12

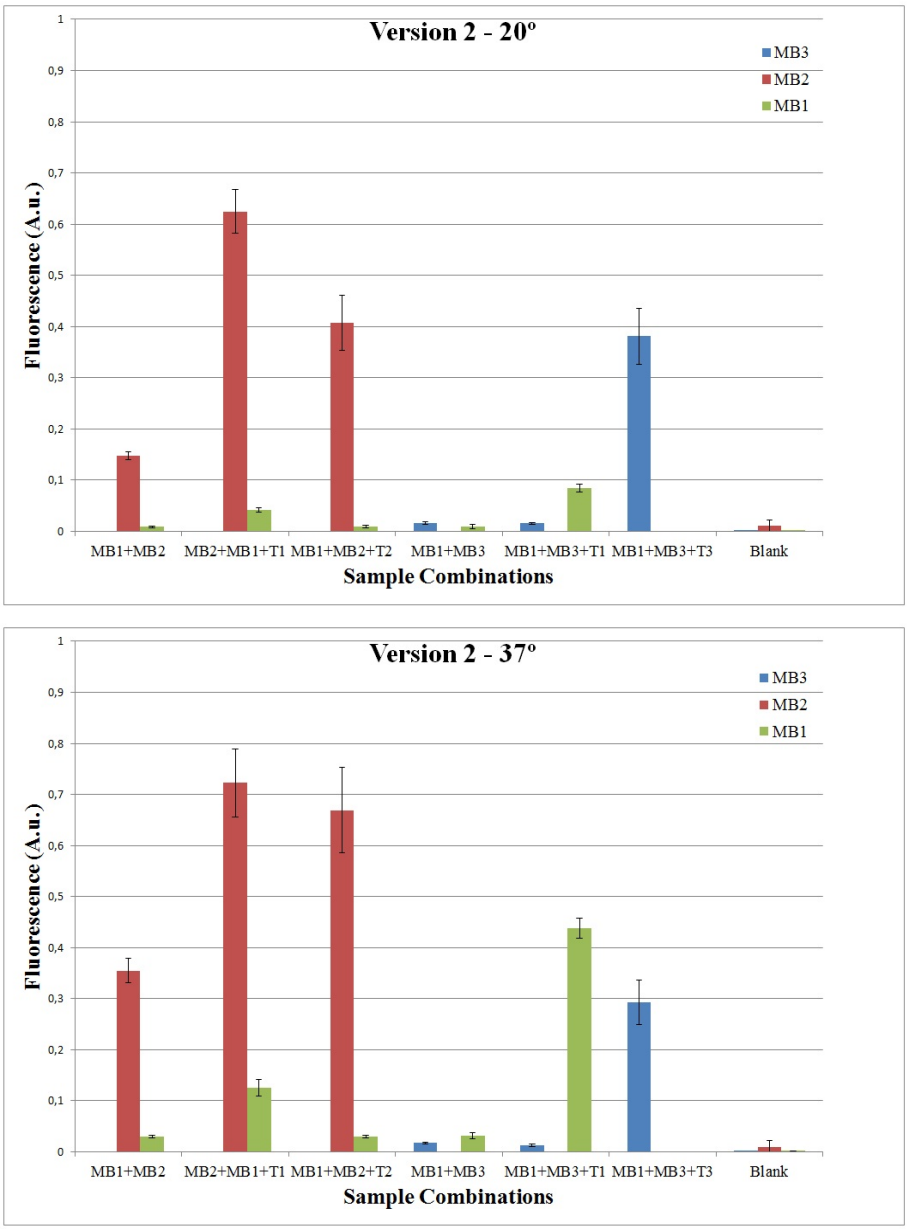

Figure 4.14: *Fluorescence results from avalanche system version 2; the cross hybridization of groups of two probes was analyzed (MB1+MB2, MB1+MB3). Each experiment was repeated 4 times.*

In figure 4.15 the fluorescence emission of the group MB2+MB3 shows that, as in the case of MB1+MB2, there is a cross hybridization even in absence of the complementary target. The maximum signal emission from this probe couple is considerably weaker than previously reported in the other experiments. The fluorescence signal coming from the entire system,

MB1+MB2+MB3 shows increased level of fluorescence which is equivalent to cross hybridization. The same mix incubated with the triggering target, T1, resulted in a weak signal generation. MB1 open and causes the partial opening of MB2, while MB3 seems to be unaffected by the cascade reaction.

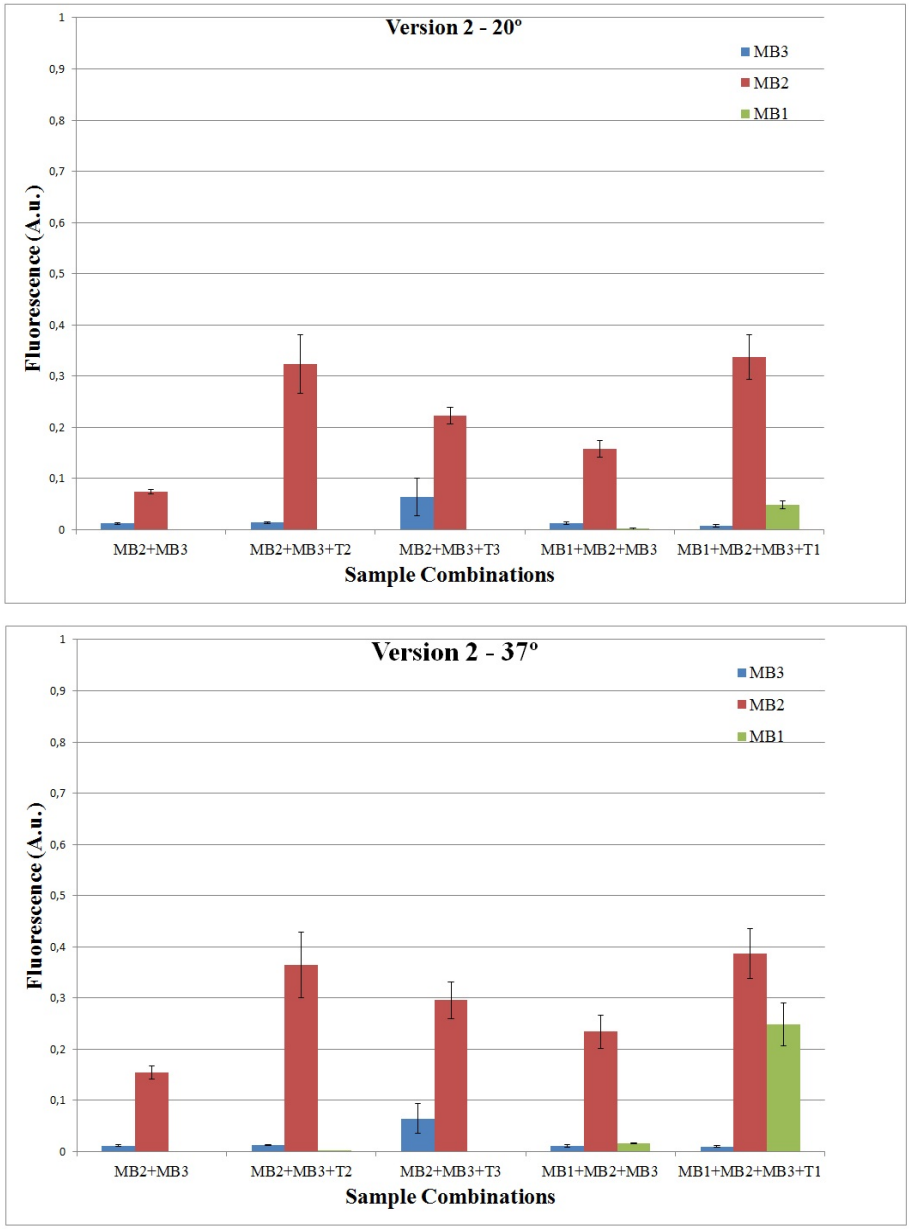

Figure 4.15: *Fluorescence results from avalanche system version 2.The cross hybridization of groups of two probes was analyzed(MB2+MB3, MB1+MB2+MB3). Each experiment was repeated 4 times.*

The fluorescence signal measurements were corroborated by electrophoresis experiment performed with an agarose gel. 4.16

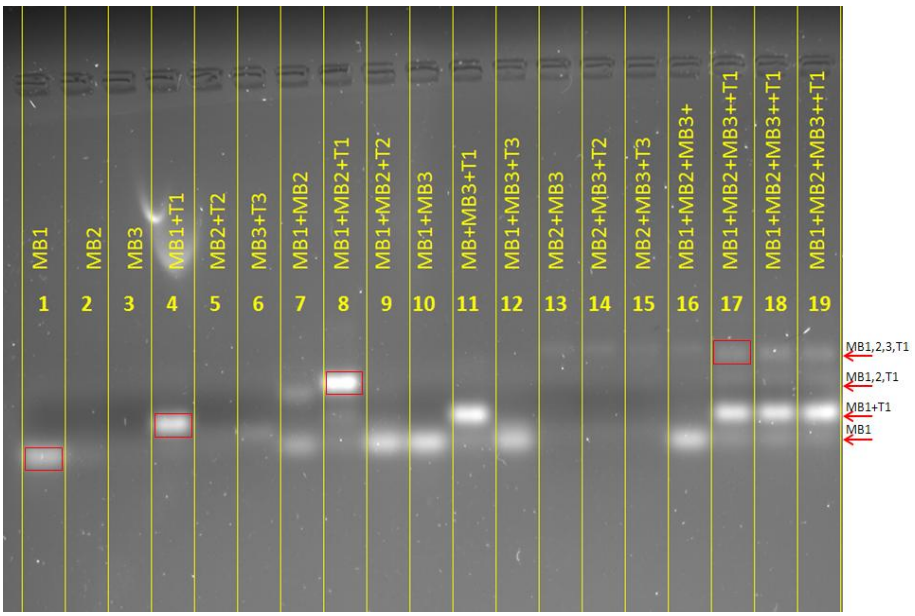

Figure 4.16: *Agarose gel of version 2 avalanche system. Most of the signal comes from the labeling dye of MB1, while MB2 and MB3 are poorly visible.*

The lanes 1-2-3 in fig.4.16 contain each probe individually and, respectively, lanes 4-5-6 contain the beacon together with their own complementary target. The hybridization of MB1 to its complementary sequence causes the rupture of the hairpin structure of the molecular beacons. The complexes migrate slower and result in the formation of a band at higher level (compare lane 1 containing the unhybridized probe, with lane 4 containing the hybridized one). The mixing of MB1+MB2 causes the formation of a band higher than the one corresponding to MB1 hybridized to its own complementary sequence (compare lane 7 with lane 4). The addition of T1 to MB1+MB2 (lane 8) causes the clear formation of another band at upper level compared to the previous ones coming from hybridized MB1 alone. This is due to the reaction between the hybridized MB1 with MB2 which forms a complex structure. When T2 is added to the mix of MB1+MB2 (lane 9), it causes the suppression of the band of high weight. MB1 and MB3 should not interact with each other and no high band formation is visible and the addition to their complementary target T1 and T3 also does not affect their mutual hybridization (see lanes 10-11-12). The result from MB2+MB3+Targets (see lane 13-14-15) is unclear because the detection capability of the system for the emission from these beacon is very poor (as explained in the materials and

methods section). When the entire system MB1+MB2+MB3 is present, the agarose gel reveals the formation of bands of higher molecular weight than the previously obtained complexes, showing that MB1+MB2+MB3 reaction is triggered by the addition of T1 (see lane 17-18-19).

4.5.3 Discussion

The signal coming from the single probe in figure 4.13 shows that each of the individual beacons alone is able to respond to its own complementary target. In particular the hybridized MB1 increases its fluorescence level considerably when the temperature is raised from 20 °C to 37 °C, this fact could originate, as previously explained, from the combination of strong stem sequence and a weak hybridization loop . Another reason, as previously described in chapter 3 part I, could be the presence of inner loop structures. The simulation of the geometrical conformation of MB1 yields a structure that has not a perfect loop, but there are two CG pairs forming a restriction. This obstacle could prevent the target complementary sequence to reach the hybridization point. Conversely, when the temperature is raised, the bonds between the two CG pairs are broken and the hindrance is removed. The mRNA target can now reach the free loop sequence and hybridize. In comparison, MB2 and MB3 do not show any conformational inner loop structure.

The analysis of the fluorescence emission of two probes in figure 4.14 and 4.15 revealed another problem. In the MB1+MB2 combination, when MB1 hybridizes to its complementary target T1 and, subsequently, to MB2, its maximum level of fluorescence emission does not increase to its highest level (that is when the alone probe is hybridized without any other beacon). Conversely, the fluorescence emission of MB2 seems to be unaffected by the presence of MB1. The schematic view of the arrangement of MB1-MB2 in fig.4.17 shows that the fluorophore of MB2 is placed on a free-single stranded flap that sticks out from the main aggregate, while the fluorophore from MB1 is in direct contact with a double stranded oligo. It has been reported that primary and secondary structure in the oligonucleotides (single strand or double strand formation in proximity of the fluorophore) could influence significantly the emission properties of a reporter. [15,16] It is of considerable importance than to label the beacon in such a way that the fluorophore will not end up positioned in a double stranded structure.

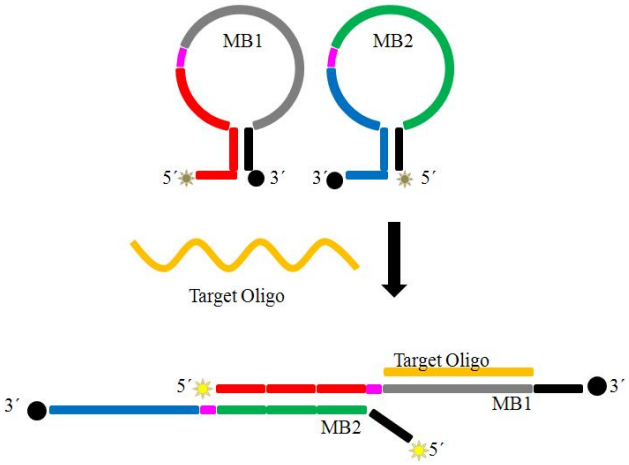

Figure 4.17: *Schematic hybridization of MB1+MB2.*

The band formation shown in the agarose gel experiment in figure 4.16 corroborates the results of the fluorescence measurements and shed some light upon the mechanism of chain hybridization. When MB1 and MB2 are put together, even in absence of a complementary sequence, they self-hybridize to one another causing the formation of a visible high level band (lane 7 in fig 4.16). This spontaneous hybridization could potentially lead to unwanted triggering of the avalanche amplification. When T1 is added to the mix of MB1+MB2, MB1 hybridizes to it, freeing its arm that hybridizes to the loop region of MB2 (lane 8 in fig 4.16); when, on the contrary, T2 (which has the exact same sequence of the protruding arm of MB1) is added to the same mix, it hybridizes to the loop of MB2 and the reaction stops. The protruding arm of MB2, now free, is supposed to react with MB3, which is not present in the solution. MB1 by contrast cannot interact any longer with MB2 because the loop of MB2 is already hybridized to T2 [Fig.4.5.3]. Because, as pointed our earlier, it is only possible to detect the signal coming from MB1, all the higher molecular weight bands from MB2 were not detectable, leaving only the bottom band corresponding to unhybridized MB1.

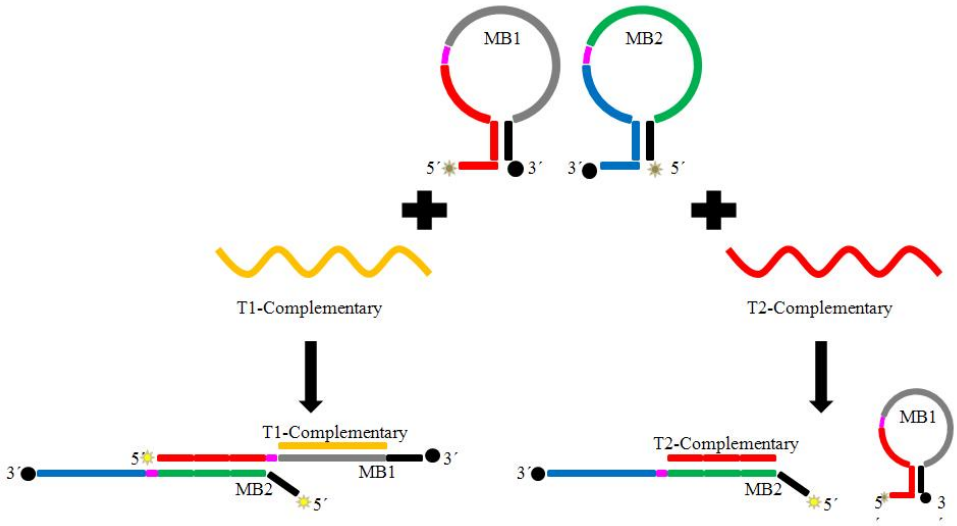

Figure 4.18: *Schematic reaction of MB1+MB2 in the presence of T1, T2 respectively; the opening of MB1 causes MB2 to open, while the hybridization of MB2 to its complementary target does not affect MB1.*

At any rate, both the fluorescence and the agarose gel, demonstrates clearly that it is possible to have formation of molecular beacons constructs and that the so-called "linear signal amplification" is feasible.

A similar fluorescence decrease was observed in figure 4.15 for the couple MB2+MB3. In this case, both the beacons showed highly reduced signal intensity. The dynamic here is somewhat different than the one previously observed for MB1+MB2. The reaction MB2+MB3 is in itself an avalanche system. Unfortunately, even if the relative position of the fluorophore-quencher pair is wisely chosen, it is impossible to avoid that the fluorophore of one probe would not be in close proximity with the quencher of the next/previous beacon (figure 4.5.3). This fact excludes the possibility of having an avalanche system based on three probes only.

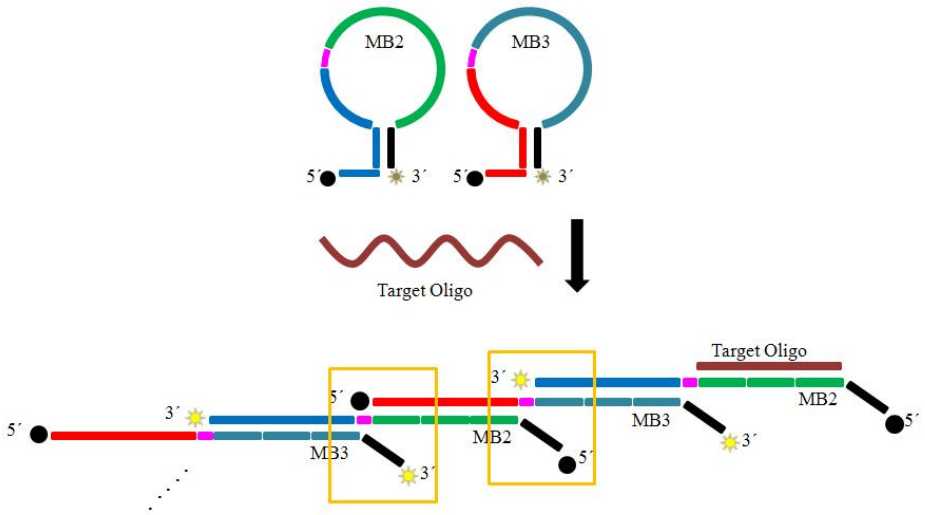

Figure 4.19: *Schematic Hybridization of MB2-MB3, independently from the relative position of the fluorophore quencher pair, there will be always proximity from the donor of one probe with the acceptor of the next/previous one (see orange boxes in the figures).*

With these considerations in mind, the apparent conflict between the fluorescence measurements and the agarose gel experiment is clearer. When the complete avalanche system was present in the test tube, the fluorescence signal measured was relatively weak (fig.4.15) suggesting that the cascade amplification was not taking place. What is probably happening is that the fluorophore of MB1 is quenched by its enclosing into a double stranded structure (as seen in fig.) while both the fluorophore from MB2 and MB3 are quenched by proximity with opposite quencher (as seen in fig). Conversely, the agarose gel experiment showed for the complete system, the formation of high molecular weight bands (see lane 17 in fig 4.16).It is important to notice that the stoichiometric ratio of 1:1:1:1 among the beacons and triggering target T1 causes another problem: in the hypothetical case in which all the complementary targets T1s will hybridize to their own MB1s, there will be a reaction with MB2 and later MB3. At this point all the beacons will be consumed and the avalanche reaction will stop because of the stoichiometric ratio. Also, the "big" complexes, requires that there is few opened MB1 that can work as starter for an avalanche reaction. For this reason, because in the agarose gel it is only possible to detect the MB1 fluorophore, the bands of higher weight (that will be statistically less abundant) are very little visible.

This apparent limitation could be solved by adding another beacon in the amplification system, bringing the total number to 4. This beacon will not be labeled and its only function will be to provide space in between the

avalanche labeled beacons. This will increase the system complexity but will allow to efficiently separation of the fluorophore quencher pairs [Fig. 4.20]

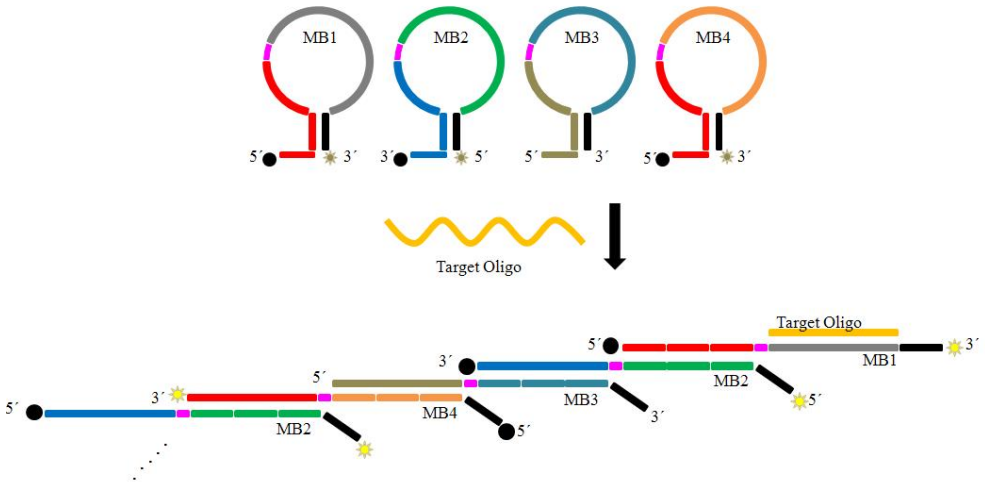

Figure 4.20: *Schematic process of the avalanche probe amplification with 4 beacons.*

At any rate it is possible to conclude that the avalanche reaction among complementary beacons, which is the principle of the SAMBA system, is demonstrated.

4.6 Amplification Third Version

4.6.1 System design and experiments

The third version of the amplification system tackles the problems highlighted in the previous version. First of all the conformational problem which brings the fluorophore from MB2, close to the quencher of MB3 was solved by introducing a fourth beacon that acts as a spacer, ensuring that the dyes are located(when possible) on the single stranded flap and far away from the quenchers [Fig.4.20]. Secondly, the problem of unwanted hybridization, initiated without the triggering through any complementary target, but only by incubation of the pure beacon combinations together was investigated. In order to investigate effects of suppression of the unwanted hybridization on the avalanche system, the temperature was varied from 5 °C to 45 °C, the buffer concentration from 1xPBS to 5xPBS and stem melting point from <20 °C to about 37 °C.

Table 4.3: Sequences of version 3 beacons - High Melting Stem

Beacon Name	Sequence	Stem T_m
MB1	aggagggctagtatattacaccttcacagctcggagccct	15.4
MB1	aggagggctagtatattacaccttcacagctcggagccctC	27.2
MB1	aggagggctagtatattacaccttcacagctcggagccctCC	37.9
MB2	aacgcttatactagccctcctttactgtagcgttgatg	14.1
MB2	Caacgcttatactagccctcctttactgtagcgttgatg	26.1
MB2	ATCaacgcttatactagccctcctttactgtagcgttgatg	36.8
MB3	ctaatgtgggcagtccttcatcaacgctacagtcccaca	13.7
MB3	ctaatgtgggcagtccttcatcaacgctacagtcccacaT	21.3
MB3	ctaatgtgggcagtccttcatcaacgctacagtcccacaTTAG	36.8
MB4	agccctggactgcccacattagaggagggctagtata	15.4
MB4	Tagccctggactgcccacattagaggagggctagtata	21.4
MB4	ACTagccctggactgcccacattagaggagggctagtata	37.4

4.6.2 Results

The first beacons avalanche system is tested in the following experiment. The beacons with low melting temperature for the stem were used: MB1 at 15.4 °C labeled with TexasRed, MB2 at 14.1 °C labeled with TexasRed, MB3 at 13.7 °C unlabeled and MB4 at 15.4 °C unlabeled. Figure 4.21 shows the results from the fluorescence measurements from MB1, MB2 and their combination at two different temperatures, 20 °C and 37 °C. These two probes were the only ones labeled and their interaction can be studied in detail.

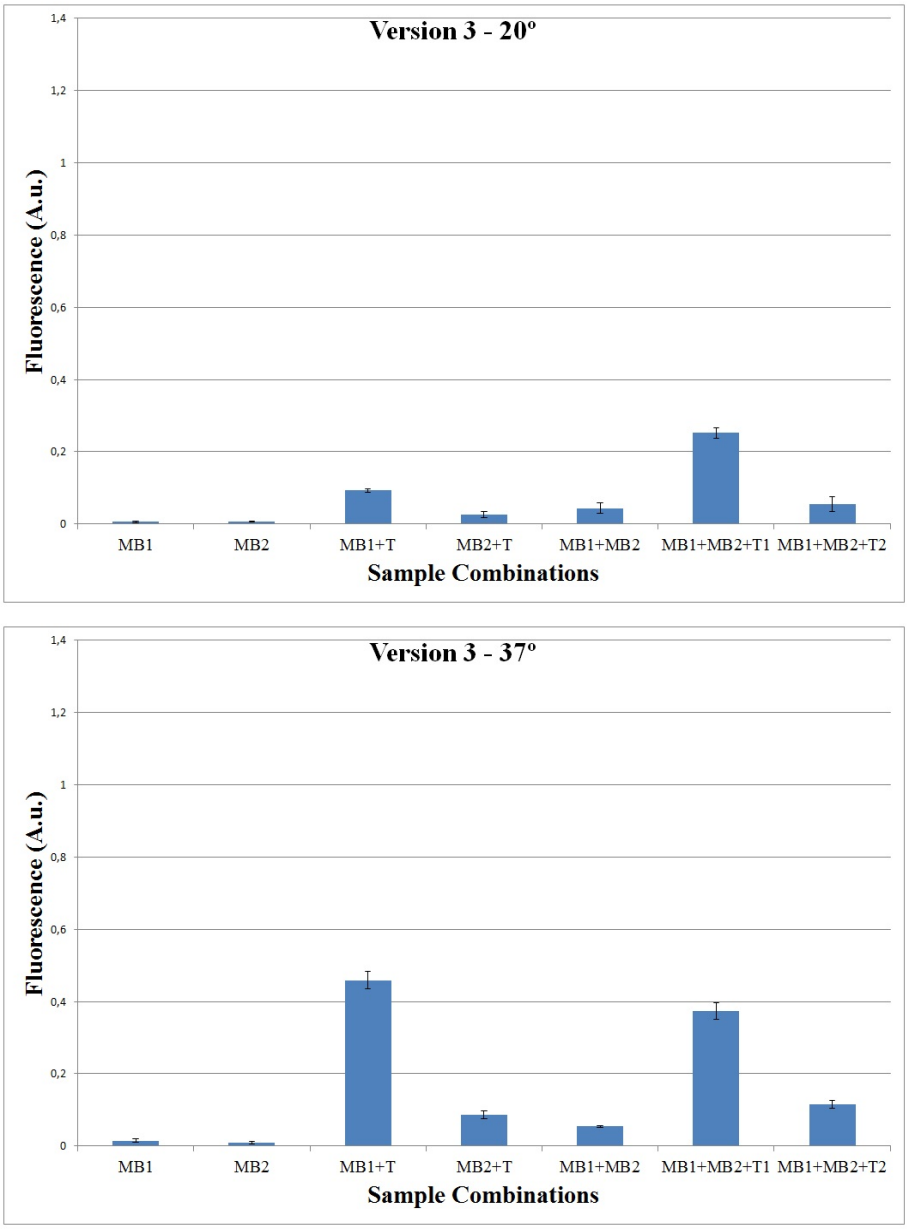

Figure 4.21: *Fluorescence measurements of MB1, MB2 combination of version 3 beacons for signal amplification. The measurements were performed at 20 °C and 37 °C. S/N and raw fluorescence value are reported for each sample.The experiment was repeated thrice. (top graph) Fluorescence measurements - SAMBA version 3 - 20 °C. (bottom graph) Fluorescence measurements - SAMBA version 3 - 37 °C.*

The signal to noise ratio of MB1 and MB2 in the presence of their own complementary target increases significantly with increasing temperature. MB1 goes from $\simeq 16$ to $\simeq 32$ and also MB2 doubles its value from 4.4 at 20

°C to 9.0 at 37 °C. The hybridization is highly promoted with temperature and the signal generation is high even though the background fluorescence emission is also doubled. The result of mixing MB1 and MB2, changes significantly with temperature. At 20 °C the addition of T1 to the mix results in high signal intensity, higher than the one generated by each single probe. On the other hand, the background fluorescence coming from incubation of MB1+MB2 alone is high and the resulting S/N is low ($\simeq$ 5.7). When the temperature is increased to 37 °C, the fluorescence emission coming from MB1+MB2+T1 increases. Anyhow, it remains much lower than the one coming from the hybridized MB1 alone. The addition of T2 to the mix of MB1+MB2 suppresses most of the signal, causing only opening of MB2.

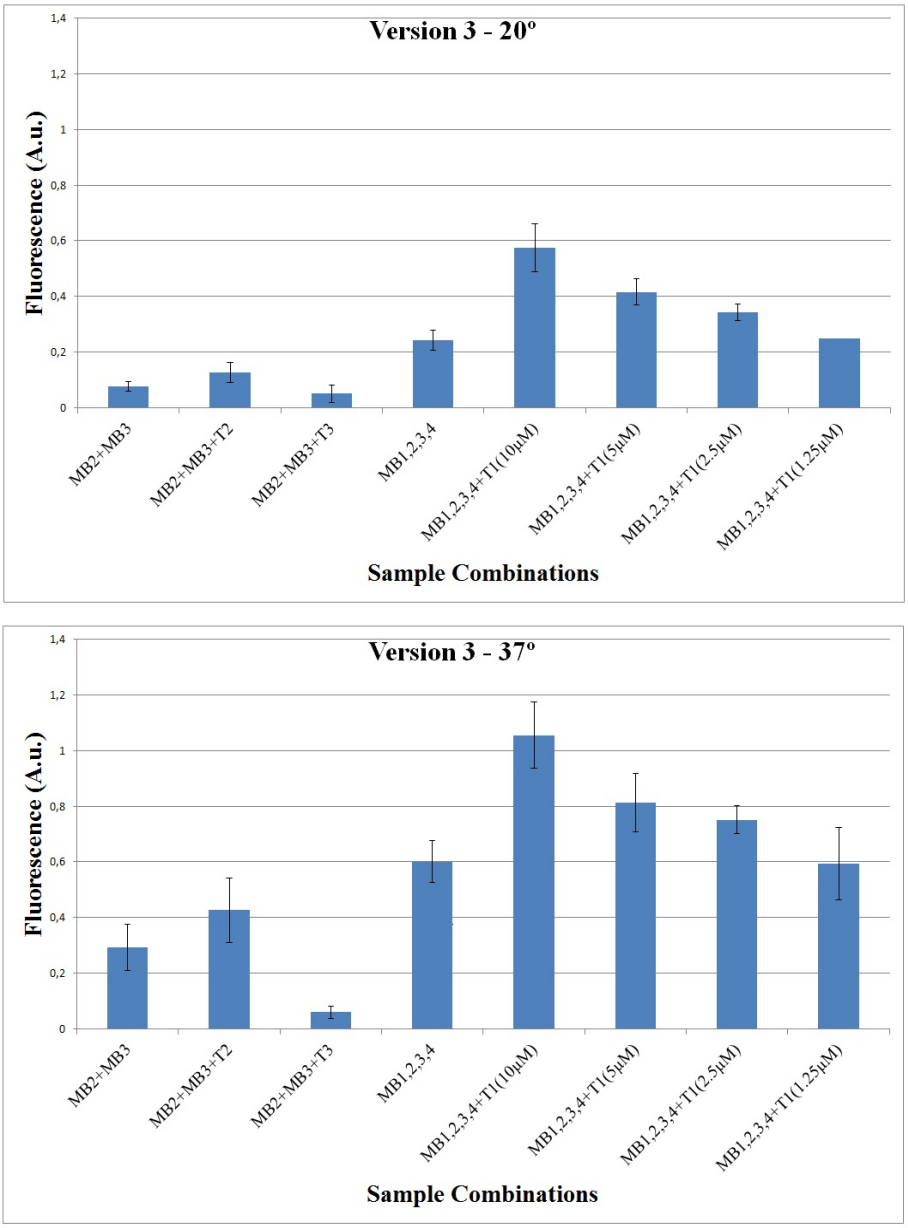

Figure 4.22: *Fluorescence measurements of MB2+MB3 combination and entire system with MB1, 2, 3, 4+ T1 at different concentrations of version 3 beacons for signal amplification. The measurements were performed at 20 °C and 37 °C. The raw fluorescence value is reported for each sample.*

Figure 4.22 shows the reaction between MB2 and MB3 for both 20 °C and 37 °C. The unwanted hybridization between these beacons is very high, their background value, corresponding to MB2+MB3 is 10 times higher than the background coming from MB2 alone (figure 4.21). MB3 is not labeled,

so the signal comparison is valid.

Finally, the entire amplification system's signal, generated by MB1+MB2 +MB3+MB4 reaches a very high level, superior to any other configuration, both at 20 °C and 37 °C. However, the high background present in absence of triggering target T1, undermine the value of S/N.

An agarose gel experiment was performed to corroborate the fluorescence data (fig.4.23). Lanes 1-3 and 2-4 contains respectively MB1 and MB1+T1 and MB2 and MB2+T2. The addition of complementary target causes the formation of a visible band for both the cases (see line 3 and 4). In the two system probe, as for MB1+MB2 in lanes 5-6-7, the same behavior of version 2 beacons is found. The addition of T1 causes the formation of a high weight band, while, if T2 is added instead, this band is suppressed, as described in figure4.21. Similar result was observed for beacons MB2+MB3 in lanes 8-9-10. The unwanted hybridization initiated without complementary target is clearly visible in lanes 5 and 8. The complete avalanche system, MB1+MB2+MB3+MB4 in lanes 11 to 15, shows the formation of higher bands which are fading along the length of the gel. It is reasonable to expect that large agglomerates will be less abundant and therefore their corresponding band will be less intense. The concentration of the triggering sequence T1 as been progressively reduced of 1/10 for each lane, but the intensity of the fluorescence emission does not seem to follow the same decreasing pattern in the gel as seen in the pure fluorescence emission, remaining here more constant.

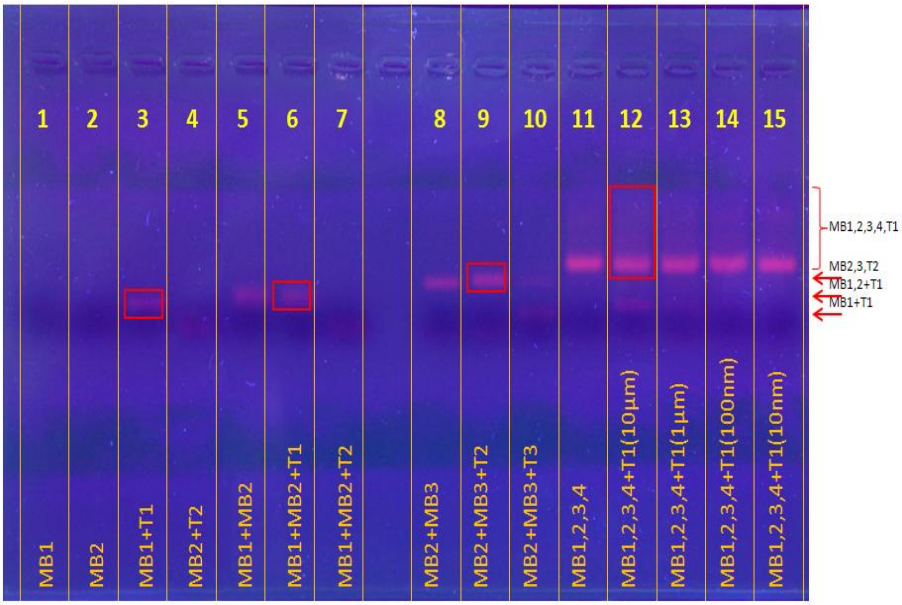

Figure 4.23: *Agarose gel of version 3 beacons. The signal comes from MB1 and MB2 both labeled in TexasRed, MB3 and MB4 are not labeled.*

The problem of background fluorescence due to cross hybridization was studied varying three main parameters, temperature, salt concentration and beaconÂ´s stem length. To simplify the analysis, it was chosen to study the effects of these variables on a restricted system, comprising only MB1 labeled with TexasRed with T_m of the stem at 21.4 °C and MB2 also labeled with TexasRed with T_m of the stem at 26.1 °C. The fluorescence results coming from the hybridization of the labeled MB1 and MB2 with the stem with melting temperature in the 30 °C range and above showed no signal when incubated with the complementary sequence, indicating that the stem strength was too high. The presence of a beacon that would not react to the hybridization could ruin the entire avalanche system and, for this reason, all the probes with stem's melting temperatures $\geq$ 30 °C were discarded form further analysis. In figure 4.24 the values for the S/N ratio of MB1 incubated with T1 and MB1+MB2+T1 are reported for different salt concentrations at different temperature. The general trend was that, when the stringency is increased, meaning higher salt concentration and lower temperature, the S/N of the two system probe is larger than that of the single MB1.

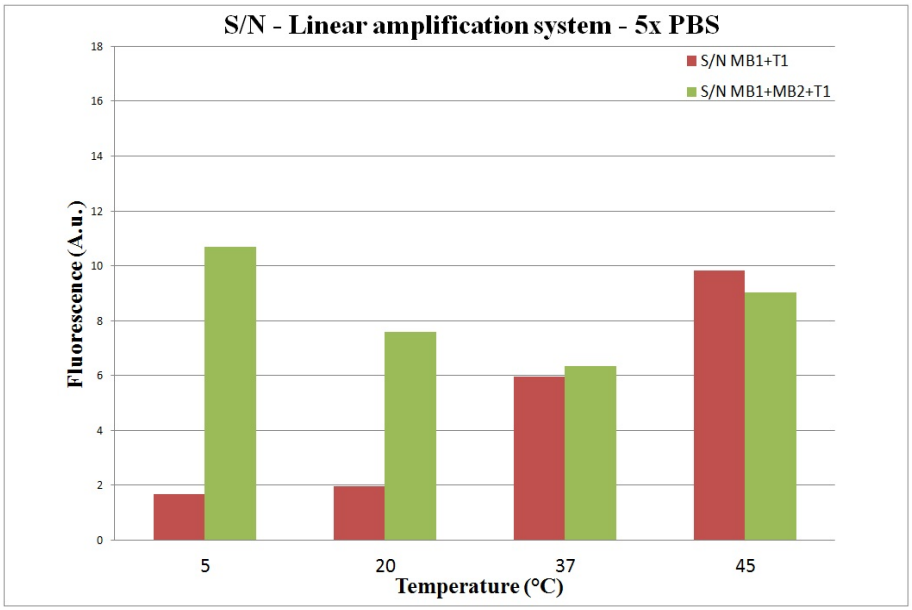
S/N - Linear amplification system - 5x PBS
S/N MB1+T1
S/N MB1+MB2+T1
Fluorescence (A.u.)
0
2
4
6
8
10
12
14
16
18
5
20
37
45
Temperature (°C)

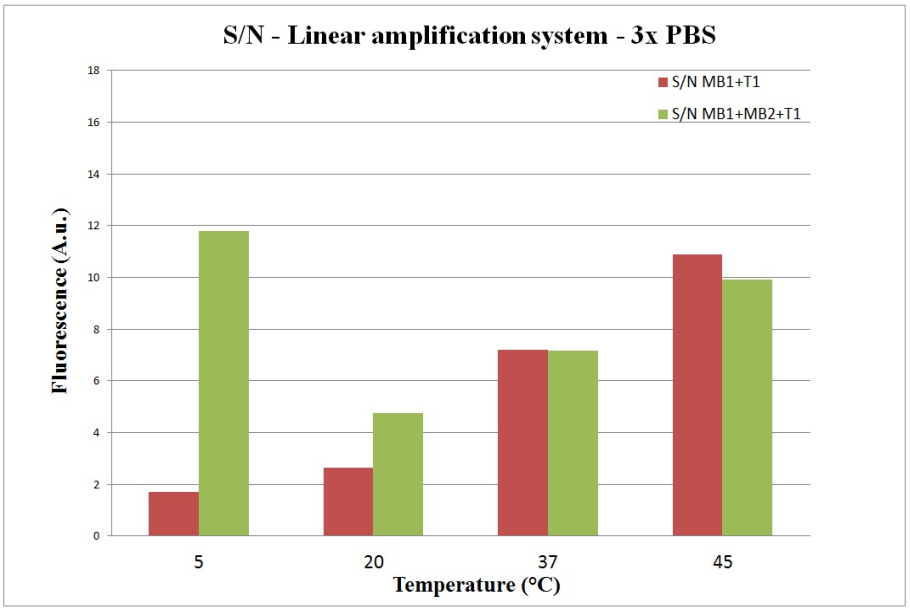
S/N - Linear amplification system - 3x PBS
S/N MB1+T1
S/N MB1+MB2+T1
Fluorescence (A.u.)
0
2
4
6
8
10
12
14
16
18
5
20
37
45
Temperature (°C)

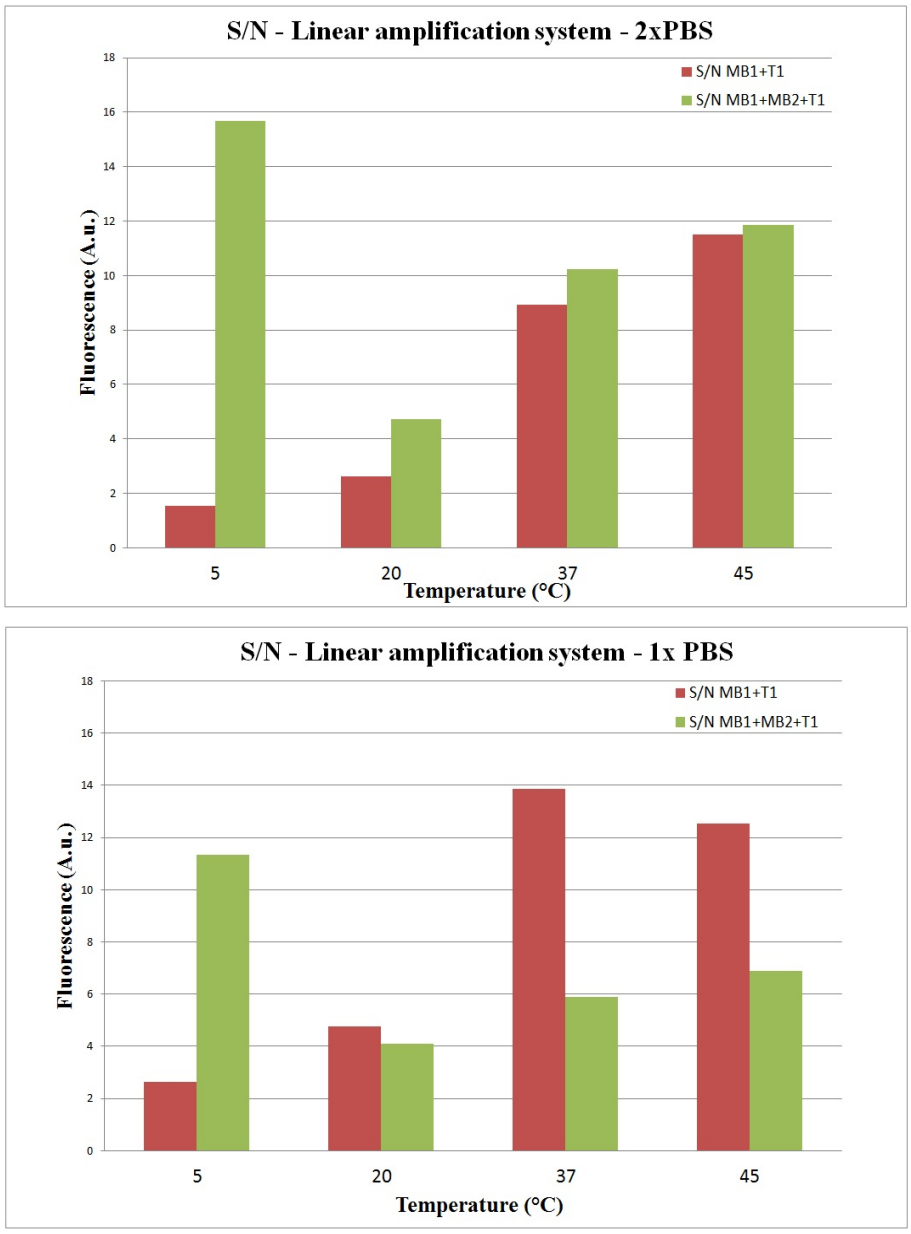

Figure 4.24: *Signal to noise ratio calculated for the single probe MB1 hybridized to T1 and the two probe system MB1+MB2 also hybridized to T1. The T_m of the stem is 21.4 °C for MB1 and 26 °C for MB2. The salt concentration was adjusted thorough different dilution of the PBS buffer. Each experiment was repeated 4 times before S/N calculation.*

The maximum value of fluorescence emission reported for the 5xPBS configuration in figure 4.25, shows that the two probe system have a significantly higher value. Even at 37 °C, the emission of the hybridized MB1+MB2 is 0.29 a.u. while the signal emission from the hybridized MB1 is only 0.15 a.u. At

45 °C the emission intensity becomes comparable for the two configurations.

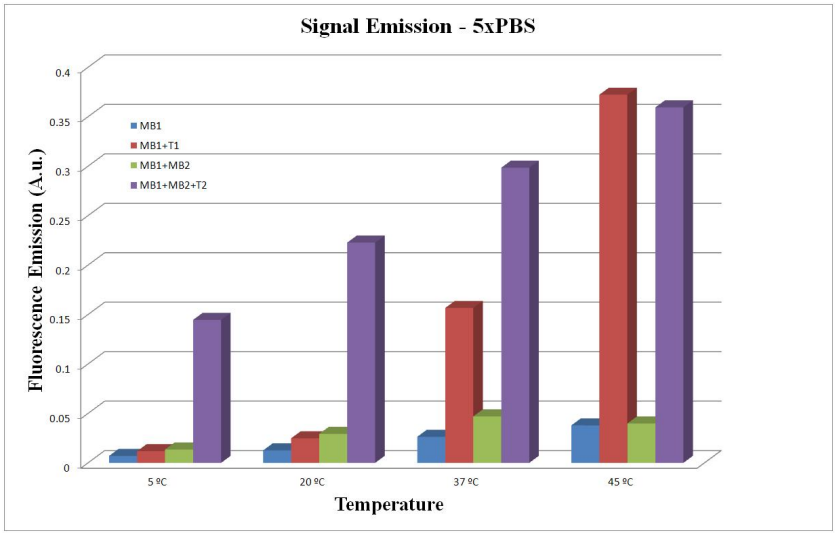

Figure 4.25: *Maximum signal emission for the two probe system in 5xPBS medium.*

4.6.3 Discussion

The fluorescence signal measured for the group MB1+MB2 in figure 4.21 shows once more the problem of proximity quenching from a double stranded DNA previously reported (see fig.4.17 for a schematic view of the reaction). From the measurements performed on the hybridized probe alone, it is clear that MB1 is the major contributor to the fluorescence signal intensity and its structural quenching jeopardizes the performances of the system. The fluorescence signal of the group MB2+MB3 in figure 4.22, shows that, when T2 is added to the mix, the fluorescence from MB2 is restored, and, conversely, when T3 is added instead, the fluorescence emission drops significantly below the background level. This fact is due to the same effect shown in figure 4.5.3. When MB3 hybridizes to its complementary target, MB2 cannot participate any longer in the hybridization process so it remains quenched in the hairpin configuration. Now, since MB2 is the only one labeled, the opening of MB3 causes the fluorescence to drop below the level of MB2+MB3, because, statistically, less MB3 will be available for unspecific hybridization. The presence of all the beacons composing the avalanche system causes the background to be significantly increased (fig.4.22). As showed before, the combination of two probes was leading to unwanted hybridizations, and here, where the avalanche process is supposed to take place, this effect is massively enhanced. The addition of complementary target for MB1 triggers the reac-

tion and boost fluorescence emission even though, given the high background level, does not lead to high signal-to-noise ratio. Anyway it is very interesting to notice that the value of the fluorescence emission for the avalanche system is more than double compared to the MB1+MB2 system (which are the only labeled beacons). This indicates that the avalanche amplification actually takes place, MB3 and MB4 in this experiment are not labeled and their addition is not contributing to the fluorescence signal.

The fluorescence results for the MB1+MB2 system in the presence of conditions able to enhance the stringency and slow down the hybridization kinetics are reported in fig 4.24. It shows that the unwanted hybridization could be effectively reduced by carefully controlling the system parameters. The two probe system performed better in both S/N and maximum emission, but when the conditions were reduced, the performance deteriorated.

4.7 Cell Experiments

Lastly the amplification system was tested inside living cells in order to determine whether the cellular environment could positively affect the avalanche reaction suppressing the unwanted hybridization. HeLa cells were cultured in a well plate and treated with SLO for the internalization of the beacons, as described in chapter 3 part I. MB1, which is the starter of the avalanche reaction, is the beacon encoded with the target sequence. In this tyrosine hydroxylase was chosen as target sequence. It is encoded by the TH gene, which is the key enzyme responsible for the synthesis of dopamine and catecholamines in the neurons and it is involved in the pathogenesis of Parkinson's disease, Segawa's dystonia, and schizophrenia. Unfortunately HeLa cells do not express this particular gene, so to go around this problem and at the same time, try to limit unwanted triggering of the hybridization the next procedure was followed: first the cells were treated with SLO and pores were formed in the membrane allowing the diffusion of a solution containing MB1, MB3 and MB4 inside the cytosol. In this way the avalanche reaction should not start because the necessary tile MB2 is missing. Then after cell recovery, the same internalization procedure was repeated, but this time MB2 and complementary target for MB1 (TH sequence) was inserted. All the beacons were version 3 with stem's melting temperatures around 25 °C. The fluorescence emission for various combinations has been evaluated after cells recovery (Fig. 4.26, 4.27).

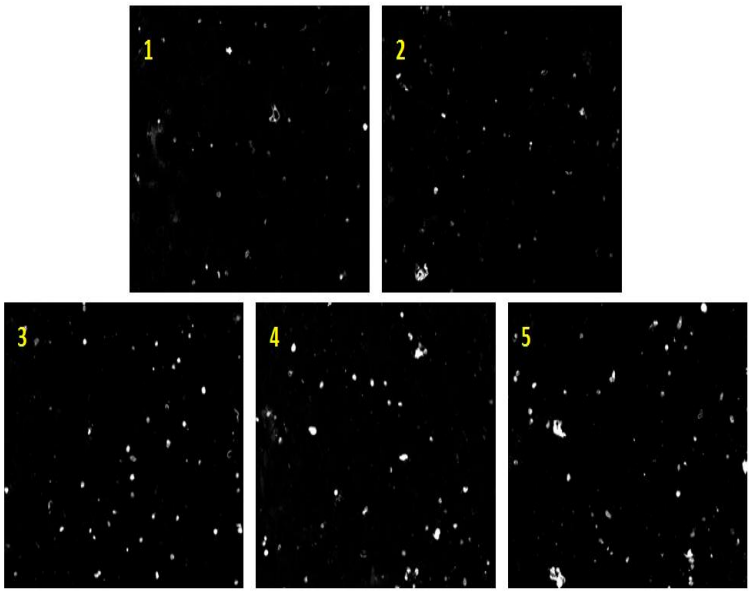

Figure 4.26: *Fluorescence signal coming from Hela cells loaded with TH avalanche system. 1) MB1 alone; 2) MB1+TH target; 3) MB1+MB2+TH target; 4) MB1+MB2+MB3+MB4; 4) MB1+MB2+MB3+MB4+TH target.*

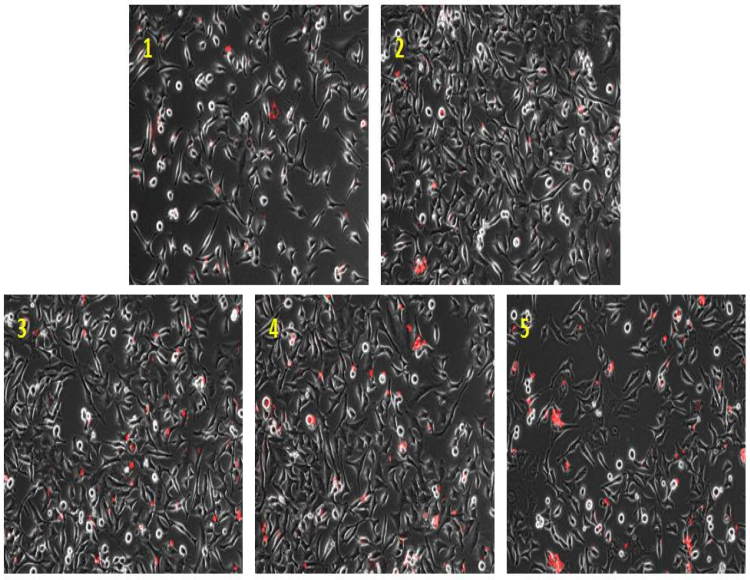

Figure 4.27: *Bright field images overlaid on fluorescence signal coming from Hela cells loaded with TH avalanche system. 1) MB1 alone; 2) MB1+TH target; 3) MB1+MB2+TH target; 4) MB1+MB2+MB3+MB4; 4) MB1+MB2+MB3+MB4+TH target.*

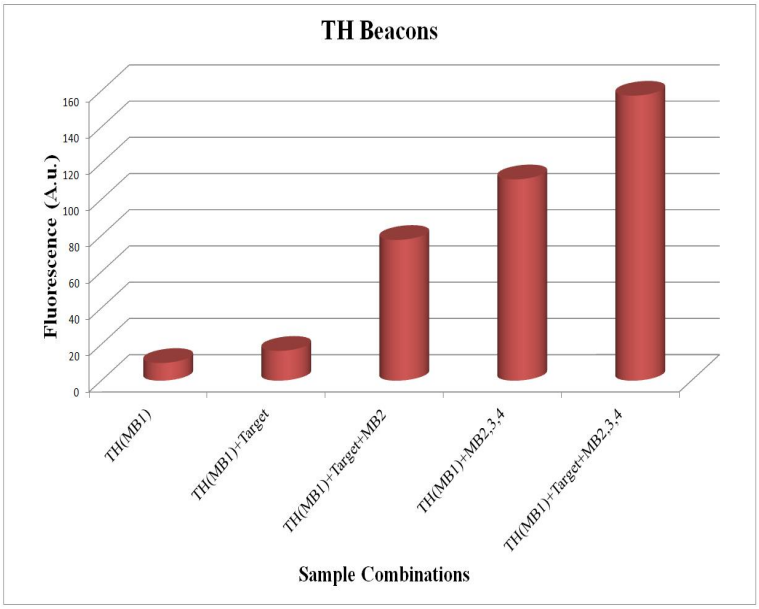

Figure 4.28: *Quantified fluorescence emission for TH expression from HeLa cells.*

The fluorescence signal was quantified for many cells and the integrated fluorescence amount was than averaged on the surface of the cell. Finally the mean value for the population of cells was found. (see fig.4.28). The resulting fluorescence intensity after 24 hours of incubation shows that the two system amplification (picture number 3 in fig.4.26) emits signal at much higher intensity than the signal probe (picture number 1 in fig.4.26). The avalanche system in the insert 4-5 of fig .4.26 shows a much higher signal than the previous configuration but also an increased background. A graph of the emitted intensity (fig.4.28) shows that MB1 hybridized to its target have S/N of 1.76 and the other configurations, if compared to this value have respectively 6.17 (MB1+MB2+T1), 8.24 (MB1+MB2+MB3+MB4), 16.02 (MB1+MB2+MB3+MB4+T1) times the signal. The same experiment was repeated substituting the sequence encoded in MB1. Glyceraldehyde 3-phosphate dehydrogenase (abbreviated GAPDH) was chosen. It is an enzyme that catalyzes the sixth step of glycolysis, thus it is expressed by all the cells type. The fluorescence emission was quantified directly after the internalization of the probes and 24 hours after incubation. The probe insertion technique and protocol was the same one used for the previous experiment. The fluorescence emission was quantified and averaged and, in fig.4.29, the results for the single probe MB1 and the double linear system MB1+MB2 are reported.

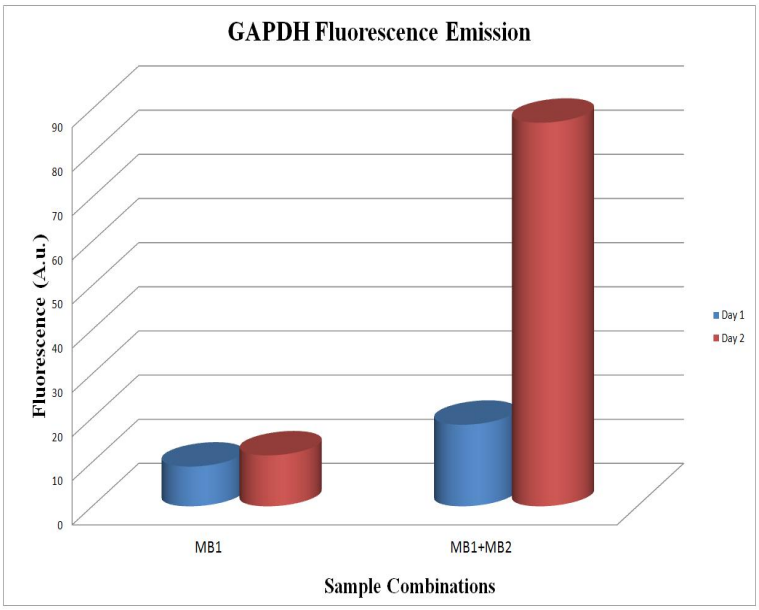

Figure 4.29: *Quantified fluorescence emission for GAPDH expression from HeLa cells.*

The signal-to-noise ratio of MB1 is 1.28, while the addition of MB2 brings the S/N at 4.70. The maximum signal emission increases, for the two system probe, by 7.53 times.

The experiment performed inside cells showed that it is possible to achieve high signal emission and, for the case of GAPDH in fig. 4.29, that the linear system amplification results in 3.6 times better s/n and in 7.53 times higher signal emission intensity. In principle, if all the beacons were equally carefully designed, the addition of one single identically labeled MB to the amplification structure would increase the performances of a maximum factor of 2. The higher values founds can be explained by the fact that each beacon design have different performances. If a particularly well designed MB2 is added to a poor MB1, the achievement of the combined probes will cause major advantages in both S/N and maximum emission.

4.8 Conclusions and outlook

The possibility of building complex structures using a sequence of molecular beacons able to interact one with another in a cascade reaction was demonstrated. Two systems were presented, the first called linear amplification in which each beacon is open by the hybridization of its foregoers and the second called avalanche amplification in which a self sustained cascade reaction is triggered by the opening of the first molecular beacon. The results were

verified by fluorescence emission analysis, agarose gel and the experiment was also repeated inside living cells. The major problem encountered was the unwanted hybridization taking place among beacons even when the complementary target was not present in the sample solution. At any rate, it was shown that, by carefully control of conditions like stem length, salt concentration and temperature, it is possible to control the reaction and suppress the cross hybridization. On the other hand the analysis point out an interesting fact regarding beacon structure and dynamics of hybridization. The melting temperature of the stem section of a common molecular beacon, which is usually 5-6 bps long, is between 10 °C and 20 °C. This means that at 37 °C, the usual temperature of operation for living cells applications, the beacon's stem must be open. Therefore, the conception of molecular beacons being either close in hairpin or open in a random coil is somehow incorrect. The random coil configuration is not to be thought as completely open and able to emit fluorescence, rather it is a conformation in which the stem is melted but still weakly keeps a semi-hairpin configuration which is poorly emissive. Both the conformational structures are present at the same time in the solution in a statistical balance, once the bulk temperature of the specimen is above the stem melting temperature. Parameters such as salt concentration, temperature and stem length just drive the reaction arrows towards one side or another (see scheme in fig.4.30). When one and only beacon is present in the solution, the balance of the reaction between semi-random coil and hairpin is a minor problem. However, when more beacons interacting with each other are present together, this semi closed state generates the triggering of the hybridization reaction that ultimately higher the background considerably. Furthermore, when the hybridization to a complementary target takes place, the particular beacon is "frozen" into an open configuration and start emitting fluorescence. The key point for the successful development of a functional amplification system resides in the suppression of the background coming from unwanted hybridization. The next step would be to redesign the entire system and choose a target sequence that would be easily traceable inside living cells. The effect of salt concentration and stem length should also be further investigated and optimized.

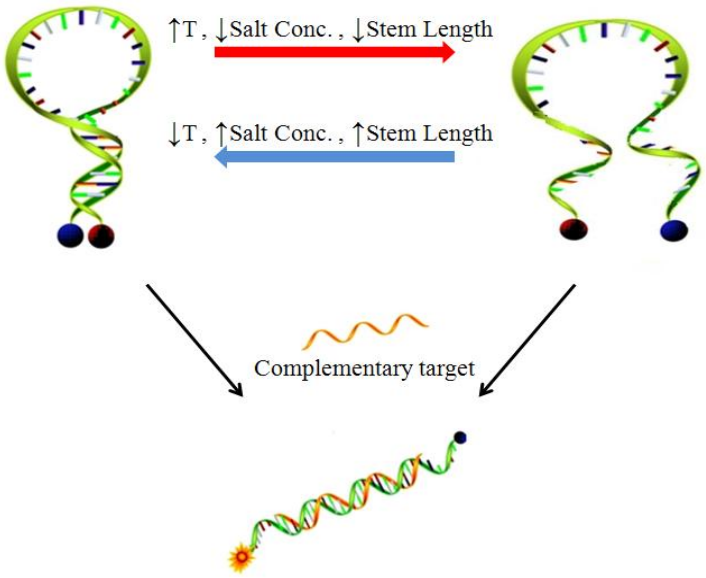

Figure 4.30: *Molecular beacons dynamics and conformational change.*

Bibliography

[1] K. Wang, Z. Tang, C. J. Yang, Y. Kim, X. Fang, W. Li, Y. Wu, C. D. Medley, Z. Cao, J. Li, P. Colon, H. Lin, e W. Tan, *Molecular engineering of DNA: molecular beacons*, **2009**, Angew. Chem. Int. Ed. Engl., vol. 48, n. 5, 856-870.

[2] C. Tan, M. R. Pinto, e K. S. Schanze, *Photophysics, aggregation and amplified quenching of a water-soluble poly(phenylene ethynylene)*, Chem. Commun., **2002**, n. 5, 446-447.

[3] C. J. Yang, M. Pinto, K. Schanze, e W. Tan, *Direct synthesis of an oligonucleotide-poly(phenylene ethynylene) conjugate with a precise one-to-one molecular ratio*, Angew. Chem. Int. Ed. Engl., **2005**, 44, n. 17, 2572-2576.

[4] J. H. Kim, D. Morikis, e M. Ozkan, *Adaptation of inorganic quantum dots for stable molecular beacons*, Sensors and Actuators B: Chemical, **2004**, vol. 102, n. 2, 315-319.

[5] P. Zhang, T. Beck, e W. Tan, *Design of a Molecular Beacon DNA Probe with Two Fluorophores*, Angewandte Chemie International Edition, **2001**, vol. 40, n. 2, 402-405.

[6] C. J. Yang, H. Lin, e W. Tan, *Molecular Assembly of Superquenchers in Signaling Molecular Interactions*, **2005**, J. Am. Chem. Soc., vol. 127, n. 37, 12772-12773.

[7] B. Dubertret, M. Calame, e A. J. Libchaber, *Single-mismatch detection using gold-quenched fluorescent oligonucleotides*, Nat. Biotechnol., **2001**, vol. 19, n. 4, 365-370.

[8] T. Jacroux, D. C. Rieck, R. Cui, Y. Ouyang, e W.-J. Dong, *Enzymatic amplification of DNA/RNA hybrid molecular beacon signaling in nucleic acid detection*, Analytical Biochemistry, **2013**, vol. 432, n. 2, 106-114.

[9] B. Wei, M. Dai, e P. Yin, *Complex shapes self-assembled from single-stranded DNA tiles*, **2012**, Nature, vol. 485, n. 7400, 623-626.

[10] J. J. Li, Y. Chu, B. Y.-H. Lee, e X. S. Xie, *Enzymatic signal amplification of molecular beacons for sensitive DNA detection*, **2008**, Nucl. Acids Res., vol. 36, n. 6, pag.e36.

[11] A. Tsourkas, M. A. Behlke, e G. Bao, *Structure-function relationships of shared-stem and conventional molecular beacons*, Nucleic Acids Res, **2002** vol. 30, n. 19, 4208-4215.

[12] M. Zuker, *Mfold web server for nucleic acid folding and hybridization prediction*, **2003**, Nucl. Acids Res., vol. 31, n. 13, 3406-3415.

[13] http://eu.idtdna.com/analyzer/Applications/OligoAnalyzer/

[14] Monroy-Contreras, R. Vaca, L. *Molecular Beacons: Powerful Tools for Imaging RNA in Living Cells*. Journal of Nucleic Acids, **2011**.

[15] Mark A. Behlke, Lingyan Huang, Lisa Bogh, Scott Rose, and Eric J. Devor *Fluorescence Quenching by Proximal G-bases*, **2005**, Integrated DNA Technologies.

[16] I. Nazarenko, R. Pires, B. Lowe, M. Obaidy, e A. Rashtchian, *Effect of primary and secondary structure of oligodeoxyribonucleotides on the fluorescent properties of conjugated dyes*, **2002**, Nucleic Acids Res., vol. 30, n. 9, 2089-2195.

Part II

Part 2 - Nanomachines

Chapter 1

Introduction

Messenger RNA (mRNA) represents the schematics for production of protein and building blocks for cells. In the recent years the importance of localization of mRNA expression has been pointed out. Various studies have shown that abnormal expression and centering of mRNA can cause serious pathology, for example alteration of cell morphology [1]. The key role of inter cellular mRNA expression is also significant; cell-to-cell variation of gene expression in a small fraction of cancerogenic cells could lead to major effects, like drug resistance [2]. There are many established techniques to monitor efficiently gene expression such as PCR [3],or micro array [4]. These approaches have two major limitations, on one hand they rely on fixed or lysed cells ignoring the dynamics of expression (temporal localization) and, on the other hand, they involve mRNA expressed by many cells, losing the ability to track down the source of the genetic material (spatial localization). Since their invention, Molecular Beacons (MBs) [5] have been a dominant technique in biotechnology because of their exquisite selectivity, sensitivity and high signal-to-noise ratio. The MB is a structure constituted of an oligonucleotide strand arranged in a hairpin configuration with a donor-acceptor pair attached. The two ends of the oligos strand are complementary and, below the melting temperature and in absence of target, form a double helix (stem region). The central part is a single stranded sequence designed to recognize a particular RNA (or DNA) target (loop region). Connected to the two ends of the stem, there is a fluorophore and a quencher, respectively. The working principle is based on Föster Resonance Energy Transfer (FRET) [6], a distance dependent nonradiative energy transfer phenomenon between the donor molecule (fluorochrome) and the acceptor (quencher). The double stranded configuration of the stem forces donor and acceptor to be in close proximity, leading to high efficiency FRET and consequent low emission of fluorescence. When a target strand is hybridized to the loop region, the

stem opens, parting the fluorophore from the quencher, reducing the FRET efficiency and consequently, increasing the emission of fluorescence from the dye. Because of their exclusive characteristic, MBs could resolve the issues of spatial and temporal localisation not addressed by standard techniques. The major disadvantages of MBs consist in a higher complexity for cell internalization and instability in cellular environment, particularly due to nuclease cleavage. Some of these problem have been solved by the use of gold nanoparticles(GNPs) as acceptor replacing the organic quencher [7–9]. Studies have shown that the quenching efficiency is enhanced [10] and also that MBs with GNPs quenchers have longer lifetime as a result of reduced aggression from nuclease [11]. The presence of GNPs also improves the delivery of the sensors inside cells though phagocytosis.

Hamad-Schifferli et al. [12] published a way to manipulate the local environment surrounding a gold nanoparticle by an external radio frequency (RF) field. Their study showed that GNPs can be heated by an external RF field. DNA linked to the GNP was able to melt as a function of RF exposure. Consequently, linking molecular beacons (MB) to GNPs would then enable their actuation by a remote RF field. Such an approach would allow for operations of molecular beacons e.g. inside living cells, which would enhance the analytical properties of MBs to sense mRNA. Examples of operations would be calibration, localization and resetting hybridized molecular beacons to study time dependent measurements of targets mRNA. Sensing mRNA in real time provides essential information about temporal gene expression for instance during differentiation.

The activation of gold nanoparticles by RF fields is, however, a highly debated issue [13]. Moran et al [14] reported that 10 nm GNPs dispersed in a solution increase the RF absorption considerably. They report that the bulk temperature of a dispersion of GNPs under the influence of an RF field at 13.56 MHz increases its temperatures by tens of degrees in less than one minute. The exposure to RF at the same frequency as previously reported, caused a pronounced augment in cancer cells death when the samples were loaded with GNPs, both in vitro [15] and in vivo [16]. In contrast, Li et al. [17] and, independently, Liu et al, [18] investigated the bulk heating in solutions of GNPs of different diameter exposed to a RF field at 13.56 MHz. They conclude that no appreciable contribution to the RF energy absorption could be detected from the addition of GNPs. In particular, Li et al. separated the GNPs from the supernatant and found that the same increase in temperature occurred after RF excitation independent of the presence of GNPs. The induced heating in the solution is therefore ascribed to the joule heating of the ionic solution. More recently Hanson et al. [**?**] carried out a theoretical analysis of the effect of spherical GNPs in enhancing the absorp-

tion of RF radiation when dispersed in a medium. Their conclusion is that the produced heating is negligible and cannot explain the effects shown earlier. We have to point out that these papers deals with the macroscopic effect caused by GNPs activation. There are a few examples in which the activation of gold nanoparticles is directly related to changes caused in the direct surrounding of the particle itself. Denver et al. [20] conjugated quantum dots (QDs) with 1.4 nm GNPs and measured the fluorescence emission of the QDs after irradiation of the sample solution with a RF field at 1 MHz. As opposed to the control solution of un-conjugated QDs and GNPs, they measured a shift in fluorescence emission compatible with a temperature enhancement of $\sim 7°C$, while the bulk temperature was unchanged. As previously reported in [12] 1.4 nm GNPs exposed to a 1 GHz field are used to cause selective dehybridization of DNA strands, which corresponds to an increase of $\sim 13°C$ above ambient temperature for the particular case. Finally, Kogan et al. [21] investigated the nanoparticle mediated local control of protein aggregation under a 12 GHz RF field, to dissolve amyloid deposit of Aβ1-42 without formation of bulk heating. To our knowledge a complete theoretical description that supports efficient heat conversion of microwave radiation by GNPs at the nanoscale does not exist, but one hypothesis is that heating is a result of field focusing effect by the nanoparticles instead of the conventional Joule heating model [22] At present, there seem to be diverging experimental and theoretical understanding of GNP heating. Furthermore, to our awareness, no one has reproduced the results of Hamad-Schifferli et al [12].

In this second part of the thesis the interaction of GNPs with RF fields will be experimentally demonstrated. Also the investigation will examine if the effects are localized to the GNP or also affects the bulk solute. To study this, MB linked to GNPs were conjugated and exposed to an external RF field. If heat is generated in bulk or localized to the GNP, the MB would linearize and fluoresce. For convenience, MB/GNP construct will be denoted as a nanomachine (NM) since it can have multiple states and possibly be actuated remotely by an RF field or by lasers [23]

Bibliography

[1] Hughes, J. R., Bullock, S. L. Ish-Horowicz, D. *Inscuteable mRNA localization is dynein-dependent and regulates apicobasal polarity and spindle length in Drosophila neuroblasts*. Curr. Biol. 14, 1950-1956, **2004**.

[2] Visvader, J. E. *Cells of origin in cancer*. Nature 469, 314-322, **2011**.

[3] K. Mullis, F. Faloona, S. Scharf, R. Saiki, G. Horn, e H. Erlich, *Specific Enzymatic Amplification of DNA In Vitro: The Polymerase Chain Reaction*, **1986**, Cold Spring Harb Symp Quant Biol, vol. 51, 263-273.

[4] Tse-Wen Chang, *Binding of cells to matrixes of distinct antibodies coated on solid surface*, **1983**, Journal of Immunological Methods, vol.65, 217-223.

[5] Tyagi S, Kramer FR.*Molecular beacons: probes that fluoresce upon hybridization.*Nat Biotechnol. **1996** Mar;14(3):303-8.

[6] Lakowicz, Joseph R, *Principles of Fluorescence Spectroscopy 3rd*, **2006**, Springer, pgg 331-348.

[7] Seferos, D. S., Giljohann, D. A., Hill, H. D., Prigodich, A. E. Mirkin, C. A. *Nano-Flares:Probes for Transfection and mRNA Detection in Living Cells*. J. Am. Chem. Soc. 129, 15477-15479, **2007**.

[8] Prigodich, A. E. et al. *Multiplexed Nanoflares: mRNA Detection in Live Cells*. Anal. Chem. 84, 2062-2066, **2012**.

[9] Jayagopal, A., Halfpenny, K. C., Perez, J. W. Wright, D. W. *Hairpin DNA-Functionalized Gold Colloids for the Imaging of mRNA in Live Cells*. J. Am. Chem. Soc. 132, 9789-9796, **2010**.

[10] Dubertret B, Calame M, Libchaber AJ. *Single-mismatch detection using gold-quenched fluorescent oligonucleotides*. Nat Biotechnol. **2001** Apr;19(4):365-70.

[11] Rosi NL, Giljohann DA, Thaxton CS, Lytton-Jean AK, Han MS, Mirkin CA. *Oligonucleotide-modified gold nanoparticles for intracellular gene regulation*. Science. **2006** May 19; 312(5776),1027-30.

[12] Hamad-Schifferli, K., Schwartz, J. J., Santos, A. T., Zhang, S. Jacobson, J. M. *Remote electronic control of DNA hybridization through inductive coupling to an attached metal nanocrystal antenna*. Nature 415, 152-155, **2002**.

[13] H. K. Kim, G. W. Hanson, e D. A. Geller, *Are Gold Clusters in RF Fields Hot or Not?*, Science, **2013**, vol. 340, n. 6131, 441-442.

[14] Moran, C. H. et al. *Size-dependent joule heating of gold nanoparticles using capacitively coupled radiofrequency fields*. Nano Res. 2, 400-405, **2009**.

[15] Cardinal, J. et al. *Noninvasive radiofrequency ablation of cancer targeted by gold nanoparticles*. Surgery 144, 125-132, **2008**.

[16] Gannon, C. J., Patra, C. R., Bhattacharya, R., Mukherjee, P. Curley, S. A. *Intracellular gold nanoparticles enhance non-invasive radiofrequency thermal destruction of human gastrointestinal cancer cells*. Journal of Nanobiotechnology 6, 2, **2008**.

[17] Li, D. et al. *Negligible absorption of radiofrequency radiation by colloidal gold nanoparticles*. J Colloid Interface Sci 358, 47-53 **2011**.

[18] Liu, X., Chen, H., Chen, X., Parini, C. Wen, D. *Low frequency heating of gold nanoparticle dispersions for non-invasive thermal therapies*. Nanoscale 4, 3945-3953, **2012**.

[19] Hanson, G. W., Monreal, R. C. Apell, S. P. *Electromagnetic absorption mechanisms in metal nanospheres: Bulk and surface effects in radiofrequency-terahertz heating of nanoparticles*. J. Appl. Phys. 109, **2011**, 124306.

[20] H. 1; G. ;Denver, *Local temperature measurement in the vicinity of remotely heated gold nanoparticles*.Proceedings of the NSTI Nanotechnology 2008, NSTI-Nanotech 2008, **2008**, Vol. 2, p 252.

[21] Kogan, M. J. et al. *Nanoparticle-mediated local and remote manipulation of protein aggregation*. Nano Lett. 6, 110-115, **2006**.

[22] Pearce, J. A. Cook, J. R. *Heating mechanisms in gold nanoparticles at radio frequencies*.2011 Annual International Conference of the IEEE Engineering in Medicine and Biology Society,EMBC 5577-5580, **2011**.

[23] N. N. Nedyalkov, S. E. Imamova, P. A. Atanasov, R. A. Toshkova, E. G. Gardeva, L. S. Yossifova, M. T. Alexandrov, e M. Obara, *Interaction of gold nanoparticles with nanosecond laser pulses: Nanoparticle heating*, Applied Surface Science, **2011**, vol. 257, n. 12, 5456-5459.

Chapter 2

Theoretical model for nanoparticle heating in a RF field

2.1 Introduction

In this chapter a simple model for the power dissipation in gold nanoparticles due to the RF near-field of a coil antenna is developed. In the nanomachine application, gold nanoparticles are dispersed in a water based solution and enclosed in a polymer based microsystem, which both are lossy dielectrics. The power dissipation in the dielectrics is therefore also important, since that adds to the (unwanted) bulk heating of the system.

The analysis is based on Maxwell's four equations that relate the five fields: the conduction current density $\mathbf{J}$, the electric field $\mathbf{E}$, the electric displacement $\mathbf{D}$, the magnetic field $\mathbf{H}$ and the magnetic flux density $\mathbf{B}$. A harmonic time dependency with the angular frequency ω is considered and accounted for by assuming the time phasor $e^{\mathrm{i}\omega t}$, which is suppressed in the equations. As a result the field quantities, e.g. $\mathbf{E}$, are complex vectors, where the physical instantaneous field value is e.g. $\mathrm{Re}[\mathbf{E}e^{\mathrm{i}\omega t}]$.

In addition to Maxwell's equations the materials equations $\mathbf{J} = \sigma\mathbf{E}$, $\mathbf{B} = \mu_0\mathbf{H}$, and $\mathbf{D} = \varepsilon_\mathrm{r}\varepsilon_0\mathbf{E}$, where μ_0 is the permeability ε_0 the permittivity of free space, σ is the conductivity, while ε_r is the relative permittivity of the dielectric material, are used. In a lossy dielectric, the relative permittivity is a complex number $\varepsilon_\mathrm{r} = \varepsilon_\mathrm{r}' - \mathrm{i}\varepsilon_\mathrm{r}''$, and both the real and imaginary parts are in general dependent on the angular frequency, which becomes explicit by considering the relaxation time model of a lossy dielectric

$$\varepsilon_\mathrm{r} = \varepsilon_\infty + \frac{\varepsilon_\mathrm{s} - \varepsilon_\infty}{1 + \mathrm{i}\omega\tau},$$

where τ is the relaxation time, ε_s is the low frequency permittivity while ε_∞

is the very high frequency permittivity.

2.2 Magnetic field generation and power dissipation in gold nanoparticles

Assume that a flat coil antenna of radius a is used to heat a small, conductive (conductivity σ or resistivity ϱ) spherical particle of radius b with is center in $\mathbf{r} = 0$. The coil antenna is located in the x-y plane with its center in $\mathbf{r} = 0$ and a current $I(t) = \mathrm{Re}\left(I_0 e^{\mathrm{i}\omega t}\right)$ at angular frequency ω is forced through it. The current generates a magnetic field which near the axis is oriented along the z-direction[Fig.2.1]. At zero frequency the field strength on the axis is [1, 2]when the sphere is not present.

$$H_z(0,z) = \frac{Ia^2}{2\left(a^2+z^2\right)^{\frac{3}{2}}}, \text{ and } H_z(0,0) = \frac{1}{2}\frac{I}{a} = H_{z0}, \tag{2.1}$$

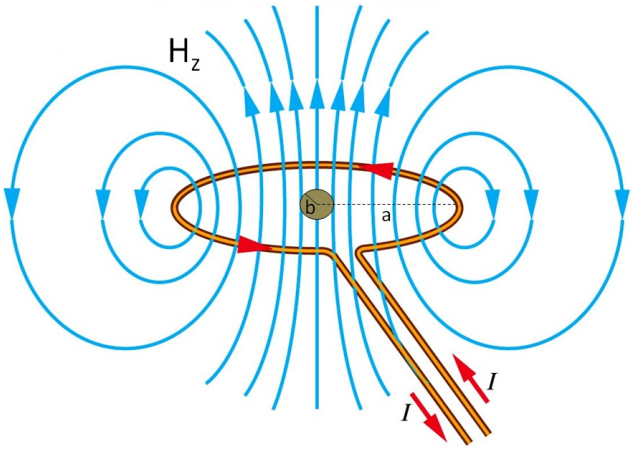

Figure 2.1: Schematic drawing of the field generated by a coil of radius a by a current I

At higher frequencies a retarded field analysis is necessary, and then the analysis becomes somewhat more involved, however, as long as the characteristic dimensions of the coil and sample are much smaller than the wavelength (here $\lambda \sim 10$ cm) this complication is fairly easy to handle as shown by Griffith and Pan [3]. They show that the vector potential $\mathbf{A}$ in the retarded case to a very good approximation is proportional to the static vector potential $\mathbf{A} = (1 + \mathrm{i}\beta R)\, e^{-\mathrm{i}\beta R}\mathbf{A}_s$ where R is the spherical radial coordinate, $\beta = \omega/c$ the propagation constant, c the speed of light in the medium and $\mathbf{A}_s$ the

static vector potential. The approximation is valid at sufficiently low angular frequencies $\omega \ll c/a$. The exact solution for the static vector potential involves elliptic integrals [3], but since the interest here is the near-field region close to the center of the coil a simple approximation to the vector potential is sufficient

$$\mathbf{A}_s = A_{s\phi}\mathbf{e}_\phi = \frac{\mu_0 I_0}{4}\frac{a^2 R\sin\theta}{(a^2+R^2)^{\frac{3}{2}}}\mathbf{e}_\phi = \frac{\mu_0 I_0}{4}\frac{a^2 r}{(a^2+r^2+z^2)^{\frac{3}{2}}}\mathbf{e}_\phi \simeq \frac{\mu_0 I_0}{4}\frac{r}{a}\mathbf{e}_\phi, \tag{2.2}$$

where $\mathbf{e}_\phi$ is the tangential unit vector in polar coordinates (Spherical (R,θ,ϕ) or cylindrical (r,ϕ,z)). By definition of the vector potential $\mathbf{B} = \nabla\times\mathbf{A}$ and from Faradays law of electromagnetic induction

$$\nabla\times\mathbf{E} = -\frac{\partial\mathbf{B}}{\partial t} = -\mathrm{i}\omega\mathbf{B} = -\,\mathrm{i}\omega\nabla\times\mathbf{A}, \tag{2.3}$$

and we may choose $\mathbf{A}$ such that $\mathbf{E} = -\,\mathrm{i}\omega\mathbf{A}$, and that is the case with the approximation used in Eq. 2.2. It follows that

$$\mathbf{E} = -\,\mathrm{i}\omega\,(1+\mathrm{i}\beta R)\,e^{-\mathrm{i}\beta R}\frac{\mu_0 I_0}{4}\frac{a^2 r}{(a^2+r^2+z^2)^{\frac{3}{2}}}\mathbf{e}_\phi \simeq -\mathrm{i}\omega\frac{\mu_0 I_0}{4}\frac{r}{a}\mathbf{e}_\phi, \tag{2.4}$$

where the approximation is valid close to the center of the coil, where the nanoparticle is placed.

At low frequencies the magnetic field is hardly affected by the presence of the particle, and thus the total magnetic field is approximately equal to the field from the coil alone, and we may calculate the time average power dissipated in the nanoparticle as

$$P = \frac{1}{2}\int_{\text{sphere}}\frac{1}{\varrho}E_\phi^2\,\mathrm{d}\Omega = \frac{1}{2\varrho}\left(\omega\mu_0\frac{I_0}{2a}\right)^2\int_0^b\left(\frac{r}{2}\right)^2 2\pi r\times 2\sqrt{b^2-r^2}\,\mathrm{d}r$$

where the integration is performed by considering a cylindrical shell of height $2\sqrt{b^2-r^2}$, radius r and thickness $\mathrm{d}r$, and $I_0/(2a) = H_{z0}$ is recognized as the static magnetic field at origin. The integral results in

$$P = \frac{1}{2\varrho}\left(\omega\mu_0 H_{z0}\right)^2\times\frac{2\pi}{15}b^5 = \frac{4\pi^3}{15}\frac{b^5}{\varrho}\left(f\mu_0 H_{z0}\right)^2.$$

This result is in perfect agreement with COMSOL finite element simulations.

At higher frequencies, where the skin depth $\delta = \sqrt{\varrho/(\pi f\mu_0)}$ becomes comparable to the nanoparticle radius this analysis becomes invalid[Fig.2.2]; at 3 GHz however the skin depth for gold is approximately 1.5 μm and

thus this limit is at frequencies beyond interest here where nanoparticles of nanometer size are considered; this is true, even if the resistivity of the nanoparticle is considerably higher than the bulk value due to size effects. [4, 5]

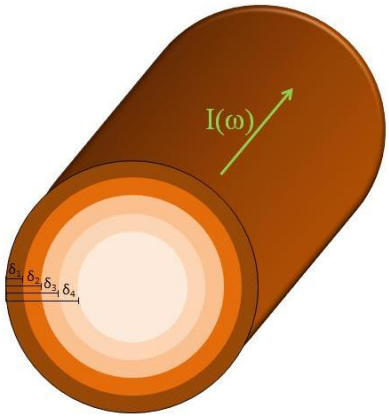

Figure 2.2: Skin effect phenomenon, the current flows through a conductor in a layer which is inversly proportional to the frequency, $\omega_1 > \omega_2 > \omega_3 > \omega_4 \Rightarrow \delta_1 < \delta_2 < \delta_3 < \delta_4$

The radiation resistance of the current loop is [1]

$$R_{\mathrm{rad}} = \sqrt{\frac{\mu}{\varepsilon}}\frac{\pi}{6}(\beta a)^4 = \sqrt{\frac{\mu}{\varepsilon}}\frac{\pi}{6}\left(\frac{\omega}{c}a\right)^4, \tag{2.5}$$

and that may be used to estimate the loop current (Note, the calculation will yield the correct magnetic field value also with a multi-turn loop). In the experiments the power incident on the antenna is $P_{\mathrm{a}} = 10$ W, and the radiated power must be less. The radiated power is $P_{\mathrm{rad}} = \frac{1}{2}R_{\mathrm{rad}}I_0^2$ and thus the current is at most $I_0 \leq \sqrt{2P_{\mathrm{a}}/R_{\mathrm{rad}}}$, and hence $H_{z0} \leq \sqrt{2P_{\mathrm{a}}/R_{\mathrm{rad}}}/(2a)$.

We may then calculate the ratio of the power absorbed in the nanoparticle to the radiated power

$$P/P_{\mathrm{rad}} = \frac{1}{5}\frac{b^5}{a^6}\sqrt{\frac{\varepsilon}{\mu_0}}\frac{1}{\varrho\omega^2\varepsilon^2}, \tag{2.6}$$

and a direct calculation using $f = 3$ GHz, $a = 1$ mm, $b = 5$ nm, $\varepsilon = \varepsilon_0$ and $\varrho = 2.44 \times 10^{-8}$ Ωm results in $P/P_{\mathrm{rad}} \simeq 2.5 \times 10^{-18}$, and thus at an incident power on the coil of $P_{\mathrm{a}} = 10$ W the expected power dissipated in a nanoparticle is $P \simeq 2.5 \times 10^{-17}$ W, indeed a very low power.

2.3 Dielectric dissipation in the medium

Since the nanoparticles or nanomachines are dispersed in an electrolyte solution contained in a polymer microsystem the time varying magnetic field will induce some dielectric heating of the liquid and polymer, since these are lossy dielectrics. The loss power density may be estimated using the expression for the electric field Eq. 2.4 and the total electric current density, which is the sum of the conduction and the displacement current densities

$$\mathbf{J}_{\mathrm{t}} = \sigma_\ell \mathbf{E} + \frac{\partial \mathbf{D}}{\partial t} = \sigma_\ell \mathbf{E} + \mathrm{i}\omega\varepsilon_{\mathrm{r}}\varepsilon_0 \mathbf{E}, \tag{2.7}$$

where σ_ℓ is the conductivity of the liquid. The time average dissipated power density is then:

$$p_w = \frac{1}{2}\,\mathrm{Re}\left(\mathbf{J}_{\mathrm{t}} \cdot \mathbf{E}^*\right) = \frac{1}{2}\left(\sigma_\ell + \omega\varepsilon_{\mathrm{r}}''\varepsilon_0\right) E^2 \simeq \frac{1}{2}\omega\varepsilon_{\mathrm{r}}''\varepsilon_0 E^2, \tag{2.8}$$

where the star indicates complex conjugation. At high frequencies, the power dissipation due to finite conductivity becomes smaller than that due to dielectric losses. By use of Eq. 2.4 the dielectric heating power density becomes:

$$p_w = \frac{1}{2}\omega\varepsilon_{\mathrm{r}}''\varepsilon_0 \frac{\left(1+\beta^2 R^2\right)\omega^2 a^4 r^2}{\left(a^2+r^2+z^2\right)^3}\left(\frac{\mu_0 I_0}{4}\right)^2 \simeq \frac{1}{2}\omega\varepsilon_{\mathrm{r}}''\varepsilon_0 \frac{\omega^2 a^4 r^2}{\left(a^2+r^2+z^2\right)^3}\left(\frac{\mu_0 I_0}{4}\right)^2$$

which obviously varies throughout the dielectric volume. By integration over the sample volume, where the dependency of the $z-$ coordinate is ignored, the power dissipated in a cylindrical volume of radius a_0 and height h becomes:

$$P_w = \frac{1}{2}\omega\varepsilon_{\mathrm{r}}''\varepsilon_0 \left(\frac{\mu_0 I_0}{4}\right)^2 \left(\frac{1}{2}\frac{\omega^2 a^2 a_o^2}{\left(a^2+a_o^2\right)^2}\right)\pi a_o^2 h.$$

By use of the expression for the radiated power, this may be recast as:

$$\frac{P_w}{P_{\mathrm{rad}}} = \frac{3}{16}\frac{\varepsilon_{\mathrm{r}}''}{\varepsilon_{\mathrm{r}}'}\frac{c}{\omega}\frac{a_o^4 h}{a^2\left(a^2+a_o^2\right)^2},$$

and assuming $h = 0.5$ mm, and $a_0 = 2$ mm, we get $0.017 < P_w/P_{\mathrm{rad}} < 0.14$ at 3 Ghz using $\varepsilon_{\mathrm{r}}''/\varepsilon_{\mathrm{r}}' \simeq 0.15$ and $\varepsilon_{\mathrm{r}}' \simeq 75$ for water, the range is related to which speed of light to use in the expression, since that is reduced in water by a factor $\sqrt{75}$, but a major part of the radiation is emitted to air. In any case a significant heating of the sample liquid is expected.

If a GNP concentration in the sample of $C = 10$ nM is assumed, the number of GNP's in the volume is $N = CN_A\pi a_0^2 h \simeq 4\times 10^{10}$ and thus the relative power dissipation due to the GNP's is at most $P_{\mathrm{GNP}}/P_{\mathrm{rad}} = 4\times 10^{10}\times 2.5\times 10^{-18} = 1\times 10^{-7}$ which is insignificant compared to dielectric heating.

Bibliography

[1] S. Ramo, J. R. Whinnery, e T. V. Duzer, *Fields and Waves in Communication Electronics*. Wiley, **1994**.

[2] D. J. Griffiths, *Introduction to Electrodynamics*, 3rd ed. Addison Wesley, **1999**.

[3] J. M. Griffith e G. W. Pan, *Time Harmonic Fields Produced by Circular Current Loops*, IEEE Transactions on Magnetics, **2011**, vol. 47, n. 8, 2029-2033.

[4] K. Fuchs, Mathematical Proceedings of the Cambridge Philosophical Society, **1938**, vol. 34, n. 01, pagg. 100-108.

[5] E. Sondheimer, Physical Review, **1950**, vol. 80, n. 3, 401-406.

Chapter 3

Radio frequency absorption

3.1 Introduction

The purpose of this chapter is to investigate the possibility of detecting the interaction of an RF field with GNPs diluted in solution with different solvents (water and isopropanol). In order to do that a simple microfluidic system comprising a coplanar waveguide (CPW) has been fabricated. The normalized loss of each sample solution have been measured in the range 0-18 GHz. The results show that GNPs diluted in a low loss medium such as isopropanol, enhance their losses while the GNPs contribution in a high absorption medium such as water, is negligible.

3.2 Experimental setup description

In order to test the interaction between gold nanoparticles dispersed in solutions and an RF field, a simple microfluidic device attached to a CPW connected to a vector network analyzer was designed and fabricated. The sample under investigation interacted with the field of the waveguide structure due to close proximity to the CPW [Fig.3.1 B]. The CPW structure was fabricated using a standard photolithographic process and was designed to have a characteristic impedance of 50 Ω. It is preferable to use a low permittivity substrate in order to maximize the intensity of the RF field in the sample. The substrate (Duroid 5870 from Rogers) used has a dielectric constant of 2.33. This substrate material has low loss ($\varepsilon_r''/\varepsilon_r' = 0.0012$ at 10 GHz) which is required to maximize the sensitivity of the setup. The CPW structure should also ensure that the electromagnetic field is mostly confined in the region around the sample, resulting in enhanced coupling. This substrate also has very little water absorption and is ideal for working in high

moisture environments.

The microfluidic setup consists of modular components of PMMA and PDMS that allows easy handling of the samples without touching the system and disturbing the measurements [1] [Fig.3.1 A]. The chip with the sample reservoir consists of a three layer sandwich structure of PMMA fabricated by micromilling; a bottom cover, that seals the reservoir, a middle structure with the actual reservoir, microfluidic channels and connections and, as the final layer, a thin top lid of 150 μm thickness that ensures close proximity between the sample solution and the CPW. The reservoir consists of a 4.5 cm long and 4 mm wide channel and is designed to match exactly the dimension of the CPW and enhance the coupling efficiency [Fig.3.1 C]. The sample holder also features curved inlet and outlet structures to ensure uniform filling of the chamber and avoid bubbles in the sensing area. The total volume of the chamber could be changed by changing the thickness of the middle layer of PMMA. We used 2 mm thick PMMA, resulting in $\simeq$ 360 μl sample volume. We tested gold nanoparticles of 12 nm diameter covered with a thin layer of silicon dioxide, diluted in two different solvents, DI water and high purity isopropanol from Sigma Aldrich (water content $\simeq$ 0.02%).

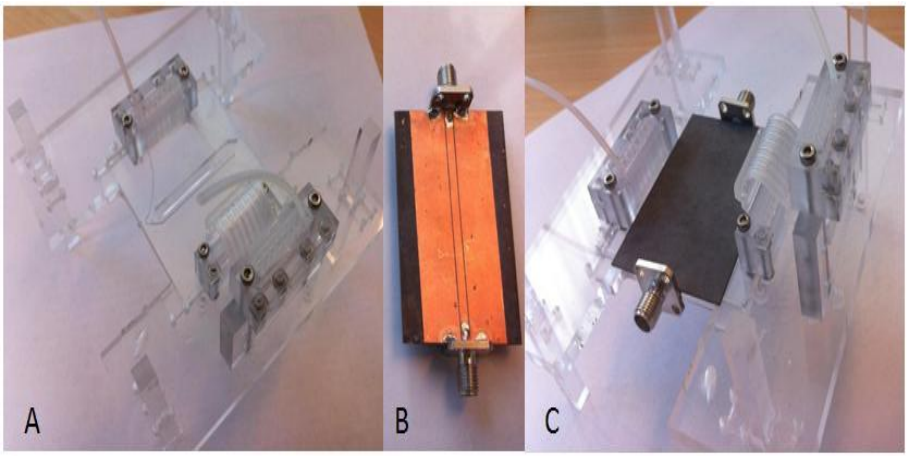

Figure 3.1: *Experimental setup; (A) Microfluidic system for sample handling, (B) Microstrip coplanar waveguide, (C) assembled system.*

A second experimental setup was based on an open radiating structure where the field was generated by a wideband monopole antenna and collected by a second identical antenna. The sample was placed between the two antennas. The antenna is a circular monopole which was designed to operate in a very wide frequency range. The setup and the matching properties of the antenna are shown in fig.3.2.

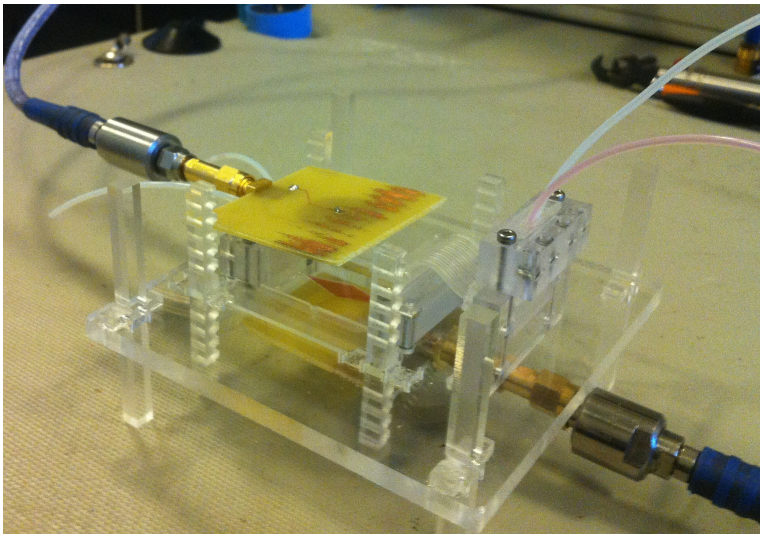

(a) Open radiant antennas setup

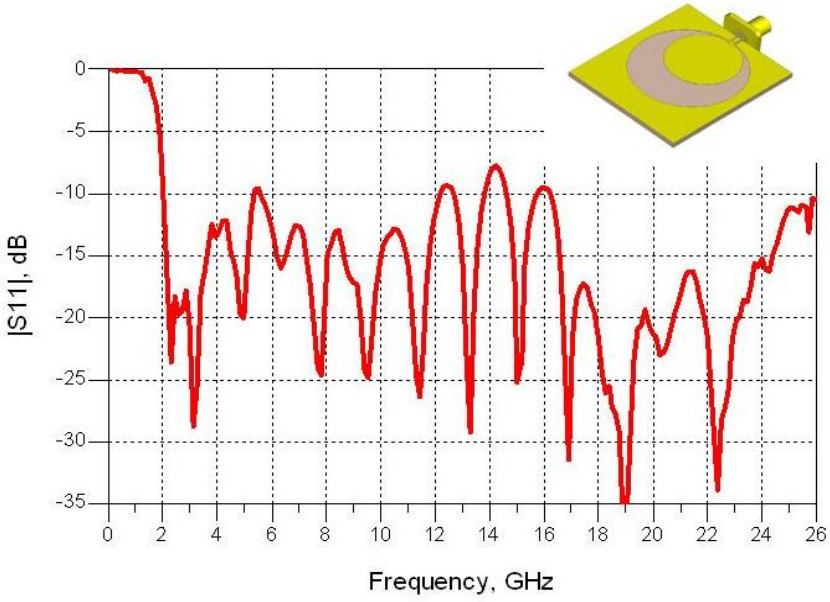

(b) Matching properties of the second antenna, design of the antenna in the insert

Figure 3.2: *Top figure: picture of the experimental setup of the double radiating antennas setup, the sample of gold nanoparticles (red fluid) is injected in the reservoir placed between the two antennas changing the transmission between them. Bottom, matching properties of the monopole antenna used in the experiment,insert, schematic drawing of the antenna layout.*

As one can see, the return loss of the antenna is typically better than 10 dB in the frequency range from 2 GHz to 26 GHz. The antenna was printed on FR4 substrate to support the structure. During experiments it was difficult to achieve repeatable results with this setup due to interaction of the antenna with the environment. The close proximity of the radiated field in the CPW setup ensure far better coupling with the sample solution enhancing the sensitivity of the measurements compared to the radiant monopole setup. For these reasons we chose to proceed with the first measurement setup.

3.2.1 Coplanar Waveguide

The coplanar waveguide [2, 5] is a peculiar type of transmission line composed of a central transmission line of width S separated from two lateral conductors by a distance W called the slot. The conducting layer of thickness t is placed on a dielectric substrate of height h and dielectric and magnetic constants ϵ_r and μ_r The extension of the two lateral electrodes is supposed to be infinite, but for practical applications, it is designed to be multiple of the signal wavelength [Fig.3.3].

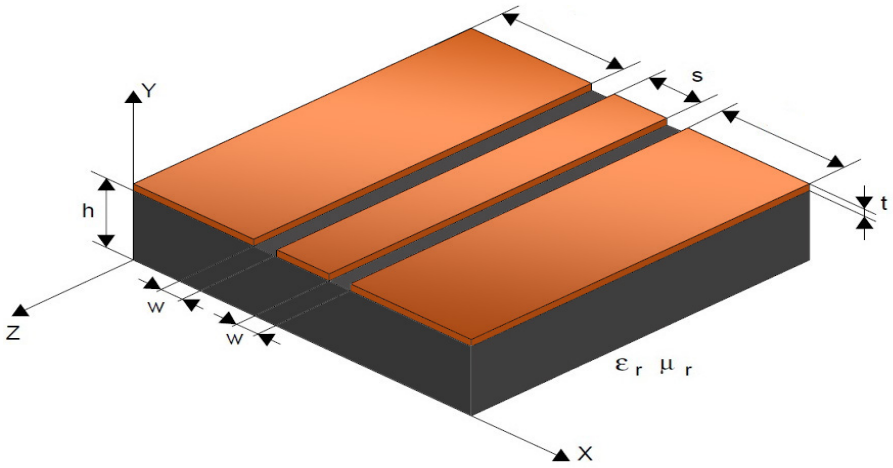

Figure 3.3: *Schematic view of a coplanar waveguide*

The CPW's low order propagation mode is indicated with *quasi*TEM, because it is not a real TEM. [3, 4] TEM is a mode where E and H fields are perpendicular to each other and to the direction of propagation. This mode can exist between two excited conductors with a dielectric material filling the region between them. Another important characteristic of TEM mode is a constant phase velocity, which means that $\beta = k$ (propagation constant=wavenumber). A good example of TEM mode waveguide is a coaxial

cable where the E-field vector is the radial direction, and the H-field lines are perpendicular so their lines create concentric circles around the center conductor. The direction of propagation is along the cable.

The TEM mode can be found whenever there are two conductors in only 1 medium. But for the case of microstrip lines, the wave is not completely confined in the dielectric, a portion of the wave propagates in the free space, therefore the wave will propagate with different speed in the two media and, as a result, a longitudinal component of the field can be found; so it is not a perfect TEM mode, but luckily the non TEM component is small and can be neglected during analysis, the resulting *quasi*TEM could be therefore approximated by the simple TEM mode. An important parameter for the CPW is the effective dielectric constant value to the structure, ε_{eff}, which for the CPW has a value between 1(air) and the dielectric constant of the material. Now it is possible to analyse the wave properties as if it was propagating through a homogenous effective media ε_{eff} supported by 2 conductors (just like TEM). The error made in evaluating the fundamental propagation mode as a pure TEM is negligible for frequencies up to some tens of GHz. Above this limit, the dispersion rises and the propagation mode tends to be nearly a TE mode, with the magnetic field elliptically polarized along longitudinal planes.

A simplified picture of the electric and magnetic field line for the *quasi*TEM mode of a CPW is shown in fig.3.4 left, for a specific position and time. We consider the lateral conductor to be at ground potential while the central line is equipotential. It is important to notice that the schematic is not complete and there are many more other possible modes that could be excited depending on, for example, frequency and feed line; especially for the magnetic field, the picture is much more complicated, the field lines have to form a closed loop on both left and right side of the conductor, going off plane compared to the cross section shown. For this reason, • indicate a vector exiting from the plane of the figure, while with an X we indicate a vector entering into this plane. A more realistic view of the magnetic field line is shown in fig.3.4 right

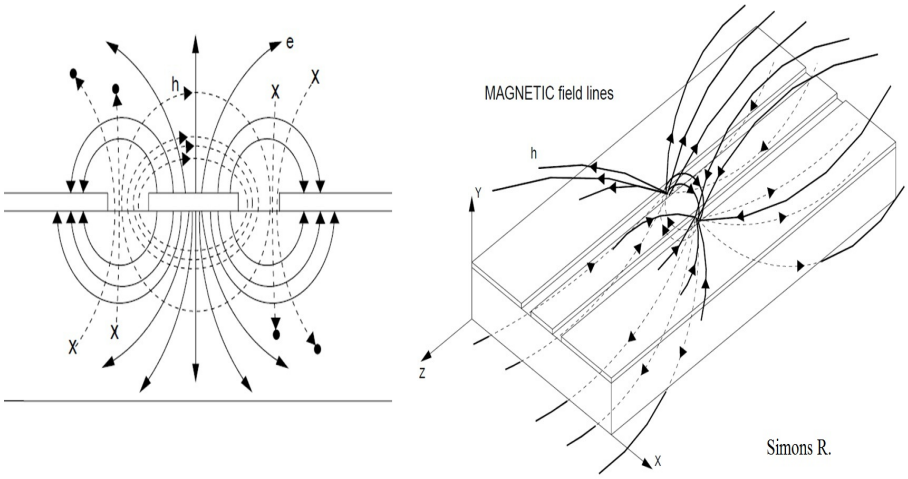

Figure 3.4: *Schematic view of a field's line of the CPW [5]*

There are many approaches for calculating the resulting parameters of the CPW, for example [5, 6]. In order to calculate the characteristic dimension of the CPW we use the derivation of [5]. The structure of our interest is a peculiar case of the conventional coplanar waveguide with the dielectric substrate having a finite thickness. By considering fig.3.5 we can derive expression for the characteristic impedance Z_0 and ε_{eff} using the approach called Quasi-static Conformational Mapping. There are a few assumptions in this method: first the thickness of the metal layer t is considered zero, second the magnetic field has zero boundary condition along the dielectric boundaries. In this way it is possible to study the CPW as composition of different zones, in which the electric field is studied individually. The capacitance of each zone is then calculated and the total behavior of the CPW is represented by the sum of all the zones.

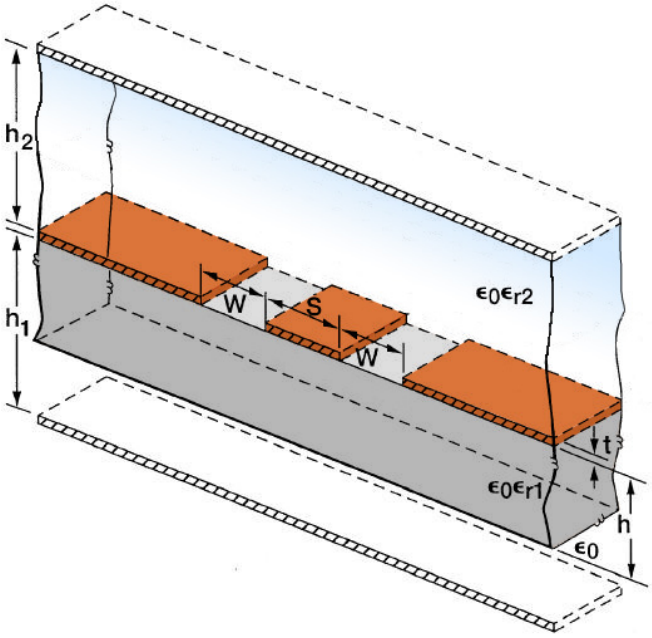

Figure 3.5: *Schematic view of the CPW divided in capacitive regions*

We consider $\varepsilon_{r2} = 1$ and $h_1 = h_2 = \infty$ and we can evaluate the expression for Z_0 and ε_{eff}:

$$\varepsilon_{\text{eff}} = \frac{\text{C}_{\text{CPW}}}{\text{C}_{\text{air}}} = 1 + \frac{(\varepsilon_{r1} - 1)}{2} \frac{K(k_1)}{K(k_1')} \frac{K(k_0')}{K(k_0)} \tag{3.1}$$

$$Z_0 = \frac{1}{c\text{C}_{\text{air}}\sqrt{\varepsilon_{\text{eff}}}} = \frac{30\pi}{\sqrt{\varepsilon_{eff}}} \frac{K(k_0')}{K(k_0)} \tag{3.2}$$

where C_{CPW} is the capacitance of waveguide itself, the region that extents in the dielectric substrate, C_{air} is the capacitance of the infinite layer that extents on top of the CPW and K is the complete elliptic integral and the moduli $(k_1)(k_1')(k_0)(k_0')$ are:

$$k_1 = \frac{\sinh(\pi S/4h_1)}{\sinh\left[\pi(S + 2W)\right]/4h} \tag{3.3}$$

$$k_1' = \sqrt{1 - k_1^2} \tag{3.4}$$

$$k_0 = \frac{S}{S + 2W} \tag{3.5}$$

$$k_0' = \sqrt{1 - k_0^2} \tag{3.6}$$

A number of online calculators to solve this equation are available [8, 9]. The dimension of the CPW are $S = 2.5$ mm, $W = 0.185$ mm and $h_1 = 0.7874$ mm, these parameters result in $Z_0 = 53.95\ \Omega$.

3.3 Measurement results

To characterize the interaction between the RF field generated by the CWG and the gold nanoparticles we made use of the scattering parameters (S-parameters)[Fig.3.6].

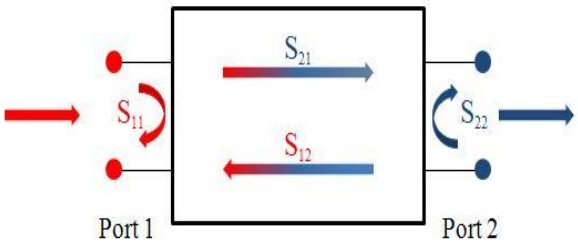

Figure 3.6: *Schematic view of the S-Parameters for a two port system*

These factors are defined as ratio of signal incident, reflected and transmitted along the port of the network. Particularly, $|S_{11}|^2$ is the ratio of the complex amplitude of the reflected wave to the complex amplitude of the incident wave at port 1, and $|S_{21}|^2$ is the ratio of the complex amplitude of the transmitted wave at port 2 to the complex amplitude of the incident wave at port 1 and so forth. For a lossless two-port system, $|S_{11}|^2 + |S_{21}|^2 = 1$, therefore the normalization loss (NL) $NL = 1 - |S_{11}|^2 - |S_{21}|^2$ is a convenient measure of the loss in the structure. We choose a sample of water and isopropanol alone and containing high concentration of 12 nm GNPs. These nanoparticles are slightly different from the one used in the conjugation of the NMs (as shown and described in the following chapters); in order to avoid problem of aggregation of the nanoparticles due to the isopropanol and the high concentration, the core of the gold was covered with a thin layer of silicon dioxide. All the samples were measured in the frequency range up to 18 GHz. In the microwave range water is a highly absorbing medium and the addition of gold nanoparticles to the solution, is not resulting in appreciable absorption difference compared to the solvent alone. As results the two curves overlay almost perfectly [Fig.3.7 top].

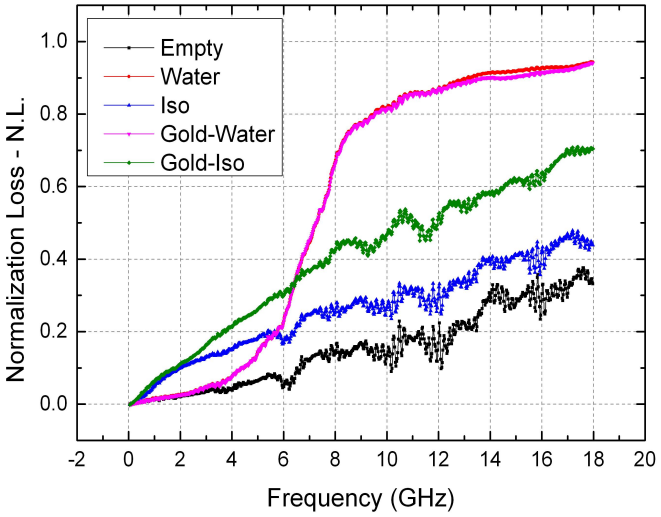

(a) NL for different solution samples

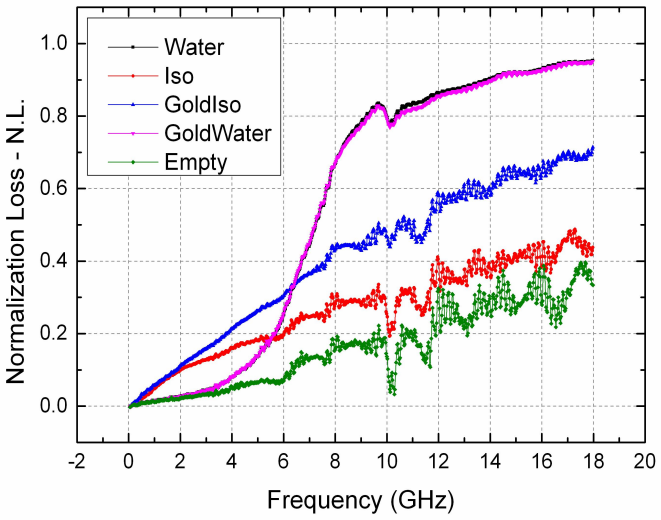

(b) Reverse NL for different solution samples

Figure 3.7: *Top figure:NL, water (red curve) and GNPs diluted in water (pink curve) show the same absorption value, while isopropanol (blue curve) and GNPs diluted in isopropanol (green curve) show significantly different NL. Bottom figures, "Backward" NL, same samples previously reported but NL calculated from the other port of the setup to ensure repeatability of the measurement.*

If instead, Isopropanol is used as solvent, it is possible to detect a signif-

icant enhancement of the normalized loss with a distinguishable increasing trend in the amplitude with increasing frequency. Moreover, to indicate the repeatability of the measurements the NL were calculated from the reverse parameters, that is $NL = 1 - |S_{22}|^2 - |S_{12}|^2$ that is as viewed from the opposite port of the system; the measured curves overlap nicely the forward plots[Fig.3.7 bottom].

In order to validate these data, a theoretical calculation of the NL was developed. In small reflection limit (i.e. the characteristic impedance of the feed waveguide and the CWG are identical) the normalization loss is:

$$NL = 1 - |(\exp(-ikl)|^2 \tag{3.7}$$

where k is the wavenumber and it is defined as $k = (\omega/c_0)\sqrt{(\varepsilon_r}$, ε_r is the complex effective relative permittivity and ω is the angular frequency. The results calculated for both water and isopropanol show good agreement with the measured parameters (data not shown).

3.4 Discussion

In the microwave range water is known to be a material with very high dielectric losses. Because of the large absorption, the contribution of gold nanoparticle in the solution, although present, is hidden by the larger loss contribution of water. When, on the other hand, gold nanoparticles are diluted in isopropanol, a relatively low loss solvent, the gold nanoparticles show a remarkable contribution to the NL. From our experiment and theoretical model we can conclude that the addition of gold nanoparticles to the solution of isopropanol causes an increase in the conductivity value of the medium and therefore results in a higher losses compared to the pure solution. The CWG method is an efficient way to confirm the interaction between the EM field and the gold nanoparticles that establish the framework for following particle activation.

Bibliography

[1] Sabourin D, Petersen J, Dufva M. *Microfluidic DNA microarrays in PMMA chips: streamlined fabrication via simultaneous DNA immobilisation and bonding activation by brief UV exposure. Biomed Microdevices.* **2010** Aug; 12(4),673-681.

[2] C. P. Wen, *Coplanar waveguide: a surface strip transmission line for nonreciprocal gyromagnetic device application.* IEEE Trans. on MTT, 1087, Dec. **1969**.

[3] Riaziat, M. et al. *Propagation Modes and Dispersion Characteristic of Coplanar Waveguide.* IEEE Transactions on Microwave Theory and Techniques, Vol.38, NO.3 ,**1990**.

[4] Mulpuri V. Rao. et al. *Microwave Dielectric Heating of Fluids in Microfluidic Devices.* Chapter 8, Pages 187-189.

[5] Simons R. *Coplanar Waveguide, Circuits, Components and Systems.*Chapter 2, Pages 11-23, Wiley, **2001**.

[6] Bhattacharya, D., *Characteristic impedance of coplanar waveguide*, Electronics Letters , vol.21, no.13, pp.557,, June 20 **1985**.

[7] DiPaolo Franco, Ph.D. *"Coplanar Waveguides" Networks and Devices Using Planar Transmission Lines*, Boca Raton: CRC Press LLC,**2000**

[8] $http://www1.sphere.ne.jp/i-lab/ilab/tool/cpw_e.html$.

[9] http://www.microwaves101.com/encyclopedia/calcpw.cfm.

Chapter 4

Gold conjugated molecular beacons

4.1 Introduction

In order to test the RF activation of gold nanoparticles, theoretically described in chapter 2 of part II, a gold-conjugated molecular beacons (MB) was developed. This sensor will not only retain all the characteristic of a conventional MB, but also, it will allow to study the fluorescence emission as function of the applied field. In this chapter, the conjugation protocol of the oligonucleotide strand to the gold nanoparticle will be described. The resulting conjugated beacon will be characterize in vitro though melting and hybridization curves to test their performances. Many different optimization in the beacons structure and morphology will be examined, namely:

- Addition of T-Base spacer to the hairpin;
- Substitution of the gold nanoparticle with other gold nanostructures;
- Substitution of the backbone of the oligo forming the hairpin.

The performances of gold conjugated MBs will finally be compared with conventional MBs in which gold quencher was replaced with an organic one.

4.2 Materials and Conjugation Protocol

2´deoxy DNA and 2´methyl RNA molecular beacons encoded with a sequence specific for recognition of tyrosine hydroxylase were purchased from DNA technology (Risskov, Denmark) and purified by high-performance liquid chromatography. Tyrosine hydroxylase is an enzyme encoded by the

TH gene [1] that is of great importance in neuronal cells; it is necessary for the production of dopamine and it is involved in disorders such as Segawa's dystonia, Parkinson's disease and schizophrenia [2]. The hairpin DNA were synthesized with the following sequences: TH5 5´ -(NH_2)-**GCGAG** *ACAC-CTTCACAGCTCGGGA* **CTCGC**-(Tamra)- 3´ and TH11 5´ -(NH_2)-**GCG AGGCGAGC** *ACACCTTCACAGCTCGGGA* **GCTCGCCTCGC**-(Tamra)-3´ ; Bolded regions indicates the stem of the hairpin while region in italic indicates the sequence encoding specific target for TH, regions in parentheses indicates the end modifications, amino group at 5´ end and the fluorochrome at 3´ . Spherical gold nanoparticles (GNPs) of 5 nm and 12 nm diameter and nanorods with carboxyl surface modification were purchased from Nanopartz^{TM}(Loveland, USA). The GNPs (concentration 0.01 μM) were covalently conjugated with amino modified oligonucleotides (concentration 10 μM) by incubation with N-ethyl-N´dimethyl-aminopropyl carbodiimide (EDC, concentration 10 μM) to enhance the coupling efficiency between amine and carboxyl groups. 2´deoxy DNA was first mixed with GNPs in cold 2-(N-morpholino) ethanesulfonic acid buffer (MES buffer, pH 6) for 5 min and then a solution of EDC was added. The reaction was performed for 2 h at 37 °C under slight agitation. The conjugation reaction is explained in detail with the following figure [Fig. 4.1]:

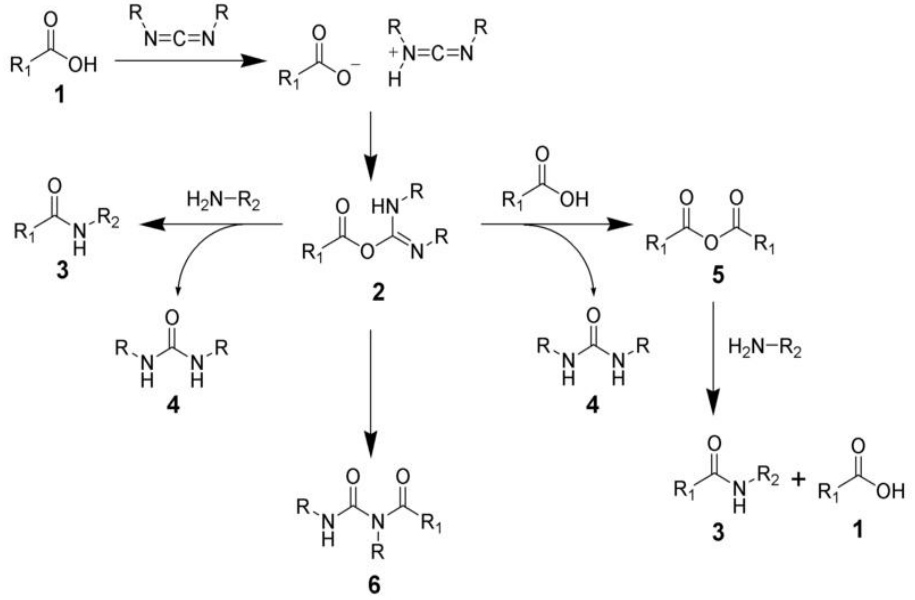

Figure 4.1: *Schematic view of the chemical reaction chain that leads to gold conjugation.*

The acid **1** will react with the carbodiimide to produce the key intermediate: the O-acylisourea **2**, which can be viewed as a carboxylic ester with an

activated leaving group. The O-acylisourea will react with amines to give the desired amide **3** and urea **4**. The side reaction of the O-acylisourea **2** produce both desired and undesired products. The O-acylisourea **2** can react with an additional carboxylic acid **1** to give an acid anhydride **5**, which can react further to give the desired amide **3**. The main undesired reaction pathway involves the rearrangement of the O-acylisourea **2** to the stable N-acylurea **6**.

Finally, the conjugated molecular beacons were centrifuged for 2 min at 735× g on Illustra Microspin S-200 HR columns (GE Healthcare, Life Sciences) to removed unconjugated oligonucleotides and EDC. The purified molecular beacons were stored in the dark at 4° C for later use.

The nanomachines have basically the same structure of the one of [3]. As competing technology, Mirkin et al. [4,5] develop a similar molecular beacon based on gold nanoparticles called *Nanoflare*[see fig. 4.2]; the main difference is that instead of having oligonucleotides strands attached on the particles arranged in hairpin, these strands are protruding from the particle's surface and they hybridize with a short sequence having a fluorophore covalently linked to one end. The fluorescence is, in this configuration, quenched by GNP proximity. When the correct target is present in the cellular environment, it hybridizes to the protruding arms pending from the gold nanoparticles knocking off the short labelled strand. Being free in the medium and far from the gold quencher, the fluorophore can now emit a detectable signal. Multiple labelling of the nanoflare enables multiple gene tracking.

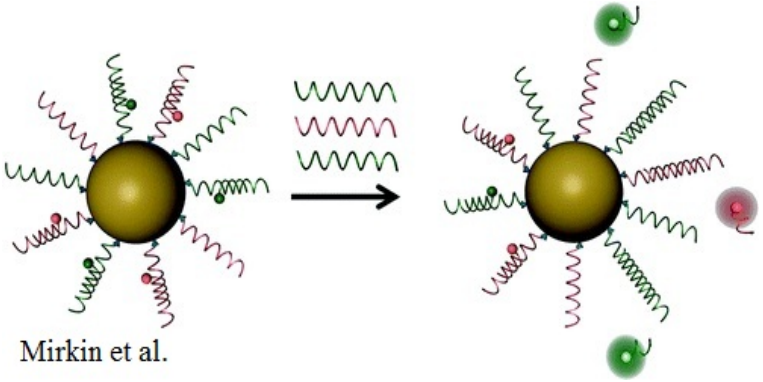

Figure 4.2: *Working principle of the nanoflare, short strands with fluorophore are hybridized to a protruding arm linked to a gold nanoparticle; when the complementary target is present, the labelled strand is knocked off and released in the cellular environment and therefore emits fluorescence.*

As opposite, in figure 4.3 A,B,C it is possible to see the working principle of the nanomachine. The conjugated oligo form an hairpin that holds

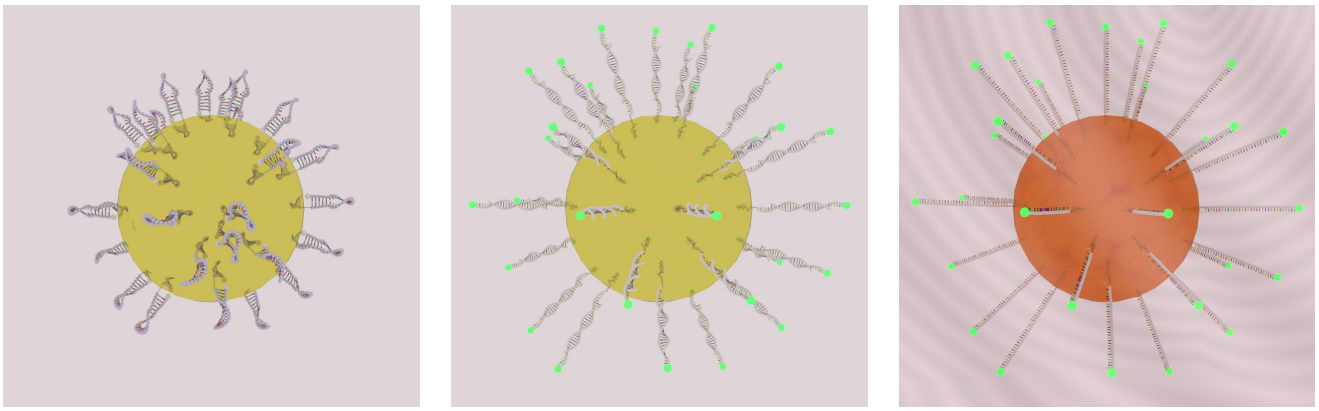

(a) Quenched Nanomachine, hairpin

(b) Hybridized nanomachine

(c) Melted Nanomachine, random coil

Figure 4.3: *Schematic view of the hairpin functionalized GNPs and working principle; A, quenched nanomachine, the stem keeps fluorophore and quencher together blocking the fluorescence emission;B, the nanomachine hybridizes to its complementary target, parting donor from acceptor; C, when the temperature rises above T_m the stem melts and the nanomachine assume the random coil configuration.*

the fluorophores close to the GNPs [Fig.4.3 A]. In this way the fluorescence emission is quenched though a FRET mechanism. If the complementary target is present in the sample solution, it hybridizes to the loop sequence of the hairpin resulting in parting the fluorophore from the GNP and restoring the fluorescence emission[Fig.4.3 B]. As opposed to the nanoflares, the hairpin strand (and therefore the fluorophore which is linked to it) remain connected with the GNP. If the bulk temperature of the solution (or the local temperature in the GNP vicinity) is increased up to the melting temperature of the loop-target duplex, the double strands denaturates and the complementary target is released in the solution leaving the "hairpin" free in a random coil configuration [Fig.4.3 C]. When the temperature decreases, the stem hybridizes and the hairpin configuration is restored.

4.3 Melting curves

In order to test the functionality of the conjugated beacons, their fluorescent emission was characterized through a melting profile. As previously described, when the temperature is increased above the melting threshold T_m, the stem melts and the beacon undergo a conformational change from hairpin[Fig.4.3 A] to random coil configuration [Fig.4.3 C]. An increase in the fluorescence emission is therefore detected and measured. The general

protocol for testing the nanomachine construct consists in ramping the temperature from 30 °C to 90 °C with steps of 0.3 °C and the fluorescence was measured at every step after 5 minutes.

Nanomachine with different T-base spacer hairpin

In order to study the effect of gold-fluorophore separation and therefore, optimize the quenching efficiency, sequences with a T-spacer placed at 5´ end have been purchased from Biomers(see sequences in table 4.1) and conjugated to a 12 nm GNP following the protocol described in the previous chapter. The contribution of 2, 5 and 10 T-bases on the behavior of the nanomachine was investigated.

Table 4.1: T-spacer's stem sequences

Name	Stem Sequence (5´end)
TH5	5´ -**GCGAG** -...
TH5T2	5´ -TT-**GCGAG** -...
TH5T5	5´ -TTTTT-**GCGAG** -...
TH5T10	5´ -TTTTTTTTTT-**GCGAG** -...
TH11	5´ -**GCGAGGCGAGC**-...
TH11T10	5´ -TTTTTTTTTT-**GCGAGGCGAGC** -...

From the melting curves it was possible to identify two major populations characterized by the length of the stem: nanomachines with 5bps stem melt at approximately 42 °C while nanomachines with 11bps stem, melt at about 62 °C. NMs with a 11bps long stem show higher intensity of signal emission probably due to longer fluorophore-quencher distance in the random coil configuration. The addition of T-spacer lowers the melting point of the different conjugation progressively, according with the length of the spacer, the effect is particularly visible with short stem. On the other hand there is not a clear improvement regarding quenching efficiency and therefore, regarding the signal to noise ratio[see fig.4.4].

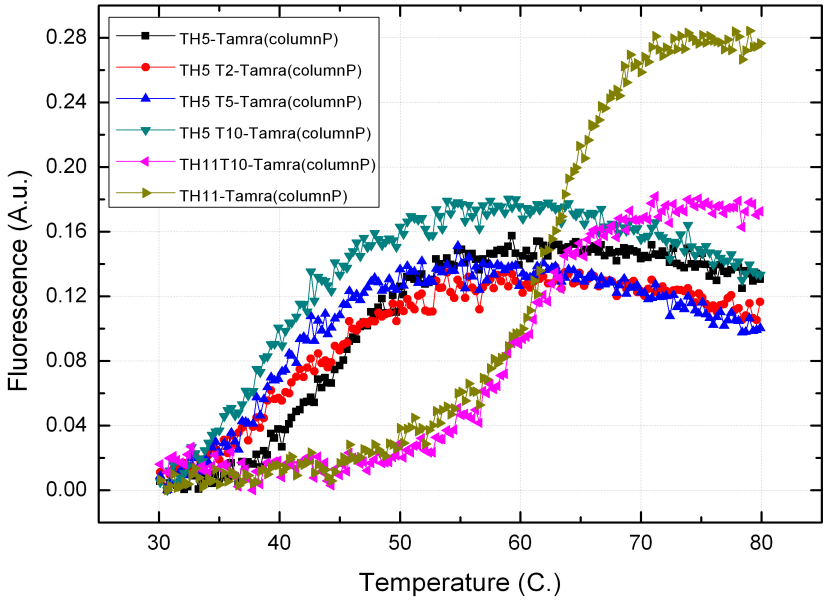

Figure 4.4: *Melting curves of conjugated Nanomachines with different T-spacer. The addition of longer T spacer lowers the melting point but does not increase the S/N.*

Nanomachine with different gold nanostructured quencher

In these experiment we studied the effect of different gold nanostructures on the quenching properties of the nanomachine. The same 2´deoxy DNA hairpin were conjugated with 5 nm and 12 nm gold nanoparticles and nanorods (38 nm long, 10 nm wide) from Nanopartz^{TM}(Loveland, USA). The melting curves are reported here only for TH5 and TH11 [Fig.4.5].

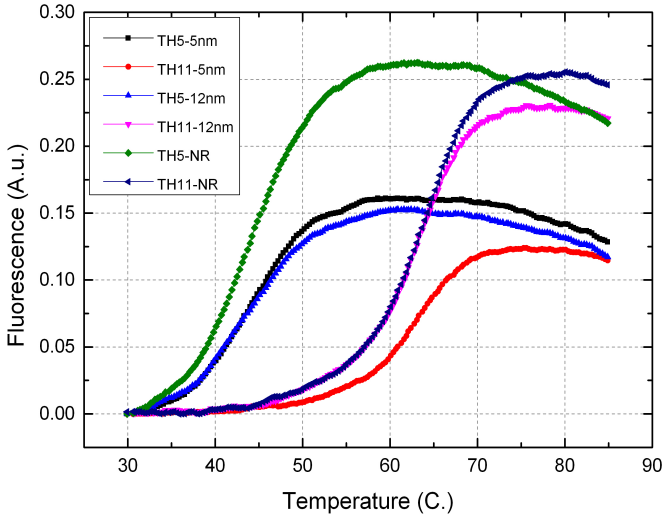

Figure 4.5: *Melting curves of nanomachines with different gold nanostructures as quencher; The conjugation has been performed using 5 nm and 12 nm gold nanoparticles and nanorods.*

It is possible to notice that the NR have the highest s/n among all the combination. On the contrary, due to their size, NR may not be the best choice in the design of a sensor for intracellular activity. As we described in chapter 3 part I, the internalization of the molecular beacon inside cells is a process dominated by diffusion. Therefore the large physical dimension of the NR, could inhibit an efficient transfection. Jin et al [6] pointed out the effect of gold nanoparticles of increasing size on the melting curve of linked oligonucleotides. They report that the FWHM of the first derivative of the melting curve was going from 0.5 °C for a 50 nm GNP to 2.5 °C for a 13 nm GNP, i.e. the curve was getting steeper with increasing size of the GNP attached. In fig.4.5 the NR, which are the largest nanostructured, exhibit a steeper curve, confirming the reported results.

Nanomachine with different hairpin backbone structure

We conjugated molecular beacons with hairpin with a different backbone structure. One is a 2´deoxy DNA backbone and the other is 2´methyl RNA backbone. It has been previously reported that the different backbone influence considerably the hybridization kinetics of the molecular beacon [7, 8] and also the lifetime of the probe inside the cellular environment is also greatly affected [9]. In general, 2´methyl RNA provides a fast hybridization

kinetics against RNA target and ensure a longer lifetime than 2´deoxy DNA backbone. The melting curve for TH5, 5 nm and 12 nm is reported in fig.4.6:

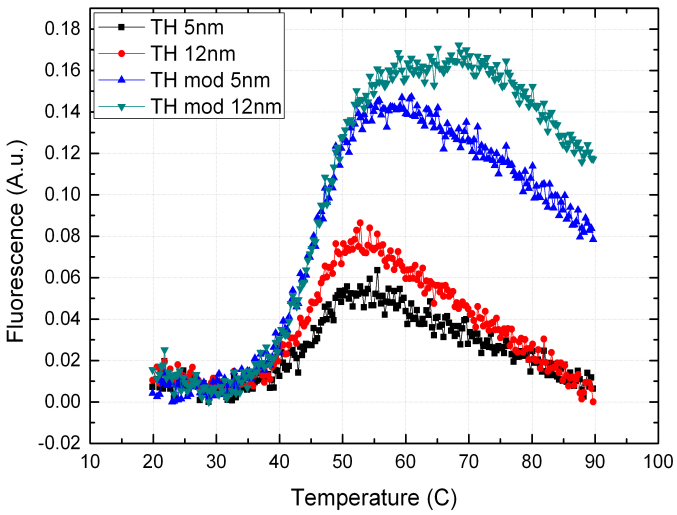

Figure 4.6: *Melting curves of nanomachines conjugated with a different backbone hairpin; 2´deoxy DNA backbone and 2´methyl RNA (referred as mod) backbone conjugated with TH5, 5 nm and 12 nm are presented.*

From the melting curve it is possible to see that the S/N seems better for 2´O-methyl RNA (referred in the picture as "mod"). It is necessary to point out that the two hairpin have a different fluorophore conjugated. 2´-deoxy DNA hairpin is connected with TAMRA while 2´O-methyl RNA is conjugated with Cy3; their emission characteristic is different and a direct comparison of the fluorescence signal cannot be carried on. The difference in maximum signal emission is therefore most likely due to the intrinsic characteristic of the fluorophore emission rather than, for example, differences in conjugation efficiency. The decreasing signal occurring during temperature increase is also an effect due to the fluorophore characteristic; Liu et al [10] report that the emission intensities of common labelling agents such as rhodamine Red, TAMRA and Cy3 at 10 °C drop up to 60% when the temperature reaches 80 °C.The melting temperature of the stem is influenced as well by the chemical composition of the oligonucleotides backbone with a decreasing value for 2´O-methyl RNA. The difference is relatively small because there are only 5bps involved in the stem formation.

Melting curves of BHQ-2 conjugated molecular beacons

With regard of supporting the analysis on RF activation of gold conjugated MBs, DNA backbone MBs with the same nucleotide sequences conjugated with TAMRA to the 5´end but with black hole quencher (BHQ-2) to the 3´end, instead of the gold nanoparticle,were purchased from Biomers.net GmbH. The melting curves obtained for TH5 and TH11 beacons (with same T-spacer combination) are shown in the fig.4.7. The behavior of the beacons is similar to the one of the nanomachines, the melting temperature is decreasing with increasing length in the T-spacer, but on the contrary, the influence on the maximum signal and, therefore, on the S/N is stronger. Especially for beacons with 5bps stem, the increase in maximum signal is more marked for higher stemÂ´s length conjugation. Beacons with a large stem on the other hand show a drop when conjugated with a long T-spacer.

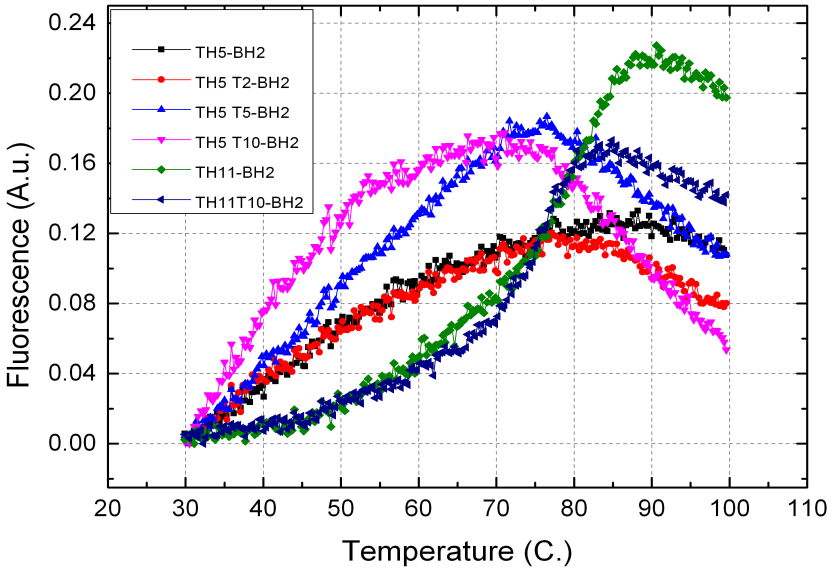

Figure 4.7: *Melting curves of BHQ2-conjugated beacons with different T-spacer length; the increase in the length of the T-spacer lowers the melting point in the 5bps stem configuration and have higher impact on the s/n than seen in nanomachines.*

4.4 Hybridization Curves

When in presence of their complementary oligonucleotide strand target, the hairpin of the nanomachine hybridizes and undergo a conformational change

that displace the fluorophore from the quencher and allow emission of fluorescence(Fig.4.3C). The 12 nm nanomachine and BH2-beacons were incubated with the same concentration of complementary target between 30 °C and 39 °C for 1hour. The resulting hybridization fluorescence was compared with the measured signal coming from samples without complementary target; The hybridization curves of TH5 and TH11 only are reported here as representative of the behavior of the different groups (i.e. different stem length). In the curves of the BHQ2-beacons it is possible to see that signal from unhybridized TH5 increases with temperature while the hybridized TH5 decreases(Fig.4.8A). This fact can be explained in sight of the low melting point of that particular beacon, when temperature approaches the value of 37 °C (see consideration and values in fig.4.7), some of the beacons in the closed state (i.e. the hairpin structure, where the stem keeps fluorophore and quencher together) are starting to melt to the random coil configuration , causing an increase in the fluorescence emission. In the same way, some of the complementary targets from the hybridized beacons are starting to detach, causing the beacon to return to the hairpin configuration and therefore decreasing the intensity of emission. TH11 beacons show a little increase in fluorescence emission in presence of complementary target, even though this increment is much lower than in TH5 beacons. This phenomena is due to the high energy of the hairpin configuration ensured by the 11bps stem that competes with the annealing of the complementary target.

The experiment was repeated for gold-conjugated NMs (Fig.4.8B). With the complementary target present the 5bps nanomachines show a clear increase in fluorescence while no increase in fluorescence emission was detected from the 11bps nanomachine. As opposed to the BHQ2 beacons, the presence of gold nanoparticle seems to play an important role in the stability of the hairpin configuration, avoiding the NM to hybridize.

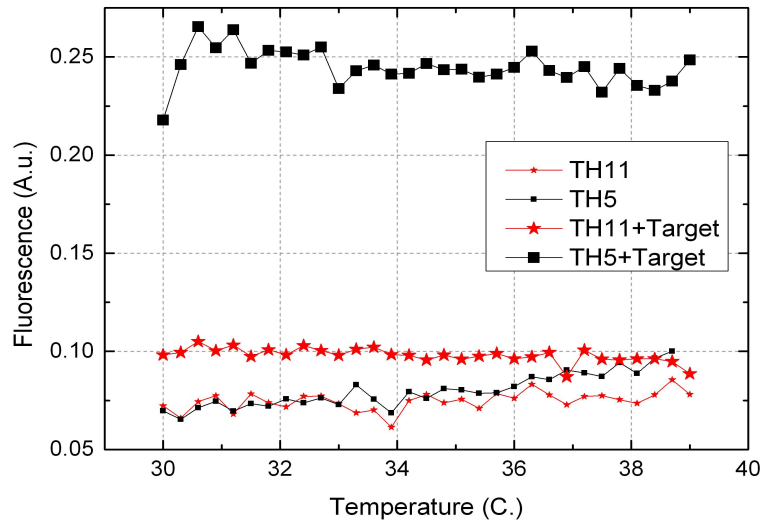

(a) Gold-Conjugated Nanomachines

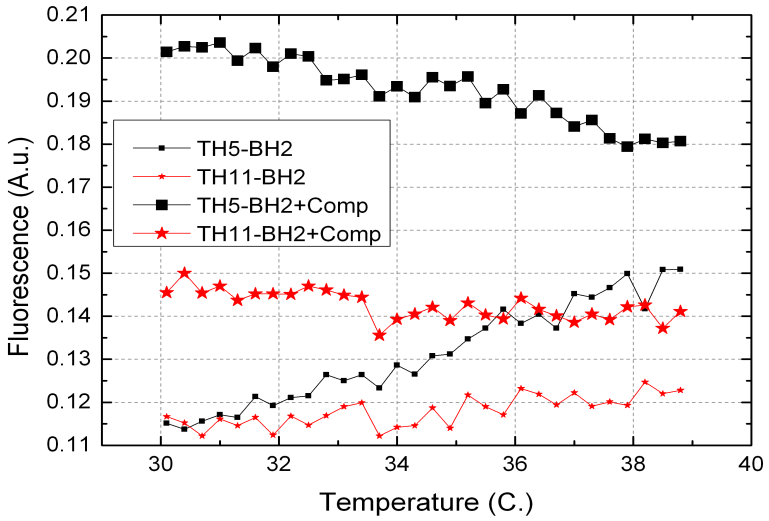

(b) BH2-Conjugated Beacons

Figure 4.8: *Hybridization curves of MBs and NMs, small symbols for unhybridized sample, big symbols for hybridized one.*

4.5 Conclusion

In conclusion, 5bps configuration responds positively to its complementary target and, among the different configuration of T-spacer, TH5 has the highest melting point. Regarding the nanostructure, we chose to perform the experiment with 12 nm gold nanoparticles because part of the protocols (i.e.

oligonucleotides concentration and purification) were optimized for that parameter.

Bibliography

[1] T. Nagatsu, Essays Biochem., **1995**, vol. 30, pagg. 15-35.

[2] K. E. Goodwill, C. Sabatier, C. Marks, R. Raag, P. F. Fitzpatrick, e R. C. Stevens, Nat. Struct. Biol., **1997**, vol. 4, n. 7, pagg. 578-585.

[3] A. Jayagopal, K. C. Halfpenny, J. W. Perez, e D. W. Wright, *Hairpin DNA-Functionalized Gold Colloids for the Imaging of mRNA in Live Cells*, **2010**, J. Am. Chem. Soc., vol. 132, n. 28, 9789-9796.

[4] D. S. Seferos, D. A. Giljohann, H. D. Hill, A. E. Prigodich, e C. A. Mirkin, *Nano-Flares: Probes for Transfection and mRNA Detection in Living Cells*, **2007**, J. Am. Chem. Soc., vol. 129, n. 50, 15477-15479.

[5] A. E. Prigodich, P. S. Randeria, W. E. Briley, N. J. Kim, W. L. Daniel, D. A. Giljohann, e C. A. Mirkin, *Multiplexed Nanoflares: mRNA Detection in Live Cells*, **2012**, Anal. Chem., vol. 84, n. 4, 2062-2066.

[6] R. Jin, G. Wu, Z. Li, C. A. Mirkin, e G. C. Schatz, *What controls the melting properties of DNA-linked gold nanoparticle assemblies?*, J. Am. Chem. Soc., **2003**, vol. 125, n. 6, 1643-1654.

[7] A. Tsourkas, M. A. Behlke, e G. Bao, *Hybridization of 2´O-methyl and 2´deoxy molecular beacons to RNA and DNA targets*, Nucl. Acids Res., **2002**, vol. 30.

[8] N. Nitin, W. J. Rhee, e G. Bao, *Translation inhibition reveals interaction of 2´deoxy and 2´O-methyl molecular beacons with mRNA targets in living cells*, Nucleic Acids Research, **2009**, vol. 37, n. 15, 4977-4986.

[9] M. Majlessi, N. C. Nelson, e M. M. Becker, *Advantages of 2´O-methyl oligoribonucleotide probes for detecting RNA targets*, Nucleic Acids Res., **1998**, vol. 26, n. 9, 2224-2229.

[10] W.-T. Liu, J.-H. Wu, E. S.-Y. Li, e E. S. Selamat, *Emission Characteristics of Fluorescent Labels with Respect to Temperature Changes and Subsequent Effects on DNA Microchip Studies*, Appl. Environ. Microbiol., **2005**, vol. 71, n. 10, 6453-6457.

Chapter 5

Nanomachine Activation

5.1 Introduction

This chapter will be focused on the activation of the nanomachines through a RF field. First of all the effect of the field on the sample solution will be evaluated, studying the dielectric heating generated upon irradiation. This study will rule out the possible activation of the nanomachine by means of bulk heating. Thereafter, the nanomachines will be exposed to a RF field and their fluorescence emission will be measured over time. The increase in fluorescence emission demonstrates the possibility of remote activation of the nanomachine by an external field.

5.2 Dielectric heating - Experimental setup and results

5.2.1 Dielectric heating - Solution sample

In order to test the effect of a RF field on the GNPs solution, we developed a small microfluidic setup to monitor the temperature increase over the RF exposure time. The system in Fig.5.1 comprises a microfluidic PMMA chip with inlet and outlet channels and a sealed chamber for sample handling. Another side channel allows to insert a small thermocouple directly in the sample chamber. The thermocouple channel is sealed thereafter by casting PDMS and curing overnight at 60 °C. On top of the sample chamber, not directly in contact with its surface to avoid heat exchange, sits a small printed circuit board (PCB) with a coil matched at the frequency of 3 GHz using an adjustable capacitor.

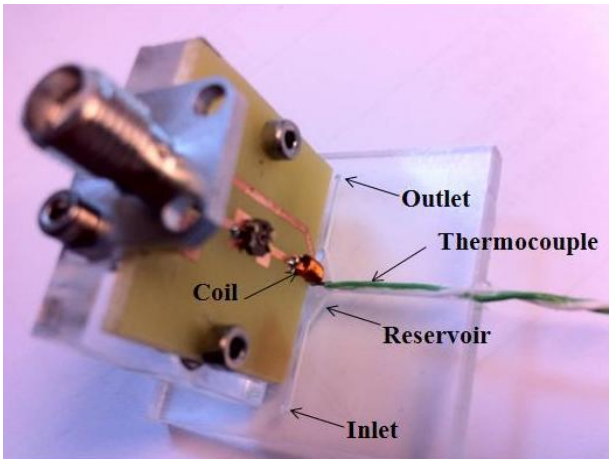

Figure 5.1: *Experimental setup for dielectric heating investigation. The thermocouple (green cable) is inserted in the reservoir and sealed with PDMS. The reservoir is in close proximity (not contact) with a small coil connected through a PCB to the signal generator.*

The samples are injected in the chamber and irradiated with an RF field generated by the coil antenna at the matched frequency. The signal was produced by a signal generator Agilent N5181A MXG and amplified with Mini-Circuits ZHL-16W-43+ high power amplifier (45 dB power gain). The result during 60 seconds irradiation is shown in fig.5.2:

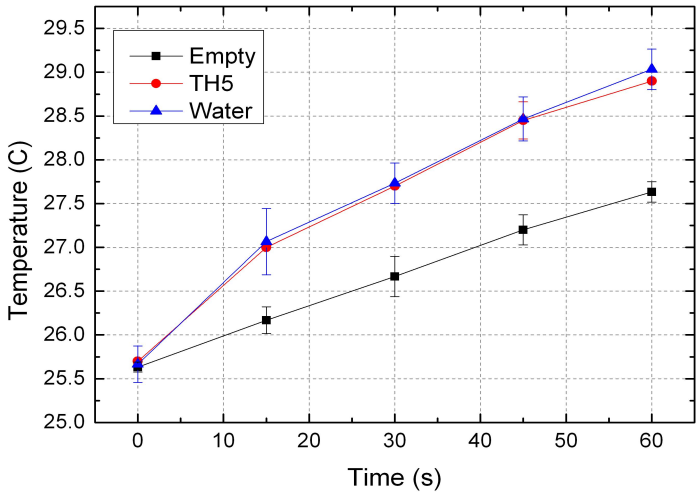

Figure 5.2: *Temperature increase during RF exposure in the empty setup, i.e. empty sample chamber with thermocouple inside (black curve),with the Nanomachine solution (red curve) and with the water buffer (blue curve) for irradiation at 40dBm at 3 GHz.*

The empty system, i.e. with the thermocouple present but the chamber

not filled, was exposed to an RF field for 1 minute generated by a small coil at 3 GHz and $P_w = 40$ dBm (-5 dBm generated by the signal generator and amplified by 45 dB by the solid state amplifier). The temperature inside the chamber only increased by 2 °C. A solution containing water alone or water with TH5 conjugated NMs was injected in the sample chamber and exposed to the same RF power and time. The water and the water with GNP heated to the same extent and the temperature increased considerably more that of the empty chamber (~ 4 °C), but it is impossible to discriminate between the two. The final temperature after RF treatment was about 29 °C and that is not sufficient temperature to melt NMs using a 5bps stem (See melting curve of the gold conjugated nanomachines). However, the dielectric heating of the water/gold nanoparticle was significant and must be taken into consideration when measuring on living cells surrounded by a water based medium in order to not induce heat shock responses by the bulk heating.

5.2.2 Dielectric heating - Ice melting

We performed a similar experiment in a different setup. Water, PBS and NMs diluted in PBS were frozen in a small cubic sample holder made of PMMA with direct insertion of a thermocouple in the frozen sample. This was done in a similar way as in the setup previously described for the other dielectric heating experiment. Subsequently the frozen sample was exposed to an RF field generated by a wideband monopole antenna. A layer of polystyrene was inserted between the monopole antenna and the sample chamber to ensure that the joule heating coming from the antenna itself was not affecting the measurements. The temperature rise was monitored over time by the thermocouple inserted inside the frozen sample and measurements are shown in fig.5.3. The graph shows a typical trend corresponding to a phase change in which the temperature rises rapidly until it reaches 0 °C, then there is a plateau in the temperature profile corresponding to the phase change from ice to liquid and finally another rapid temperature rise. Under RF excitation the temperature rise was faster, but, as shown in the previous experiment, it was impossible to discriminate between the three samples. The data corroborates previous conclusions [1,2], that the main source of bulk heating in a solution of gold nanoparticles under RF excitation is by the absorption in the medium itself.

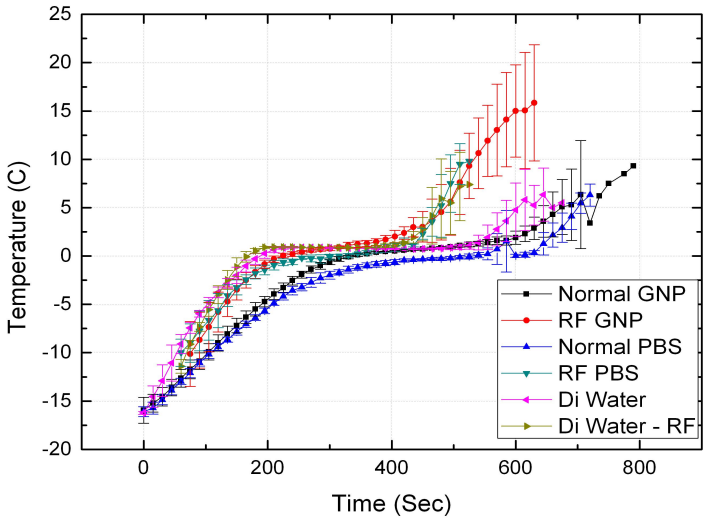

Figure 5.3: *Temperature rise of frozen samples with and without a RF field. The graph display mainly two curve populations, the RF exposed samples in which ice melting is completed after around 400 s and the same samples not exposed to RF in which the transition is completed after around 600 s.*

5.3 Dielectric Heating - Discussion

In addition to Maxwell's equations the materials equations $\mathbf{J} = \sigma\mathbf{E}$, $\mathbf{B} = \mu_0\mathbf{H}$, and $\mathbf{D} = \varepsilon_\mathrm{r}\varepsilon_0\mathbf{E}$, where μ_0 is the permeability ε_0 the permittivity of free space, σ is the conductivity, while ε_r is the relative permittivity of the dielectric material, are used in a description of electromagnetic waves. In a lossy dielectric, the relative permittivity is a complex number $\varepsilon_\mathrm{r} = \varepsilon'_\mathrm{r} - \mathrm{i}\varepsilon''_\mathrm{r}$, and both the real and imaginary parts are in general dependent on the angular frequency ω, which becomes explicit by considering the relaxation time model (Debye model) of a lossy dielectric

$$\varepsilon_\mathrm{r} = \varepsilon_\mathrm{h} + \frac{\varepsilon_\mathrm{s} - \varepsilon_\mathrm{h}}{1 + \mathrm{i}\omega\tau},$$

where τ is the relaxation time, ε_s is the low frequency permittivity while ε_h is the very high frequency permittivity.

Since the nanoparticles or nanomachines are dispersed in an electrolyte solution contained in a polymer microsystem the time varying electric field will induce some dielectric heating of the liquid and polymer, since these are lossy dielectrics. The loss power density may be estimated using the total electric current density, which is the sum of the conduction and the displacement current densities

$$\mathbf{J}_\mathrm{t} = \sigma_\ell\mathbf{E} + \frac{\partial\mathbf{D}}{\partial t} = \sigma_\ell\mathbf{E} + \mathrm{i}\omega\varepsilon_\mathrm{r}\varepsilon_0\mathbf{E} \tag{5.1}$$

where σ_ℓ is the conductivity of the liquid. The time average dissipated power density p_w is then

$$p_w = \frac{1}{2}\,\mathrm{Re}\left(\mathbf{J}_\mathrm{t}\cdot\mathbf{E}^*\right) = \frac{1}{2}\left(\sigma_\ell + \omega\varepsilon''_\mathrm{r}\varepsilon_0\right)E^2 \underset{\omega\gg\sigma_\ell/\varepsilon''_\mathrm{r}\varepsilon_0}{\rightarrow} \frac{1}{2}\omega\varepsilon''_\mathrm{r}\varepsilon_0 E^2 \tag{5.2}$$

where the star indicates complex conjugation. At high frequencies ($\omega \gg \sigma_\ell/\varepsilon''_\mathrm{r}\varepsilon_0$), the power dissipation due to finite conductivity becomes insignificant compared to that due to dielectric losses and the simplified expression on the righthand side may be used.

It follows that the imaginary part of the dielectric function is essential for estimating the dielectric losses, and for water the Debye parameters are $\varepsilon_\mathrm{h} = 4.5$, $\varepsilon_\mathrm{s} = 78.3$, and the characteristic frequency $f_c = 1/(2\pi\tau) = 19.5$ GHz [3]. In Fig. 5.4 the two components of the dielectric function of water are plotted as a function of frequency, and in Fig. 5.5 the ratio $\varepsilon''_\mathrm{r}/\varepsilon'_\mathrm{r} \equiv \tan\delta$ is plotted. Obviously water is a very lossy dielectric in the GHz range. Also the PMMA material used in the for fabrication of the microsystem is a lossy dielectric. The permittivity of PMMA is 2.61, while the loss tangent is approximately 0.01 [4] . Obviously, the loss due to the PMMA material are much smaller than that due to water.

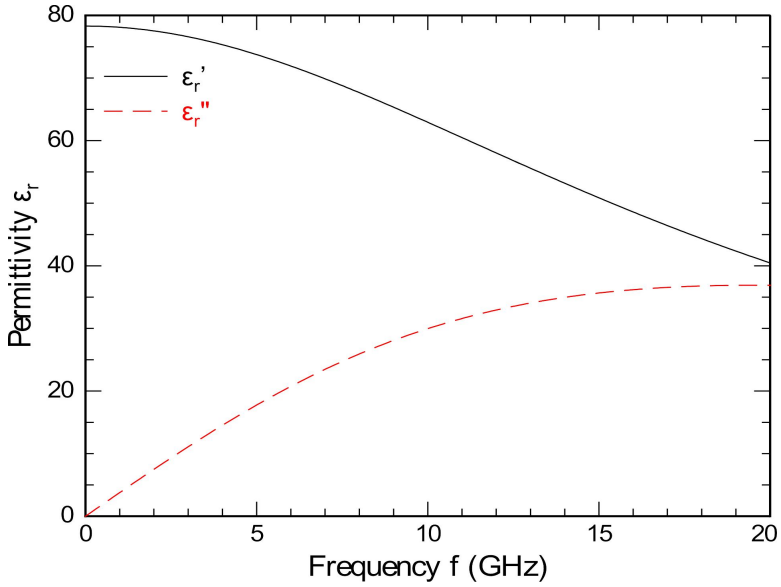

Figure 5.4: *Dielectric function of water calculated using the Debye model. The real value* ε_r' *is shown in the black curve while the imaginary part* ε_r'' *is shown in the red dashed curve.*

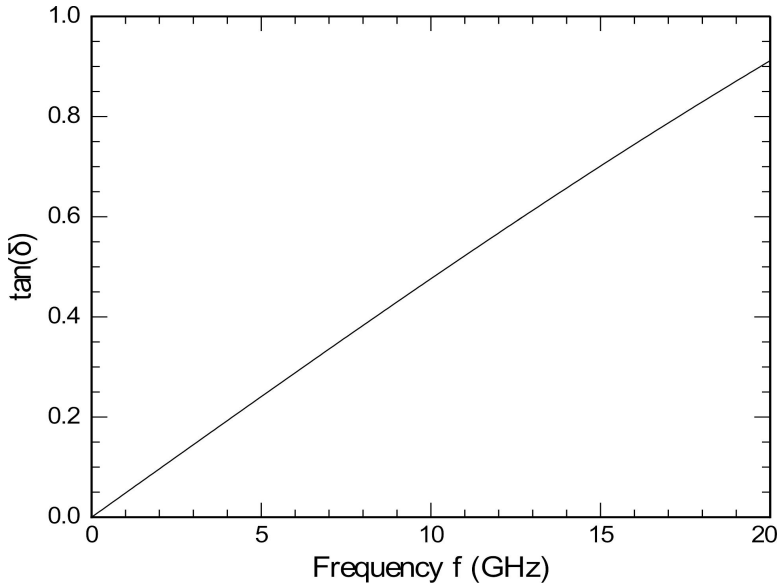

Figure 5.5: *The loss factor* $\tan\delta$ *of water as a function of frequency.*

5.4 Nanomachine Irradiation - Material and Methods

To test the fluorescence response of the nanomachine to the RF field, we developed a combined setup that integrates a coil (Coilcraft, Cumbernauld) for field generation with a sample holder. The signal was generated by an analog signal generator Agilent N5181A MXG and sent to a solid state linear amplifier ZHL-16W-43+ from Minicircuits, through a circulator that dissipates the reflected wave on a 50 Ω load to avoid instrument damage. The sample platform can be placed directly inside the microscope chamber for direct fluorescence measurements. For safety reasons, we fabricated a compact Faraday cage that wrap around the entire system and shield the external equipment from the radiation field [Fig.5.6]; the antenna for field generation was designed to have the same characteristic frequency as the one used in the dielectric heating experiment.

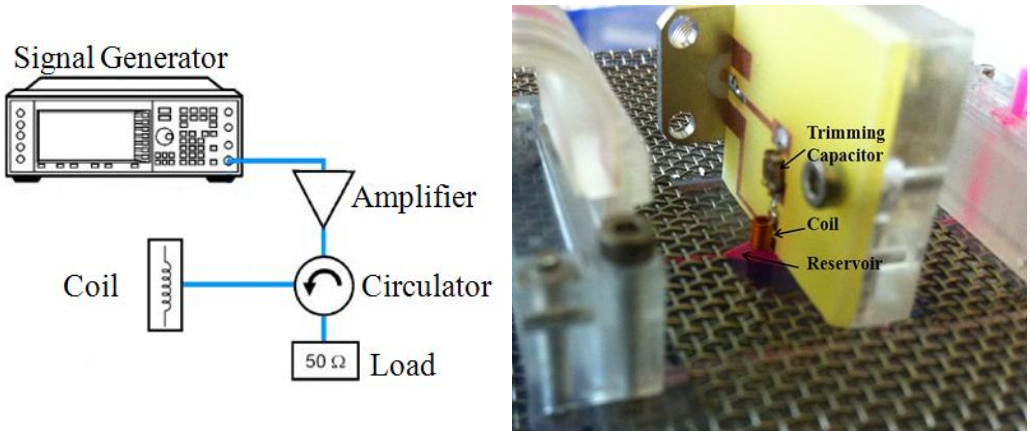

Figure 5.6: *Experimental setup for fluorescence measurement, schematic drawing (left) and real setup (right); the chamber is filled with a colored dye to highlight the structure. The coil and the PCB have the same structure when used in the dielectric heating experiment.*

5.5 Nanomachine Irradiation - Results and discussion

A solution of TH5 nanomachines NMs was injected in the sample holder chamber and exposed to an RF field generated by a small coil at 40 dBm for 15 seconds, the same power as used in the dielectric heating experiment above. The samples were considered to be at room temperature (25 °C)

at the start of the experiment and maximally heated by bulk heating to about 27.5 °C [see fig.5.2]. Figure 5.7 shows a 3D map of the fluorescence emission before (left) and after (right) the RF irradiation of a MB cluster. The nanomachines were clustering in various locations of the sample chamber and the specific point chosen, showed a high concentration of MB's, and was representative for the entire sample area.

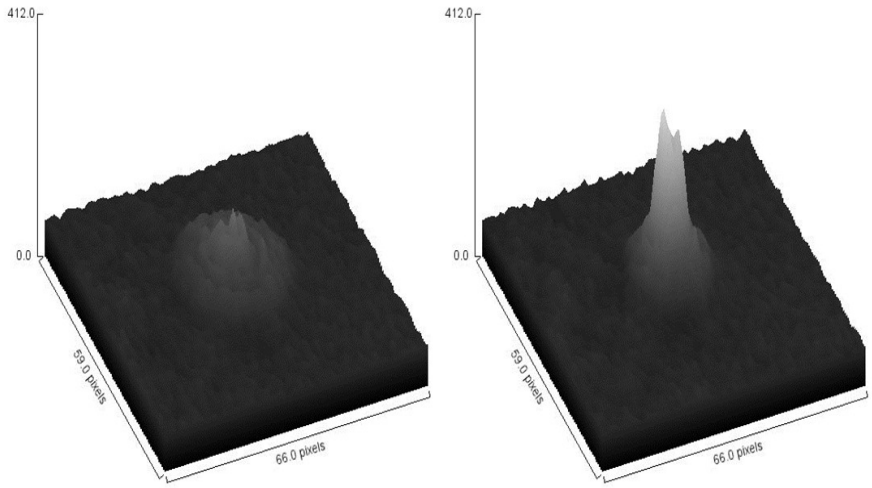

Figure 5.7: *3D map of fluorescence emission of solution of gold-conjugated molecular beacons before (left) and after (right) RF irradiation for 15 seconds. The images were taken at a representative spot in the sample chamber.*

The images show a significant increase in fluorescent emission after RF irradiation. The bulk temperature increase alone was not enough to induce such an effect. In order to verify that RF activation of the gold nanoparticles was the key to the signal rise, we conjugated nanomachines composed of the same DNA sequence (loop and stem) but with the gold quencher substituted with an organic one (back hole, BHQ2). The 3D fluorescence maps for a BHQ2-nanomachine solution before and after exposure to the same RF field show no increase in fluorescence after RF exposure [Fig.5.8]. This confirms that the signal increase seen with the gold NMs after RF exposure is not related to the bulk temperature increase but to localized heating around the GNP.

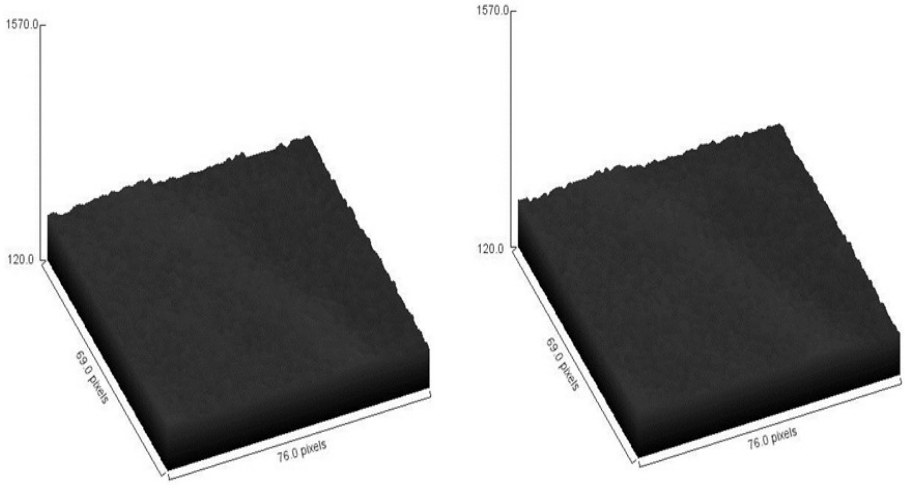

Figure 5.8: *3D map of fluorescence emission of solution of BHQ2-conjugated molecular beacons before (left) and after (right) irradiation. The image was taken at a representative spot in the sample chamber.*

Next, we irradiated a sample of TH5 GNP-conjugated probes for 1 min and measured fluorescence over time [Fig.5.9]. Without RF irradiation the fluorescent emission is was stable with time, but during with RF irradiation the emission increases significantly with time.

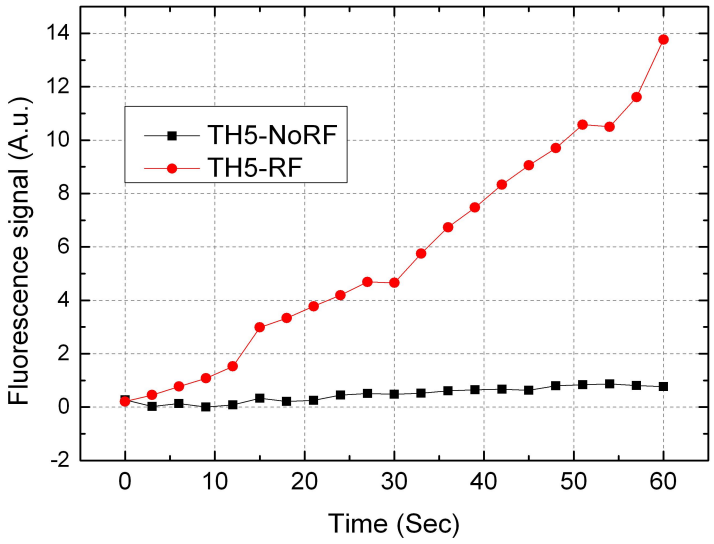

Figure 5.9: *Integrated value of the fluorescence emission over time for TH5 NMs. Black squares show emission without and red dots with RF irradiation. The integrated value of the fluorescence emission of the entire sample chamber was quantified for each time point.*

Because, as previously shown, the dielectric heating was minor while the fluorescence of GNP conjugated MB was significant, we speculate that the fluorescence increase is due to a local increase of temperature around the GNP.

Bibliography

[1] Li, D. et al. J Colloid Interface Sci, 2011, 358, 47-53.

[2] Liu, X., Chen, H., Chen, X., Parini, C. Wen, D. Nanoscale, 2012, 4, 3945-3953

[3] E. Sassaroli, K. C. P. Li, B. E. O'Neill, *Radio frequency absorption in gold nanoparticle suspensions: a phenomenological study*, J. Phys. D: Appl. Phys., **2012**, vol. 45, n. 7, 075303.

[4] B. Riddle, J. Baker-Jarvis, e J. Krupka, *Complex permittivity measurements of common plastics over variable temperatures*, IEEE Transactions on Microwave Theory and Techniques, **2003**, vol. 51, n. 3, 727-733.

Chapter 6

Conclusion

We have successfully conjugated GNPs with single stranded DNA in order to create a sensor for mRNA recognition. The so-called Nanomachine was tested through melting curves and hybridization curves. The nanomachines were then activated by means of a RF field generated by a small coil and we showed that an increase in fluorescence emission results for GNP-conjugated machines with 5bps stem length. The negative control experiment, where the GNPs were replaced by organic quenchers, showed no significant increase in fluorescence emission. The quantification of the fluorescence emission from figure 4.9 compared to the fluorescence emission of the NM calculated using the melting curve in figure 4.7 left, indicates a temperature rise up to 44.5 °C. This value, even if much higher than that calculated theoretically, might not be sufficient to perform tasks like resetting hybridized molecular beacons, for which, a temperature increase up to 60 °C would be needed. We found a significant bulk heating caused by RF absorption in the buffer solution, and that is crucial in specific applications, for example when living cells are involved. This issue on the other hand, could be tackled in many ways, for example by setting up a perfusive flow that continuously replace the heated buffer, and thus carry away the excessive heat. We have also shown that it is possible to detect the presence of GNPs dissolved in solution using a simple setup comprising a coplanar waveguide. We pointed out that, even though the calculated temperature increase is not sufficient to explain the effects we have shown, numerous size effect, not accounted for, could play a crucial role in understanding the behavior of GNPs heat dissipation under RF irradiation. Our conclusion is that further studies are necessary to investigate the phenomena of heat generation and dissipation at the nanoscale in order to solve the discrepancy between theory and experimental results, but our results indicates that the heat generation around gold nanoparticles might not be sufficient for applications in which a high temperature increase needs

to be achieved.

Part III

Appendixes

Nanomachine based optical sensors

P. Della Vedova, M.Ilieva, O.Hansen and M.Dufva.

Introduction

Molecular beacons (MBs) are powerful biological probes that exhibit high selectivity and affinity and can be easily fabricated [1]. One of the major limitations of these probes is the inability to be restored to the sensing state after a hybridization reaction. Sensor regeneration is critical for online sensing.

Here we present a novel MB configuration, comprising a gold nanoparticle (GNP) acting simultaneously as a fluorescence quencher [2] and an actuator (nanosized heater) which is controlled remotely by an external microwave field [3]. Localized heating allows for control of the structure and chemical state of the MB. The novel gold-based MB nanomachine will allow regeneration and calibration of MB by melting hybridized targets off the machine. (Fig.1, left)

Materials and Methods

Gold nanoparticles are conjugated through an aminogroup to a MB having a flourochrome at the opposite end. MBs designed this way are carefully characterized by melting and hybridization curves to ensure optimal functionality (Fig. 2,B). Stem cells are transfected with these MBs and cultured in a custom made microfluidic system that includes an actuation coil and enables simultaneous observation of the fluorescence signal under the microscope (Fig.1, right).

Results

The interaction between the EM field and GNPs creates eddy currents on the surface of the metal particle, which becomes a highly localized point source of heat. Our simulations show that the heat is highly localized in the particle surroundings and the heat dissipates within 1-2 particle radii (Fig.2, A).

Our experiments show an increase in fluorescence after irradiation of the MBs (Fig2, C-D).

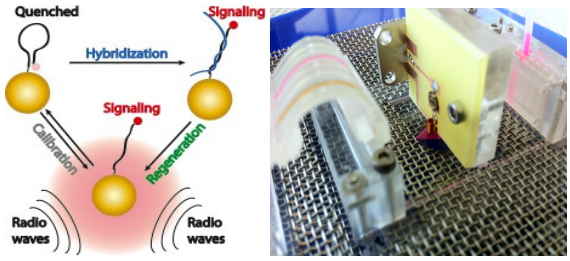

Fig. 1. Working principle of the nanomachine (left) and close-up of the microfluidic setup used in the experiment (right).

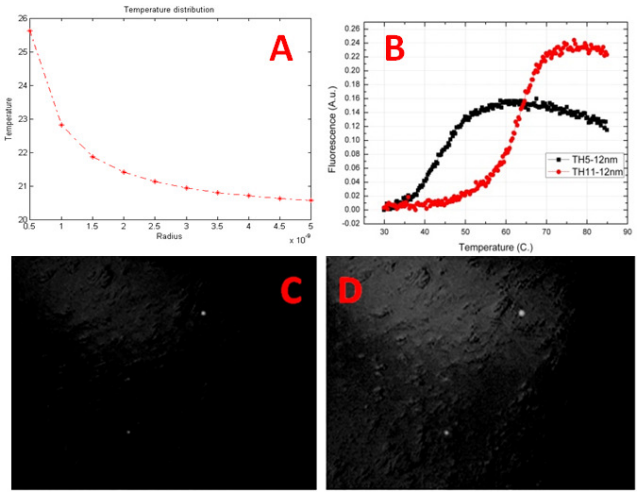

Fig. 2. (A)Temperature distribution around the nanoparticle, (B) melting curves of MB, (C-D) Fluorescence signal before (left) and after (right) irradiation.

The increase in fluorescence could be explained by the selective heating of the GNPs that causes melting the stem of the MB and therefore a displacement of the fluorophore quencher pair (Fig1. right).The control experiment has been performed using the same setup with a different kind of MBs in which the gold nanoparticle has been replaced by an organic quencher. In this case, no increase in fluorescence signal has been detected after irradiation with the EM field. Irradiation tests performed on liquid solutions containing different salt concentrations, show that bulk heating of the medium is not sufficient for MBs melting.

This tool opens new possibilities such as following down regulation of gene expression in living cells, something that cannot be done today because of technical limitation.

Manuscript received August 10, 2012. This work was supported by FTP grant number 09-070568.

P. Della Vedova, M. Ilieva, O. Hansen and M Dufva are with DTU Nanotech, Kgs.Lyngby, DK-2800, Denmark(phone: +45258159; e-mail: pdve@ nanotech.dtu.dk).

References

[1] S. Tyagi et al., «Molecular beacons: Probes that fluoresce upon hybridization», *Nat. Biotechnol.*, vol. 14, n°. 3, pagg. 303–308, Mar 1996.

[2] Lakowicz, J. R. *Principles of Fluorescence Spectroscopy,* 2nd ed.; Springer: New York, 1999.

[3] K. Hamad-Schifferli, et al., «Remote electronic control of DNA hybridization through inductive coupling to an attached metal nanocrystal antenna», *Nature*, vol. 415, n°. 6868, pagg. 152–155, Gen 2002.

Molecular beacon technology based sensor for real-time detection and tracking neural stem cell differentiation

Mirolyuba Ilieva, Paolo Della Vedova, Martin Dufva

Introduction

Molecular beacon (MB) technology is based on fluorescent resonance energy transfer (FRET) and complementary pairing principles. A stem-loop forming oligonucleotide with fluorochrom on one side and quencher on the other is a highly specific and sensitive sensor which can be introduced inside living cell. Hybridizing with specific target "closed" MB became in "open" state when the fluorescent dye and quencher separate and signal occurs. [1] Thus, it allows detection and monitoring of gene expression and following fundamental cellular events like differentiation, regeneration, and cancer genesis.

Materials and Methods

Molecular beacon probes for stem cell marker Sox 2, marker for differentiated neurons Tyrosine hydroxylase (TH) and house-keeping gene GAPDH were design and synthesized as DNA oligos or 2'-O-methyl RNA backbone and stem length of 5 bp.

Human mesencephalic cell line (LUHMES) were grown adherently on Matrigel or as neurospheres on fibronectin in medium containing bFGF. They can differentiate into morphologically and biochemically mature dopamine-like neurons. MBs were derived inside cells by Streptolysin O based membrane permeabilization [2]. 24 h after transfection of MB, growth medium was switched to differentiation medium. Gene expression was detected on different time points after transfection by fluorescent microscopy.

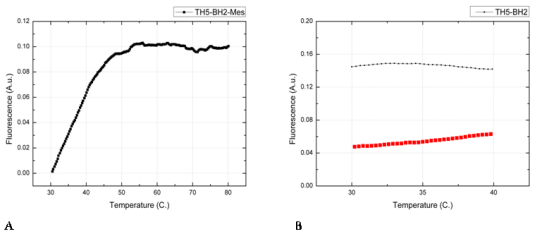

Fig 1. A. Melting and B. Hybridization curves of BHQ2/TAMRA DNA molecular beacon, 5 bp stem length.

Manuscript received August 10, 2012. This work was supported in part by the FTP project 09-070568. M.I, P. D. V., and M. D. are with with the DTU Nanotech, Technical University of Denmark, Oersted Plads, Building 345B, Kgs. Lyngby, DK-2800, Denmark e-mail: miil@nanotech.dtu.dk

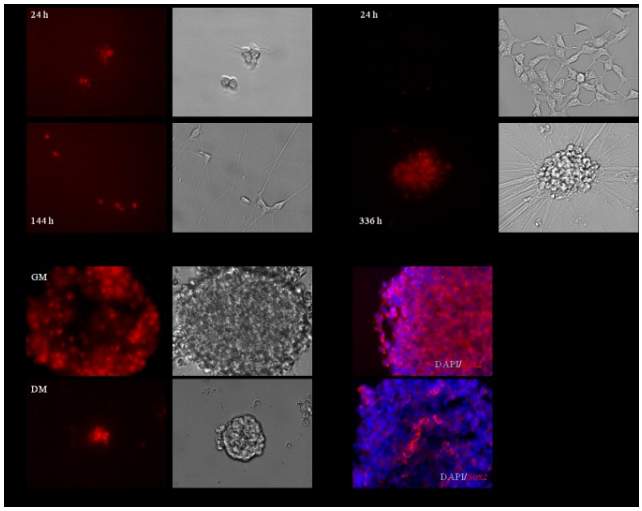

Fig 2. Detection of gene expression inside living cells. A. GAPDH – house-keeping gene with constant expression. MB – DNA/Texas red/BHQ2. B. Tyrosine hydroxylase (TH) – marker for specialized neural cells. Expression increasing upon differentiation. MB - 2'-O-methyl RNA backbone/Cy3/BHQ2. C. Sox 2 expression in neurospheres. Neural stem cells are localized in the center of the neurosphere. MB – DNA/Texas red/BHQ2. D. Immunostaining for Sox 2.

Results

A two-fold increase in the signal in the presence of the complementar oligo was detected (Fig 1B). A melting point of the stem of 40°C verifies that spontaneous opening of MB is not occurring inside the cells (Fig. 1A). The signal inside living cells is detectable 1 h after transfection and it is stable for up to 14 days. The MBs sensors were able to track gain-of expression of neural marker TH and loss-of-expression of stem cell marker Sox2, whereas house-keeping gene expression remains constant (Fig. 2). This suggests that the MBs can "regenerate" from open hybridized state to closed non-hybridized state inside cell. The gene expression change recorded with molecular beacon was confirmed by qPCR and immunostaining for the expression on protein level. The results suggest that MBs are simple to use sensors inside living cells and will be useful for studying transient and dynamic gene expression.

References

[1] S. Tyagi, FR. Kramer, "Molecular beacons: probes that fluoresce upon hybridization," *Nature Biotechnology,* 1996 Mar; 14(3): 303-8.

[2] A.K. Chen, et al., "Delivery of Molecular Beacons for Live-Cell imaging and Analysis of RNA," J. Gerst (ed.), RNA Detection and Visualization: Methods and protocols, Methods in Molecular Biology, vol 714.

Submitted to small

DOI: 10.1002/smll.((please add manuscript number))

Nanomachines – Gold Nanoparticle Based Sensors Activated by External Radio Frequency Fields

Paolo Della Vedova[1*], Mirolyuba Ilieva[1], Vitaliy Zhurbenko[2], Martin Dufva[1], Ole Hansen[1,3]

[1]Department of Micro- and Nanotechnology, Technical University of Denmark, DTU Nanotech, Building 345E, DK-2800 Kgs. Lyngby, Denmark.
[2]Department of Electrical Engineering, Technical University of Denmark, DTU Elektro, Building 348, DK-2800 Kgs. Lyngby, Denmark
[3]CINF - Center for Individual Nanoparticle Functionality, Technical University of Denmark, DK-2800 Kgs. Lyngby, Denmark.

[*] Prof. A. B. Corresponding-Author, Dr. C. Author-Two
Address line 1
Address line 2, postcode (Country)
E-mail: ((insert))
Dr. D. E. F. Author-Three
Address line 1
Address line 2, postcode (Country)

Supporting Information is available on the WWW under http://www.small-journal.com or from the author.

Keywords: Gold Nanoparticle, Molecular Beacon, RF Field, RF absorption.

Abstract

We report the construction of a novel molecular beacon construct (nanomachine) that can be actuated by a radio frequency (RF) field. The nanomachine consists of the following elements arranged in molecular beacon configuration: (a) a gold nanoparticle that acts both as quencher for fluorescence and a localized heat source, (b) one reporter fluorochrome and (c) a piece of DNA as hinge and recognition sequence. When the nanomachines are irradiated with a 3 GHz RF field the fluorescence signal increases due to melting of the stem of the molecular beacon. This fact may be explained by the creation of eddy current in the gold nanoparticle causing joule heating due to interaction with the RF field. This localized source of heat is able to melt the stem of the molecular beacon, displace fluorochrome from the quencher and, in this way, generate a detectable fluorescence signal. A control experiment, performed using molecular beacons synthesized by substituting the gold nanoparticle by an organic quencher, shows no increase in fluorescence signal when exposed to the RF field. Due to the biocompatibility of the construct and RF treatment, the nanomachines may possibly be used inside living cells. In a separate experiment we show that a substantial increase in the dielectric losses can be detected in a RF waveguide set-up coupled to a microfluidic channel when gold nanoparticles are added to a low RF loss liquid. This work was done in order to shed some light on RF heating of gold nanoparticles, which is a subject of significant controversy in literature.

1-Introduction

Hamad-Schifferli et al.[7] published a way to manipulate the local environment surrounding a gold nanoparticle by an external radio frequency (RF) field. Their study showed that GNPs can be heated by an external RF field. DNA linked to the GNP was able to melt as a function of RF exposure. Consequently, linking molecular beacons (MB) to GNPs would then enable actuation of the molecular beacons by a remote RF field. Such an approach would allow for operations of molecular beacons e.g. inside living cells, which would enhance the analytical properties of MBs to sense mRNA. Examples of operations would be calibration, localization and resetting hybridized molecular beacons to study time dependent measurements of targets for the MBs. Sensing mRNA in real time provides necessary information about temporal gene expression for instance during development.

The activation of gold nanoparticles by RF fields is, however, a highly debated issue. [13] Moran et al [18] reported that 10 nm GNPs dispersed in a solution increase the RF absorption considerably. They report that the bulk temperature of a dispersion of GNPs under the influence of an RF field at 13.56 MHz increases its temperatures by tens of degrees in less than one minute. The exposure to RF at the same frequency as previously reported, caused a pronounced augment in cancer cells death when the samples were loaded with GNPs, both in vitro[20] and in vivo.[17] In contrast, Li et al.[14] and, independently, Liu et al,[15] investigated the bulk heating in solutions of GNPs of different diameter exposed to a RF field at 13.56 MHz. They conclude that no appreciable contribution to the RF energy absorption could be detected from the addition of GNPs. In particular, Li et al. separated the GNPs from the supernatant and found that the same increase in temperature occurred after RF excitation independent of the presence of GNPs. The induced heating in the solution is therefore ascribed to the joule heating of the ionic solution. More recently Hanson et al. [30] carried out a theoretical analysis of the effect of spherical GNPs in enhancing the absorption of RF radiation when dispersed in a medium. Their conclusion is that the produced heating is negligible and cannot explain the effects shown earlier. We have to point out that these papers deals with the macroscopic effect caused by GNP activation. There are a few examples in which the activation of gold nanoparticles is directly related to changes caused in the direct surrounding of the particle itself. Denver et al.[20] conjugated quantum dots (QDs) with 1.4 nm GNPs and measured the fluorescence emission of the QDs after irradiation of the sample solution with a RF field at 1 MHz. As opposed to the control solution of un-conjugated QDs and GNPs, they measured a shift in fluorescence emission compatible with a temperature enhancement of ~7 ºC, while the bulk temperature was unchanged. As previously reported in [7] 1.4 nm GNPs exposed to a 1 GHz field are used to cause selective de-hybridization of DNA strands, which corresponds to an increase of ~13 ºC above ambient temperature for the particular case. Finally, Kogan et al.[16] investigated the nanoparticle mediated local control of protein aggregation under a 12 GHz RF field, to dissolve amyloid deposit of $A\beta_{1-42}$ without formation of bulk heating. To our knowledge a complete theoretical description that supports efficient heat conversion of microwave radiation by GNPs at the nanoscale does not exist, but one hypothesis is that heating is a result of field focusing effect by the nanoparticles instead of the conventional Joule heating model.[21] At present, there seem to be diverging experimental and theoretical understanding of GNP heating. Furthermore, to our awareness, no one has reproduced the results of Hamad-Schifferli et al.

The molecular beacon [5] is a structure constituted of an oligonucleotide strand arranged in a hairpin configuration with a donor-acceptor pair attached. The two ends of the oligo strand are complementary and, below the melting temperature and in absence of target, form a double helix (stem region). The central part is a single stranded sequence designed to recognize a

particular RNA (or DNA) target (loop region). Connected to the two ends of the stem, there is a fluorophore and a quencher, respectively. The working principle is based on Föster Resonance Energy Transfer (FRET),[6] a distance dependent nonradiative energy transfer phenomenon between the donor molecule (fluorochrome) and the acceptor (quencher). The double stranded configuration of the stem forces donor and acceptor to be in close proximity, leading to high efficiency FRET and consequent low emission of fluorescence. When a target strand is hybridized to the loop region, the stem opens, parting the fluorophore from the quencher, reducing the FRET efficiency and consequently increases the emission of fluorescence from the dye. Because of their exclusive characteristic, MBs could resolve the issues of spatial and temporal localization not addressed by standard techniques, such as PCR.[3] The major disadvantages of MBs consist of a higher complexity for cell internalization and instability in cellular environment, particularly due to nuclease cleavage. Gold nanoparticles (GNPs) can also serve the purpose of replacing the organic quencher.[8-10] Studies have shown that the quenching efficiency is enhanced [11] and also that MBs with GNP quenchers have longer lifetime as a result of reduced aggression from nuclease.[12]

In this paper we will experimentally demonstrate the interaction of GNPs with RF fields and if the effects are localized to the GNP or also affects the bulk solute. To study this, we used MB conjugated to GNPs and exposed these constructs to an external RF field. If heat is generated in bulk or localized to the GNP, the MB would linearize and fluoresce. For convenience we denote MB/GNP construct as a nanomachine (NM) since it can have multiple states and possibly be actuated remotely by an RF field or by lasers.[29]

2-Results and Discussion

Gold nanoparticles of 12 nm diameter were conjugated with a single stranded oligonucleotide chain equipped with a fluorophore at one end to form the nanomachine sensor (**Figure 1**) (see material and methods). The loop region of the nanomachine was encoded with a sequence specific for recognition of tyrosine hydroxylase, encoded by the *TH* gene.[22] Tyrosine hydroxylase is an enzyme which tracking is of great importance since it defines a functional neuron, is necessary for the production of dopamine and is involved in disorders such as Segawa's dystonia, Parkinson's disease and schizophrenia.[23]

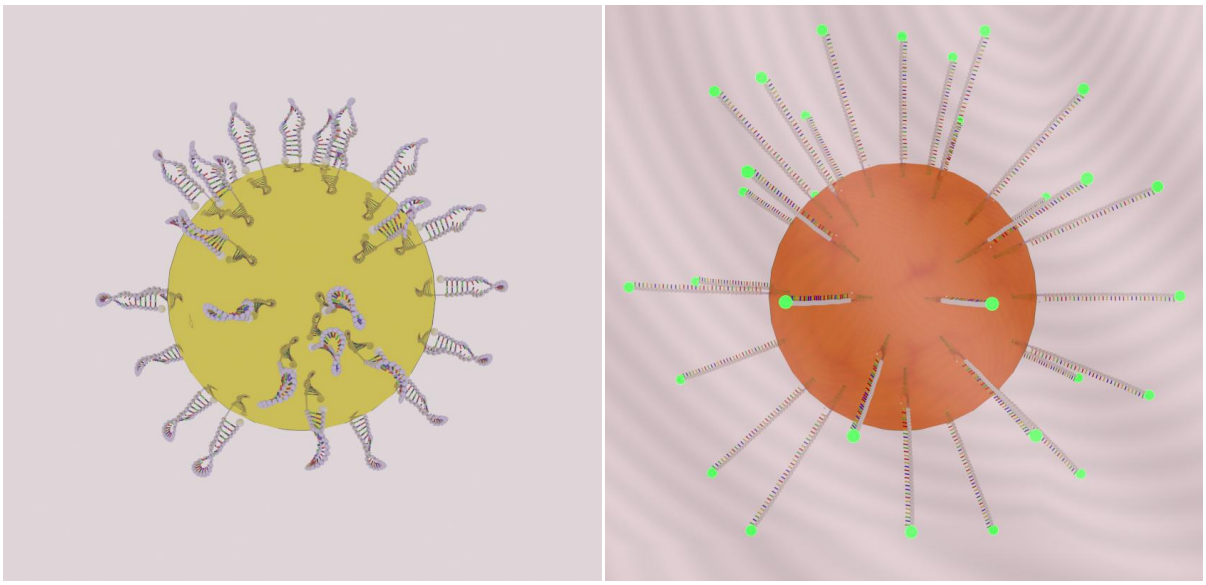

Figure 1. Schematic view of the hairpin functionalized GNPs and the working principle; left, a quenched nanomachine, the stem keeps the fluorophore and quencher together blocking the fluorescence emission; right, in presence of the RF field the nanoparticle heats up and melt the stem of the hairpin, displacing the fluorophore from the quencher.

In order to test the functionality of the conjugated beacons, we characterized their fluorescent emission through a melting profile. The temperature was ramped from 30 °C to 90 °C in steps of 0.3 °C and the fluorescence was measured at every step after 5 minutes [**Figure 2** left].

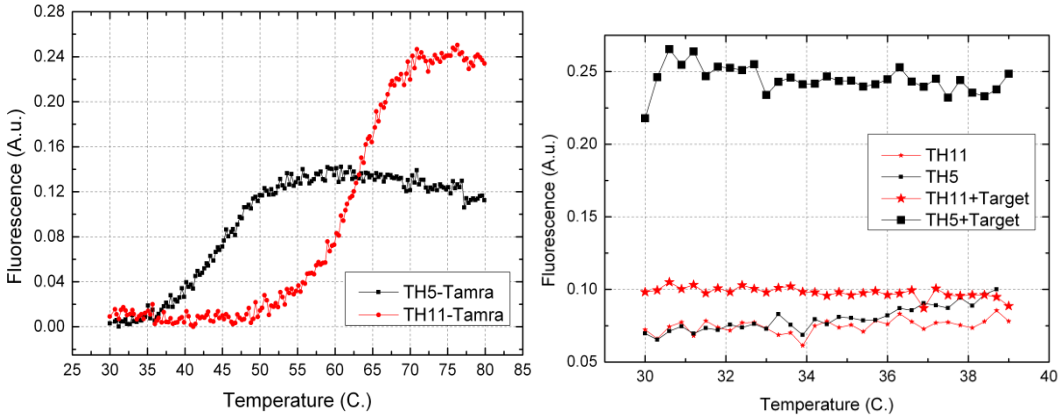

Figure 2.
Melting curves of nanomachines (left). The melting curve of NMs with a 5bps stem is shown in black symbols, while that of NMs with a 11bps stem is shown in red symbols. Hybridization curves of NMs incubated with complementary target (right); small symbols for un-hybridized, large symbols for hybridized nanomachines.

From the melting curves it is possible to estimate the melting point for the different conjugations; nanomachines with 5bps stem melt at approximately 42 °C while nanomachines with 11bps stem, melt at about 62 °C. NMs with an 11bps long stem show higher signal emission probably due to longer fluorophore-quencher distance in the random coil configuration.
The NMs were incubated with their complementary target and the fluorescence profile was recorded over time and temperature (**Figure 2**, right). With the complementary target present the 5bps nanomachines show a clear increase in fluorescence while no increase in fluorescence emission was detected from the 11bps nanomachine. This was expected, since a longer stem suppresses hybridization of the MB to the complementary target and thus the opening of the MB. For this reason we chose to use TH5 nanomachines for further experiments. The melting and hybridization curves obtained for TH5 and TH11 beacons conjugated with the organic quencher BHQ-2 were similar to those obtained with the gold nanoparticles (Supporting information, **Figure S3.1**).

In order to test the effect of a RF field on the GNPs solution, we developed a microfluidic system to monitor the temperature increase over the RF exposure time due to dielectric heating (see supporting info, **Figure S.2.1**). The empty system, i.e. with the thermocouple present but chamber not filled, was exposed for 1 minute to an RF field generated by a small coil at 3 GHz and $P_w = 40$ dBm (-5 dBm generated by the signal generator and increased by 45 dB by the solid state amplifier). The temperature inside the empty chamber did only increase by 2 ºC (Supplementary **Figure S.2.2**). Solutions containing pure water and water with TH5 conjugated NMs were injected in the sample chamber and exposed to the same RF

power and time. The pure water and the water with NMs heated to the same extent and considerably more that the empty chamber (~4 ºC). The final temperature after RF treatment was about 29 ºC and that is not a sufficient temperature to melt NMs using a 5bps stem (Figure 1 and supplementary figure S.2.2). However, the dielectric heating of the water/gold nanoparticle solutions was significant and must be taken into consideration when measuring on living cells surrounded by a water based medium in order to not induce heat shock responses by the bulk heating. We performed a similar experiment in a different setup. Water, PBS and TH5 NMs diluted in PBS were frozen and subsequently exposed to an RF field generated by a wideband monopole antenna. The temperature rise was monitored over time by a thermocouple inserted in the frozen sample (data not shown). Under RF excitation the temperature rise was faster, but, as previously shown, it was impossible to discriminate between the three samples. The theoretical power due to the addition of gold nanoparticles to the solution has been theoretically derived and calculated. The result indicates that the relative power dissipation due to the GNP's compared to the power radiated by the coil is at most $P_{GNP}/P_{rad} = 4 \times 10^{10} \times 2.5 \times 10^{-18} = 1 \times 10^{-7}$which is insignificant compared to a power dissipation due to the dielectric heating of the medium of $0.017 < P_w = P_{rad} < 0.14$ [see supporting info for detailed derivation].These data corroborates previous conclusions,[14] that the main source of bulk heating in a solution of gold nanoparticles under RF excitation is by the absorption of the medium itself and not the GNPs.

In order to test the effective heating of the nanomachines specifically, a solution of TH5 NMs was injected in the sample holder chamber and exposed to an RF field generated by a small coil (see material and methods) at 45 dBm for 15 seconds, the same power as used in the dielectric heating experiment above. The samples were at room temperature (25 ºC) at the start of the experiment and maximally heated by bulk heating to about 27.5 ºC (Supplementary information 2.2). **Figure 3** shows 3D maps of the fluorescence emission before (left) and after (right) the RF irradiation of a MB cluster. The nanomachines were clustering in various locations of the sample chamber and the specific point chosen, showed a high concentration of MB's, and was representative for the entire sample area.

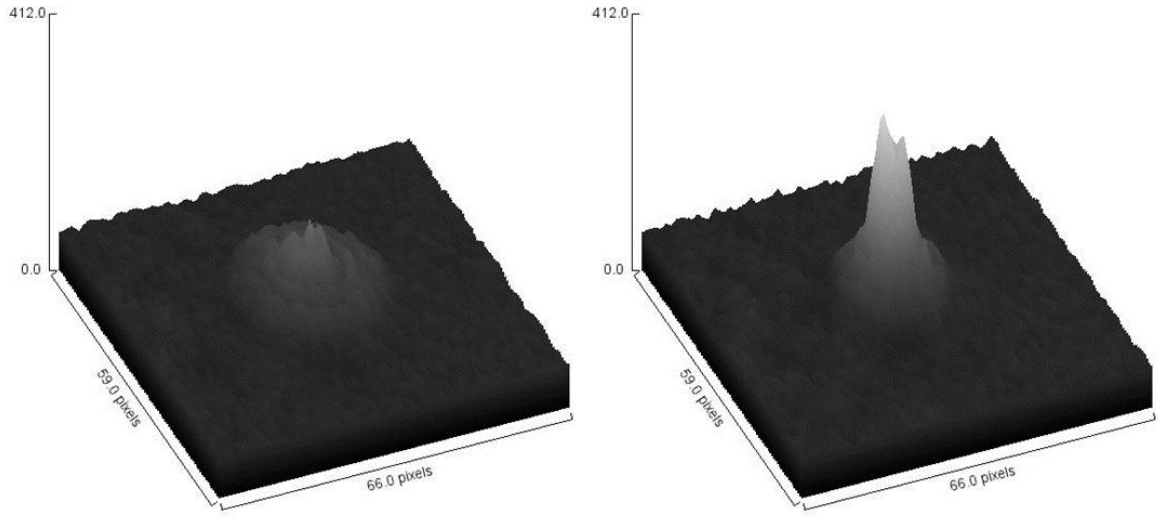

Figure 3. 3D maps of fluorescence emission of a solution of gold-conjugated molecular beacons before (left) and after (right) RF irradiation for 15 seconds. The images were taken at a representative spot in the sample chamber.

The images show a significant increase in fluorescent emission after RF irradiation. The bulk temperature increase alone was not enough to induce such an effect. In order to verify that RF activation of the gold nanoparticles was the key to the signal rise, we conjugated nanomachines composed of the same DNA sequence (loop and stem) but with the gold quencher substituted by an organic one (back hole, BHQ2). The 3D fluorescence maps for a BHQ2-nanomachine solution before and after exposure to the same RF field show no increase in fluorescence after RF exposure (Supplementary **Figure S.4**). This confirms that the signal increase seen with the NMs after RF exposure is not related to the bulk temperature increase but to localized heating around the GNP.

Next, we irradiated a sample of TH5 GNP-conjugated probes for 1 min and measured fluorescence over time. Without RF irradiation the fluorescent emission was stable with time, but with RF irradiation the emission increases significantly with time.

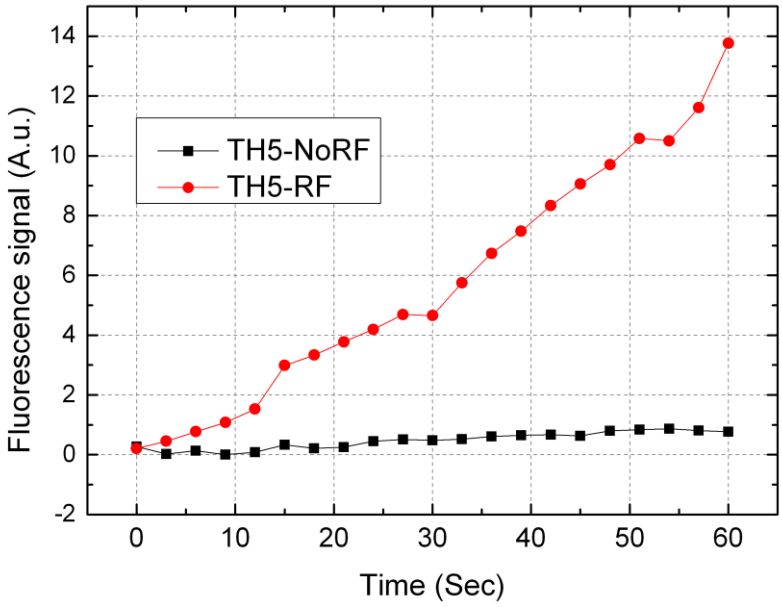

Figure 4. Integrated value of the fluorescence emission over time for TH5 NMs. Black squares show emission without and red dots with RF irradiation. The integrated value of the fluorescence emission of the entire sample chamber was quantified for each time point.

Because the dielectric heating was minor while the fluorescence of GNP conjugated MB was significant, we speculate that the fluorescence increase is due to a local increase of temperature around the GNP. The increase in temperature was probably due to an induction mechanism caused by the interaction of the GNP with the RF field.
It is then possible to calculate the ratio of the power absorbed in the nanoparticle to the radiated power by the antenna [see supporting info for analytical derivation]:

$$P/P_{\mathrm{rad}} = \frac{1}{5}\frac{b^5}{a^6}\sqrt{\frac{\varepsilon}{\mu_0}}\frac{1}{\varrho\omega^2\varepsilon^2} \qquad (1)$$

and a direct calculation using a frequency of f = 3 GHz, an coil antenna radius a = 1 mm, GNP radius b = 5 nm, absolute permittivity $\varepsilon = \varepsilon_0$ and GNP resistivity $\varrho = 2.44 \times 10^{-8}$ Ωm results in $P/P_{\mathrm{rad}} \cong 2.5 \times 10^{-18}$, and thus at an incident power on the coil of P_a = 10 W the

expected power dissipated in a nanoparticle is at most $P \cong 2.5 \times 10^{-17} W$, indeed a very low power.
For comparison, in [7] the following equation for the power dissipation density was reported:

$$p_w = 4\pi H^2 \mu_0 \mu_r f F \frac{\delta}{2b} \quad (2)$$

Here F is a transmission factor and its value can be found in[16] , and for a 10 nm GNP is F=0.27, while δ is the skin depth. The calculated power at the same conditions as above is 3.46×10^{-13} W, which is 5 orders of magnitude higher but still a relatively low power.
The temperature increase due to this power was calculated starting from the classical Fourier heat equation and was predicted to be in the order of μK[16] due to efficient heat transfer in the liquid. This temperature increase is insufficient to explain melting of the MB stem that leads to the observed fluorescence increment. We have to point out, however, the limitation of the classical approach to heat transfer at this scale. Many scale effects that are not accounted for, could come into play; for instance, the resistivity of the gold nanoparticle differs considerably from its bulk value. The theory developed by Fuchs-Sondheimer,[24,25] which is valid for thin films, reports that the surfaces of the film scatter the conduction electrons partially or completely diffusively and reduce their effective mean free path which in turn results in a large increase in the resistivity. This effect could have a larger impact in nanoparticles due to presence of constraints in all dimensions and not only in one, such as is the case in films. Furthermore, the classic approach for treating heat dissipation may be incorrect at the nanometer scale. In the classic Fourier´s law of heat conduction heat exchange is a diffusive process and this is only valid when there are enough scattering events in vicinity of the nanoparticle, so that the heat carriers can exchange energy with the surrounding medium to achieve local thermal equilibrium. When the dimension of the particle is on the same order, or even smaller than the mean free path of the heat carriers (i.e. the distance travelled by the heat carriers between two consecutive collisions), Fourier´s law does not apply and the heat transport should be considered ballistic. For this reason a calculation of the temperature profile inside the GNPs may be meaningless, since a thermal gradient may be impossible to define. A few studies [26,27] suggest that the temperature rise of a nanoparticle subject to a certain power dissipation is significantly higher than the values predicted by heat equation, this effect is mainly due to a significant reduction is heat flux away from the particle and a dis-continuous temperature at the interface. The presence of an attached DNA sequence could influence the energy transport providing an efficient dissipation pathway along its length.

To characterize the interaction between the RF field and the gold nanoparticles we developed a setup comprising a coplanar waveguide (CWG) and a PMMA holder (see experimental section) and we made use of the scattering parameters (S-parameters) for the measurements [Top insert in **Figure 5**]. The scattering parameters are ratios of complex wave amplitudes, i.e. S_{11} is the ratio of the reflected wave amplitude to the incident wave amplitude at port 1, while S_{21} is the ratio of the transmitted wave amplitude to port 2 to the incident wave amplitude at port 1. In particular, $|S_{11}|^2$ is the ratio between incident and reflected power at port 1, and $|S_{21}|^2$ is the ratio between the transmitted power to port 2 and the incident power at port 1. For a lossless two-port system, $|S_{11}|^2 + |S_{21}|^2 = 1$, therefore the normalization loss (NL): $NL = 1 - |S_{11}|^2 - |S_{21}|^2$ is a convenient measure of the loss in the structure.
We chose samples of pure water and pure isopropanol and the same media with a high concentration of 12 nm GNPs. These nanoparticles were slightly different from the ones used in the conjugation of the NMs; in order to avoid problem of aggregation of the nanoparticles due to the isopropanol and the high concentration, the core of the gold was covered with a

thin layer of silicon dioxide. All samples were measured in the frequency range up to 18 GHz. In the microwave range water is a highly absorbing medium and the addition of gold nanoparticles to the solution, did not result in a measurable absorption difference compared to pure water. As results the two NL curves shown in Figure 5 for water and water+GNP overlay almost perfectly.

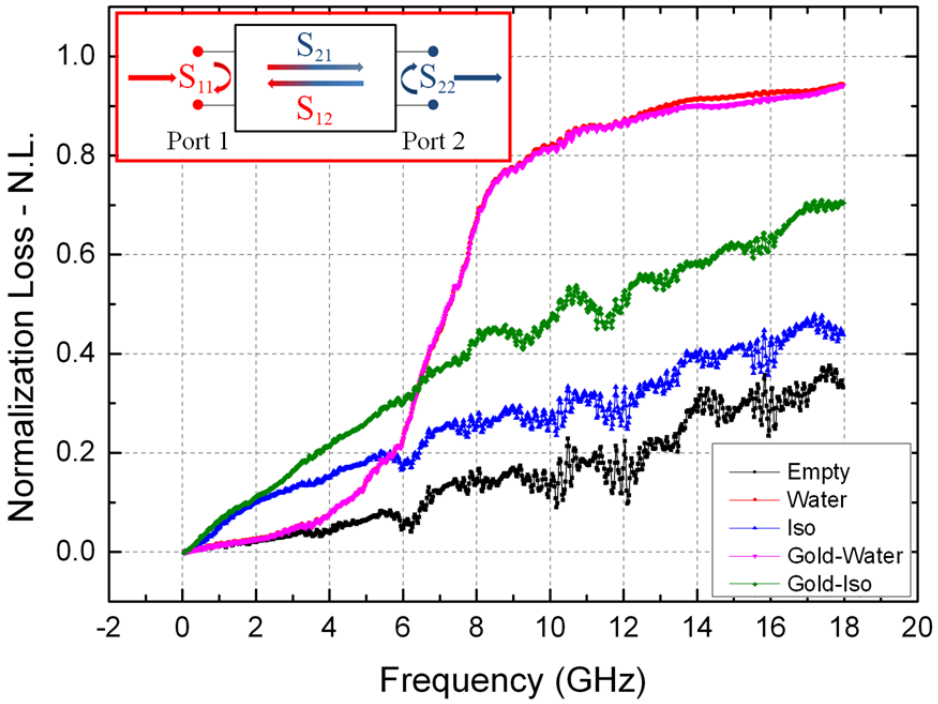

Figure 5. Normalized Loss measurements in different samples: water (red curve) and GNPs diluted in water (pink curve) show the same absorption value, while isopropanol (blue curve) and GNPs diluted in isopropanol (green curve) show significantly different *NL*.

In contrast, GNPs dispersed in isopropanol showed significant absorption when compared to isopropanol without GNPs.
In order to validate these data, a simplified theoretical calculation of the *NL* was considered. In small reflection limit (i.e. the characteristic impedance of the feed waveguide and the CWG are identical) the normalization loss is:

$$NL = 1 - |(\exp(-i\beta L))|^2 \quad (4)$$

where β is the wavenumber defined as $\beta = (\omega/c_0)\sqrt{\varepsilon_r}$, with ε_r the relative permittivity, ω is the angular frequency and L is the length of the waveguide. The results calculated for both water and isopropanol show good agreement with the measured parameters [data not shown].

In the microwave range water is known to be a material with very high dielectric losses. Because of the large absorption, the contribution of gold nanoparticle in the solution, although present, is hidden by the much larger loss contribution of water. When, on the other hand, gold nanoparticles are diluted in isopropanol, a relatively low loss solvent, the gold nanoparticles show a remarkable contribution to the *NL*, however, existing models for the power dissipation in the GNP's does not predict such a large effect.

From our experiment and theoretical model we can conclude that the addition of gold nanoparticles to the solution of isopropanol results in higher losses compared to that of the pure solution. The CWG method is an efficient way to confirm the interaction between the RF field and the gold nanoparticles that corroborates our previous findings.

3-Conclusions

We have successfully conjugated GNPs with single stranded DNA in order to create a sensor for mRNA recognition. The so-called Nanomachine was tested through melting curves and hybridization curves. The nanomachines were then activated by means of a RF field generated by a small coil and we showed that an increase in fluorescence emission results for GNP-conjugated machines with 5bps stem length. The negative control experiment, where the GNPs were replaced by organic quenchers, showed no significant increase in fluorescence emission. The quantification of the fluorescence emission from figure 3 compared to the fluorescence emission of the NM calculated using the melting curve in figure 2 left, indicates a temperature rise up to 44.5 ºC. This value, even if much higher than that calculated theoretically, might not be sufficient to perform tasks like resetting hybridized molecular beacons, for which, a temperature increase up to 60 ºC would be needed. We found a significant bulk heating caused by RF absorption in the buffer solution, and that is crucial in specific applications, for example when living cells are involved. This issue on the other hand, could be tackled in many ways, for example by setting up a perfusive flow that continuously replace the heated buffer, and thus carry away the excessive heat. We have also shown that it is possible to detect the presence of GNPs dissolved in solution using a simple setup comprising a coplanar waveguide. We pointed out that, even though the calculated temperature increase is not sufficient to explain the effects we have shown, numerous size effect, not accounted for, could play a crucial role in understanding the behavior of GNPs heat dissipation under RF irradiation. Our conclusion is that further studies are necessary to investigate the phenomena of heat generation and dissipation at the nanoscale in order to solve the discrepancy between theory and experimental results, but our results indicates that the heat generation around gold nanoparticles might not be sufficient for applications in which a high temperature increase needs to be achieved.

4-Experimental section

4.1-Nanomachine Conjugation

HPLC purified DNA based molecular beacons specific for TH targets were purchased from DNA technology (Risskov, Denmark). The hairpin DNA were synthesized with the following sequences: TH5 5’ -(NH_2)-**GCGAG***ACACCTTCACAGCTCGGGA* **CTCGC**-(Tamra)- 3’ and TH11 5’ -(NH_2)-**GCGAGGCGAGC** *ACACCTTCACAGCTCGGGA* **GCTCGCCTCGC**-(Tamra)- 3’; where bold indicates stem region and italics is the sequence encoding the specific target for TH. Regions in parentheses are the end modifications, an amino group at the 5’ end and the fluorochrome at the 3’ end. Spherical gold nanoparticles (GNPs) of 12 nm diameter with a carboxyl surface modification were purchased from Nanopartz (Loveland, USA). The GNPs (concentration 0.01 µM) were covalently conjugated with amino modified oligonucleotides (concentration 10 µM) by incubation with N-ethyl-N´-dimethyl-aminopropyl carbodiimide (EDC, concentration 10 µM) to enhance the coupling efficiency between amine and carboxyl groups. DNA was first mixed with GNPs in cold 2-(N-morpholino) ethanesulfonic acid buffer (MES buffer, pH 6) for 5 min and then a solution of EDC was added. The reaction was performed for 2 h at 37 °C under slight agitation. Finally, the conjugated molecular beacons were centrifuged for 2 min at 735x g on Illustra Microspin S-

200 HR columns (GE Healthcare, Life Sciences) to removed unconjugated oligonucleotides and EDC. The purified molecular beacons were stored in the dark at 4 °C for later use. Molecular beacons with the same sequences but conjugated with the BHQ-2 Black hole quencher were purchased from Biomers (Ulm/Donau, Germany).

4.2 Nanomachine activation setup

To test the fluorescence response of the nanomachine to an RF field, we developed a combined setup that integrates a coil (Coilcraft, Cumbernauld, Scotland) for field generation with a sample holder. The reservoir was fabricated by micromilling in a PMMA substrate of 1mm thickness and the final volume of 37 µl. The signal was generated by an analog signal generator Agilent N5181A MXG and sent to a solid state linear power amplifier ZHL-16W-43+ from Minicircuits (power gain 45 dB), through a circulator that directs the reflected wave to be dissipated in a 50 Ω load resistor to avoid instrument damage. The sample platform can be placed directly inside the microscope chamber for direct fluorescence measurements. For safety reasons, we fabricated a compact Faraday cage that wrap around the entire system and shield the external equipment from the radiation field [**Figure 6**]. The antenna for field generation was designed to be used at 3 GHz, where it was matched to a 50 Ω waveguide by means of an adjustable capacitor; this is the same frequency as used in the dielectric heating experiment.

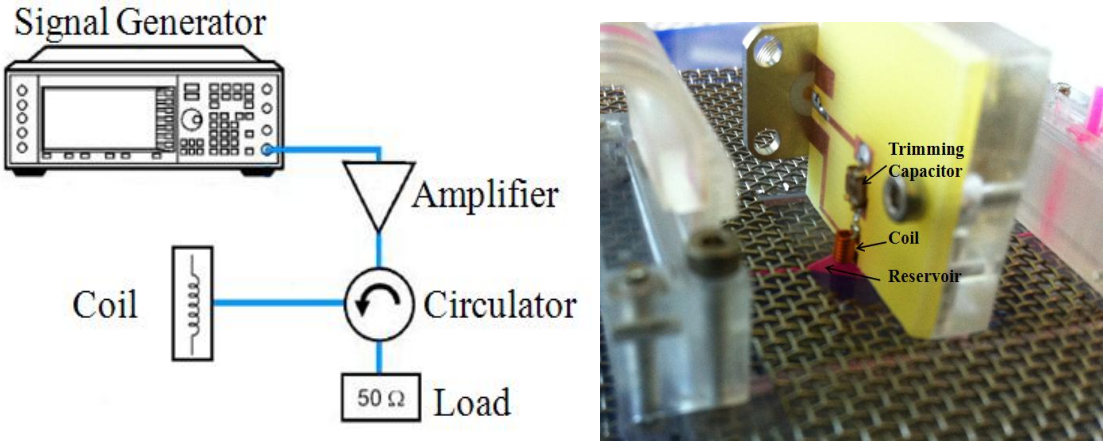

Figure 6*:* Experimental setup for fluorescence measurement, schematic drawing (left) and real setup (right); the chamber is filled with a colored dye to highlight the structure. The coil and the PCB have the same structure when used in the dielectric heating experiment.

4.3 Coplanar Waveguide Experiment

In order to test the interaction between gold nanoparticles dispersed in solutions and an RF field, we designed a simple microfluidic device from microfluidic components published elsewhere[28] attached to a coplanar waveguide (CPW) connected to a vector network analyzer (Hewlett Packard 8510). The sample under investigation interacted with the field of the waveguide structure due to close proximity to the CPW [**Figure 7 B**]. The CPW structure was fabricated using a standard photolithographic process and was designed to have a characteristic impedance of 50 Ω. It is preferable to use a low permittivity substrate in order to maximize the intensity of the RF field in the sample. The substrate (Duroid 5870 from Rogers) used has a dielectric constant of 2.33. This substrate material has low loss ($\varepsilon_r''/\varepsilon_r' = 0.0012$ at 10 GHz) which is required to maximize the sensitivity of the setup. The CPW structure should also ensure that the electromagnetic field is mostly confined in the region

around the sample, resulting in enhanced coupling. This substrate also has very little water absorption and is ideal for working in high moisture environments.
The sample holder consists of modular components of PMMA and PDMS that allows easy handling of the samples without touching the system and disturbing the measurements [28] [**Figure 7 A**]. The chip with the sample reservoir consists of a three layer sandwich structure of PMMA fabricated by micromilling; a bottom cover, that seals the reservoir, a middle structure with the actual reservoir, microfluidic channels and connections and, as the final layer, a thin top lid of 150 µm thickness that ensures close proximity between the sample solution and the CPW. The reservoir consists of a 4.5 cm long and 4 mm wide channel and is designed to match exactly the dimension of the CPW and enhance the coupling efficiency [**Figure 7 C**]. The sample holder also features curved inlet and outlet structures to ensure uniform filling of the chamber and avoid bubbles in the sensing area. The total volume of the chamber could be changed by changing the thickness of the middle layer of PMMA. We used 2 mm thick PMMA, resulting in ≈ 360 µl sample volume.
We tested gold nanoparticles of 12 nm covered with a thin layer of silicon dioxide, diluted in two different solvents, DI water and high purity isopropanol from Sigma Aldrich (water content ≈ 0.02%).

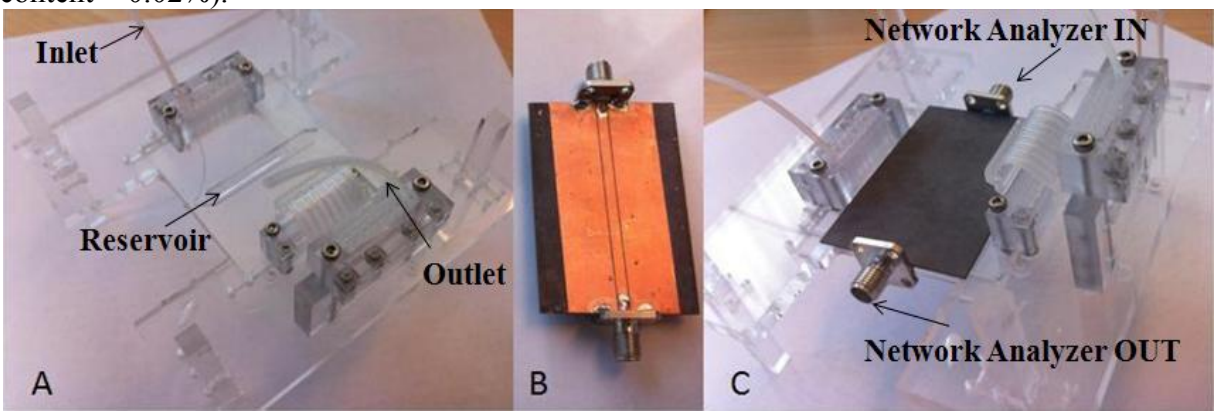

Figure 7: Experimental setup; (A) Microfluidic system for sample handling, (B) Coplanar waveguide, (C) assembled system.

Bibliography

[1] Hughes, J. R., Bullock, S. L. Ish-Horowicz, D. *Curr. Biol*. **2004,** 14, 1950-1956.
[2] Visvader, J. E. *Nature*.**2011**, 469, 314-322.
[3] K. Mullis, F. Faloona, S. Scharf, R. Saiki, G. Horn, e H. Erlich, *Cold Spring Harb Symp Quant Biol*, **1986**, vol. 51, pagg. 263–273.
[4] Tse-Wen Chang, *Journal of Immunological Methods*, **1983**, vol. 65, n. 1–2, pagg. 217–223.
[5] Tyagi S, Kramer FR.*Nat Biotechnol*. **1996**, 14, 303-308.
[6] Lakowicz, Joseph R**,** *Springer*, **2006**, pg. 331-348.
[7] Hamad-Schifferli, K., Schwartz, J. J., Santos, A. T., Zhang, S. Jacobson, J. M. *Nature*, **2002,** 415, 152-155.
[8] Seferos, D. S., Giljohann, D. A., Hill, H. D., Prigodich, A. E. Mirkin, C.A. *J. Am. Chem. Soc*. **2007,** 129, 15477-15479.
[9] Prigodich, A. E. et al. *Anal. Chem*. **2012,** 84, 2062-2066.
[10] Jayagopal, A., Halfpenny, K. C., Perez, J. W. Wright, D. W. Hairpin. *J. Am. Chem. Soc*. **2010,** 132, 9789-9796.
[11] Dubertret B, Calame M, Libchaber AJ. *Nat Biotechnol*. **2001** , 19, 365-370.
[12] Rosi NL, Giljohann DA, Thaxton CS, Lytton-Jean AK, Han MS, Mirkin CA. *Science*. **2006**, 312, 1027-1030.
[13] H. K. Kim, G. W. Hanson, e D. A. Geller,*Science*, **2013**, vol. 340, n. 6131, pagg. 441–442.
[14] Li, D. et al. *J Colloid Interface Sci*, **2011,** 358, 47-53.
[15] Liu, X., Chen, H., Chen, X., Parini, C. Wen, D. *Nanoscale*, **2012**, 4, 3945-3953
[16] Kogan, M. J. et al. *Nano Lett*. **2006,** 6, 110-115.
[17] Gannon, C. J., Patra, C. R., Bhattacharya, R., Mukherjee, P. Curley, S. A. *Journal of Nanobiotechnology*, **2008,** 6, 2.
[18] Moran, C. H. et al. *Nano Res*.**2009,** 2, 400-405.
[19] Denver, H., Gupta, A., Joshi, A., Kane, R., Hella, M. and Borca-Tasciuc, D.-A., *Proceedings of the NSTI Nanotechnology 2008*, NSTI-Nanotech 2008, **2008**, Vol. 2, p 252
[20] Cardinal, J. et al. *Surgery*, **2008,** 144, 125-132.
[21] Pearce, J. A. Cook, J. R. *2011 Annual International Conference of the IEEE Engineering in Medicine and Biology Society, EMBC*, **2011**, 5577-5580.
[22]T. Nagatsu, *Essays Biochem.*, **1995**, vol. 30, pagg. 15–35.
[23]K. E. Goodwill, C. Sabatier, C. Marks, R. Raag, P. F. Fitzpatrick, e R. C. Stevens, *Nat. Struct. Biol.*, **1997**, vol. 4, n. 7, pagg. 578–585.
[24] K. Fuchs, *Mathematical Proceedings of the Cambridge Philosophical Society*, **1938,** vol. 34, n. 01, pagg. 100–108.
[25]E. Sondheimer, *Physical Review*, **1950**, vol. 80, n. 3, pagg. 401–406.
[26] G. Chen, *J. Heat Transfer*, **1996,** vol. 118, n. 3, 539–545.
[27]M. E. Siemens, Q. Li, R. Yang, K. A. Nelson, E. H. Anderson, M. M. Murnane, e H. C. Kapteyn, *Nat Mater*, **2010**, vol. 9, n. 1, pagg. 26–30.
[28] D. Sabourin, P. Skafte-Pedersen, M. J. Søe, M. Hemmingsen, M. Alberti, V. Coman, J. Petersen, J. Emnéus, J. P. Kutter, D. Snakenborg, F. Jørgensen, C. Clausen, K. Holmstrøm, e M. Dufva, *J Lab Autom*, **2013**.vol. 18, n. 3, pagg. 212–228.

[29] N. N. Nedyalkov, S. E. Imamova, P. A. Atanasov, R. A. Toshkova, E. G. Gardeva, L. S. Yossifova, M. T. Alexandrov, e M. Obara, *Applied Surface Science*, **2011**, vol. 257, n. 12, pagg. 5456–5459.

Submitted to small

Supporting Information

S.1Theoretical model for nanoparticle heating in a RF field

S.1.1 Introduction

In this chapter a simple model for the power dissipation in gold nanoparticles due to the RF near-field of a coil antenna is developed. In the application of the gold nanoparticles in nanomachines, they are dispersed in a water based solution and enclosed in a polymer based microsystem, which both are lossy dielectrics. The power dissipation in the dielectrics is therefore also important, since that adds to the (unwanted) bulk heating of the system. The analysis is based on Maxwell's four equations that relate the five fields: the conduction current density **J**, the electric field **E**, the electric displacement **D**, the magnetic field **H** and the magnetic flux density **B**. A harmonic time dependency with the angular frequency ω is considered and accounted for by assuming the time phasor $e^{i\omega t}$, which is suppressed in the equations. As a result the field quantities, e.g. **E**, are complex vectors, where the physical instantaneous field value is e.g. Re[$\mathbf{E}e^{i\omega t}$]. In addition to Maxwell's equations the materials equations $\mathbf{J} = \sigma\mathbf{E}$, $\mathbf{B} = \mu_0\mathbf{H}$, and $\mathbf{D} = \varepsilon_r\varepsilon_0\mathbf{E}$, where μ_0 is the permeability ε_0 the permittivity of free space, σ is the conductivity, while ε_r is the relative permittivity of the dielectric material, are used. In a lossy dielectric, the relative permittivity is a complex number $\varepsilon_r = \varepsilon_r' - i\varepsilon_r''$, and both the real and imaginary parts are in general dependent on the angular frequency, which becomes explicit by considering the relaxation time model of a lossy dielectric

$$\varepsilon_r = \varepsilon_\infty + \frac{\varepsilon_S - \varepsilon_\infty}{1 + i\omega\tau} \qquad \text{(S.1.1)}$$

where τ is the relaxation time, ε_S is the low frequency permittivity while ε_∞ is the very high frequency permittivity.

S.1.2 Magnetic field generation and power dissipation in gold nanoparticles

Assume that a flat coil antenna of radius *a* is used to heat a small, conductive (conductivity σ_ or resistivity $\varrho = 1/\sigma$) spherical particle of radius *b* with is center in **r** = 0. The coil antenna is located in the x-y plane with is center in **r** = 0 and a current $I(t) = \mathrm{Re}(I_0 e^{i\omega t})$ at angular frequency ω is forced through it. The current generates a magnetic field which near the axis is oriented along the *z*-direction. At zero frequency the field strength on the axis is [1, 2]

$$H_z(0,z) = \frac{Ia^2}{2(a^2+z^2)^{\frac{3}{2}}}, \text{ and } \qquad H_z(0,0) = \frac{1}{2}\frac{I}{a} = H_{z0} \qquad \text{(S.1.2)}$$

when the sphere is not present. At higher frequencies a retarded field analysis is necessary, and then the analysis becomes somewhat more involved, however, as long as the characteristic dimensions of the coil and sample are much smaller than the wavelength (here $\lambda = 10cm$) this complication is fairly easy to handle as shown by Griffith and Pan [3]. They show that the vector potential **A** in the retarded case to a very good approximation is proportional to the static vector potential $\mathbf{A} = (1 + i\beta R)e^{-i\beta R}\mathbf{A}_S$where *R* is the spherical radial coordinate, $\beta = \omega/c$ the propagation constant, *c* the speed of light in the medium and $\mathbf{A}_S$ the static vector potential. The approximation is valid at sufficiently low angular

frequencies $\omega \ll c/a$. The exact solution for the static vector potential involves elliptic integrals [3], but since the interest here is the near-field region close to the center of the coil a simple approximation to the vector potential is sufficient

$$\mathbf{A}_S = A_{S\phi}\mathbf{e}_\phi = \frac{\mu_0 I_0}{4}\frac{a^2 R\sin\theta}{(a^2+R^2)^{\frac{3}{2}}}\mathbf{e}_\phi = \frac{\mu_0 I_0}{4}\frac{a^2 r}{(a^2+r^2+z^2)^{\frac{3}{2}}}\mathbf{e}_\phi \cong \frac{\mu_0 I_0}{4}\frac{r}{a}\mathbf{e}_\phi \qquad \text{(S.1.3)}$$

where $\mathbf{e}_\phi$ is the tangential unit vector in polar coordinates (Spherical coordinates (R,θ,ϕ) or cylindrical coordinates (r,θ,z). By definition of the vector potential $\mathbf{B} = \nabla \times \mathbf{A}$ and from Faradays law of electromagnetic induction

$$\nabla \times \mathbf{E} = -\frac{\partial \mathbf{B}}{\partial t} = -i\omega\mathbf{B} = -i\omega\nabla \times \mathbf{A} \qquad \text{(S.1.4)}$$

and we may choose $\mathbf{A}$ such that $\mathbf{E} = -i\omega\mathbf{A}$, and that is the case with the approximation used in Eq. S.3. It follows that

$$\mathbf{E} = -i\omega(1+i\beta R)e^{-i\beta R}\frac{\mu_0 I_0}{4}\frac{a^2 r}{(a^2+r^2+z^2)^{\frac{3}{2}}}\mathbf{e}_\phi \cong -i\omega\frac{\mu_0 I_0}{4}\frac{r}{a}\mathbf{e}_\phi \qquad \text{(S.1.5)}$$

where the approximation is valid close to the center of the coil, where the nanoparticle is placed.

At low frequencies the magnetic field is hardly affected by the presence of the particle, and thus the total magnetic field is approximately equal to the field from the coil alone, and we may calculate the time average power dissipated in the nanoparticle as

$$P = \frac{1}{2}\int_{\text{sphere}}\frac{1}{\varrho}E_\phi^2 \mathrm{d}\Omega = \frac{1}{2\varrho}(\omega\mu_0\frac{I_0}{2a})^2\int_0^b\left(\frac{r}{2}\right)^2 2\pi r \times 2\sqrt{b^2-r^2}\mathrm{d}r \qquad \text{(S.1.6)}$$

where the integration is performed by considering a cylindrical shell of height $2\sqrt{b^2-r^2}$, radius r and thickness dr, and $\frac{I_0}{2a} = H_{0z}$ is recognized as the static magnetic field at origin.

The integral results in

$$\mathrm{P} = \frac{1}{2\varrho}(\omega\mu_0 H_z^{(c)})^2 \times \frac{2\pi}{15}b^5 = \frac{\pi}{15}\frac{b^5}{\varrho}(\omega\mu_0 H_z^{(c)})^2 = \frac{4\pi^3}{15}\frac{b^5}{\varrho}(f\mu_0 H_z^{(c)})^2 \qquad \text{(S.1.7)}$$

This result is in perfect agreement with COMSOL finite element simulations.

At higher frequencies, where the skin depth $\delta = \sqrt{\varrho/(\pi f\mu_0)}$ becomes comparable to the nanoparticle radius this analysis becomes invalid; at 3 GHz however the skin depth for gold is approximately 1.5 μm and thus this limit is at frequencies beyond interest here where nanoparticles of nanometer size are considered; this is true, even if the resistivity of the nanoparticle is considerably higher than the bulk value due to size effects. [4, 5]

The radiation resistance of the current loop is [1]

$$R_{\text{rad}} = \sqrt{\frac{\mu}{\varepsilon}}\frac{\pi}{6}(\beta a)^4 = \sqrt{\frac{\mu}{\varepsilon}}\frac{\pi}{6}(\frac{\omega}{c}a)^4 \qquad \text{(S.1.8)}$$

and that may be used to estimate the loop current (Note, the calculation will yield the correct magnetic field value also with a multi-turn loop). In the experiments the power incident on the antenna is P_a = 10 W, and the radiated power must be less. The radiated power is $P_{\text{rad}} = \frac{1}{2}R_{\text{rad}}I_0^2$ and thus the current is at most $I_0 \le \sqrt{2P_a/R_{rad}}$, and hence $H_{z0} \le \sqrt{2P_a/R_{rad}}/(2a)$

We may then calculate the ratio of the power absorbed in the nanoparticle to the radiated power

$$P/P_{\text{rad}} = \frac{1}{5}\frac{b^5}{a^6}\sqrt{\frac{\varepsilon}{\mu_0}}\frac{1}{\varrho\omega^2\varepsilon^2} \qquad \text{(S.1.9)}$$

and a direct calculation using f = 3 GHz, a = 1 mm, b = 5 nm, $\varepsilon = \varepsilon_0$ and $\varrho = 2.44 \times 10^{-8}$ Ωm results in $P/P_{\mathrm{rad}} \cong 2.5 \times 10^{-18}$, and thus at an incident power on the coil of P_a = 10 W the expected power dissipated in a nanoparticle is $P \cong 2.5 \times 10^{-17}\ W$, indeed a very low power.

Bibliography

1. S. Ramo, J. R. Whinnery, e T. V. Duzer, *Wiley*, **1994**.
2. D. J. Griffiths,. *Addison Wesley*, **1999**.
3. J. M. Griffith e G. W. Pan, *IEEE Transactions on Magnetics*, **2011**, vol. 47, n. 8, 2029-2033.
4. K. Fuchs, *Mathematical Proceedings of the Cambridge Philosophical Society*, **1938**, vol. 34, n. 01, pag. 100-108.
5. E. Sondheimer, *Physical Review*, **1950**, vol. 80, n. 3, 401-406.

S.2 Dielectric heating

Since the nanoparticles or nanomachines are dispersed in an electrolyte solution contained in a polymer microsystem the time varying magnetic field will induce some dielectric heating of the liquid and polymer, since these are lossy dielectrics. The loss power density may be estimated using the expression for the electric field Eq. S.1.5 and the total electric current density, which is the sum of the conduction and the displacement current densities

$$\mathbf{J}_t = \sigma_l \mathbf{E} + \frac{\partial \mathbf{D}}{\partial t} = \sigma_l \mathbf{E} + i\omega\varepsilon_r\varepsilon_0\mathbf{E}$$

where σ_l is the conductivity of the liquid. The time average dissipated power density is then:

$$p_w = \frac{1}{2} Re(\mathbf{J}_t \cdot \mathbf{E}^*) = \frac{1}{2}(\sigma_l + \omega\varepsilon_r''\varepsilon_0)E^2 \cong \frac{1}{2}\omega\varepsilon_r''\varepsilon_0 E^2$$

where the star indicates complex conjugation. At high frequencies, the power dissipation due to finite conductivity becomes smaller than that due to dielectric losses. By use of of Eq. S.1.4 the dielectric heating power density becomes:

$$p_w = \frac{1}{2}\omega\varepsilon_r''\varepsilon_0\left(\frac{\mu_0 I_0}{4}\right)^2 \frac{(1+\beta^2R^2)\omega^2a^4r^2}{(a^2+r^2+z^2)^3} \cong \frac{1}{2}\omega\varepsilon_r''\varepsilon_0\left(\frac{\mu_0 I_0}{4}\right)^2 \frac{\omega^2a^4r^2}{(a^2+r^2+z^2)^3}$$

which obviously varies throughout the dielectric volume. By integration over the sample volume, where the dependency of the z- coordinate is ignored, the power dissipated in a cylindrical volume of radius a_0 and height h becomes:

$$P_w = \frac{1}{2}\omega\varepsilon_r''\varepsilon_0\left(\frac{\mu_0 I_0}{4}\right)^2\left(\frac{1}{2}\frac{\omega^2a^2a_0^2}{(a^2+a_0^2)^2}\right)\pi a_0^2 h$$

By use of the expression for the radiated power, this may be recast as:

$$\frac{P_w}{P_{rad}} = \frac{3}{16}\frac{\varepsilon_r''}{\varepsilon_r'}\frac{c}{\omega}\frac{a_0^4 h}{a^2(a^2+a_0^2)^2}$$

and assuming h = 0.5 mm, and a_0 = 2 mm, we get 0.017 < P_w/P_{rad} < 0.14 at 3 Ghz using $\varepsilon_r''/\varepsilon_r' = 0.15$ and $\varepsilon_r' = 75$ for water. The range is related to which speed of light to use in the expression, since that is reduced in water by a factor of $\sqrt{75}$, but a major part of the radiation is emitted to air. In any case a significant heating of the sample liquid is expected. If a GNP concentration in the sample of C = 10 nM is assumed, the number of GNP's in the volume is $N = CN_A\pi a_0^2 h \cong 4 \times 10^{10}$ and thus the relative power dissipation due to the GNP's is at most $P_{\mathrm{GNP}}/P_{\mathrm{rad}} = 4 \times 10^{10} \times 2.5 \times 10^{-18} = 1 \times 10^{-7}$ which is insignificant compared to dielectric heating.

In order to test the effect of RF field on the GNPs solution, we developed a small microfluidic setup to monitor the temperature increase over the RF exposure time. The system in **Figure S.2.1** shows a microfluidic PMMA chip with inlet and outlet channels and a sealed chamber for sample handling. Another side channel allows to insert a small thermocouple directly in the sample chamber. The thermocouple channel is sealed thereafter by casting PDMS and curing overnight at 60° C. On top of the sample chamber, not directly in contact with its surface to avoid heat exchange, sits a small printed circuit board (PCB) with a coil (Coilcraft Cumbernauld, Scotland) matched at the frequency of 3 GHz through an adjustable capacitor.

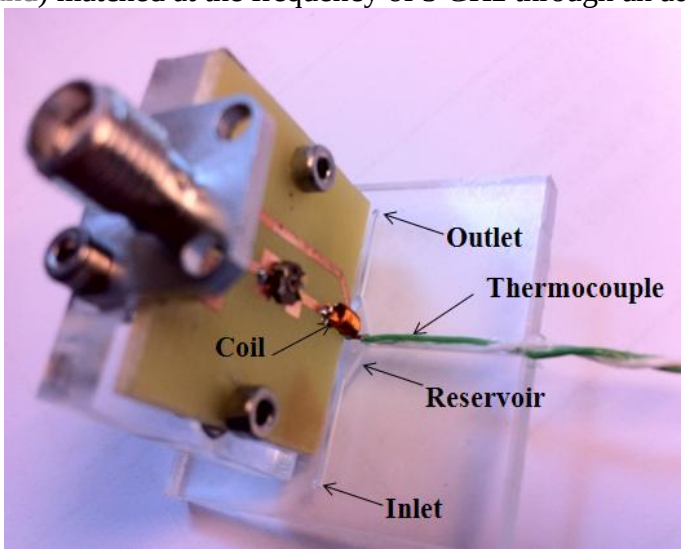

Figure S.2.1: Experimental setup for dielectric heating investigation. The thermocouple (green cable) is inserted in the reservoir and sealed with PDMS. The reservoir is in close proximity (not contact) with a small coil connected through a PCB to the signal generator.

The sample is injected in the chamber and irradiated with an RF field generated by the coil antenna at the matched frequency. The signal is produced by a signal generator Agilent N5181A MXG and amplified with Mini-Circuits ZHL-16W-43+ high power amplifier to 40 dBm.
The results after 60 seconds irradiation are shown in **Figure S.2.2**

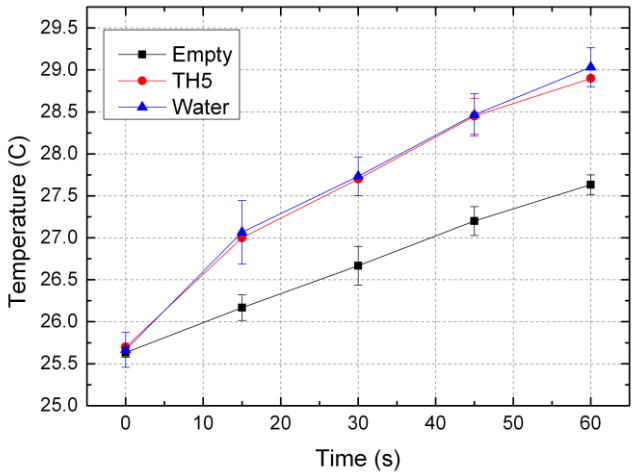

Figure S.2.2: Temperature increase in the empty setup, i.e. empty sample chamber with thermocouple inside (black curve), in the Nanomachine solution (red curve) and in the water buffer for irradiation at 40 dBm at 3 GHz.

S.3 Melting and Hybridization curve of BH2-conjugated beacons.

In order to compare the performances of the nanomachine and have a negative control we purchased molecular beacons encoded with the same sequence, but having an organic quencher (BHQ-2) instead of the gold nanoparticle. The beacons were characterized with a melting and hybridization curve in the same way performed for the nanomachines. The temperature was ramped from 30 °C to 100 °C with steps of 0.3 °C and the fluorescence was measured at every step after 5 minutes [**Figure S.3.1 left].** The hybridization curve of the BHQ2-beacons shows that signal from unconjugated TH5 increases with temperature while the conjugated TH5 decreases (**Figure S.3.1 right).** This fact can be explained in sight of the low melting point of that particular beacon, when temperature approaches the value of 37 °C, some of the beacons in the closed state (i.e. the hairpin structure, where the stem keeps fluorophore and quencher together) are starting to melt to the random coil configuration , causing an increase in the fluorescence emission. In the same way, some of the complementary targets from the hybridized beacons are starting to detach, causing the beacon to return to the hairpin configuration and therefore decreasing the intensity of emission. TH11 beacons show a little increase in fluorescence emission in presence of complementary target, even though this increment is much lower than in TH5 beacons. This phenomenon is due to the high energy of the hairpin configuration ensured by the 11bps stem that competes with the annealing of the complementary target.

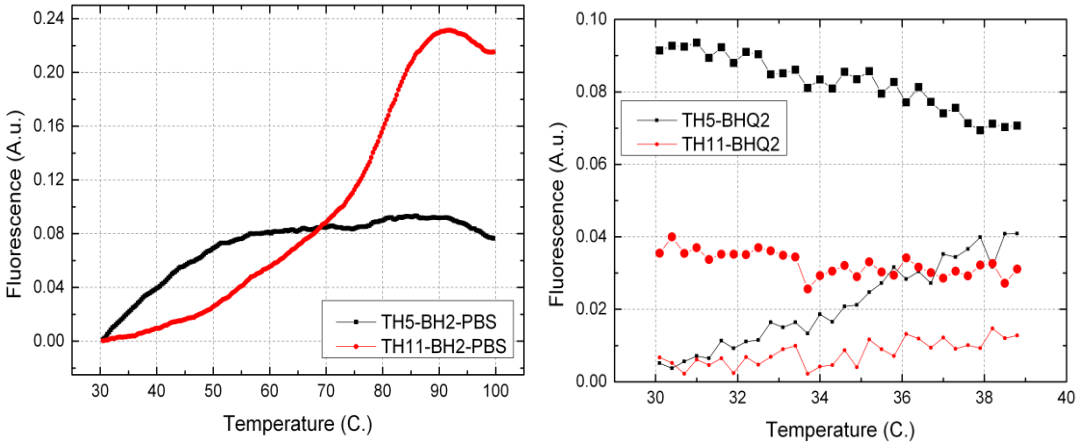

Figure S.3.1: Left, melting curves of the BHQ2-conjugated molecular beacons. Beacons with 5bps stem are shown in the black curve, 11bps in red. Right, hybridization curves of beacons incubated with complementary target; small symbols for unhybridized, large symbols for hybridized MBs.

S.4 3D map of fluorescence emission of BHQ2 conjugated MBs

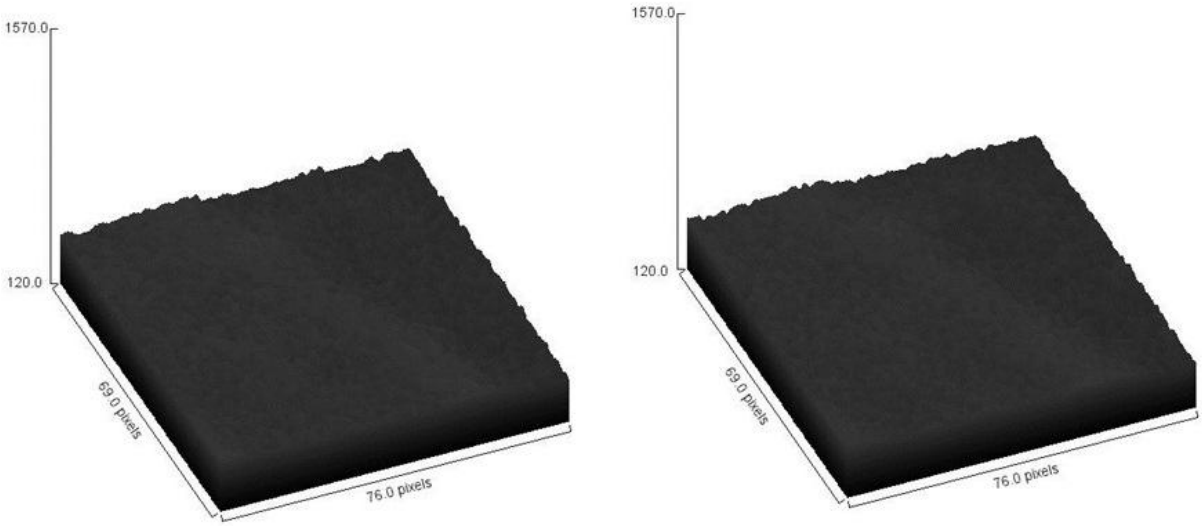

Figure S.4: 3D map of fluorescence emission from a solution of BHQ2-conjugated molecular beacons before (left) and after (right) irradiation. The images were taken at a representative spot in the sample chamber.

Dynamic tracking of expression of neuronal markers in living human neurons detected using molecular beacons

Mirolyuba Ilieva[1*], Paolo Della Vedova[1], Ole Hansen[1,2], Martin Dufva[1]

[1]Department of Micro- and Nanotechnology, Technical University of Denmark,DTU Nanotech, Building 345E, DK-2800 Kgs. Lyngby, Denmark. [2]CINF - Center for Individual Nanoparticle Functionality, Technical University of Denmark, DK-2800 Kgs. Lyngby, Denmark. **Corresponding Author: Mirolyuba Ilieva, Department of Micro- and Nanotechnology, Technical University of Denmark, Ørsteds Plads 345 Ø, building 344, 2860 Kgs. Lyngby, Tel. +45 45258159, Fax. +45 45 88 77 62, miil@nanotech.dtu.dk, www.nanotech.dtu.dk*

Abstract

Monitoring gene expression is an important tool for elucidating mechanisms of cellular signaling, especially when gene expression is followed in real time in living cells. In order to monitor gene expression during nerve cell development, molecular beacon (MB) probes targeting markers representing different stages of neuronal differentiation were designed and synthesized as 2'-O-methyl RNA backbone oligonucleotides. MBs targeted against GAPDH mRNA were designed and used as a positive control. MBs were transfected into human mesencephalic cells (LUHMES) using streptolysin-O-based membrane permeabilization. Mathematical modeling and simulations predicted that approximately 56000 MB copies were transfected into each cell over a few seconds. Gene expression was detected at different time points using fluorescence microscopy. Nestin and NeuN were expressed approximately 35% of LUHMES cells grown in growth medium, and in 80-90% of cells after differentiation. MAP2 and tyrosine hydroxylase mRNAs were expressed 48 and 72h post induction of differentiation. In contrast, GAPDH mRNA was detected in >95% of cells. The gene expression changes measured using MBs were confirmed using qRT-PCR. These results suggest that MBs are simple to use living cell sensors, and particularly useful for dynamically studying gene expression.

Introduction

The ability to detect RNAs in individual live cells allows investigators to exactly pinpoint when a gene is turned on and off in response to a stimulus. Detecting and

measuring gene expression has traditionally been limited to the use of technologies such as DNA microarrays, reverse-transcription polymerase chain reaction (RT-PCR), northern blotting, and fluorescence *in situ* hybridization (FISH), all of which examine gene expression in lysed or chemically-fixed cell populations. In contrast to these destructive methods, green fluorescent protein labeling (GFP) can be used to track gene expression in living cells. However, GFP and other similar reporter systems cannot measure endogenous mRNA expression in living cells, since a) the GFP gene must be fused to the promoter region of interest in order to function, b) GFP/promoter constructs might be integrated into the host genome or be transfected as plasmids, and c) the GFP gene product is not necessarily processed in the same way as the native gene in terms of transcription, maturation, or translation, which can lead to errors in measurement (Dobek *et al*, 2011, Lee *et al.*, 2006). In practical experimental terms, GFP reporter systems require genetic modification of the cell and are time and labor consuming, and sometimes impossible to realize.

Molecular beacon technology was first described in Tyagi and Kramer (1996). Molecular beacons (MBs) are stem-loop forming oligonucleotides with a fluorochrome on one end, and a quencher on the other that recognize and report the presence of specific nucleic acids in homogeneous solutions (Tyagi and Kramer, 1996). When a closed-state MB hybridizes to a specific nucleic acid target via a specific recognition sequence, the stem breaks and the MB unfolds into an open state. The fluorochrome is quenched in the closed, but not in the open state. Therefore, MBs are ideally suited to monitoring gene expression of specific genes inside living cells. However, to date, only a handful of reports describe the use of MBs for monitoring gene expression in living cells. Bratu *et al.* (2004) used MBs to visualize the distribution and transport of oskar mRNA in Drosophila oocytes, while Santangelo *et al.* (2004) used MBs to analyze the distribution and transport of mRNA in intracellular organelles (Santangelo *et al*., 2004), and elegantly demonstrated that both mRNAs for GAPDH and K-Ras are localized in mitochondria. The combination of protein detection with antibodies and mRNA detection with MBs has been used to detect and isolate rare cancer stem cells from populations of normal cells, using fluorescence activated cell sorting (FACS) (Rhee and Bao, 2009). MBs targeted against the Oct4 mRNA transcription factor, which is highly expressed in embryonic and cancer stem cells, were introduced into mouse carcinoma cell line without affecting cell function; the fluorescent signal from Oct4 mRNA-targeting MBs provided clear discrimination between undifferentiated and retinoic acid-differentiated cells. Recently, MBs targeted against Sox2 mRNA were used as the sole discriminator to sort mouse embryonic and neural stem cells (Larsson *et al.*, 2012), and Sox2 mRNA-positive cells formed neurospheres more efficiently than Sox2 mRNA-negative cells. The clinical and diagnostic utility of MBs has been demonstrated in a feasibility study on bladder cancer (Zhao et al., 2010), in which MBs were used to detect survivin mRNA, which is specifically expressed in bladder cancer cell lines. However, the MB-based assay produced some false positive results,

which compromised its immediate use for routine diagnosis. Further clinical diagnostic development is required.

MBs have also been used to monitor expression of two microRNAs (miR-26a and miR-206) during myogenesis (Kang *et al.*, 2011). This study used two MBs with different dyes and quenchers, allowing simultaneous visualization of both miRNAs during myogenesis. Real-time changes in β1-integrin expression in osteoblasts in response to surface modification were tracked with MBs over short periods of time; this study was particularly powerful since changes in mRNA localization were visualized in the same live cells (Lennon *et al.*, 2010). Finally, MBs were used to monitor the temporal gene expression of osteogenic markers, including alkaline phosphatase, type I collagen and osteocalcin during differentiation of adipose-derived stem cells (Desai *et al.*, 2013).

Despite this broad range of uses of MBs inside living cells, the routine application of MBs in cell research, especially in dynamic studies of gene expression, still appears to be a challenge for many investigators. The aim of this work was to demonstrate the utility of MBs for studying molecular events inside living cells, particularly to detect and dynamically trace changes in gene expression during differentiation of stem cells into neural lineage. We describe the design and use of MBs towards GAPDH, NeuN, MAP, nestin, and tyrosine hydroxylase (TH) mRNAs to track neural stem cell progression from neuronal progenitors, via mature neurons, into highly specialized dopaminergic neurons. Time lapse imaging of growing and differentiating cells allowed us to determine the differentiation status of each cell in the population throughout a seven-day experiment.

Materials and methods

Cell culture and media

LUHMES (Lund human mesencephalic cell line, ATCC, CRL-2927) are a subclone of the tetracycline-controlled, v-myc-overexpressing human mesencephalic-derived cell line MESC2.10 immortalized with a LINX v-myc retroviral vector, as described by Lotharius et al. (2002), but which possess robust dopaminergic characteristics (Lothalius *et al.*, 2005). Undifferentiated cells were cultured and expanded in cell culture flasks pre-coated with Geltrex®, which is a reduced growth factor basement membrane extract purified from murine Engelbreth-Holm-Swarm tumor (Invitrogen). The flasks were coated by incubating for 1 h at 37°C with Geltrex® diluted 1:100 in phosphate buffered saline (PBS). Cultures were maintained in growth medium (GM), consisting of advanced DMEM/F12 (Sigma), 1x N2 supplement (Gibco), 2 mM L-glutamine, 1% penicillin/streptomycin, and 40 ng/ml recombinant basic fibroblast

growth factor (bFGF; Invitrogen). Cells were maintained at 37°C in a humidified atmosphere with 5% CO_2.

HeLa Tet-On® Advanced cells (631155, Clontech) were cultured in DMEM/F12 supplemented with 10% fetal bovine serum (FBS), penicillin 100 U/ml and streptomycin 100 µg/ml.

Differentiation of LUHMES

The differentiation process was initiated by adding differentiation medium (DM) consisting of advanced DMEM/F12, 1x N2 supplement, 2 mM L-glutamine, 1 mM dbcAMP (Sigma), 1 µg/ml tetracycline (Sigma), and 2 ng/ml recombinant human glial cell-derived neurotrophic factor (GDNF; R&D Systems).

Design of molecular beacons

mRNA-targeting MBs were designed using Beacon Designer 7.9 (Premier Biosoft). The target sequence for each MB was analyzed using Human Genome BLAST (http://blast.ncbi.nlm.nih.gov/Blast.cgi) to minimize the risk of non-specific binding to unrelated mRNA. The program was used to avoid cross homology, repeats, and low complexity regions based on expect (E)-value and percentage identity. The E-value is the number of hits expected with similar or better score, and it depicts the significance of the match (an E-value of 0 indicates complete homology). Regions with E-value greater than the target value were avoided. Percentage identity is the percentage of identical bases between query and subject sequence in an alignment. A percentage identity of 100 indicates complete homology. The regions with percentage identity greater than the percentage identity criterion (default = 98 for the human genome) were avoided. Regions not satisfying both the E-value and the percentage identity criteria were avoided.

It is important to design the MB in an area of the target with minimal secondary structure formation. This helps prevent the template from preferentially annealing to itself faster than to the MB. The program identified and avoided template sequence predicted to give rise to significant secondary structures.

The parameters for MB design were set to ensure that the search succeeded in finding the best possible sequence. The length of the MBs was between 18 and 30 bp. The melting temperature (T_m) values of the probes were calculated using the nearest neighbor thermodynamic calculation with Santa Lucia values (SantaLucia *et al.*, 1998). The parameters were set as follows: hairpin maximum d*G* (the free energy of the most stable alternate hairpin that is acceptable) 4 -kcal/mol; self-dimer maximum d*G* (the free energy of the most stable self-dimer that is acceptable) 7 -kcal/mol; cross-dimer maximum d*G* (the free energy of the most stable cross-dimer that is acceptable in a multiplex reaction) 7 - kcal/mol; run/repeat maximum five bp/dinucleotide probes with single (e.g. AAAAA) runs or dinucleotide (e.g. ATATATATAT) repeats of length greater than the specified value were discarded.

After selecting a probe sequence, two complementary arm sequences were added, one on each side of the probe sequence. The stem region of the MBs was five bp long, with a CG content of 80%.

All calculations performed with this program used the following conditions: temperature for beacon free energy calculation 55°C, monovalent ion concentration 100 mM, free Mg^{2+} concentration 3 mM, and target concentration 250 nM.

In Beacon Designer the search algorithm calculates all the properties of every possible probe within the allowed length and positional boundaries, and rates them. This rating determines how well the designed oligonucleotide meets the search parameters relative to the tolerance limits specified for each parameter. The parameters used in the rating are maximum hairpin d*G*, maximum self-dimer d*G*, maximum run/repeat length, and maximum cross-dimer d*G* and T_m; if all parameters are exactly on target, the rating is 100. The rating of the probe depends on two factors: how close the probe is to the target value of each parameter, and how tightly the tolerances (permissible value of variation acceptable by the program from a pre-set standard value) are specified. Highly rated probes have most or all parameters near their ideal values, and are very likely to work well. For the MB probe search the quality of the designed probe is displayed as 'best' (rating greater or equal to 75), 'good' (rating between 74 and 50), 'poor' (rating below 50), or 'not found'. Only MBs with a 'best' rating were chosen for synthesis and further evaluation. MBs were synthesized with a 2'-O-methyl RNA backbone, Cy3 molecule attached to the 5'-end, and black hole quencher 2 (BHQ-2) attached to the 3'-end (Eurofins MWG Operon). The sequences of the MBs used in the study are listed in Table 1. MBs were diluted in RNase/DNase free dH_2O to yield stock concentrations of 100 µM, and stored at -20°C.

Toxin-based membrane permeabilization

MBs were introduced into the cytoplasm of living cells using toxin-based membrane permeabilization using streptolysin-O (SLO, Sigma), which is a bacterial exotoxin that reversibly forms pores in the cell surface (Chen et al 2011). SLO at a concentration 1 µg/ml was activated with the reducing agent tris(2-carboxyethyl)phosphine hydrochloride solution (TCEP, Sigma), at a final concentration 5 mM for at least 30 min at 37°C. Cells were washed with Dulbecco's PBS (DPBS) without Ca^{2+} and Mg^{2+}, trypsinized for 3 min at 37°C, and collected by centrifugation for 5 min at 190 x g. The activated SLO was diluted in serum free medium (Opti-MEM) to concentrations between 1 and 800 ng/ml, and mixed with MB (2 µM final concentration). Cells ($1x10^5$) were incubated with the SLO/MB mixture in a final volume of 100 µl for approximately 15 min. Afterwards, the permeabilized cells were resealed by washing in DPBS containing Ca^{2+} and Mg^{2+}, and plated in 12-well plates precoated with Geltrex® and containing GM. The differentiation process was started 24 h after plating by exchanging GM for DM.

HeLa cells were transfected as a monolayer with 230 ng/ml (17 U/ml) activated SLO. Cells ($1x10^5$) were washed three times with pre-warmed DPBS and incubated with toxin and MB (2 µM final concentration) in 200 µl Opti-MEM for 15 min. Cells were washed three times with DPBS containing Ca^{2+} and Mg^{2+} and complete growth medium was added.

Detection of cellular viability

Cellular viability was detected using calcein-propidium iodide staining. Medium from each well was carefully removed and cells were incubated for 30 min with 3 µM calcein AM (live cell dye) and 2.5 µM propidium iodide (dead cell dye) diluted in warm 1x DPBS without Ca^{2+} and Mg^{2+}.

Imaging and image analysis

Phase contrast and fluorescent images were acquired using a Carl Zeiss Axio Vision 4.8.2 equipped with ApoTome Imaging system, 40x/0.75 Plan-Neofluar objective, HBO lamp, and a Zeiss Axiocam MRm B/W camera. The same exposure time and filter set (43 HE Ds Red 538-570 nm) were used for all experiments. Single-cell image analysis was performed using ImageJ software (http://rsb.info.nih.gov/ij/). A region of interest (ROI) was drawn around the cells and the total fluorescent intensity (FI) measured. The background fluorescence was detected by drawing a ROI in an area outside the cell of interest, and the total FI measured. In ImageJ, the total fluorescence intensity is reported as integrated density (ID), which is the sum of the values of the pixels in the selection. The background measurement of FI was subtracted from the cellular measurement [15]. Cells expressing the gene of interest were calculated as the number of cells with positive fluorescent signal emitted from each specific MB per 100 counted cells.

Quantitative polymerase chain reaction

Total RNA was isolated from cultured cells using the RNeasy Mini Kit (Qiagen). Cells were lysed directly on the dish. The lysates were collected and purified according to the manufacturer's instructions. Single-stranded cDNA was prepared from total RNA using random RT primers under standard conditions using MultiScribe Reverse Transcriptase (Applied Biosystems). The cDNA from each sample was diluted and used for real-time PCR analysis for quantification of neuronal marker expression. TaqMan assays (Invitrogen) for target genes were used as follows: GAPDH (ID Hs03929097_g1), nestin (ID Hs00707120_s1), MAP2 (ID Hs00258900_m1), NeuN (RBFOX3 ID Hs01370653_m1), and TH (ID Hs00165941_m1). PCR amplifications were performed in duplicate using the Chromo4 Real-Time Detection system (BioRad) at 95°C for 10 s, followed by 40 cycles of 95°C for 5 s and 60°C for 30 s. To quantify the relative expression of each gene, the C_t (threshold cycle) values were normalized to the C_t value of GAPDH (e.g. $\Delta C_t = C_t(\text{target}) - C_t(\text{GAPDH})$). All experiments included negative controls containing no cDNA template.

Statistical analysis

Results are expressed as mean ± standard error of the mean (SEM). qPCR was analyzed using a Student's t-test (n=5). Analyses were performed using Graph Pad Prism v.6 (GraphPad Software Inc., CA, USA).

Results

Introduction of MBs into cells

Cell viability and transfection efficiency were investigated as a function of SLO concentration ranging from 1 ng/ml (corresponding to 0.07 U/ml) to 800 ng/ml (corresponding to 59.7 U/ml). Transfection efficiency was evaluated using a MB targeting GAPDH mRNA. Cell viability was evaluated using calcein/propidium iodide staining. An SLO concentration of 17 U/ml (230 ng/ml) was determined to be the optimal concentration, with 75% of the cells showing signal from MB targeting GAPDH 24 h post-transfection, and >95% cell viability (Supplementary Figure S1A). However, GAPDH expression was detected as early as 1 h post transfection (earliest time point investigated) suggesting that hybridization to target is a rapid process. Moreover, cells showed no defects in growth or differentiation and they exhibited the same morphology as non-transfected cells (untransfected cells are shown in supplementary Figure S1B, and transfect cells in Figure 3). An SLO concentration of 17 U/ml (230 ng/ml) was therefore used in further experiments.

The transport of MBs into cells during transfection is a diffusion process, whereby the MBs diffuse through open pores in the cell membrane. In order to estimate the number of MBs that are effectively transfected into the cells, two simplified diffusion models were used. The cells were assumed to be spherical with a radius $a = 5$ μm, a cell membrane $x_m = 10$ nm thick, and in the membrane $N_p \simeq 600$ pores (2 pores per μm^2) with a pore radius of $a_p = 15$ nm open during transfection (Keyel et al., 2011). MBs were modeled as solid spheres with a radius of $a_b = 2.5$ nm, and a concentration $C_0 = 2$ μM was used in a medium with a viscosity $\eta = 0.85 \times 10^{-3}$ Pa s at 300 K; the viscosity of the cell interior was assumed to be identical.
Diffusion problems in dilute systems are governed by Fick's first and second laws, as shown in equations (1) and (2), respectively:

$$\boldsymbol{J} = -D\nabla \mathrm{C}, \tag{1}$$

where C is the concentration, $\boldsymbol{J}$ is the diffusion flux density, and D the diffusivity. Fick's second law is a conservation law:

$$\frac{\partial C}{\partial t} = -\nabla \cdot J \simeq D\nabla^2 C, \tag{2}$$

where t is time. The approximation is valid if the diffusivity is constant. The diffusivity of the MBs may be estimated using the Stokes-Einstein equation:

$$D = \frac{k_B T}{6\pi\eta a_b}, \tag{3}$$

where η is the viscosity of the medium, k_B is Boltzmann's constant, and T the absolute temperature. A direct evaluation at 300 K yields a diffusivity of $D = 100\ \mu m^2 s^{-1}$ that agrees well with values in the literature (Lukacs et al., 2000). The real diffusion problem is a complicated 3D problem; however, the different length scales involved in the problem suggest that approximations can be made. Using typical diffusion times of $t_d = \lambda^2/(2D)$, where λ is the characteristic length scale, results in diffusion times for the pore regions that are five orders of magnitude lower than the diffusion times relevant to the cell scale, and therefore a quasi steady-state approximation may be applied to the pore regions. Furthermore, the pores are so far apart that they hardly interact during the diffusion process. As a result, we can estimate the diffusion flux through a single pore by the net flux *I* that results from: 1) the quasi steady-state diffusion to a disc of radius $a_p - a_b$ (to compensate for the finite size of the MBs), 2) the steady state diffusion through a tube of radius $a_p - a_b$ and length x_m, and 3) the quasi steady-state diffusion from a disc of radius $a_p - a_b$ to the cell interior. The fluxes 1) and 3) are given by $I_{1,3} = 4(a_p - a_b)D\Delta C_{1,3}$, where $\Delta C_{1,3}$ is the concentration difference that drives the flux (Carslaw and Jaeger, 1959). The flux 2) is $I_2 = \left[\pi(a_p - a_b)^2/x_m\right]D\Delta C_2$, where the symbols are the same as above. The three fluxes are identical and the sum of concentration differences is $\Delta C_1 + \Delta C_2 + \Delta C_3 = C_0 - C_c$, where C_c is the concentration inside the cell, which is considered approximately uniform. As a result, the flux through a single pore is:

$$I_p = \left(\frac{2}{4(a_p - a_b)D} + \frac{x_m}{\pi(a_p - a_b)^2 D}\right)^{-1}(C_0 - C_c), \tag{4}$$

and the total flux through all pores is N_p times larger. Integrating Fick's second law, equation (2) over the volume $V = \frac{4}{3}\pi a^3$ of the cell yields:

$$\frac{\partial C_c}{\partial t} = \frac{N_p I_p}{V} = \frac{3DN_p(a_p - a_b)^2}{2a^3\left[\pi(a_p - a_b) + 2x_m\right]}(C_0 - C_c) \equiv \frac{C_0 - C_c}{\tau_c}, \tag{5}$$

where τ_c is the time constant relevant for the transfection

$$\tau_c = \frac{2a^3\left[\pi(a_p - a_b) + 2x_m\right]}{3DN_p(a_p - a_b)^2}. \tag{6}$$

With the parameters given, the resulting time constant is $\tau_c \simeq 0.53$ s. The solution to equation (4) is obtained by

$$C_c = C_0\left(1 - \exp\frac{-t}{\tau_c}\right), \tag{7}$$

and within a few time constants (a few seconds) the concentration of MBs saturates at C_0.

In an alternative approach, we may use a mean field approximation and calculate an

effective diffusivity D_e of MBs in the porous membrane (Grathwohl, 1998):

$$D_e = D\,\frac{\varepsilon(1-\delta)}{\tau}, \tag{8}$$

where ε is the porosity (i.e. the ratio of total pore volume to total membrane volume), δ is the constrictivity (i.e. the ratio of the radius of the diffusing particle to the pore radius), and τ is the tortuosity, which corrects for the curvature of the pores. Since the pores are short and straight we take $\tau = 1$, and then the effective diffusivity is estimated as $D_e \simeq 0.12\ \mu m^2 s^{-1}$, approximately three orders of magnitude smaller than the diffusivity in the free fluid. With this model, the time constant may be estimated from

$$\tau_{c2} = \frac{V}{4\pi a^2}\frac{x_m}{D_e} = \frac{a x_m}{3 D_e}, \tag{9}$$

and a numerical value of $\tau_{c2} \simeq 0.14\ s$ is estimated, which is lower than the first estimate, which we regard as more reliable. At such low porosity, the mean field approximation may not be sufficiently accurate since the effects of diffusion to and from the pores are excluded from the model, and in the first model these effects are seen to be dominant; this is the cause for a difference by a factor of three in magnitude of the two time constants. In both cases, the transfection is completed within a few seconds, well in advance of the closing of the pores after 15 min of transfection, and the concentration reaches the final value of $C_0 = 2\ \mu M$.

We also performed a Finite Element Model (FEM) simulation using COMSOL 4.2 (http://www.comsol.com) to verify the first diffusion model, with Figure 1 showing the simulated average concentration of MBs inside the cell as a function of transfection time. In the FEM model, a cone segment of the spherical cell with exactly one pore was used to represent a $1/N_p$ fraction of the cell volume. The cone region was extended far into the free fluid volume in order to also represent a $1/N_p$ fraction of that. Figure 1 also illustrates the results of the analytical model using the calculated time constant of $\tau_{c2} \simeq 0.53\ s$ as the solid line; the agreement between the FEM simulation and the analytic model is almost perfect.

Given the cell size and the MB concentration, the number of MBs in the cell becomes approximately 56000 if the cell volume is corrected for the volume of the nucleus (approximately 10%), where MBs do not penetrate. Bustin (2000) found that there are about 10^8 mRNA copies of GAPDH per microgram of total RNA. Assuming that there is about 4 pg total RNA per cell, there would be about 400 GAPDH mRNA copies per cell, indicating that there is about 100-fold more MB than possible target.

Direct experimental verification of the diffusion model by tracking the fluorescence during transfection is difficult due to the high background from MBs in the medium. Therefore we instead tracked the decay of fluorescence from cells loaded with MBs after a second treatment with SLO to re-open pores and thus allow out-diffusion of

MBs from the loaded cells to an initially MB free medium. The adherent cell line HeLa was transfected using the SLO protocol (material and methods) with MB towards TH, but without a quencher attached. The pores were closed and cells were washed three times and incubated for 1 h to let cells recover while hybridization was not expected since TH is not expressed in this particular cell line. The cells were fluorescent as expected and had their normal morphology (data not shown) after transfection. At this point the cells were again treated with SLO reagent to re-open the pores and the fluorescent decay from the cells was monitored by time laps microscopy for 20 minutes. Figure 2 shows the fluorescence emission from a representative cell. After about 10 minutes, the fluorescence reached the base line level suggesting that all the transfected fluorescent MBs had diffused out of the cells (Figure 2). The resulting time constant (~200 s) however was much longer than that expected from the theoretical model. This suggests that other factors may dominate the transfection kinetics than diffusion of MBs over the membrane or that the parameters (number of pores and pore size) used in the diffusion model are incorrect.

Gene expression of neuronal markers detected by MBs

MBs targeted against mRNAs specific for neural progenitors (nestin), mature neurons (NeuN and MAP2), and highly specialized dopamine neurons (TH) were delivered into embryonic midbrain neurons (LUHMES). MBs targeting GAPDH were used as a control. Cells were left to attach to culture plates for 24 h after transfection in GM supplemented with bFGF. 24 h after transfection, the differentiation process was induced by switching GM to DM containing dbcAMP, tetracycline, and GDNF. The measurement of fluorescence was commenced 24 h after transfection, and images were taken every 24 h for 192 h. The patterns of fluorescence signal emitted from cells varied (Figure 3), and included small dotted signals (Figure 3 A1), more compact punctate signals (Figure 3 A2), or widespread cytoplasmic cluster-like fluorescence (Figure 3 A3). The last pattern was more often observed in differentiated cells (Figure 3A), due to the compact cell body and tight perinuclear cytoplasmic organization. Non-differentiated cells showed signals in the lamellipodia and cell body space (Figure 3 A2), while differentiated cells showed only cell body-localized MB signals (Figure 3 A4-6). All signal categories were included in the analysis when the calculating percentage of positive cells (see below). Large bright signals were interpreted as false positives, being emitted from cells with dead cell morphology (Figure 3 A7). These false positive signals were excluded from the analysis.

The expression pattern for the respective target investigated during the differentiation process. GAPDH MB that was used as transfection control, and approximately 75% of cells were positive 24 h post-transfection and after differentiation close to 100% of

the cell were positive for GAPDH mRNA. Nestin, an intermediate filament protein expressed in dividing cells during the early stages of development of the CNS, and nuclear protein antigen (NeuN), were also detected 24 h after transfection in about 40% of cells (Figure 3B). In contrast, no MAP2 and TH expression was detected in cells 24 h post induction of differentiation (Figures 3B and 4). Expression of MAP2 was present in 30% of cells 48 h post induction of differentiation (Figure 6), while the first TH-positive cells appeared 72 h post induction (Figure 6). The number of cells positively expressing neuronal markers reached their maximum at different time points as follows: 85% nestin and NeuN-positive cells 120 h post induction, 85% MAP2-positive cells 144 h post induction, and 70% TH-positive cells 192 h post induction.

The intensity of the nestin-MB signal increased about two-fold compared to point-of-induction levels. The maximum increase in nestin-MB signal was observed 120 h post induction. A slight decrease in the signal was detected 192 h after induction. The signal intensity changes observed for NeuN-MB were similar. However, the maximal signal of NeuN was observed 168 h post induction (Figure 7). In contrast, no signal was recorded for MAP2-MB and TH-MB 24 h post induction. The MAP2-MB signal plateaued 120 h post induction, while TH-MB signal plateaued 72-96 h post induction. MAP2-MB signal intensity decreased slightly 192 h post induction, while TH levels remained constant.

Correlation between qRT-PCR and MB signal intensities

To corroborate the results using different MBs, qRT-PCR was used to measure the respective mRNA expression before and 168 h after differentiation. GAPDH was used as an internal positive control. Expression of nestin and NeuN was detected in non-differentiated cells, and it significantly increased after seven days of differentiation (Figure 8). In contrast, expression of the neuronal markers MAP2 and TH was not detected in non-differentiated cells, but was later expressed, corroborating the accuracy of the measurements made using MBs (Figures 5, 6, and 7).

Discussion

Since MBs were first described, their multiple applications in detecting gene expression by targeting RNA inside living cells have only been exploited in a limited number of studies. Here we described the use of a panel of MBs targeting molecular markers specific for the progressive stages of neuronal differentiation, and demonstrate that MBs can be used as a routine gene expression assay, as well as a reporter gene technology.

The design of MBs requires careful consideration, in particular with regards to target specificity. Our results suggest that the detected signals are specific, since signal from MBs targeting different markers during differentiation following the correct

biological sequence. The expression of the housekeeping gene GAPDH (constant expression), the progenitor marker nestin (expressed during the early stages of differentiation of neuronal progenitors), and the neuronal nuclear antigen NeuN were all detected. The total number of positive cells for each marker differed, as expected. Thus, the number of GAPDH positive cells was twice the number of cells positive for the neuronal markers. Following differentiation, signal from the mature neuron marker MAP2 was detectable. Finally, TH expression was detected 72 h after differentiation was induced, as described by Scholz et al. (2011).All these findings were corroborated by qRT-PCR.

In contrast to hybridization in solution where the physicochemical conditions are simplified, hybridization of MBs to mRNA in living cells is complicated by the formation of secondary structures in mRNA molecules, RNA-binding proteins, and the degradation of the probes due to enzymes with nuclease activity (Rhee et al., 2008). If the target sequence has a double-stranded structure MBs compete with RNA strands, while when the target is a binding site for proteins, MBs compete with RNA-binding proteins in order to hybridize. These factors could make target sequence inaccessible to MBs in spite of unique probe sequence design. Software programs such as mFOLD and Beacon Designer can predict the formation of secondary structures so that these sequences can be avoided during the selection of probes in the design process. The prediction of protein binding sites in the target is more complicated due to only limited data existing for RNA-binding proteins (Rhee et al., 2008). Competition with RNA or RNA-binding proteins can result in a significant decrease in signal level due to inefficient hybridization between the MB and the target sequence. To overcome this, many studies have used 2'-O-methyl RNA MBs in order to increase affinity for the target mRNA (Tsourkas et al., 2002); in addition, a modified backbone is less vulnerable to nuclease activity. On the other hand, the formation of double-stranded RNA can lead to RNA silencing, and therefore influence cellular function. In this study, MBs with 2'-O-methyl backbones were tested. Probe-target hybridization did not have any measurable effect on cell physiology including gene expression, self-renewal, or differentiation. Other authors (Lennon et al., 2010 and Desai et al., 2013) have successfully used non-modified MBs in their living cell studies, although over a shorter length of time. This suggests that it is a matter of choice for individual researchers to use either 2'-deoxy or 2'-O-methyl modified bases in the design of their MBs, although modified backbone MBs may be more appropriate in studies tracking gene expression over prolonged periods of time.

False positive signals due to MB-protein interaction and degradation are a further limitation that reduces the usability of MBs in live cell imaging applications. Chen et al. (2007) observed that MBs with non-modified backbones incubated with phosphodiesterase I and II show a small increase in fluorescence. They concluded that the fluorochrome and quencher conjugated on each end of MBs limit exonuclease activity. However, MBs are highly sensitive to degradation by S1 endonucleases, and Mung Bean endonucleases that cleave the hairpin loops. Single-strand binding (SSB)

proteins also cause significant increases in fluorescence. Although SSB proteins and nucleases are present in the cell cytoplasm, previous studies have shown that there are fewer DNA-protein interactions in the cytoplasm compared to the nucleus, and that the nuclease activity is in fact low (Chen et al., 2007). MBs remain in their quenched hairpin conformation when localization is limited to the cytoplasmic compartment. Our data show signal retained in the cytoplasm with perinuclear localization, but not within nucleus (Figure 4). This pattern of expression and the appearance of signal at different time points during development suggest that these do not represent false-positive signals, but are due to specific hybridization between MB and target sequence.

One limitation that needs to be considered could be the theoretical decrease in the MB signal through dilution during cell division, especially in rapidly dividing cells and for highly expressed genes. Differentiated neurons are out of cell cycle and decreases in signal intensity due to MB dilution are therefore not observed.

It is difficult to predict how many beacons penetrate each cell during transfection, and cell-to-cell variations in MB delivery might exist (Desai et al., 2013). However, our COMSOL simulation demonstrates that a steady-state concentration is reached inside the cell after only a few seconds. After subtracting the volume of the nucleus, which is not pierced by MBs, the average cell is predicted to contain 56000 beacons. This suggests that a pool of MBs exists in the cell after transfection, and not all MBs are used up, especially in the case of genes with low expression. Therefore all mRNAs targeted by MBs should be saturated, and the signal intensity detected from individual cells in the same developmental stage should be relatively equal. We detected different signal patterns and intensities of the same MB between cells in the same stage of differentiation (Figure 4). This might be explained not by variation in the number of penetrating MBs inside each cell, but by noise in gene expression, i.e. the variation in the number of copies of mRNA between cells due to the fundamentally stochastic nature of the biochemistry of gene expression. MB intensity was positively correlated with quantification of gene expression by qRT-PCR, supporting the conclusion that detection of gene expression using MBs accurately reflects cellular mRNA levels.

The diffusion model suggests that within seconds MBs are moving into opened cells while the measured data suggest that steady state levels is reached after 10 minutes. While the discrepancy does not have any practical impact on a 15 minute transfection procedure, it points to other factors than diffusion of MBs affecting the speed of transfection. Firstly, the model takes into account only the diffusion process, assuming that all the pores are already open from the start. It is known from literature (Niedermeyer et al., 1985 and Palmer et al., 1998) that the pore formation involves the binding of streptolysin O molecules in arc- or ring- shaped structures comprising about 50-80 subunits that progressively form on the cellular membrane and cause lysis. This process depends on the SLO to cell concentration ratio. Furthermore, pore

forming times between 10 s and 300 s have been recorded. Secondly, the pores exhibit a size distribution and 30 nm is considered an upper limit for the diameter. Hence, an overall smaller pore size could be used in the model resulting in a lower permeability. Third, in the model the entire surface of the cells contains pores, while the adherent HeLa cells likely only had pores on cell surfaces facing the medium since it is likely that surfaces facing the bottom are inaccessible by SLO reagent and by MBs. Finally, the number of fully developed pores may be lower than assumed in the model. By contrast, the LUHMES cells are transfected in solution phase which of natural reasons provides pore formation all around the cells but also shorter diffusion distances of SLO reagents to the cells suggesting that LUHMES cells are more rapidly transfected than HeLa cells. In conclusion, the theoretical model shows that diffusion process alone is not a limiting factor and other time constants may play an important role in the transfection procedure. Despite that, since the standard transfection procedure was 15 minutes and all the MBs diffuse out of a HeLa cell in 10 minutes (figure 3); it is likely that LUHMES cells have the same concentration of MB inside as the concentration added to the medium. Based on this reasoning, it is likely that the calculated number of about 56000 MBs inside LUHMES cells after transfection is correct.

One significant advantage of *in situ* methodologies is the ability to gather spatial data on biological phenomena of interest. In these experiments, each cell appears follow its own course during differentiation; some cells express the genes of interest very early, while the percentage of neuronal marker-expressing cells increases more rapidly during the later stages of neurogenesis. This suggests that there are different expression pattern and population-level heterogeneity during neuronal differentiation. In contrast to PCR-based assays, which collect data from the differentiating population as a whole, MBs accurately measure expression of genes of interest on a single cell level. MBs can be used to repeatedly assess gene expression in the same cell population over time, which is not possible using the destructive methods.

Commonly utilized transfection methods for oligonucleotide delivery, such as lipid and dendrimer-based delivery methods, have often failed to deliver MBs into cells. MB-transfection agent complexes do not always dissociate efficiently once internalized, leading to brightly fluorescing punctate aggregates that interfere with fluorescent measurements. Furthermore, MB-transfection agent complexes can often lead to entrapment and degradation of the probes within endosome/lysosome compartments, thus increasing background signal. The transfection efficiency of neurons is particularly limited (Karra and Dahm, 2010), and indeed LUHMES represent a particularly challenging system, since they cannot be transfected using standard methods, such as with lipo- or nucleofection. One routinely used method for direct introduction of MBs into the cytoplasmic compartment of living cells is toxin-based membrane permeabilization using streptolysin-O (SLO), as used in this study. Although it has been successfully used to deliver MBs into a wide variety of cell types, including human dermal fibroblasts, stem cells, and cancer cells (Chen et al.,

2011), SLO is not a popular method for neuronal transfection. Here we show that the SLO-membrane permeabilization delivery method is a rapid, efficient, and gentle method for the delivery of MBs into neurons. Cells viability was high and the transfection efficiency nearly 100%.

Despite all the disadvantages described, we show here that MBs are a powerful tool for the spatiotemporal detection of gene expression inside living cells. Measurements can be performed at the single cell level, allowing for the study of changes in mRNA expression and localization in the same cell. In contrast to widely used GFP–reporter constructs, MBs represent a rapid method for targeting endogenous gene expression without genetic modifications.

Conclusions

We designed MBs targeting multiple factors in order to profile cells during neuronal differentiation, and optimized the method for delivering MBs to living neurons. Our simulations show that during transfection the concentration of MBs reach a steady state after few seconds and that we end up with 100-fold more MB than possible target. MBs offer significant advantages over traditional techniques because they allow for real-time imaging of individual cells and preserve spatial information. They overcome the need to lyse cells for qPCR, or fix cells for molecular imaging techniques such FISH. Time-consuming and technically challenging genetic manipulations are not required.

Acknowledgements

This work was supported by FTP grant 09-070568, and partly supported by The Danish National Research Foundation's Center for Individual Nanoparticle Functionality (DNRF54).

[1]Department of Micro- and Nanotechnology, Technical University of Denmark,DTU Nanotech, Building 345E, DK-2800 Kgs. Lyngby, Denmark.
[2]CINF - Center for Individual Nanoparticle Functionality, Technical University of Denmark, DK-2800 Kgs. Lyngby, Denmark.
*Corresponding Author: Mirolyuba Ilieva, Department of Micro- and Nanotechnology, Technical University of Denmark, Ørsteds Plads 345 Ø, building 344, 2860 Kgs. Lyngby, Tel. +45 45258159, Fax. +45 45 88 77 62, miil@nanotech.dtu.dk, www.nanotech.dtu.dk

References

Bratu DP, Cha BJ, Mhlanga MM, Kramer FR, Tyagi S. Visualizing the distribution and transport of mRNAs in living cells. PNAS 2003;100:13308-13.

Bustin SA. Absolute quantification of mRNA using real-time reverse transcription polymerase chain reaction assays. J Mol Endocrinol 2000;25:169–93.

Carslaw HS, Jaeger JC. Conduction of heat in solids. In: London: Oxford University Press 2nd Ed. 1959. p. 215.

Chen A, Rhee W J, Bao G, Tsourkas A. Delivery of molecular beacons for live-cell imaging and analysis of RNA. RNA detection and visualization. In: Jefferey E. Gerst, editors. Methods and Protocols, Methods in Molecular Biology 2011;714:159-174.

Chen AK, Behlke MA, Tsourkas A. Avoiding false-positive signals with nuclease-vulnerable molecular beacons in single living cells. Nucleic Acids Res 2007;35:e105.

Desai HV, Voruganti IS, Jayasuriya C, Chen Q, Darling EM. Live-cell, temporal gene expression analysis of osteogenic differentiation in adipose-derived stem cells. Tissue Engineering 2013;19:40-8.

Dobek GL., Zhang X, Balazs DA, Godbey WT. Analysis of promoters and expression-targeted gene therapy optimization based on doubling time and transfectability. The FASEB Journal 2011;25:3219-28.

Grathwohl P. Diffusion in natural porous media: Contaminant transport, sorption/desorption and dissolution kinetics. In: Kluwer Academic 1998. p. 29-34.

Kang WJ, Cho YL, Chae JR, Lee JD, Choi KJ, Kim S. Molecular beacon – based bioimaging of multiple microRNAs during myogenesis. Biomaterials 2011;32:1915-22.

Karra D, Dahm R. Transfection techniques for neuronal cells. J Neurosci 2010;30:6171-7.

Keyel PA, Loultheva L, Roth R, Salter RD, Watkins SC, Yokoyama WM, Heuser J. Streptolysin O clearance through sequestration into blebs that bud passively from the plasma membrane. J Cell Sci 2011;124:2414-23.

Larsson HM., Lee ST, Roccio M, Velluto D, Lutolf MP, Frey P, Hubbell JA. Sorting live stem cells based on Sox 2 mRNA expression. PLOS ONE 2012;7:e49874.

Lee JY, Colinas J, Wang JY, Mace D, Ohler U, Benfey P. Transcriptional and posttranscriptional regulation of transcription factor expression in Arabidopsis roots. PNAS 2006;103:6055–60.

Lennon FE, Hermann CD, Olivares-Navarrete R, Rhee WJ, Schwartz Z, Bao G, Boyan BD. Use of molecular beacons to image effects of titanium surface microstructure on β1 integrin expression in live osteoblast-like cells. Biomaterials 2010;31:7640-47.

Lotharius J, Barg S, Wiekop P, Lundberg C, Raymon HK, Brundin P. Effect of mutant α-synuclein on dopamine homeostasis in a new human mesencephalic cell line. J Biol Chem 2002;277:38884-94.

Lotharius J, Falsig J, van Beek J, Payne S, Dringen R, Brundin P, Leist M. Progressive degeneration of human mesencephalic neuron-derived cells triggered by

dopamine-dependent oxidative stress is dependent on the mixed-lineage kinase pathway. J Neurosc 2005;25:6329-42.

Lukacs GL, Haggie P, Seksek O, Lechardeur D, Freedman N, Verkman AS. Size-dependent DNA mobility in cytoplasm and nucleus. J Biol Chem 2000;275:1625-9.

Niedermeyer W. Interaction of streptolysin-O with biomembranes: kinetic and morphological studies on erythrocyte membranes. Toxicon 1985;23:425–39.

Palmer M. et al. Streptolysin O: A Proposed Model of Allosteric Interaction between a Pore-Forming Protein and Its Target Lipid Bilayer. Biochemistry 1998;37:2378–2383.

Rhee WJ, Bao G. Simultaneous detection of mRNA and protein stem cell markers in live cells. BMC Biotechnology 2009;9:30.

Rhee WJ, Santangelo PJ, Jo H, Bao G. Target accessibility and signal specificity in live-cell detection of BMP-4 mRNA using molecular beacons. Nucleic Acids Res 2008;36:e30.

SantaLucia Jr. A unified view of polymer, dumbbell, and oligonucleotide DNA nearest-neighbor thermodynamics. PNAS 1998;95:1460-65.

Santangelo PJ, Nix B, Tsourkas A, Bao G. Dual FRET molecular beacons for mRNA detection in living cells. Nucleic Acids Res 2004;32:e57.

Scholz D, Pöltl D, Genewsky A, Weng M, Waldmann T, Shildknecht S, Leist M. Rapid, complete and large-scale generation of post-mitotic neurons from the human LUHMES cell line. J Neurochem 2011;119:957-71.

Tsourkas A, Behlke MA, Bao G. Hybridization of 2'-O-methyl and 2'-deoxy molecular beacons to RNA and DNA targets. Nucleic Acids Res 2002;30:5168-74.

Tyagi S, Kramer FR. Molecular beacons: probes that fluoresce upon hybridization. Nat Biotechnol 1996;14:303-8.

Zhao J, Wang ZQ, Wang XY, Yang XJ, He D. Preliminary Study of diagnostic utility of molecular beacons in bladder cancer. Urology 2010;76:512.e8-512.e13.

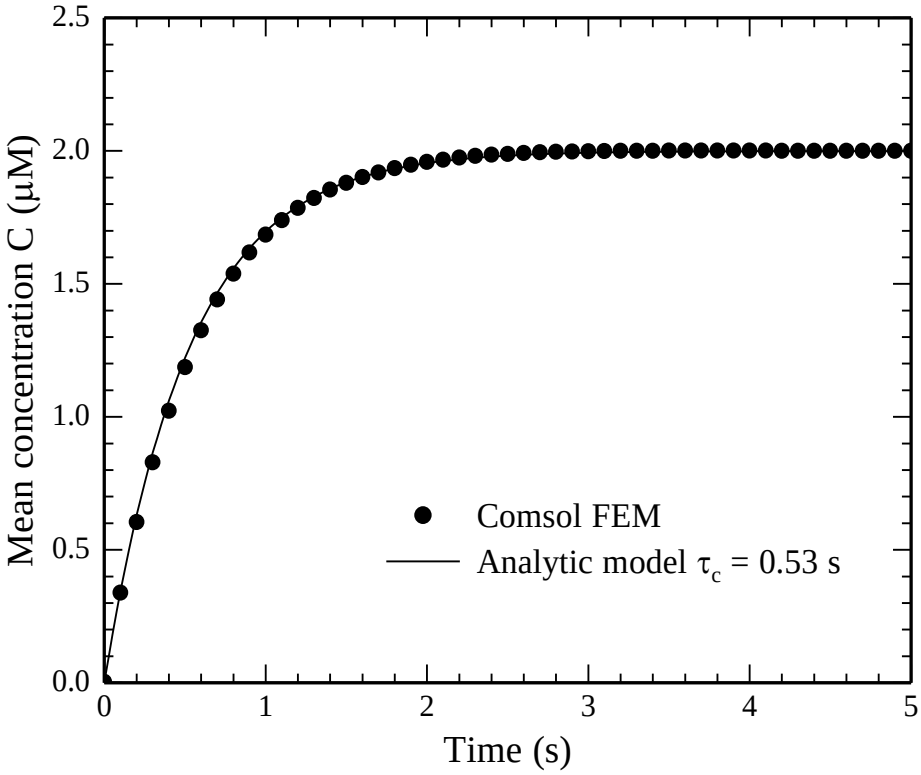

Figure 1

Fluorescence emission decay as a function of time for a representative HeLa cell after the second treatment with SLO. The resulting time constant is $\tau_{exp} \simeq 198$ s.

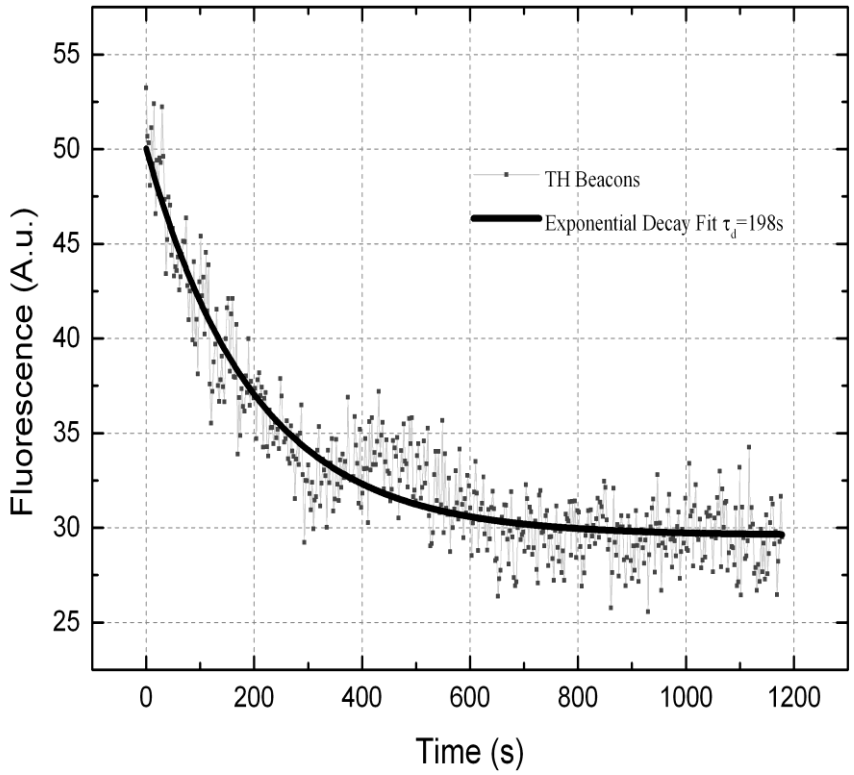

Figure 2. The average concentration of MBs in the cell as a function of transfection time. Results from a COMSOL FEM model (dots) are compared to the analytical model (black line) with the time constant $\tau_{c2} \simeq 0.53$ s.

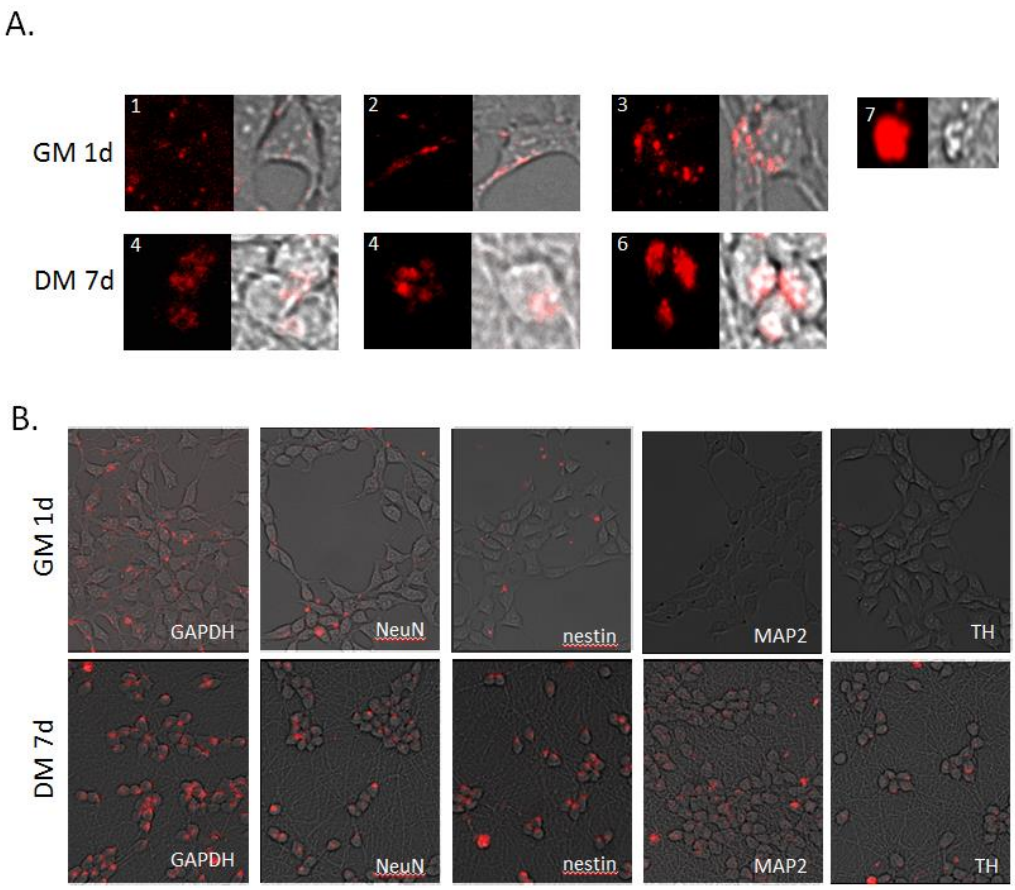

Figure 3. Different MB signal patterns observed in LUHMES cells grown in GM 24 h after transfection (A) and 168 h post differentiation (B). A1, B1 - dotted signals; A2, B2 - compact punctate shape; A3, B3 - cluster-like fluorescence. (C) C1 - Large bright fluorescent clusters originating from apoptotic cells (artifact). This pattern of signal was excluded from calculations of the number of positive cells and signal intensity. C2 - Morphology of apoptotic cell with blebbing. The signal shown is using GAPDH-MBs.

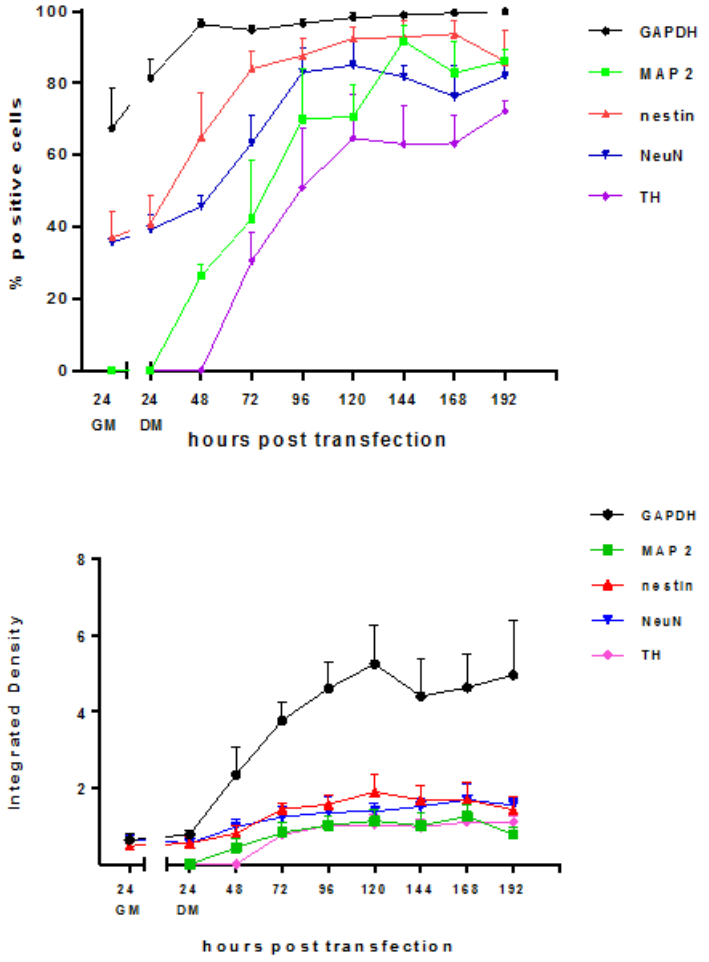

Figure . Signals from molecular beacons targeting housekeeping gene expression of GAPDH, intermediate filament protein, and markers for neuronal progenitors (nestin), microtubule-associated protein 2 (MAP2), neuronal nuclear antigen (NeuN), and tyrosine hydroxylase (TH). Cells were SLO transfected and seeded in growth medium (GM), containing 40 ng/ml bFGF. The differentiation process was started 24 h later culturing in differentiation medium (DM) supplemented with dbcAMP, tetracycline, and GDNF.

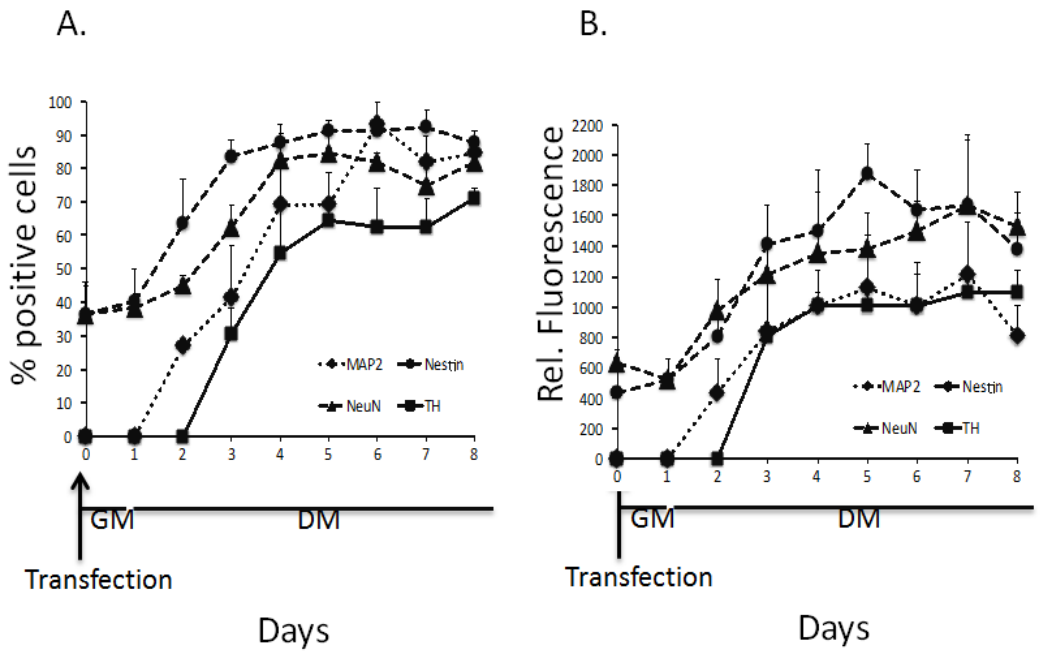

Figure 4. A. Percentage of cells expressing the neuronal markers nestin, MAP2, NeuN, and TH. Results are presented as mean ± standard error of the mean (SEM). B. Integrated density of MBs targeting the neuronal markers. Data are displayed as mean ± standard error of the mean.

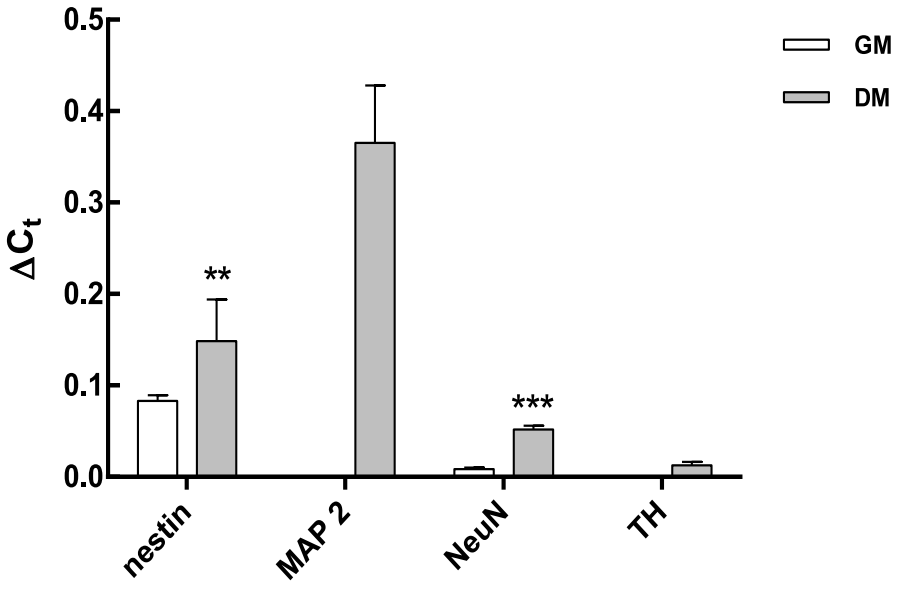

Figure 5. Analysis of mRNA expression levels of neuronal markers using qRT-PCR in non-differentiated and dopamine-like differentiated LUHMES. Expression was normalized to GAPDH mRNA expression. Data are expressed as mean ± SEM. **P<0.01, ***P<0.001.